THÈSE DE DOCTORAT

Soutenue à Aix-Marseille Université
le 22 Septembre 2020 par

Giorgio Sarno

A numerical approach to spin foam models of quantum gravity

Approche numérique aux modèles de mousse de spin de la gravité quantique

Discipline
Physique et Sciences de la Matière

Spécialité
Physique Théorique et Mathématique

École doctorale
ED 352 Physique et sciences de la matiere

Laboratoire
Centre de Physique Théorique de Marseille

Composition du jury

Bianca Dittrich Perimeter Institute	Rapporteure
Jonathan Engle Florida Atlantic University	Rapporteur
John Barrett Nottingham University	Examinateur
Sebastian Steinhaus Universität Jena	Examinateur
Federico Piazza Aix-Marseille Université	Examinateur
Alejandro Perez Aix-Marseille Université	Examinateur
Simone Speziale Aix-Marseille Université	Directeur de thèse

Je soussigné, Giorgio Sarno, déclare par la présente que le travail présenté dans ce manuscrit est mon propre travail, réalisé sous la direction scientifique de Simone Speziale, dans le respect des principes d'honnêteté, d'intégrité et de responsabilité inhérents à la mission de recherche. Les travaux de recherche et la rédaction de ce manuscrit ont été réalisées dans le respect à la fois de la charte nationale de déontologie des métiers de la recherche et de la charte d'Aix-Marseille Université relative à la lutte contre le plagiat.

Ce travail n'a pas été précédemment soumis en France ou à l'étranger dans une version identique ou similaire à un organisme examinateur.

Abstract

Spin foam models provide a Lorentz-covariant definition of the dynamics of loop quantum gravity. They offer a background-independent and non-perturbative quantization of gravity, and in their semiclassical limit, they are related to discretized General Relativity. However, the analytic complexity of the models is such that key questions concerning their theoretical consistency and physical predictions are still open. In this thesis, I introduce a systematic framework to perform numerical computations in this domain, to go beyond the limitations of the analytical techniques. The thesis contains an introduction to spin foam theories from a theoretical and a numerical standpoint, in particular to the EPRL model. I then present four of the six papers I published during my Ph.D., where the numerical framework was used to study critical open problems in the field. These include the numerical study of the semiclassical limit of a 4-simplex, recovering its Regge action and confirming known analytical computations ; a study of non-simplicial spin foams to offer an insight into the continuum limit of the theory ; a new approach to investigate extended triangulations and their semiclassical limit. Applied to a particular transition amplitude, the new approach allowed me to recover geometrical configurations compatible with curved boundary data, and to argue against an important dispute in the literature referred to as flatness problem. These results open a window for calculations in spin foam theories and they provide a new path to address their still unresolved questions.

Résumé

Les modèles de mousse de spin proposent une définition covariante de Lorentz de la dynamique de la gravité quantique en boucle. C'est une approche non-perturbative qui a deja obtenu un resultat important, reproduire la Relativité Générale discrétisée dans une limite semi-classique. Cependant, la complexité analytique des modèles est telle que des questions clés concernant leur cohérence théorique et leurs prédictions physiques restent ouvertes. Dans cette thèse, j'introduis un cadre systématique pour effectuer des calculs numériques dans ce domaine, afin de dépasser les limites des techniques analytiques. La thèse contient une introduction aux théories de mousse de spin d'un point de vue théorique et numérique, en particulier au modèle EPRL. Je présente ensuite quatre des six articles que j'ai publiés au cours de mon doctorat, où le cadre numérique a été utilisé pour étudier des problèmes critiques ouverts dans le domaine. Il s'agit notamment de l'étude numérique du modèle semi-classique limite d'un 4-simplexe, en récupérant son action de Regge et en confirmant des calculs analytiques connus ; une étude des mousses de spin non-simplexes pour offrir un aperçu de la limite du continuum de la théorie ; une nouvelle approche pour étudier les triangulations étendues et leur limite semi-classique. Appliquée à une amplitude de transition particulière, la nouvelle approche m'a permis de retrouver des configurations géométriques compatibles avec des paramètres de bord courbes, et d'argumenter contre un litige important dans la littérature appelé flatness-problem. Ces résultats ouvrent une fenêtre pour les calculs dans les théories de mousse de spin et ils fournissent une nouvelle voie pour aborder leur questions encore non résolues.

Contents

Résumé

La gravité quantique

La notion de gravité quantique renvoie au développement d'une théorie quantique de la relativité générale et à la découverte du monde caché du champ gravitationnel quantique. Depuis un siècle, les physiciens on entrepris cette quête qui s'est avérée si complexe d'avoir pris des contours presque mythiques. Après ces décennies de recherche, nous sommes encore loin d'une réponse. Dans ce cadre, les deux théories les plus significatives - la théorie des cordes et celle de la gravité quantique à boucle - vieillissent sans qu'il y ait une seule vérification expérimentale dans le meilleur des cas, ou une confirmation de leur cohérence théorique dans le pire des cas. Des alternatives existent, et le domaine semble parsemé de nombreuses approches, idées et modèles différents qui méritent d'être explorés, mais qui ne sont pas, à ce stade, suffisamment convaincants pour orienter la recherche dans une direction ou l'autre.

Cependant, dans ce scénario insatisfaisant, les progrès se poursuivent. La gravité quantique est un sujet fascinant et théoriquement fondamental qui mérite notre attention et qui continue de stimuler l'imagination des chercheurs. Cela reste un défi qui, si couronné de succès, changerait le monde. Certaines des meilleures introductions, et en particulier aux idées qui guident l'approche de la gravité quantique en boucle, se trouvent dans les premiers chapitres de [1] et [2]. Leurs motivations et explications m'ont guidé dans le choix de ce sujet de recherche, et les relire aujourd'hui me fait ressentir la même excitation que j'ai eu quand j'ai commencé ce voyage.

Dans cette thèse, nous travaillerons dans le contexte de l'approche de mousse de spin à la dynamique de la gravité quantique à boucle, ou gravité quantique à boucle covariante, avec l'objectif pratique d'effectuer des calculs numériques dans le cadre de la théorie. La gravité quantique a souvent été représentée, à juste titre, comme un problème éminemment conceptuel. En dépit de cette conception, ce travail se veut plus concret. L'objectif était d'étudier un modèle particulier, et d'être capables d'effectuer des calculs précis sur lesquels construire des interprétations physiques. Dans cette thèse, nous résumons le résultat de nos explorations.

Mousse de spin pour la gravité quantique

La théorie de mousse de spin fournit une approche particulière à la dynamique de la gravité quantique à boucle qui est à la fois indépendante du bruit de fond et covariante de Lorentz. Le plus réussi des modèles est celui proposé par Engle, Pereira, Rovelli et Livine (EPRL) [3, 4, 5] et par Freidel et Krasnov (-FK) [6]. Il est formulé comme une somme di triangulations ds simplexes, avec des paramètres de bord fixes. Il fournit des amplitudes de transition pour les états de réseaux de spin de la gravité quantique à boucle canonique limitée à des nœuds quatre valents. Une généralisation à des complexes et réseaux de spin arbitraires a également été développée [7]. L'approche de mousse de spin a pour but d'être équivalente à une somme sur des histoires de géométries quantiques et de réaliser une intégrale de chemin de gravité quantique bien définie.

Dans ce cadre, les calculs sont particulièrement complexes, et de nombreuses caractéristiques des mousses de spin demeurent inconnues. Deux des calculs analytiques les plus réussis sont les suivants.

D'une part, la présence de l'action discrète de Regge dans l'amplitude de mousse de spin d'un état semi-classique [8, 9]. Ce résultat met en relation la limite semi-classique de la théorie avec le calcul de Regge, une discrétisation de la relativité générale proposée initialement par Tullio Regge [10]. En 3-dimensions, un modèle quantique pour la gravité discrétisée, le modèle de Ponzano-Regge, a été introduit dès les années soixante [11], mais il a fallu des décennies pour obtenir un analogue en 4-dimensions. D'autre part, la fonction gravitationnelle à n-points reproduit, à l'ordre principal, celle du calcul de Regge dans la limite semi-classique [12, 13, 14, 15]. Ce résultat est d'une importance historique particulière puisqu'il a révélé les lacunes du modèle Barrett-Crane et a conduit au développement du modèle EPRL-FK. Le modèle BC ne peut pas mettre en ouvre correctement les contraintes de simplicité, responsables de la réduction de la théorie topologique BF à la gravité. La réussite du modèle EPRL est sujette à discussion dans la communauté : il s'agit d'une question ouverte qui sera partiellement abordée dans cette thèse. Pour motiver cette thèse, permettez-nous d'évoquer d'emblée deux questions cruciales qui font l'objet de discussions au sein de la communauté. Premièrement, dans le cas des triangulations étendues, la limite semi-classique de la théorie n'est pas encore bien comprise. Demeure notamment ouverte la question de savoir quelles géométries semi-classiques dominent les sommations sur les degrés de liberté globaux. Différents calculs suggèrent que la somme des degrés de liberté globaux est dominée par des géométries plates, à savoir des géométries avec un angle de déficit autour des faces globales multiples de $4\pi/\gamma$,, soit γ, le paramètre d'Immirzi. Cette observation est appelée *flatness-problem*, et a été mentionnée par Freidel et Conrady [16], Bonzom [17], et Han [18]. De plus, Hellmann et Kamiński [19] ont proposé une analyse différente, basée sur le calcul de l'ensemble du wavefront set de la fonction de partition de mousse de spin et d'une interprétation géométrique de ses variables, et ils ont trouvé un problème similaire. Une autre analyse en phase stationnaire du modèle EPRL euclidien a été réalisée par Oliveira dans [20] en étudiant une triangulation particulière composée de trois 4-simplexes, appelée Δ_3. Ils incluent toutes les contraintes sur les paramètres de bord pour obtenir une amplitude non exponentiellement supprimée. Cependant, cette affirmation initiale a récemment été remise en question par Kaminski et Engle [21]. Un deuxième problème ouvert concerne la limite du continuum de la théorie qui n'est pas bien comprise puisqu'il n'y a pas de hiérarchie claire tout en augmentant la complexité d'une amplitude de transition. De plus, même si le modèle est exempt de divergences dans l'ultraviolet, il existe des divergences potentielles dans l'infrarouge à grand volume. En principe, celles-ci peuvent nécessiter une procédure de renormalisation et leur étude pourrait être importante pour la définition correcte de la limite du continuum. Cela a été largement étudié et peut être réalisé de différentes manières : en affinant le 2-complexe comme dans [22, 23, 24], ou via une résumation comme proposé dans [25, 26]. Dans [27], a été proposé un algorithme permettant de déterminer systématiquement la divergence potentielle de tous les diagrammes de mousse de spin dans le modèle EPRL.

Tous ces arguments attendent une réponse claire, et ils constituent des préoccupations quant à la cohérence de la théorie. L'objectif de cette thèse est de répondre à certaines de ces questions.

Au cours de mon doctorat, nous avons travaillé sur un problème précis et technique : comment calculer numériquement les amplitudes de transition des mousses de spin. Malheureusement, les calculs analytiques dans ce cadre ne sont pas toujours disponibles, et ils s'accompagnent de nombreuses approximations et hypothèses. Pour cette raison, nous avons décidé de nous tourner vers les méthodes numériques. Lorsque nous avons commencé, si certaines méthodes numériques étaient disponibles – particulièrement dans le modèle $SO(4)$ EPRL [28] [29] - il manquait une approche systématique. Nous avons décidé de concentrer nos efforts sur deux modèles différents. D'une part, la théorie tridimensionnelle $SU(2)$ BF utilisée comme modèle-jouet, et d'autre part, le modèle complet $SL(2,\mathbb{C})$ EPRL. Mon travail a conduit à la publication de six articles, dont trois co-rédigés avec mon superviseur. Dans cet aperçu, je présenterai les recherches qu'ils contiennent et les liens qui les unissent. Dans les chapitres 2 et 3, je présenterai, respectivement, une introduction théorique et numérique des outils et des techniques que j'ai exploités. Je me concentrerai ensuite sur quatre de nos articles. Dans ces travaux et dans cette thèse, je conserverai ce que nous appelons *une approche opérationnelle*. Je veux être capable de calculer les quantités que nous définissons et de spéculer sur le contenu physique de la théorie seulement après qu'un calcul ait été effectué et réalisé. Du moment que de nombreuses caractéristiques de la théorie ne

sont pas encore connues, je considère que cette approche puisse conduire à des résultats originaux et éviter les interprétations trompeuses.

En collaboration avec un postdoctorant de mon laboratoire, nous avons introduit dans [30] la bibliothèque `sl2cfoam` où nous avons fourni les outils pour évaluer numériquement l'amplitude de vertex du mousse de spin $SL(2,\mathbb{C})$ EPRL et $SU(2)$ BF. Elle est basée sur la décomposition de l'amplitude EPRL en termes de fonctions booster et des invariants $SU(2)$ introduits dans [31], un outil fondamental que nous allons brièvement passer en revue dans 3.1.3. Dans les chapitres suivants, nous fournissons une introduction théorique et numérique, et nous passons en revue les méthodes communes utilisées tout au long de nos travaux. Ensuite, nous présentons nos travaux [33, 35, 37, 38], qui peuvent être divisés en deux parties conceptuellement différentes. Dans la première partie, nous avons appliqué des méthodes numériques pour confirmer des résultats d'analyse déjà connu dans le domaine. Cela nous a permis, à la fois d'effectuer un contrôle de cohérence de nos outils numériques, mais aussi de compléter l'analyse analytique (hessian cc, validité à petits spin, etc.). Nous avons étudié la limite asymptotique d'un 4-simplex euclidien dans la théorie BF [32] et dans le modèle EPRL $SL(2,\mathbb{C})$ [33]. Nous avons récupéré la limite de spin large étudiée dans [34] et dans [8] même si, dans cette thèse, nous ne présentons que le cas $SL(2,\mathbb{C})$, plus complexe des autres. Dans le chapitre 5, nous présentons les difficultés analytiques et numériques d'un calcul de large-spin. Nous avons récupéré la limite asymptotique d'un 4-simplex euclidien ; cependant, nous n'avons pas pu obtenir le même résultat pour un 4-simplex lorentzien, en raison de difficultés techniques qui y seront détaillées. Dans la deuxième partie, nous avons appliqué nos méthodes numériques pour explorer de nouveaux territoires. Dans [35], nous avons considéré les mousses de spin EPRL généralisées de KKL avec des vertex non-simplexes, du type de ceux qui ont été suggérés pour la cosmologie des mousses de spin [36]. Dans ce contexte, on n'a pas la relation directe avec la gravité en termes d'action de Regge, mais l'amplitude de vertex est plus simple à calculer, ce qui permet d'étudier comment différentes amplitudes contribuent à un réseau de spin avec des paramètres de bord fixes. Nous avons examiné les amplitudes de transition entre deux réseaux de spins avec un graphique de dipole et leurs propriétés de décroissance tout en augmentant le nombre d'arêtes, de faces et de vertices. Ce travail est présenté dans 6 et vise à mettre en lumière la hiérarchie des amplitudes des mousses de spin lorsque la complexité augmente. Ensuite, nous présentons un article dans la théorie tridimensionnelle $SU(2)$ BF, également appelée modèle Ponzano-Regge. Nous étions confrontés à des difficultés difficilement surmontables lors du calcul de la grande limite de spin d'une amplitude. Comme nous le verrons, le redimensionnement homogène de l'amplitude de vertex EPRL dans la base cohérente nécessite d'énormes ressources numériques pour être réalisé. Outre les problèmes liées au temps de calcul et de précision, il faut savoir a priori à quoi s'attendre (comme la fréquence et la phase de l'oscillation de l'amplitude, la décroissance de sa loi de puissance, etc). En d'autres termes : dans cette approche, nous devions connaître analytiquement de nombreux détails pour récupérer des informations utiles à partir de nos calculs. Pour surmonter ces difficultés, dans [37], nous avons proposé une nouvelle façon numérique de rechercher des géométries semi-classiques dans des amplitudes de mousse de spin avec de nombreuses faces internes. Nous avons développé et testé nos algorithmes dans le modèle Ponzano-Regge, qui nous permettait d'avoir un contrôle analytique complet. Les résultats sont passionnants. En analysant une amplitude de transition composée de trois tétraèdres collés ensemble, une Δ_3 tridimensionnel, nous avons compris le comportement semi-classique de sa grande limite de spin de la manière suivante. À paramètres de bord fixes, nous cherchons des points de phase stationnaires dans la sommation globale interne pour récupérer son comportement semi-classique. Nous présentons cet article dans le chapitre 7. Cette méthode est ensuite appliquée à la théorie quadridimensionnelle $SU(2)$ BF [38]. Même si elles sont plus simples que dans le modèle EPRL, elles en partagent certaines caractéristiques. Par exemple, tous les arguments en faveur de la planéité des amplitudes de mousse de spin peuvent être formellement appliqués aux deux modèles. Là encore, nous avons décidé d'étudier l'amplitude Δ_3, désormais formée par trois 4-simplex partageant un triangle. Même dans ce contexte plus simple, nous avons trouvé quelque chose de surprenant. Des points de phase stationnaires apparaissent pour les configurations de limites plates et non plates, ce qui contredit certaines des analyses mentionnées précédemment. Nous avons ensuite analysé les points où les arguments de planéité peuvent s'effondrer, et nous en avons parlé dans l'article. Ce document est présenté au chapitre 8. Toutefois, ces résultats ne suffisent pas à

eux seuls pour apporter une réponse à la question de la planéité dans le modèle EPRL. Tout d'abord, le même calcul doit être effectué dans le modèle EPRL. Deuxièmement, la triangulation Δ_3 est plutôt triviale du point de vue du calcul de Regge. Dans le Regge Calculus, les variables fondamentales sont les longueurs d'une triangulation mais, en 4-dimensions, la Δ_3 n'a pas de longueurs de bulk, seulement une aire de bulk. En principe, on voudrait récupérer les solutions des équation du mouvement de Regge dans la limite semi-classique de la théorie. Pour surmonter ce problème, nous travaillons actuellement sur un calcul impliquant une triangulation qui permet une équation de Regge du mouvement non triviale. Nous voulons comparer les points de phase stationnaires dans le modèle BF et dans le modèle EPRL pour comprendre si les contraintes de simplicité sont correctement imposées. De plus, nous pensons que l'approche du « wavefront set », utilisée par Hellman et Kaminski dans le cas de $SO(4)$, pourraît conduire à une analyse intéressante de la théorie physique de $SL(2,\mathbb{C})$ et de sa fonction de partition. Nous travaillons également dans cette direction, en espérant qu'elle pourra apporter un éclairage sur l'analyse semi-classique des triangulations étendues.

Il devrait être maintenant clair qu'une grande partie de notre travail a été consacrée à des questions techniques, tant d'un point de vue numérique qu'analytique. Toutefois, il est possible d'en tirer des enseignements intéressants et généralisables. Les modèles de mousse de spin sont confrontés à plusieurs questions ouvertes, dont certaines existent maintenant depuis près d'une décennie. Comme nous l'avons déjà mentionné, de nombreux arguments concernant la planéité ont été avancés au fil des ans. Mais en l'absence de calculs concrets et précis, il s'agit encore de spéculations. Nous avons trouvé un contre-exemple pour prouver que, dans un cas simple, elles ne sont pas valables. Même si ce résultat ne détermine pas en soi la validité du modèle, il montre que certains calculs peuvent être effectués avec précision et qu'ils peuvent nous aider à comprendre la théorie. De nombreuses difficultés dans l'exécution des calculs numériques sont encore présentes, et nous en aborderons quelques-unes dans 3.2. Je suis de l'avis que les calculs avec de nombreux vertices dans le cadre du model EPRL soient une possibilité qui mériterait d'être explorée davantage, numériquement ou analytiquement, employant de nouvelles méthodes. Nous avons décidé de prendre ces modèles au sérieux, en les poussant à leurs limites. Au lieu de céder à la tentation de la construction de nouveaux modèles, nous pensons qu'une voie différente puisse être suivie. Nous devons explorer les théories dont nous disposons déjà et en révéler les caractéristiques.

Ce manuscrit vise à fournir une introduction technique aux mousses de spin, en particulier au modèle EPRL, d'un point de vue opérationnel. Nous souhaitons que cela aide le lecteur intéressé à comprendre comment, au cours des dernières années, a été travaillée à Marseille la théorie de mousse de spin, avec l'espoir que cela la fasse avancer.

Chapter 1

Overview

1.1   Quantum Gravity

Quantum Gravity is the task of developing a quantum theory of General Relativity to unveil the hidden world of the quantum gravitational field. It has been undertaken by physicists already a century ago, and it has proven to be so challenging to assume almost mythological contours. After decades of research, we are still far away from an answer. The two most significant theories facing the challenge, string theory and loop quantum gravity, are growing old without a single experimental check in the best scenario, or a confirmation of their theoretical consistency in the worst. Alternatives exist, and the field seems scattered with many different approaches, ideas and models worth to be explored but still not convincing enough to guide research in one direction or another.

However, in this unsatisfactory scenario, progress continues. Quantum Gravity is a fascinating and theoretically fundamental topic that deserves our attention and that still drives the imaginations of researchers. It still is a game that, if won, would change the world. Some of the best introductions to it, and in particular to the ideas guiding loop quantum gravity's approach to the problem, can be found in the initial chapters of both [1] and [2]. Their motivations and explanations guided me in choosing this topic of research, and rereading them today make me feel the same thrill I had when I began this journey.

In this thesis, we will work in the context of spin foam approach to the dynamics of loop quantum gravity, or covariant loop quantum gravity, with the practical goal of performing numerical computations within the theory. Quantum Gravity can be rightly considered a very conceptual problem. Despite that, our work has been more down to earth. We wanted to study a particular model, and to be able to perform precise computations on which we could build physical interpretations. In this thesis, we summarize the result of our explorations.

1.2   Spin Foam for Quantum Gravity

The spin foam framework provides an approach to the dynamics of loop quantum gravity that is both background-independent and Lorentz covariant. The most successful model is the one proposed by Engle, Pereira, Rovelli and Livine (EPRL) [3, 4, 5] and independently by Freidel and Krasnov (-FK) [6]. It is formulated as a sum over simplicial triangulations with a given boundary. It provides transition amplitudes for spin network states of canonical Loop Quantum Gravity restricted to four valent nodes, and a generalization to arbitrary complexes and spin-networks has also been developed [7]. The spin foam approach aims to be equivalent to a sum over histories of quantum geometries and to realize a well-defined quantum gravity path integral.

Computations in this framework are particularly complex, and many features of spin foams are still not known. Two of the most successful analytical calculations are the following. On the one hand, the presence of the discrete Regge action in the spin foam amplitude of a semiclassical state [8, 9] relating the semiclassical limit of the theory with Regge calculus, a discretization of general relativity firstly proposed by Tullio Regge [10]. In 3-dimensions, a quantum model for discretized gravity, the Ponzano-Regge model, was introduced already in the sixties [11], but it took decades to obtain a 4-dimensional analogous. On the other hand, the graviton n-point function reproduces at the leading order the one of Regge calculus in the semiclassical limit [12, 13, 14, 15]. This result is of particular historical importance since it revealed the Barrett-Crane model's shortcomings and led to the development of the EPRL-FK model. The BC model cannot correctly implement the simplicity constraints, responsible for reducing the topological BF theory to gravity. The question if the EPRL model is succeeding in implementing them is a subject of discussion in the community and an open issue that will be partially addressed in this thesis.

As motivations for this thesis, let me mention upfront two crucial open questions discussed in the community. First, in the case of extended triangulations, the theory's semiclassical limit is still not well understood. In particular, the question of what semiclassical geometries dominate the summations over bulk degrees of freedom is still open. Different calculations suggest that the summation over bulk degrees of freedom is dominated by flat geometries, namely by geometries with a deficit angle around bulk faces multiple of $4\pi/\gamma$, being γ the Immirzi parameter. This observation is called *flatness problem*, and it has been mentioned by Freidel and Conrady [16], Bonzom [17], and Han [18]. Moreover, Hellmann and Kamiński [19] proposed a different analysis, based on the calculation of the wavefront set of the spin foam partition function and a geometrical interpretation of its variables, and they found a similar problem. Another stationary phase analysis of the euclidean EPRL model has been carried out by Oliveira in [20] studying a particular triangulation composed of three 4-simplex called Δ_3. They include all the constraints on the boundary data to obtain a non-exponentially suppressed vertex amplitude. However, this initial claim has been recently questioned by Kaminski and Engle [21]. A second open problem regards the continuum limit of the theory which is not well understood since there is not a clear hierarchy while increasing the complexity of a transition amplitude. Also, even if the model is free of ultraviolet divergences, there are potential large-volume infrared divergences. In principle, these may require a renormalization procedure and their study could be important for the correct definition of the continuum limit. This has been extensively studied and can be achieved in different ways: refining the 2-complex as in [22, 23, 24], or via a resummation as proposed in [25, 26]. In [27] an algorithm to systematically determine the potential divergence of all spin foam diagrams in the EPRL model has been proposed.

All these arguments are still waiting for a clear answer, and they are major concerns regarding the consistency of the theory. With this thesis, we want to address some of these questions.

During my Ph.D., I have worked on a precise and technical problem: how to compute spin foam transition amplitudes numerically. Unfortunately, analytical calculations in this framework are not always available, and they come with many approximations and assumptions. For this reason, we decided to look at numerical methods. When we started, some numerics was available, especially in the $SO(4)$ EPRL model [28] [29] but a systematic approach was lacking. We decided to concentrate our efforts on two different models. On one side, the 3 and 4 dimensional $SU(2)$ BF theory used as a toy model, and on the other, the complete $SL(2, \mathbb{C})$ EPRL model. My work has led to six published papers, three with my supervisor and three without. In this overview, I will present the research contained in these and how they relate to one another. In Chapter 2 and 3, I will present a theoretical and a numerical introduction to the tools and techniques I have used. I will then focus on four of our papers. In these works and this thesis, I will keep what we call *an operational approach*. I want to be able to compute the quantities we define and to speculate about the physical content of the theory only after a computation has been carried out and performed. Since many of the features of the theory are still not known, I think that this approach can lead to original results and to avoid misleading interpretations.

In collaboration with a postdoc in my group, we introduced in [30] the library `sl2cfoam` where

we provided the tools to evaluate the $SL(2, \mathbb{C})$ EPRL and $SU(2)$ BF spin foam vertex amplitude numerically. It is based on the decomposition of the EPRL vertex amplitude in terms of booster functions and $SU(2)$ invariants introduced in [31] a fundamental tool that we will briefly review in 3.1.3. In the following Chapters, we provide a theoretical and numerical introduction, and we review the common methods used throughout our works. Then, we present our papers [33, 35, 37, 38], which can be divided into two conceptually different parts. In the first, we applied numerical methods to confirm analytical results already established. This allowed us to perform a consistency check of our numerical tools but also to complete the analytical analysis (hessian cc, small spin validity, etc). We studied the asymptotic limit of an euclidean 4-simplex in BF theory [32] and in the $SL(2, \mathbb{C})$ EPRL model [33]. We recovered the large spin limit studied in [34] and in [8] even if, in this thesis, we present only the much more challenging $SL(2, \mathbb{C})$ case. In Chapter 5, we present the analytical and numerical difficulties of a large spin limit computation in spin foam. We recovered the asymptotic limit of a euclidean 4-simplex. However, we could not obtain the same result for a lorentzian 4-simplex due to technical difficulties that will be addressed and explained.

In the second part, we applied our numerical methods to explore new territories. In [35], we considered the generalized EPRL spin foams of KKL with non-simplicial vertices, of the type that have been suggested for spin foam cosmology [36]. In this context, one does not have the direct relation to gravity in terms of the Regge action, but the vertex amplitude is simpler to compute, allowing to study how different foams contribute at fixed boundary spin-network. We looked at transition amplitudes between two spin networks with dipole graphs and their decaying properties while increasing the number of edges, faces and vertices. This work is presented in 6 and aims to shed some light on the hierarchy of spin foam amplitudes when complexity increases. We then present a paper in the 3-dimensional $SU(2)$ BF theory, also called the Ponzano-Regge model. In fact, we had to take a step back: we were facing difficulties hardly surmountable when computing the large spin limit of an amplitude. As we will see, the homogeneous rescaling of the EPRL vertex amplitude in the coherent basis requires enormous numerical resources to be accomplished. Also, aside from computational time and accuracy problems, one needs to know a priori what to expect (such as the frequency and phase of the amplitude's oscillation, its power law decay, etc) to be able to obtain semiclassical information from numerics. In other words: in that approach, we had to analytically know many details to recover useful information from our computations. To overcome these difficulties, in [37], we proposed a new numerical way of searching for semiclassical geometries in spin foam amplitudes with many internal faces. We developed and tested our algorithms in the Ponzano-Regge model, where we have full analytical control. The results are exciting. Analyzing a transition amplitude composed by three tetrahedra glued together, a 3-dimensional Δ_3, we understood the semiclassical behaviour of its large spin limit in the following way. At fixed boundary data, we look for stationary phase points in the internal bulk summation to recover the semiclassical behavior of a particular set of boundary geometry. We report this paper in Chapter 7. This method is then applied to 4-dimensional $SU(2)$ BF theory [38]. Even if simpler than the EPRL model, they share some features. For instance, all the arguments for the flatness of spin foam amplitudes can formally be applied to both models. Again, we decided to study the Δ_3 amplitude, now formed by three 4-simplex sharing a triangle. Even in this simpler context, we found something somewhat surprising. Stationary phase points arise for flat and non-flat boundary configurations contradicting some of the analyses mentioned before. We then analyzed where the flatness arguments may break down, and we discussed those. This paper is reported in Chapter 8. However, these results alone are not enough to draw an answer to the question of flatness in the EPRL model. First of all, the same computation should be performed in the EPRL model. Secondly, the Δ_3 triangulation is rather trivial from a Regge Calculus point of view. In Regge Calculus, the fundamental variables are the lengths of a triangulation but, in 4 dimensions, the Δ_3 has no bulk lengths, only a bulk area. In principle, one would like to recover solutions of the Regge equation of motions in the semiclassical limit of the theory. To overcome this problem, we are currently working on a computation involving a triangulation that allows non-trivial Regge equation of motions. We want to compare stationary phase points in BF and in the EPRL model to understand if the simplicity constraints are imposed correctly. Moreover, we think that the wave front set approach, used by Hellman and Kaminski in the $SO(4)$ case, could lead to an

3

interesting analysis of the $SL(2,\mathbb{C})$ physical theory and of its partition function. We are also working in this direction, hoping it could shed some light on the semiclassical analysis of extended triangulations.

It should now be clear that a large part of our work has addressed technical questions from a numerical and analytical standpoint. However, we believe that some interesting and generalizable lessons can be drawn from it. Spin foam models face many open questions, and some have now been around for nearly a decade. As mentioned before, many arguments concerning the flatness have been carried out throughout the years. But without actual and precise computations, these remain speculations. We found a counterexample to prove that, in a simple case, these are not valid. Even if this result in itself does not determine the validity of the model, it shows that some computations can precisely be done and that they can help us in understanding the theory. Many difficulties in performing numerical calculations are still present, and we will address some of those in 3.2. Anyway, we believe that they can be overcome with some more work and that computations with many vertices in the EPRL framework are a possibility worth to be further explored. Both numerically or analytically, using new methods. In general, we decided to take these models seriously, pushing them to their limits. Instead of surrender to the temptation of model-building, we believe that a different path can be taken. We need to explore the theories that we already have, and to unveil some of their features.

This manuscript aims to provide a technical introduction to spin foam, particularly to the EPRL model, from an operational perspective. We hope that this can help an interested reader in understanding the work that has been done in spin foam theory in Marseille during the last years, and hopefully in pushing it forward.

Chapter 2

Theoretical Introduction

In this Chapter we introduce the theoretical framework and the definition of spin foam models for quantum gravity. We introduce the notation and the theoretical tools that will be used throughout the following chapters and in the papers presented in this thesis. We divide the Chapter into two sections. The first concerns classical General Relativity (GR) and its relations with BF theory, we recommend [39, 40] for more details. We also introduce Regge Calculus, a discretization of General Relativity that will play an important role in understanding the quantum theory's semiclassical limit. In the second part, we define the partition function of BF theory and its discretization on a triangulation. Finally, we introduce the EPRL model as a proposal for the quantization of constrained BF theory. We follow [41]. We also provide a brief review of the coherent states of the theory that will play an important role in understanding the semiclassical limit studied in Chapter 5.

2.1 Classical BF Theory and General Relativity

2.1.1 General Relativity and the Holst Action

General Relativity describes the spacetime structure as a 4-dimensional differentiable manifold $\mathcal{M}$. The relative distance between its spacetime points is specified by the metric tensor $g_{\mu\nu}$ which defines the line element

$$ds^2 = g_{\mu\nu}dx^\mu dx^\nu \tag{2.1}$$

where x^μ is a set of coordinates on $\mathcal{M}$. To compare geometries at different spacetime points, one defines a connection on $\mathcal{M}$. In GR, this is achieved with the torsionless Levi Civita connection $\Gamma^\rho_{\mu\nu}$, as a function of the gravitational field. The curvature of spacetime is encoded in the Riemann tensor $R^\sigma_{\mu\rho\nu}$. In its original formulation, GR is encoded by the Hilbert-Einstein action

$$S_{HE}[g_{\mu\nu}] = \frac{1}{2\kappa} \int d^4x \sqrt{-g} R[g_{\mu\nu}] \tag{2.2}$$

with $\kappa = 8\pi G$, G as the gravitational constant. g is the determinant of the metric tensor and R is the scalar curvature of $g_{\mu\nu}$. The Einstein equations of motion are

$$R_{\mu\nu} - \frac{1}{2}g_{\mu\nu}R = 8\pi G T_{\mu\nu} \tag{2.3}$$

where $T_{\mu\nu}$ is the covariant version of the energy-momentum tensor and $R_{\mu\nu}$ the Ricci tensor. GR can be rewritten using the tetrad formalism and with the connection as an independent field. A tetrad is a quadruple of 1-forms, $e^I_\mu(x)$ such that

$$g_{\mu\nu}(x) = e^I_\mu(x)e^J_\nu(x)\eta_{IJ}. \tag{2.4}$$

Here $I = 0, 1, 2, 3$ are internal flat indices and come together with an additional invariance under a local gauge group $G = SO(3, 1)$. Tetrads provide a local isomorphism between a general reference frame and an inertial one, characterized by the flat metric η_{IJ}. The definition is invariant under

$$e^I_\mu(x) \longrightarrow e'^I_\mu(x) = \Lambda^I_J(x)e^J_\mu(x). \tag{2.5}$$

Now the connection ω is treated as an independent variable, and its curvature is given by

$$F^{IJ}_{\mu\nu} = \partial_\mu \omega^{IJ}_\nu - \partial_\nu \omega^{IJ}_\mu + \omega^I{}_{K\mu}\omega^{KJ}_\nu - \omega^J{}_{K\mu}\omega^{KI}_\nu. \tag{2.6}$$

If the conncection is Levi-Civita, namely if $\omega = \omega(e)$, then

$$F^{IJ}_{\mu\nu}(\omega(e)) \equiv e^{I\rho}e^{J\sigma}R_{\mu\nu\rho\sigma}(e). \tag{2.7}$$

In these variables, the Hilbert-Einstein action can be rewritten as

$$S(e^I_\mu, \omega^{IJ}_\mu) = \frac{1}{2\kappa}\varepsilon_{IJKL} \int e^I \wedge e^J \wedge F^{KL}\left(\omega(e)\right), \tag{2.8}$$

and the field equations become

$$\omega^{IJ}_\mu = e^I_\nu \nabla_\mu e^{J\nu}, \qquad G_{\mu\nu}(e) = 0. \tag{2.9}$$

Since the connection is now considered a fundamental field, a new term compatible with all the action's symmetries can be added to the Lagrangian. This is

$$\delta_{IJKL}e^I \wedge e^J \wedge F^{KL}(\omega), \tag{2.10}$$

where $\delta_{IJKL} \equiv \delta_{I[K}\delta_{L]J}$. In fact

$$\delta_{IJKL}e^I \wedge e^J \wedge F^{KL}(\omega(e)) = \epsilon^{\mu\nu\rho\sigma}R_{\mu\nu\rho\sigma}(e) \equiv 0. \tag{2.11}$$

This term (with a coupling constant $1/\gamma$) can be added to the Hilbert-Einstein action without changing the equation of motions for non-degenerate tetrads. The action obtained is called the Holst's action

$$\begin{aligned} S\left(e, \omega\right) &= \frac{1}{2\kappa}\left(\varepsilon_{IJKL} + \frac{1}{\gamma}\delta_{IJKL}\right) \int e^I \wedge e^J \wedge F^{KL}\left(\omega\right) \\ &= \frac{1}{2\kappa} \int (^\star e^I \wedge e^J + \frac{1}{\gamma}e^I \wedge e^J) \wedge F_{IJ}(\omega). \end{aligned} \tag{2.12}$$

This action plays an essential role in the definition of the Loop Quantum Gravity canonical quantization and, therefore, in spin foam models. GR and the Holst action 2.12 can also be rewritten as a constrained BF theory but before moving into that we review topological BF theory.

2.1.2 BF theory as a topological theory

Consider a Lie Group G, $\mathfrak{g}$ as its Lie Algebra and $\mathcal{M}$ d-dimensional manifold. Classical BF theory is defined by the action

$$S[\mathrm{B}, \omega] = \int_{\mathcal{M}} B^{IJ} \wedge F_{IJ}(\omega), \tag{2.13}$$

with B as $\mathfrak{g}$ valued $(d-2)$-form and ω connection on a G principal bundle over $\mathcal{M}$. $F(\omega)$ is the curvature of ω . This theory has no local excitations: gauge transformations locally relate all the solutions of its equations of motion. The equations of motion are obtained imposing $\delta S = 0$ and we get

$$F = 0, \qquad d_\omega B = 0, \tag{2.14}$$

where d_ω stands for the exterior covariant derivative. All their solutions look the same locally. BF theory describes a world with no local degrees of freedom. $F = 0$ forces the spin connection ω to be flat, and all flat connections are locally the same up to gauge transformations. The second equation $d_\omega B = 0$ is subtler. It is not true that its solutions are locally the same up to a gauge transformation in the usual sense. But BF theory has another symmetry given by

$$\omega \mapsto \omega, \qquad B \mapsto B + d_\omega \eta, \tag{2.15}$$

for some $(d-3)$-form η. These transformations leave the action unchanged, when ω is flat, any B field with $d_\omega B = 0$ can be locally written as $d_\omega \eta$ for some η. We can conclude that, locally, all solutions of the BF theory field equations are equal modulo gauge transformations and transformations such as 2.15. In a BF theory, the gauge symmetries are so vast that all the solutions to the equations of motion are locally pure gauge. If we specialize $G = SU(2)$ and $d = 3$ we recover Riemannian General Relativity in which the field B_a^i is given by the tetrad frames e_a^i. General Relativity in 4 dimensions, however, can not be recover so easily. It is necessary to impose constraints on the B field, as we do in the next section.

2.1.3 Constrained BF Theory

For a 4-dimensional spacetime, GR can be written as a constrained BF theory. We study the action

$$S[B, \omega, \lambda] = \frac{1}{2\kappa} \int_{\mathcal{M}} \left[B^{IJ} \wedge F_{IJ}(\omega) + \lambda_{IJKL} \, B^{IJ} \wedge B^{KL} \right], \tag{2.16}$$

called the Plebansky action. It depends on the fields B and ω while $\lambda_{IJKL} = -\lambda_{JIKL} = -\lambda_{IJLK} = \lambda_{KLIJ}$ is a Lagrange multiplier, a tensor in the internal space satisfying $\epsilon^{IJKL}\lambda_{IJKL} = 0$. To study the equations of motion for B we perform the variation respect to λ. On the 36 components of the field B, we obtain 20 algebraic equations

$$\epsilon^{\mu\nu\rho\sigma} B_{\mu\nu}^{IJ} B_{\rho\sigma}^{KL} = e \, \epsilon^{IJKL}, \tag{2.17}$$

with $e = \frac{1}{4!}\epsilon_{OPQR} B_{\mu\nu}^{OP} B_{\rho\sigma}^{QR} \epsilon^{\mu\nu\rho\sigma}$ [42]. This quadratic expression has two solutions [41]

$$B^{IJ} = \pm^*(e^I \wedge e^J), \quad \text{and} \quad B^{IJ} = \pm e^I \wedge e^J, \tag{2.18}$$

in terms of the remaining 16 degrees of freedom of the tetrad field e_a^I. Here $*$ is the Hodge operator. If these two sectors are related using a free parameter γ in the following way

$$B^{IJ} = \pm^*(e^I \wedge e^J) + \frac{1}{\gamma}(e^I \wedge e^J), \tag{2.19}$$

then the constrained BF action 2.16 reduces to the Holst-Palatini's action of General Relativity 2.12. γ is called the Barbero-Immirzi parameter.

$$S(e, \omega) = \frac{1}{2\kappa} \int \left({}^\star e^I \wedge e^J + \frac{1}{\gamma} e^I \wedge e^J \right) \wedge F_{IJ}(\omega). \tag{2.20}$$

It is the Hilbert-Einstein action modified by a term proportional to the Immirzi parameter that does not affect the classical equations of motion. GR is then recovered as a BF theory plus constraints, called the simplicity constraints.

Linear Simplicity Constraint

The simplicity constraints 2.18 play an important role in the construction of the spin foam models, and we need to analyze them more carefully. We want to explicitly write the two-form B^{IJ} on a boundary hypersurface Σ of $\mathcal{M}$. To do so, we choose a gauge, called the time gauge, for which the normal N^I

to all the tangent vectors in Σ is a time- like unit vector $N^I = (1, 0, 0, 0)$. In doing so, we break the $SO(1,3)$ invariance of the theory, choosing a $SU(2)$ subgroup on the boundary. The pullback to Σ of the two form B^{IJ} allows us to decompose it in its rotational and boost part as

$$N_I B^{IJ} = K^I \qquad N_I \star B^{IJ} = L^I. \tag{2.21}$$

Since we know that $B^{IJ} = \pm^*(e^I \wedge e^J) + \frac{1}{\gamma}(e^I \wedge e^J,)$ and that on the boundary Σ, $N_I e^I = 0$, we get

$$N_I B^{IJ} = N_I(e^I \wedge e^J,) = K^I \qquad N_I \star B^{IJ} = N_I \frac{1}{\gamma}(e^I \wedge e^J) = L^I. \tag{2.22}$$

We obtain an equation relating K^I and L^I.

$$K^I = \gamma L^I. \tag{2.23}$$

This important relation is called linear simplicity constraint. It connects the boost and the rotational part of the two form B^{IJ}. They are proportional, and the Barbero-Immirzi parameter gives the proportionality constant. This relation will play an essential role in the quantum theory.

2.1.4   Regge Calculus

A discretization of GR was firstly introduced by Tullio Regge in the sixties [10], an accurate review and a discussion on its relations with GR can be found in [43]. In Regge Calculus, as the new theory was called, the continuous $d-$dimensional spacetime $\mathcal{M}$ is replaced with a discretization made by $d-$simplices. A $d-$simplex σ is defined as the convex hull of its $n + 1$ vertices. These are connected by $d(d + 1)/2$ segments whose (euclidean) lengths we call l_{ij}. They specify the metric $g_{ij}(x)$ at any point $x \in \mathcal{M}$. Even if the metric is flat inside every $d-$simplex, non-flat metrics can be generated by gluing more simplices together. In a cluster of $d-$simplices, the metric is flat anywhere except on $(d - 2)$ simplices, called hinges h, where we can define curvature. A vector parallel transported on a closed loop around a hinge can come back rotated by a deficit angle

$$\delta_h(l_{ij}) = 2\pi - \sum_{\sigma > h} \Theta_h^\sigma(l_{ij}), \tag{2.24}$$

where Θ_h^σ is the dihedral angle at the corner σ, which hinges on h.

For instance, in $d = 2$, a discretization is made of triangles glued together. The hinges are the vertices and we obtain a flat discretized manifold everywhere except on the vertices. The deficit angle is given by $\delta_h(l_{ij}) = 2\pi - \sum_t \Theta_h^\sigma$ where the sum in this case runs over the triangles sharing a vertex. If $\delta_h(l_{ij}) = 2\pi$ it means that the Regge space is flat on h. The Regge Calculus provides the dynamics for a simplicial discretization. The dynamical variables are the length l_{ij} and they are ruled by the Regge action

$$\mathcal{S}_\mathcal{R}(l_{ij}) = \frac{1}{2\kappa} \sum_h A_h(l_{ij}) \delta_h(l_{ij}), \tag{2.25}$$

with A_h as the $(d - 2)$ volume of h. The remarkable result of Regge is that this action leads to the Hilbert-Einstein action in the continuum limit. When a triangulation in the Regge space $(\mathcal{M}, l_{ij})$ is refined in such a way that, given two points x and y in $\mathcal{M}$, the difference between the Regge distance and the Riemannian distance is less then a ϵ then 2.25 converges to the Hilbert-Einstein action. The equation of motion obtained from 2.25 are

$$\sum_h \frac{\partial A_h(l_{ij})}{\partial l_{ij}} \delta_h(l_{ij}) = 0, \tag{2.26}$$

because the variation of the deficit angles for all h vanishes. These equations are a discrete version of Einstein's equations. Moreover, Ponzano and Regge introduced in [11] a quantum version of Regge Calculus for three-dimensional gravity where the equations of motion impose $\delta_h = 0$. We will briefly review this model in 2.2.2 and we will study some of its features in one of the papers here presented, Chapter 7.

2.2 Quantum BF theory and Quantum Gravity models

In this section, we present a covariant quantization of BF theory. We write its partition function and we discretize it on a given triangulation. Finally, we can introduce spin foam models and then analyze how to impose the simplicity constraints at the quantum level. We present the $SL(2,\mathbb{C})$ EPRL model as a discrete model for lorentzian quantum gravity.

2.2.1 Quantized BF Theory

Formally, we can write the partition funcion for BF theory 2.13 as

$$\mathcal{Z} = \int \mathcal{D}B\mathcal{D}\omega \ \ \exp(i \int_{\mathcal{M}} B^{IJ} \wedge F_{IJ}(\omega)), \tag{2.27}$$

where $\mathcal{M}$ is taken to be compact. For simplicity, in this paragraph, we assume the gauge group G to be compact. Integrating over the B field we obtain

$$\mathcal{Z} = \int \mathcal{D}\omega \ \ \delta\left(F(\omega)\right). \tag{2.28}$$

This expression is formal: the functional integration is not well defined. To proceed, we need to step from the continuous to the discrete. We start by replacing the manifold $\mathcal{M}$ with an arbitrary cellular decomposition Δ. We introduce its dual 2-complex $\Delta^\star$ defined by a set of vertices $v \in \Delta^\star$ (dual to d-cells in Δ), edges $e \in \Delta^\star$ (dual to (d$-$1)-cells in Δ) and faces $f \in \Delta^\star$ (dual to (d$-$2)-cells in Δ). The field B is discretized associating a Lie algebra elements B_f to each $f \in \Delta^\star$. It is definded throught the smearing of the continuous $(d-2)$ form B on the $(d-2)$ cell in Δ

$$B_f = \int_{(d-2)cell} B. \tag{2.29}$$

The connection ω is discretized with group elements $g_{ev} \in G$ assigned to the half-edges of $\Delta^\star$. They are defined as the holonomy of ω along the edge $e \in \Delta^\star$.

$$g_{ev}g_{ev'} = \mathcal{P}\exp(-\int_e \omega), \tag{2.30}$$

where $\mathcal{P}$ stands for the path-ordered product. The discretized version of the path integral 2.27 reads

$$\mathcal{Z}_\Delta = \int \prod_{ev} dg_{ev} \prod_f dB_f \ e^{iB_f U_f} = \int \prod_{ev} dg_{ev} \prod_f \delta(g_{e_1 v_1} \cdots g_{e_n v_1}), \tag{2.31}$$

where $U_f = g_{e_1 v_1} \cdots g_{e_n v_1}$ represents the holonomy around a face and dg_{ev} the Haar measure on the group G. The integration in B_f is performed with the group delta function. Using the Peter-Weyl theorem, we can expand the delta function on the group

$$\delta(g) = \sum_\rho d_\rho \text{Tr}[\rho(g)], \tag{2.32}$$

where ρ are irreducible unitary representations of G (irrep), d_ρ the dimensions of the vector spaces given by the representations ρ_f and $\chi = \text{Tr}[\rho(g)]$ is the character of ρ. Using this result in 2.31

$$\mathcal{Z}_\Delta = \sum_{\{\rho\}} \int \prod_{ev} dg_{ev} \prod_f \text{Tr}[\rho_f(g_{e_1 v_1} \ldots g_{e_n v_1})]. \tag{2.33}$$

In a triangulation Δ the edges e bound exactly d different faces. So, every group element g_{ev} appears in d traces. We can use the following formula defining the projector over the invariant states of the theory

$$P_{inv}^{ev}(\rho_1, \ldots, \rho_d) := \int dg_{ev}\rho_1(g_{ev}) \otimes \rho_2(g_{ev}) \otimes \cdots \otimes \rho_d(g_{ev}), \tag{2.34}$$

where the representations matrices ρ are contracted following the structure of the triangulation. The tensor product of d ρ matrices defines a space $\mathcal{H} = \mathcal{H}^{\rho_1} \otimes \ldots \mathcal{H}^{\rho_d}$. P^e_{inv} is the projector over the invariant states in $Inv[\mathcal{H}^{\rho_1} \otimes \mathcal{H}^{\rho_1} \otimes \ldots \mathcal{H}^{\rho_d}]$. For a BF theory with a compact group, we finally get

$$\mathcal{Z}_\Delta = \sum_{\{\rho\}} \prod_f d_{\rho_f} \prod_{ev} P^{ev}_{inv}(\rho_1 \otimes \cdots \otimes \rho_d).$$ (2.35)

This expression can be rewritten as a graphical formula. The graphical notation here introduced has been used extensively throughout all our works; more details can be found in [44, 45, 35]. The projector reads

$$P^e_{inv}(\rho_1 \otimes \rho_2 \otimes \cdots \otimes \rho_d) = \text{\includegraphics{}}.$$ (2.36)

Every representation becomes a strand, every integral over the group a box. The connectivity of strands and boxes is given by the triangulation structure, namely by the pattern of indices contraction between representations.

Some examples

Fix $d = 2$ as the dimension of $\mathcal{M}$. Then, a triangulation is made by triangles glued together. At every vertex of a triangle we associate a representation ρ_i and at every edge, an integration over the group. At every element g_{ev} are assigned two representations, two wires. The BF partition function is

$$\mathcal{Z}_\Delta = \sum_{\{\rho\}} \prod_{f \in \Delta^\star} \mathrm{d}_\rho \quad ,$$ (2.37)

the open ends on the right side are linked to neighboring vertices according to the triangulation structure.

For $d = 3$ instead, Δ is made by tetrahedra. In this case, every triangle is associated with a box, and every strand is associated with the triangle's segments. We have

$$\mathcal{Z}_\Delta = \sum_{\{\rho\}} \prod_f \mathrm{d}_\rho \quad .$$ (2.38)

The 3-dimensional model with gauge group $SU(2)$ is studied more carefully in the next paragraph 2.2.2 and in one of the papers of the thesis: it is precisely the well known Ponzano-Regge model.

In $d = 4$, the triangulation is made of 4-simplices glued together. Five tetrahedra and ten triangles

compose every 4-simplex. In the graphical notation, we have that

$$\mathcal{Z}_\Delta = \sum_{\{\rho\}} \prod_f \mathrm{d}_\rho \quad , \tag{2.39}$$

where every tetrahedron is a box sharing four strands (triangles) with other tetrahedra. This model with gauge group $SU(2)$ will prove to be an important test for computations within spin foam models, as we will see in 2.2.3 and in Chapter 8.

2.2.2 The Ponzano Regge model

One of the theories studied in this thesis is the 3-dimensional BF model with gauge group $G = SU(2)$, also called the Ponzano-Regge model. General relativity in three dimensions has no propagating gravitational degrees of freedom. It is a perfect example of topological theory, and the BF quantization can be here easily implemented. In this case, the delta function is obtained on the basis of Wigner functions $D^j(g)$ and Eq. 2.38 becomes

$$\mathcal{Z}_\Delta = \sum_{j_f} \int \prod_e dg_{ev} \prod_f (2j_f + 1) Tr(D^{j_f}(g_{e_1 v_1} \cdots g_{e_n v_1})) \tag{2.40}$$

$$= \sum_{j_f} \prod_f (2j_f + 1) \prod_v \quad . \tag{2.41}$$

We can organize the product over faces as a product over vertices that are connected to each other following the connectivity of the two-complex $\Delta^\star$. The integrals over $SU(2)$ can be performed exactly and expressed in terms of $SU(2)$ invariants as

$$\int dg D^{j_1}_{m_1 n_1}(g) D^{j_2}_{m_2 n_2}(g) D^{j_3}_{m_3 n_3}(g) = \begin{pmatrix} j_1 & j_2 & j_3 \\ m_1 & m_2 & m_3 \end{pmatrix} \begin{pmatrix} j_1 & j_2 & j_3 \\ n_1 & n_2 & n_3 \end{pmatrix}. \tag{2.42}$$

where on the left we have two $\{3jm\}$ symbols, that are easily related to Clebsch-Gordan coefficients [31]. The same equation graphically reads

$$\begin{matrix} j_1 & j_2 & j_3 \\ & & \\ & = & \\ & & \\ j_1 & j_2 & j_3 \end{matrix} \quad \begin{matrix} j_1 & j_2 & j_3 \\ & & \\ & & \\ j_1 & j_2 & j_3 \end{matrix} \quad . \tag{2.43}$$

The resulting spin foam partition function can be written in the following form

$$\mathcal{Z}_\Delta = \sum_{j_f} \prod_f A_f \prod_e A_e \prod_v A_v, \tag{2.44}$$

11

where the sum is over all the possible spins of the product of face amplitudes A_f, edge amplitudes A_e, and vertex amplitudes A_v. In the Ponzano-Regge model, we have a trivial edge amplitude $A_e = 1$, face amplitude equal to the $SU(2)$ irrep dimension $A_f = 2j_f + 1$ and vertex amplitude is given by the Wigner $\{6j\}$ symbol

$$A_v(j_f) = \left\{ \begin{array}{ccc} j_1 & j_2 & j_3 \\ j_4 & j_5 & j_6 \end{array} \right\} = \quad . \tag{2.45}$$

For $SU(2)$ recoupling theory, we follow the notation in [44] and for their graphical representation. The $\{6j\}$ symbol is composed of four $\{3jm\}$ symbols contracted together.

This spin foam model reproduces the theory firstly proposed by Ponzano and Regge [11]. In this seminal work they discovered an important relation between the large spins asymptotic of the $\{6j\}$ symbol and discrete GR. In fact, if an euclidean tetrahedron with lengths given by $j_f + 1/2$ exists, namely its squared volume is positive $V^2 > 0$, then:

$$A_v \sim \frac{1}{\sqrt{12\pi V}} \cos(S_\mathcal{R}(j_f) + \frac{\pi}{4}) \ , \tag{2.46}$$

where $S_\mathcal{R}$ is the Regge action of the tetrahedron, and Θ_f are the corresponding external dihedral angles. The Regge action is

$$S_\mathcal{R}(j_f) = \sum_f (j_f + \frac{1}{2})\Theta_f \ . \tag{2.47}$$

If such euclidean tetrahedron does not exist, namely if $V^2 < 0$, the amplitude is exponentially suppressed. Much of the work done in spinfoam theory aims to find an analogous model for Lorentzian 4d gravity.

2.2.3 4-dimensional $SU(2)$ BF model

The 4-dimensional $SU(2)$ case is similar to the 3-dimensional one. Again, we can write the partition function as

$$\mathcal{Z}_\Delta = \sum_{j_f} \int \prod_e dg_e \prod_f (2j_f + 1) Tr(D^{j_f}(g_{e_1} \dots g_{e_n})) \tag{2.48}$$

$$= \sum_{j_f} \prod_f (2j_f + 1) \prod_v \quad . \tag{2.49}$$

where we expanded the delta function over irrep. We perform integration over $SU(2)$ as

$$\int dg D^{j_1}_{m_1 n_1}(g) D^{j_2}_{m_2 n_2}(g) D^{j_3}_{m_3 n_3}(g) D^{j_4}_{m_4 n_4} = \sum_i d_i \left(\begin{array}{cccc} j_1 & j_2 & j_3 & j_4 \\ m_1 & m_2 & m_3 & m_4 \end{array} \right)^{(i)} \left(\begin{array}{cccc} j_1 & j_2 & j_3 & j_4 \\ n_1 & n_2 & n_3 & n_4 \end{array} \right)^{(i)} . \tag{2.50}$$

Here we introduce the $\{4jm\}$ symbol as the contraction of two $\{3jm\}$ symbols

$$\begin{pmatrix} j_1 & j_2 & j_3 & j_4 \\ m_1 & m_2 & m_3 & m_4 \end{pmatrix}^{(i)} = \sum_{m_i}(-1)^{i-m_i}\begin{pmatrix} j_1 & j_2 & i \\ m_1 & m_2 & m_i \end{pmatrix}\begin{pmatrix} i & j_3 & j_4 \\ -m_i & m_3 & m_4 \end{pmatrix}. \tag{2.51}$$

i is an intertwiner, it represents an invariant tensor in $Inv[\mathcal{H}^{j_1} \otimes \cdots \otimes \mathcal{H}^{j_4}]$. d_i is the dimension of this space.

Graphically eq 2.50 is given by

$$\tag{2.52}$$

Using these simple rules, the partition function can again be written as

$$\mathcal{Z}_\Delta = \sum_{j_f} \prod_f A_f \prod_e A_e \prod_v A_v, \tag{2.53}$$

with $A_f = 2j_f + 1$ and edge amplitude given by $A_e = 2i_e + 1$. The vertex amplitude A_v is now represented by a $\{15j\}$ symbol

$$A_v(j_f, i_e) = \quad \begin{Bmatrix} i_1 & j_5 & i_4 & j_{10} & i_2 \\ j_4 & j_6 & j_9 & j_1 & j_2 \\ j_7 & i_5 & j_8 & i_3 & j_3 \end{Bmatrix} =$$

$$= (-1)^{\sum_{i=1}^5 j_i + l_i + k_i}\sum_s (2s+1)$$

$$\times \begin{Bmatrix} i_1 & j_7 & s \\ i_5 & j_5 & j_4 \end{Bmatrix}\begin{Bmatrix} j_5 & i_5 & s \\ j_8 & i_4 & j_6 \end{Bmatrix}$$

$$\times \begin{Bmatrix} i_4 & j_8 & s \\ i_3 & j_{10} & j_9 \end{Bmatrix}\begin{Bmatrix} j_{10} & i_3 & s \\ j_3 & i_2 & j_1 \end{Bmatrix}\begin{Bmatrix} i_2 & j_3 & s \\ i_1 & j_7 & j_2 \end{Bmatrix}, \tag{2.54}$$

following the conventions in [45] for the $\{15j\}$ symbol of the first type. This 4-dimensional model will be used for the computations performed in Chapter 8. It is an important toy model, even if simple and topological, it still contains essential features for the following reason. As we saw in the previous paragraph, a remarkable result by Ponzano and Regge shows that the large spin limit of the $SU(2)$ $\{6j\}$ symbol can be approximated with the cosine of the Regge action for a euclidean tetrahedron. Barrett and collaborators in [34] obtained a 4-dimensional analog, based on linear combination o $SU(2)$ $\{15j\}$ symbols and the notion of coherent intertwiners that we will introduce in 2.2.6. In this case, the large spin limit is related to the cosine of the Regge action for a euclidean 4-simplex. More analytical details can be found in [34]. In [32] we performed a numerical confirmation of Barret's analysis finding an excellent agreement between the rescaling of the coherent vertex amplitude and the cosine of the Regge action even at relatively low spins.

13

2.2.4 Quantized Constrained BF Theory: the EPRL model

The discrete quantum BF models studied so far are topological. In 2.1.3, we recovered GR in 4 dimensions using constraints on the B field at the continuum level. Unfortunately, the action 2.16 can not be discretized in its form. We need to impose the simplicity constraints at the quantum level as a selection of the unitary irrep allowed by the theory. The vertex amplitude is built from the topological $SL(2, \mathbb{C})$ BF spin foam vertex amplitude by imposing, weakly, the simplicity constraints resulting into a restriction of the unitary irreducible representations in the principal series. We review this model here. We start analyzing the representation theory for $SL(2, \mathbb{C})$, and we translate the classical continuous constraints described in 2.1.3 into the quantum discrete language.

$SL(2, \mathbb{C})$ representation theory and the linear simplicity constraint

The gauge group is $G = SL(2, \mathbb{C})$, double covering of the Lorentz group $SO(1, 3)$. An analogous analysis can be done in the euclidean domain with gauge group $SO(4)$ [41], but this case will not be considered here. $SL(2, \mathbb{C})$ unitary irreducible representations $\mathcal{H}_{\rho,k}$ are infinite-dimensional, labelled by a positive real number $\rho \in \mathbb{R}$ and an half integer $k \in \mathbb{N}/2$. For reference see [47] and [46] for a detailed review. The group has two Casimirs

$$C_1 = \frac{1}{2} J_{IJ} J^{IJ} = L^2 - K^2 \qquad C_2 = \frac{1}{2} {}^\star J_{IJ} J^{IJ} = K \cdot L, \tag{2.55}$$

where J^{IJ} are the generators. L^i are the generators of an arbitrary rotation subgroup and K^i those of the corresponding boosts. For the definition of the EPLR model, we need to introduce an arbitrary subgroup $SU(2) \subset SL(2, \mathbb{C})$. This is the internal gauge group of the gravitational phase space in connection variables appearing in the canonical approach of Loop Quantum Gravity. The link between the unitary representations of $SL(2, \mathbb{C})$ and those of $SU(2)$ is established by

$$\mathcal{H}_{\rho,k} = \bigoplus_{j=k}^{\infty} \mathcal{H}_j. \tag{2.56}$$

The full characterization of the algebra can be found in [41, 46] and we move on to impose the linear simplicity constraint at the quantum level. The relation 2.23 becomes a constraint between the generators of the group, once a $SU(2)$ subgroup is chosen for every tetrahedron of the triangulation. In the time gauge

$$N_I J^{IJ} = K^I \qquad N_I \star J^{IJ} = L^I, \tag{2.57}$$

and, if we identify the two form J^{IJ} with B^{IJ}, we know from 2.1.3 that

$$K^I = \gamma L^I. \tag{2.58}$$

To write this relation in terms of the quantum numbers ρ and k we recall that the two Casimirs act on a state $|\rho, k\rangle \in \mathcal{H}_{\rho,k}$ as

$$\begin{aligned} C_1 |\rho, k\rangle &= (k^2 - \rho^2 - 1) |\rho, k\rangle \\ C_2 |\rho, k\rangle &= \rho k |\rho, k\rangle. \end{aligned} \tag{2.59}$$

Imposing 2.58 we get

$$\begin{aligned} (L^2 - K^2) &= (1 - \gamma^2) L^2 \\ K \cdot L &= \gamma L^2, \end{aligned} \tag{2.60}$$

and on the quantum numbers, using 2.59

$$\begin{aligned} k^2 - \rho^2 - 1 &= (1 - \gamma^2) j(j+1) \\ \rho k &= \gamma j(j+1), \end{aligned} \tag{2.61}$$

14

that for large quantum number are solved by

$$\rho = \gamma k$$
$$k = j. \tag{2.62}$$

We obtain a restriction on the quantum number of the theory. The constraints on the B field imply a restriction on the representations of the theory, on the representations labeling the triangles of Δ. To obtain this result, we choose a preferred $SU(2) \subset SL(2,\mathbb{C})$ at each tetrahedron of the triangulation, meaning we fix a preferred four normal for each tetrahedron of Δ. In the dual picture, on each $e \in \Delta^\star$ we fix a $SU(2) \subset SL(2,\mathbb{C})$ and a restriction on each $f \in \Delta^\star$ to $\rho_f = \gamma k_f, k_f = j_f$. The allowed quantum states Ψ are elements of $\mathcal{H}_j \subset \mathcal{H}_{\gamma j,j}$ that satisfy, in the semiclassical limit
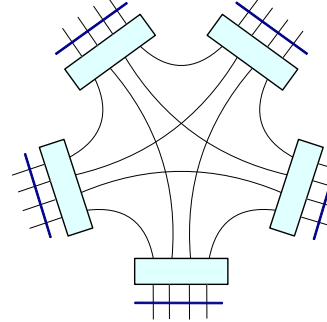
$$(K_f^I - \gamma L_f^I)\Psi = 0. \tag{2.63}$$

The embedding of a preferred $SU(2)$ on each tetrahedron can be seen as a map Y

$$Y : \mathcal{H}_j \to \mathcal{H}_{\gamma j,j} \tag{2.64}$$

The Y map sends states of $SU(2)$ to states on $SL(2,\mathbb{C})$ restricted with the linear simplicity constraint and it is one of the most important elements of the EPRL model.

2.2.5 EPRL Partition Function

The definition of the linear simplicity constraint and the Y map allows writing the partition function of the theory.

$$\mathcal{Z}_\Delta = \sum_{j_f} \prod_{j_f} d_{j_f} \tag{2.65}$$

Now the boxes are associated with integrations over $SL(2,\mathbb{C})$ group elements, and blue lines represent the insertion of the Y map at every tetrahedron of the triangulation. Analytically it reads

$$\mathcal{Z}_\Delta = \sum_{\{j_f\}} \prod_f d_{j_f} \int_{SL(2,\mathbb{C})} \prod_e dg_{ev} \, D^{(\gamma j_f, j_f)}_{j_f m_f, j_f m_f}(g_{e_1 v_1} Y^\dagger Y g_{e_1 v_2}^{-1} g_{e_2 v_2} Y^\dagger Y \dots Y^\dagger Y g_{e_n v_1}^{-1}) \tag{2.66}$$

The group elements g_{ev} are represented by the infinite dimensional unitary matrices

$$D^{(\rho,k)}_{jmln}(g), \qquad (j,l) \geq |k|, \quad -j \leq m \leq j, \quad -l \leq n \leq l, \qquad g \in SL(2,\mathbb{C}). \tag{2.67}$$

in which $\rho = \gamma k$ and $k = j$ due to the Y map. The Y map is inserted at every tetrahedron while the number of group elements n depends on how many tetrahedra share one triangle or, equivalently, on how many boxes are shared by one strand. It acts restricting the unitary irrep for every group element. For instance, with $n = 2$

$$D^{(\gamma j,j)}_{jm,jm}(g_{e_1 v_1} Y^\dagger Y g_{e_1 v_2}^{-1} g_{e_2 v_2} Y^\dagger Y g_{e_2 v_1}^{-1}) = D^{(\gamma j,j)}_{jm,jm'}(g_{e_2 v_1}^{-1} g_{e_1 v_1}) D^{(\gamma j,j)}_{jm',jm}(g_{e_1 v_2}^{-1} g_{e_2 v_2}). \tag{2.68}$$

We recall that [47, 31]

$$D^{(\gamma j,j)}_{jmjm'}(g_{e_2 v_1}^{-1} g_{e_1 v_1}) = \sum_{l \geq j} \sum_{n=-l}^{l} D^{(\gamma j,j)}_{jmln}(g_{e_2 v_1}^{-1}) D^{(\gamma j,j)}_{lnjm'}(g_{e_1 v_1}). \tag{2.69}$$

15

This relations allows to write the partition function as

$$\mathcal{Z}(\Delta) = \sum_{j_f} \sum_{l_f} \prod_f d_{j_f} \int_{SL(2,\mathbb{C})} \prod_e dg_{ev} \prod_{a=1}^{4} D_{j_{fa} m_{fa}, l_{fa} n_{fa}}^{(\gamma j_{fa}, j_{fa})}(g_{ev}). \tag{2.70}$$

However, it is divergent: the group is non-compact and there is one redundant integration for each vertex. To obtain a well-defined amplitude, as shown in [48], one has to reabsorb this redundant integral using the properties of the Haar measure. The finite partition function is graphically given by

$$\mathcal{Z}_\Delta = \sum_{j_f} \prod_{j_f} d_{j_f} \qquad \qquad , \tag{2.71}$$

where we cancel one redundat integral per-vertex. As previously done for the SU(2) BF case in 2.2.3, we want to explicitly perform the integrations over $SL(2,\mathbb{C})$. Following [31] we introduce the Cartan decomposition [47] for an $SL(2,\mathbb{C})$ group element

$$g = u e^{\frac{r}{2}\sigma_3} v^{-1}, \tag{2.72}$$

with u and v arbitrary elements of $SU(2)$ and $r \in [0,\infty)$ as the rapidity parameter of a boost along the z axis. The Haar measure becomes

$$dg = d\mu(r)\, du\, dv, \qquad d\mu(r) = \frac{1}{4\pi}\sinh^2 r\, dr, \tag{2.73}$$

and an arbitrary irreducible representation can be re-written as

$$D_{jmln}^{(\rho,k)}(g) = \sum_p D_{mp}^{(j)}(u) d_{jlp}^{(\rho,k)}(r) D_{pn}^{(l)}(v^{-1}), \tag{2.74}$$

where $D^{(j)}$ are Wigner's matrices for SU(2) and the boost matrix elements $d^{(\rho,k)}$ (also called d-small) are given by sums of hypergeometric function. The explicit form of the boost matrix elements can be found in the literature in its general form [47, 49, 50, 31], here we just report them in the case of simple irreducible representation:

$$d_{jlp}^{(\gamma j, j)}(r) = (-1)^{\frac{j-l}{2}} \frac{\Gamma(j + i\gamma j + 1)}{|\Gamma(j + i\gamma j + 1)|} \frac{\Gamma(l - i\gamma j + 1)}{|\Gamma(l - i\gamma j + 1)|} \frac{\sqrt{2j+1}\sqrt{2l+1}}{(j+l+1)!} \tag{2.75}$$

$$\times \left[(2j)!(l+j)!(l-j)! \frac{(l+p)!(l-p)!}{(j+p)!(j-p)!} \right]^{1/2}$$

$$\times e^{-(j-i\gamma j+p+1)r} \sum_s \frac{(-1)^s e^{-2sr}}{s!(l-j-s)!} {}_2F_1[l+1-i\gamma j, j+p+1+s, j+l+2, 1-e^{-2r}].$$

Then, the integral in 2.70 reads

$$\int dg \prod_{a=1}^{4} D_{j_a m_a l_a n_a}^{(\gamma j_i, j_i)}(g) = \int du\, dv\, d\mu(r) \prod_{a=1}^{4} \sum_{p_a} D_{m_a p_a}^{(j_a)}(u) d_{j_a l_a p_a}^{(\gamma j_a, j_a)}(r) D_{p_a n_a}^{(l_a)}(v^{-1})$$

$$= \sum_{i,k} d_i d_k \left(\begin{array}{c} j_a \\ m_a \end{array} \right)^{(i)} \left(\begin{array}{c} l_a \\ n_a \end{array} \right)^{(k)} B_4^\gamma(j_a, l_a; i, k),$$

16

where we performed the integrations over $SU(2)$ explicitly, using Eq. 2.50. Here we called

$$B_4^\gamma(j_a, l_a; i, k) := \sum_{p_a} \begin{pmatrix} j_a \\ p_a \end{pmatrix}^{(i)} \begin{pmatrix} l_a \\ p_a \end{pmatrix}^{(k)} \int dr \prod_{a=1}^{4} d_{j_a l_a p_a}^{(\gamma j_a, j_a)}(r) \tag{2.76}$$

$$:= \tag{2.77}$$

the booster function. In it, we absorb the "non-compactness" of the group. We also introduced a simplified notation for the $\{4jm\}$ symbols

$$\begin{pmatrix} j_a \\ m_a \end{pmatrix}^{(i)} = \begin{pmatrix} j_1 & j_2 & j_3 & j_4 \\ m_1 & m_2 & m_3 & m_4 \end{pmatrix}^{(i)}. \tag{2.78}$$

We establish a graphical notation for equation 2.76

$$= \sum_{i,k} d_i d_k \tag{2.79}$$

Using these relations, we can write $\mathcal{Z}$ as before

$$\mathcal{Z}_\Delta = \sum_{j_f, i_e} \prod_f A_f(j_f) \prod_e A_e(i_e) \prod_v A_v(j_f, i_e) , \tag{2.80}$$

defined in terms of the face amplitude A_f, the edge amplitude A_e and the vertex amplitude A_v. The face amplitude is $A_f(j_f) = 2j_f + 1$, the edge amplitude $A_e(i_e) = 2i_e + 1$. The vertex amplitude A_v defined by the EPRL model is given by

$$A_v(j_f, i_e) = \sum_{l_f, k_e} \left(\prod_e (2k_e + 1) B_4(j_f, l_f; i_e, k_e) \right) \{15j\}_{j_f, i_4}(l_f, k_e) \tag{2.81}$$

$$= \sum_{l_f, k_e} d_{k_e} \qquad .,$$

An important part of our work is focused on the numerical evaluation of the vertex amplitude A_v here defined. Before moving to the next Chapter, we introduce coherent states for spin foam amplitude, and we define the coherent vertex amplitude.

17

2.2.6 Coherent states and coherent intertwiners

Coherent states are a fundamental ingredient in studying the semiclassical behavior of a spin foam amplitude. We briefly review the conventions used in our works. For more details we refer to [51] or to other numerical works [32] and [30]. A $SU(2)$ coherent state $|j, \vec{n}\rangle$ in the irreducible representation of spin j is given by the action on the lowest weight state $|j, -j\rangle$ of a $SU(2)$ group element g_n corresponding to the rotation that transforms the unitary vector $\vec{z} = (1, 0, 0)$ into $\vec{n} = (\sin\Theta\cos\Phi, \sin\Theta\sin\Phi, \cos\Theta)$. This coherent state minimizes the uncertainty in the two directions orthogonal to $\vec{n}$. The Euler angles of group element g_n are related to the angles Θ and Φ by

$$g_n = e^{-i\Phi\frac{\sigma_z}{2}} e^{-i\Theta\frac{\sigma_y}{2}} e^{i\Phi\frac{\sigma_z}{2}} \ , \tag{2.82}$$

where we expressed the $SU(2)$ generators $i\vec{\sigma}/2$ in terms of the Pauli matrices. The scalar product between a coherent state and a state in the magnetic basis is given by

$$\langle j, m | j, \vec{n}\rangle = \langle j, m | D^{(j)}(g_n) | j, \vec{n}\rangle = D^{(j)}_{m-j}(g_n) = D^{(j)}_{m-j}(\Phi, \Theta, -\Phi) \ , \tag{2.83}$$

where $D^{(j)}_{m-j}(\Phi, \Theta, -\Phi)$ is the Wigner matrix element of g_n parametrized in terms of its Euler angles.

$SU(2)$ coherent states form an overcomplete basis in the irreducible representation of spin j space

$$\mathbb{1}^{(j)} = (2j+1) \int_{S^2} \mathrm{d}\vec{n} \, |j, \vec{n}\rangle \langle j, \vec{n}| \ , \tag{2.84}$$

where $\mathrm{d}\vec{n}$ is the normalized measure on the sphere.

A 4-valent intertwiner in the recoupling basis is given by

$$|j_a; i\rangle = \sum_{m_1} \begin{pmatrix} j_1 & j_2 & j_3 & j_4 \\ m_1 & m_2 & m_3 & m_4 \end{pmatrix}^{(i)} |j_1 m_1\rangle |j_2 m_2\rangle |j_3 m_3\rangle |j_4 m_4\rangle \tag{2.85}$$

Finally, we can define a coherent tetrahedron as the projection on the intertwiner space of the tensor product of four $SU(2)$ coherent states. Each one of them is associated to a face of the tetrahedron with area j_a and normal $\vec{n}_a$

$$c_i(\vec{n}_a) := \langle j_a; i | j_1, \vec{n}_1; j_2, \vec{n}_2; j_3, \vec{n}_3; j_4, \vec{n}_4\rangle \tag{2.86}$$

$$= \begin{pmatrix} j_1 & j_2 & j_3 & j_4 \\ m_1 & m_2 & m_3 & m_4 \end{pmatrix}^{(i)} D^{(j_1)}_{m_1-j_1}(g_{n_1}) D^{(j_2)}_{m_2-j_2}(g_{n_2}) D^{(j_3)}_{m_3-j_3}(g_{n_3}) D^{(j_4)}_{m_4-j_4}(g_{n_4}) \ . \tag{2.87}$$

A coherent state's graphical representation is given by a line ending on a little circle while the coefficients of the coherent state are represented by

$$|j, \vec{n}\rangle = \quad c_i(\vec{n}_a) = \quad . \tag{2.88}$$

2.2.7 Vertex Amplitude in the coherent state basis

We can write the vertex amplitude for $SU(2)$ BF theory and for the $SL(2, \mathbb{C})$ EPRL model in the coherent state basis. To express the amplitudes in the coherent state representation, one has to use relation 2.84 and insert a resolution of the identity for every strand connecting two vertices. The partition function for the two models becomes

$$\mathcal{Z}_\Delta = \sum_{j_f} \prod_f A_f(j_f) \prod_v \int d\vec{n}_{ef} d_{j_f} A_v(j_f, \vec{n}_{ef}) \ . \tag{2.89}$$

The vertex amplitudes for the two models are

$$A_v^{SU(2)}\left(j_f, \vec{n}_{ef}\right) = \sum_{i_e} d_{i_e} \qquad , \qquad (2.90)$$

and, for the EPRL case

$$A_v^{EPRL}\left(j_f, \vec{n}_{ef}\right) = \sum_{l_f, i_e, k_e} d_{i_e} d_{k_e} \qquad . \qquad (2.91)$$

These vertex amplitudes have been extensively studied analytically by Barrett and collaborators in a series of important papers [34, 8, 9]. Depending on the coherent boundary data they contain the Regge action of a 4-simplex in the large spin limit. This connection with discrete gravity has been extensively studied in one of the articles here presented in Chapter 5, and we report any discussion to that work.

Chapter 3

Numerical Introduction

In this chapter, we introduce the library `sl2cfoam` where we provide the tools to evaluate the EPRL and $SU(2)$ spin foam vertex amplitude numerically. It is based on the decomposition of the EPRL vertex amplitude in terms of booster functions introduced in the previous chapter. These utilities are indicated for the study of vertex amplitudes with coherent boundary data and non, opening new windows on the covariant formulation of loop quantum gravity. The library `sl2cfoam` can be found at: `https://github.com/qg-cpt-marseille/sl2cfoam` and we published a detailed paper to present it [30], on which this chapter is based. Some updates have been made in the last year and a second version has been released with the fundamental help and knowledge of Francesco Gozzini.

The vertex amplitude is built from the topological $SL(2, \mathbb{C})$ BF spin foam vertex amplitude by imposing, weakly, the simplicity constraints resulting into a restriction of the unitary irreducible representations in the principal series. To evaluate it in its original form one should perform four group integrals, as in Eq. 2.71. Each group integral is, in general, a six dimensional unbounded highly oscillating integral for which numerical integration methods are very inefficient. To solve this issue, a more computational friendly form for the amplitude, has been proposed [31] and we summarize it in 2.81. The result is a superposition of $SU(2)$ $\{15j\}$ symbols weighted by one booster functions B_4 per edge minus one in the considered vertex. To obtain this form each $SL(2, \mathbb{C})$ integral is decomposed in a $SU(2)$ "rotation", a boost along a fiducial axes and another $SU(2)$ "rotation". The compact integrals are then evaluated exactly composing the SU(2) invariants. The summation is over a set of auxiliary spins l_f for each face involved in the vertex (but excluding the gauge fixed edge) for a total of 6 distinct l_f, with lower bound $l_f \geq j_f$, and a set of auxiliary intertwiners k_e for each edge in the vertex (excluding the gauge fixed one) for a total of 4 that can assume all the values compatible with triangular inequalities.

The expression (2.81) is far more convenient than the original one for numerical evaluation. We decomposed the amplitude into smaller building blocks, which are easier to compute. We trade four six dimensional unbounded integrals with a summation of $SU(2)$ invariants, which are widely studied, and a class of one-dimensional integrals that we need to perform and we can characterize independently. On one hand, the introduction of booster functions brings a drastic simplification to the computation of the vertex amplitude because it reduces the problem of dealing with many high oscillatory integrals to the study a family of one dimensional integrals, which are easier to handle and manipulate. On the other hand, we introduce a large amount of convergent summation in the computation which need to be dealt with. The net gain of this operation is evident once we realize that each element of the sum can be computed in a fast way and with high precision.

Our tools can be generalized to arbitrary valency, as we will see in one of the papers here presented 6. In the library `sl2cfoam` , in addition to the simplicial lorentzian amplitude, we also provide the tools to evaluate amplitudes for $SU(2)$ BF theory both in 3 and 4 dimensions.

3.1 The `sl2cfoam` library

3.1.1 General strategy

We can summarize the evaluation of the vertex amplitude (2.81) in three main ingredients that we need to mix in the right way:

- all the necessary $\{15j\}$ symbols,

- all the required booster functions,

- the sum over the auxiliary spins and intertwiners.

In the next sections we will discuss in detail the problems we encounter in these three steps and their possible solutions. Here we want to give a general overview. The first valuable lesson we learned is to not waste time computing vanishing contributions. Many $SU(2)$ invariants and booster functions are zero because of symmetries (triangular inequalities, odd symmetries under permutations), we avoid computing objects that are part of amplitudes that we can identify as vanishing a priori.

Symmetries also play a secondary but equally important role. The objects in the summation repeat themselves, instead of wasting time doing the same computation over and over again, we store them in the RAM and, at the end, we dump them to disk. To make it possible and not saturate the memory in a couple of iterations, we optimize the computation factoring the symmetries and consider only one representative per equivalence class. The bottleneck of the computation while dealing with $SU(2)$ invariants is not the evaluation time but the memory needed. In an equivalence class of $\{6j\}$ symbols there are approximately a hundred elements, we store only one representative per class reducing by two orders of magnitude the amount of necessary memory.

When dealing with summations with a huge amount of terms we need to be extremely careful. In our calculation, apart from the summation over auxiliary spins and intertwiners itself, these sums appear also in the evaluation of the booster functions. In particular, to deal effectively with interference effects we need to resort to arbitrary precision libraries [52, 53, 54]. How to sum a large number of finite precision floating point numbers is a well-studied problem in numerical analysis. The bound of the worst-case error on the sum of N numbers with floating point precision grows proportional to N. By using a compensated summation algorithm [55] we can make this error independent of N, and having it depend only on the floating-point precision of the addends. Moreover, we employ compensated summation algorithms to significantly reduce the numerical error in the addition of finite precision floating point numbers.

The full computation is divided into a large number of small tasks and we can efficiently parallelize it with `OpenMP`. We parallelize the computation of the booster functions and the summation over the auxiliary spins but not the evaluation of the $SU(2)$ invariants. The computational time needed for the evaluation of the $SU(2)$ invariants is negligible respect to all the other steps.

The sums over the six auxiliary spins are unbounded and convergent, therefore to extract a number from them we need to truncate. We introduce a homogeneous cutoff on all the spins $j_f \leq l_f \leq j_f + \Delta$ and we sum over all compatible intertwiners k_e. The details of the convergence of this summation strongly depend on the value of the face spins and edge intertwiners, hindering our ability to provide a consistent estimate of the systematical error due to the truncation. We are then forced to perform an analysis a posteriori: we report some examples in Figure 3.5 where it is possible to estimate it between 1 and 5 percent for $\Delta \approx 5$.

The error on the booster functions, due to the discretization of the integral, and the one on the $SU(2)$ invariants are completely irrelevant with respect to the one due to the truncation. We will discuss them in more detail in the following sections.

For a single 4-simplex with fixed intertwiners, the bottleneck of the computation is the evaluation of the booster functions. If we need to compute the amplitude for all the possible intertwiners, for example, because we are contracting more than a single vertex, most of the computational time is used in performing the summation. Having in mind the goal of performing the computation of spin foam

diagrams with many vertices, since the number of elements grows exponentially with it, we are studying selection rules based on the asymptotic of the booster functions or with the machine learning techniques.

3.1.2 SU(2) invariants

Evaluating a significant amount of $SU(2)$ invariants can be a resources draining task. An SU(2) invariant is defined as a summation over the magnetic indices of intertwiners (and them as a sum of $(3jm)$ symbols). Their evaluation, directly from the definition, is not convenient, as it will exhaust too many computational resources, both in time and memory. To compute an amplitude we need to evaluate a large number of invariant, requiring a technique that is both fast and memory lightweight. We can solve the time issue by reducing to one the number of summation. We can reduce every SU(2) invariant in a sum of $\{6j\}$ and $\{9j\}$ symbols that can be directly computed using prebuilt libraries [56]. We tackled this problem for the first time in [32] where the asymptotic of a general $SU(2)$ invariant has been studied analytically and also numerically in the simplicial case. We employ a similar technique in sl2cfoam . Following the notation of the monography [45] we identify five different kinds of $\{15j\}$ symbols. For example, we can write the $\{15j\}$ symbols of the first kind as a sum of the product of five $\{6j\}$s symbols:

$$\{15j\}_I := \quad = \sum_x (2x+1)(-1)^{\sum_i l_i + j_i + k_i + i_4} \left\{ \begin{array}{ccc} k_1 & l_7 & x \\ k_5 & j_5 & l_4 \end{array} \right\} \left\{ \begin{array}{ccc} j_5 & k_5 & x \\ l_8 & i_4 & l_6 \end{array} \right\}$$

(3.1)

$$\times \left\{ \begin{array}{ccc} i_4 & l_8 & x \\ k_3 & j_{10} & j_9 \end{array} \right\} \left\{ \begin{array}{ccc} j_{10} & k_3 & x \\ l_3 & k_2 & l_1 \end{array} \right\} \left\{ \begin{array}{ccc} k_2 & l_3 & x \\ k_1 & l_7 & l_2 \end{array} \right\}.$$
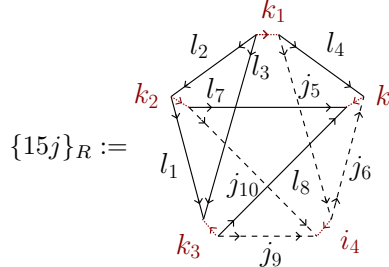
where we gauge fix the edge corresponding to the fourth tetrahedron as in 2.81. To compute a single amplitude at a fixed cutoff Δ, we need to evaluate an enormous amount of $\{15j\}$ symbols, and consequently of $\{6j\}$ (or $\{9j\}$) symbols. We recall that all the spins l_f vary in the range between the face spin j_f and the cutoff $j_f + \Delta$, while the intertwiners k_e assume all the values allowed by the triangular inequalities. Note that the SU(2) BF amplitude 2.54 is given by this $\{15j\}$ where $\Delta = 0$ and $l_i = j_i$.

The development of algorithms that allow for a fast and accurate computation of $\{6j\}$ symbol is a fascinating and challenging topic studied by mathematicians and computer scientist, and a significant amount of libraries for the job are available. In our work, we adapt the C library wigxjpf developed in [56] that can be used to compute $(3jm)$, $\{6j\}$ and $\{9j\}$ symbols. We refer to their original paper for a detailed discussion of the library's performances, accuracy and memory management.

We also solved the memory usage issue by efficiently storing $\{6j\}$ symbols taking into account the various symmetries of the symbols. The right data structure for this job is the hash table, a structure that efficiently maps keys to values. We associate to each $\{6j\}$ symbol a key that is automatically shared by the whole class of symbols with the same value (because of symmetries). Every $\{6j\}$ symbols share its value with other 143 [57] symbols due to permutation symmetries. Notice that an extension of the library wigxjpf named fastwigxj provides a hash table implementation for $(3jm)$, $\{6j\}$ and $\{9j\}$ symbols but, since it is designed for more general applications, it stores all possible combinations of the desired invariants with *all* spins smaller than a cutoff. This amount of data is way more of what we need in an ordinary EPRL four simplex computation resulting in a huge memory consumption, and consequently being an obstacle when exploring larger values of the spins. To circumvent this limitation,

we implement our own hash tables based on `khash` provided in the library `Klib` [58]. We generate the keys of the hash table with the hash functions discussed in [57], and we store the $\{6j\}$ symbols assigning a unique six integers key to each symmetry class, saving one representative value.

We can introduce an additional simplification to improve the performance, as already used in [32]. We can use the freedom of choosing the intertwiners recoupling basis of the spin foam edges to rewrite the $\{15j\}$ symbols as:

$$
\{15j\}_R := \quad \vcenter{\hbox{}} \quad = (-1)^{2(l_4+l_3)+2k_1-(k_2+k_3+i_4+k_5)} \tag{3.2}
$$

$$
\times \begin{Bmatrix} k_1 & k_3 & k_2 \\ l_1 & l_2 & l_3 \end{Bmatrix} \begin{Bmatrix} k_1 & i_4 & k_5 \\ j_6 & l_4 & j_5 \end{Bmatrix} \begin{Bmatrix} k_2 & k_3 & k_1 \\ j_{10} & j_9 & i_4 \\ l_7 & l_8 & k_4 \end{Bmatrix} ,
$$

and then rewrite the $\{9j\}$ symbol as a sum of three $\{6j\}$ symbols:

$$
\{15j\}_R = (-1)^{2(l_4+l_3)+2k_1-(k_2+k_3+i_4+k_5)} \begin{Bmatrix} k_1 & k_3 & k_2 \\ l_1 & l_2 & l_3 \end{Bmatrix} \begin{Bmatrix} k_1 & i_4 & k_5 \\ j_6 & l_4 & j_5 \end{Bmatrix} \tag{3.3}
$$

$$
\times \sum_x (2x+1)(-1)^{2x} \begin{Bmatrix} k_2 & j_{10} & l_7 \\ l_8 & k_5 & x \end{Bmatrix} \begin{Bmatrix} k_3 & j_9 & l_8 \\ j_{10} & x & i_4 \end{Bmatrix} \begin{Bmatrix} k_1 & i_4 & k_5 \\ x & k_2 & k_3 \end{Bmatrix} .
$$

Comparing with (3.1) we are still using five $\{6j\}$ symbols but we are summing only over three of them, resulting in a relevant save of time and memory.

The function where we implemented the evaluation and the storing of the $SU(2)$ invariants is called `J15Symbol_Hash`. It prepares all the $\{6j\}$ symbols in (3.3) needed for the computation of a vertex amplitude given the 10 spins j_f $f = 1, \ldots, 10$ and a cutoff Δ. Following the conventions of (3.3) the gauge fixed edge is identified by the four spins j_5, j_6, j_9 and j_{10} in the recoupling basis (j_5, j_6) with intertwiner i_4. This simplification is quite in general, (is free if the edges are not boundary ones), but we need to be careful in computations of spin foams transition amplitudes with many vertices, since the base choice on one edge affects both vertices it connects, and the split (3.3) needs to be done consistently in every vertex.

After the evaluation, the hash tables with the $\{6j\}$ symbols are stored on disk and can be used for further computations.
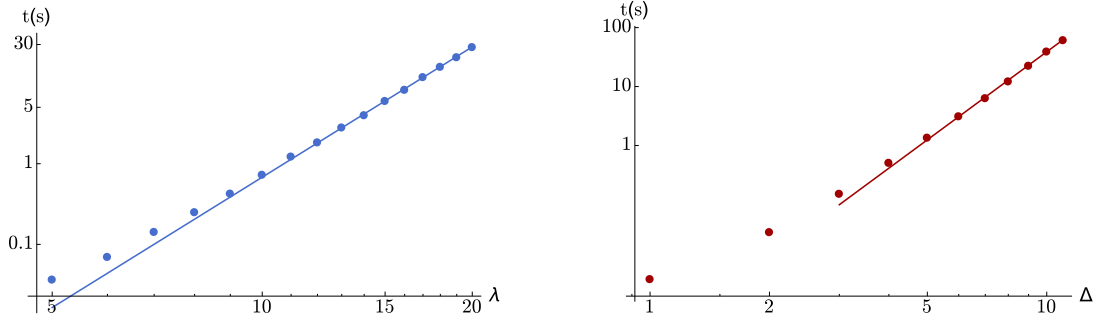
Figure 3.1: Evaluation time of the function *J15Symbol_Hash*. *Left panel:* Scaling of the configuration with all the spins and the gauge fixed intertwiner equal $j_f = i_4 = \lambda$ and a vanishing cutoff $\Delta = 0$, we compute the $\{15j\}$ symbols for all the values of the intertwiners k_e. We see a power law trend $a \times j^b$ with $a = 2.9 \times 10^{-6} s$ and $b = 5.3$. *Right panel:* Scaling in the cutoff of the configuration with all the spins and the gauge fixed intertwiner equal to $j_f = i_4 = 1$. We see a power law trend $a \times j^b$ with $a = 4 \times 10^{-4} s$ and $b = 5.0$.
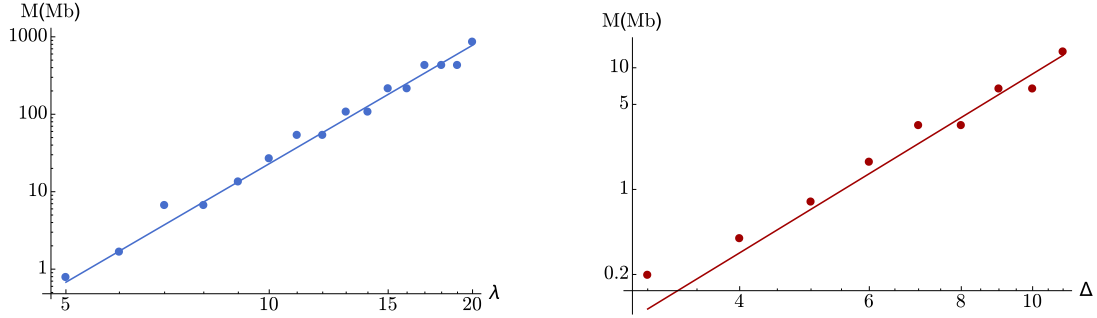

Figure 3.2: Memory usage of the function *J15Symbol_Hash*. *Left panel:* Scaling of the configuration with all the spins and the gauge fixed intertwiner equal $j_f = i_4 = \lambda$ and a vanishing cutoff $\Delta = 0$, we compute the $\{15j\}$ symbols for all the values of the intertwiners k_e. We see a power law trend $a \times j^b$ with $a = 1.8 \times 10^{-4}$Mb and $b = 5.1$. *Right panel:* Scaling in the cutoff of the configuration with all the spins and the gauge fixed intertwiner equal to $j_f = i_4 = 1$. We see a power law trend $a \times j^b$ with $a = 1.8 \times 10^{-3}$Mb and $b = 3.7$.

3.1.3 Booster functions

The expression for the booster functions (2.76) requires the calculation of the integral over the rapidity of four boost matrix elements (2.75) and a sum over magnetic indices. The latter is not a problem in this case since the number of terms to be summed over is relatively small (for all equal spins j is less than $(2j)^3$ terms). However, the numerical integration is still very challenging. The integrand is a superposition of highly oscillating hypergeometric functions that, when multiplied together, interfere resulting in a localized, smooth and regular function. Moreover, for specific values, the hypergeometric functions are evaluated near one of their poles. These apparent divergences will cancel with other terms in the superposition but would require extremely high precision to control the accuracy of the result. We solved these issues by attacking them from a different angle. A direct computation is very slow, and with this motivation an alternative formula was proposed in [31] and numerically explored by [35]. Nevertheless, the situation improves significantly using a different representation for the boost matrix elements (2.75). This problem has been explored in [59] where each boost matrix elements (2.75) is rewritten as a finite sum of exponentials with complex coefficients. For simple irreducible representations

and $\gamma \neq 0$, the result is given by:

$$d_{jlp}^{(\gamma j,j)}(r) = \frac{1}{(e^r - e^{-r})^{j+l+1}} \tag{3.4}$$

$$\times \left[\sum_{m=0}^{j+l-|j-p|} Y_m^{\gamma j,j;j,l;p} e^{(j+l-|j-p|-2m-i\gamma j)r} + (-1)^{l-j} \sum_{n=0}^{j+l-|j-p|} \overline{Y}_n^{\gamma j,j;j,l;-p} e^{(j+l-|j-p|-2n+i\gamma j)r} \right],$$

where Y are complex coefficients [1]. In the same work they provide a C++ implementation of the booster functions based on this formula. We integrated this code in `sl2cfoam` porting it in C, we added the evaluation of the $(4jm)$ symbols in (2.76) with `wigxjpf` and we provided an hash table data structure similar to the one we introduced for the SU(2) invariants in the previous section. The evaluation of these functions requires arbitrary precision floating point numbers, implemented with `MPFR` and `MPC`. These tools allow us to compute the booster functions in an accurate way and to test some of theirs properties.

The integral is performed using the trapezoidal rule with 3000 points as a default number. We explored this choice in Figure 3.3. The convergence looks very fast in the number of points; we observe a slight worsening with the increase of the l_f. The number of integration points can be increased arbitrarily to reduce even further the admissible error on the single booster function.
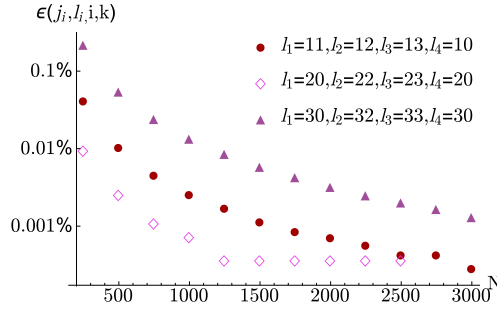

Figure 3.3: Dependence of the booster function on the number of points in the rapidity integral. We plot the relative difference ϵ with respect to the value with 10^4 points. All three booster functions reported here have all equal spins $j_f = 10$ and intertwiner $i = 0$. The four spins l_f and intertwiner k are respectively: $l_f = 11, 12, 13, 10$ and $k = 1$, $l_f = 20, 22, 23, 20$ and $k = 2$, $l_f = 30, 32, 33, 30$ and $k = 2$.

The sampling of the integration interval is parallelized with `OpenMP`. The library `sl2cfoam` implement the evaluation of all the booster functions needed in the computation of a vertex amplitude with the function `B4_Hash`.

The values of the booster functions are stored in hash tables and then in a file indexed with the name of the gauge fixed edge and the cutoff Δ. We store in each file the booster functions with all the possible combinations of the six l_f spins appearing in a vertex amplitude and every compatible intertwiner. We report a typical time consumption of `B4_Hash` in Figure 3.4 and the scaling of the time as a function of the number of cores used in the computation in Figure **??**. The memory's use of booster functions is negligible compared to $\{6j\}$ symbols' one.

When computing the booster functions, one notices that, for a fixed set of spins j_f and l_f, not all combinations of intertwiners contributes with values of similar order of magnitude. An example of this can be seen in [31] and in [60], for the case $l_f = j_f$ (called simplified model), where the main contribution is given by the same intertwiners $i_e = k_e$. The generalization of this result for any set of l_f is unfortunately still unknown. This result, or an equivalent method to localize the dominant contribution from the booster functions, will immediately translate into a significant save of time in the evaluation of the amplitude, especially in the case of multiple vertices.

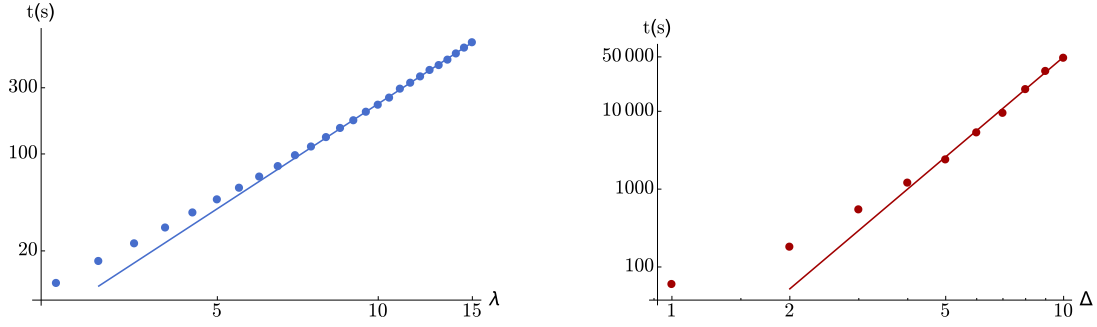[1] We refer to [59] for their full expression.

Figure 3.4:   Evaluation time of the function `B4_Hash`. *Left panel:* Scaling of the configuration with all the spins and the gauge fixed intertwiner equal $j_f = i_4 = \lambda$ and a vanishing cutoff $\Delta = 0$. We compute all the booster functions for all the values of the intertwiners k_e. We see a power law trend $a \times j^b$ with $a = 0.7s$ and $b = 2.5$. *Right panel:* Scaling in the cutoff of the configuration with all the spins and the gauge fixed intertwiner equal to $j_f = i_4 = 1$. We see a power law trend $a \times j^b$ with $a = 2.7s$ and $b = 4.3$.

3.1.4   Four simplex amplitude

In the previous two sections we illustrated the evaluation of the constituents of the vertex amplitude (2.81). In this section we will discuss how all the contributions are summed together. The summation is performed over six auxiliary spins l_f and four k_e intertwiners, whose ranges depends on the l_f but are generally bounded. The main problem in this step is the extension of these summations. They are, generally, unbounded and numerous. As we already stressed multiple times, the full amplitude is well defined [48], implying that the summations over the l_f are convergent, thus being unbounded is not a problem. Nevertheless, to be able to do a numerical evaluation of the sum we need to introduce a homogeneous cut-off Δ. In the following, we will denote as the Nth *shell* the set of factors contributing to the sum with maximum spin difference Max $\{l_f - j_f\} = N$. To be concrete we studied the convergence of the amplitude as a function of the cutoff, generally, it is quite rapid. We report some explicit examples in some particular cases in Figure 3.5. It is not possible to have a unique prescription to set the optimal Δ, since the convergence of the amplitude depends on the details of the data like the face spins j_f and the Immirzi parameter. We explored other configurations and the convergence is qualitatively the same. However, the ratio between the amplitude value with a different number of shells varies.
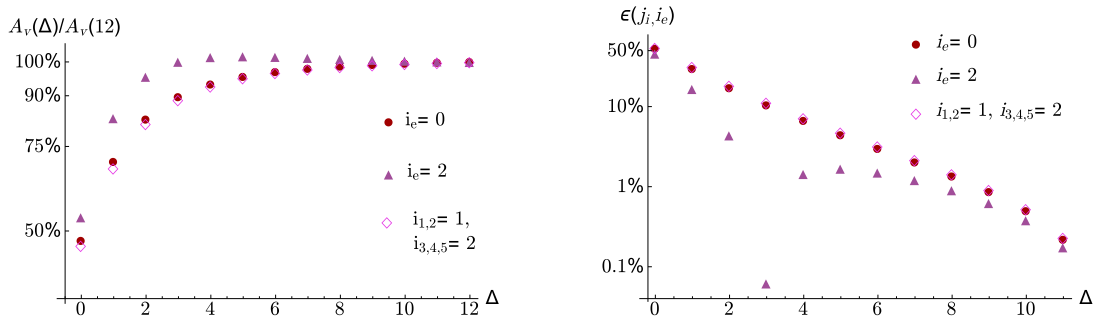
Figure 3.5:   Convergence of the vertex amplitude. *Left panel:* Convergence of the vertex amplitude while increasing the cutoff Δ for a configuration with all $j_f = 1$ and three different set of boundary intertwiners. *Right panel:*   The relative error ϵ between the shell Δ and the shell $\Delta = 12$, that has been taken as the correct value of the amplitude. The error for the simplified model ($\Delta = 0$) is $\sim 50\%$ while from $\Delta = 5$ it decreases to $1\% - 5\%$. The convergence of the vertex amplitude depends on many factors including the chosen boundary configuration and the Immirzi parameter.

In the library `sl2cfoam` the function `sl2cfoam_four_simplex` performs the summation of the 4-

simplex vertex amplitude. The algorithm at the base of the implementation is described in Figure 3.9, where we also show the hierarchy respect to the other main functions previously described. `sl2cfoam_four_simplex` is the main result of our numerical work and the big star of the library. Given the ten face spins, the five edge intertwiners, the cutoff Δ and the Immirzi parameter, it uses the functions `J15Symbol_Hash` and `B4_Hash` described in the previous sections to precompute all the needed $SU(2)$ invariants and booster functions and then proceed to the summations. In the case of an $SU(2)$ BF vertex amplitude, instead, we implemented its computation in a command called `sl2cfoam_four_simplex_BF`

Given the vast number of factors to be summed over we need to employ a compensated summation algorithm to reduce the numerical error caused by the sum of finite precision floating point numbers. Furthermore, to minimize the error, we convert and multiply the components of the factors to arbitrary precision floating point numbers (using the library `MPFR`). Parallelization is needed at this step but, while we have implemented it for the summation over the face spins l_f, it was counterproductive to do it also for the four intertwiner sums k_e because of triangular inequalities: when we fix a set of l_f we set the bounds over the k_e and the remaining four sums depend on them. In Figure 3.6 we show a parallelization test at fixed workload while increasing the number of cores.
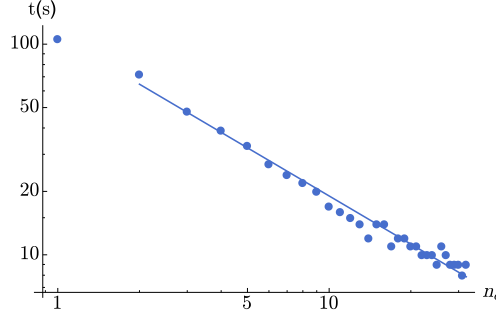
Figure 3.6: Parallelization at fixed workload: Scaling of the time required by the computation of a 4-simplex configuration with $j_f = 1$ and $\Delta = 11$ while increasing the number of cores. The power law $a \times j^b$ is given by $a = 109s$ and $b = -0.76$. Since the parallelization acts only on the l_f summations and not on the k_e ones the code performs better, in this regard, when a large Δ is considered.

We stress that selection rules, to find the important terms within the sums, would be an essential step forward. At the present stage, we can set an empirical cut-off over boosters to reduce the number of terms to be summed over but it would be exciting to study, with new methods such as machine learning's techniques, selection rules for the vertex amplitude.
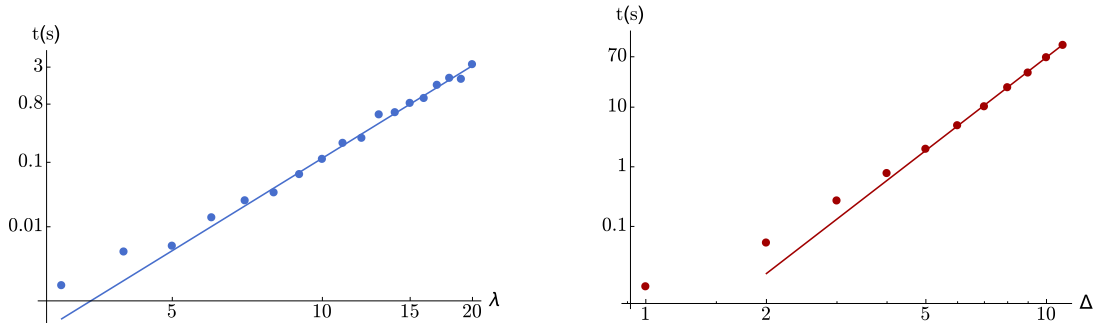
Figure 3.7: Evaluation time of the function *sl2cfoam_four_simplex*. *Left panel:* Scaling of the configuration with all the spins and the gauge fixed intertwiner equal $j_f = i_4 = \lambda$ and $\Delta = 0$. We see a power law trend $a \times j^b$ with $a = 2.0 \times 10^{-6}s$ and $b = 4.8$. *Right panel:* Scaling in the cutoff of the configuration with all the spins and the gauge fixed intertwiner equal to $j_f = i_4 = 1$. We see a power law trend $a \times j^b$ with $a = 4 \times 10^{-4}s$ and $b = 5.2$.

27
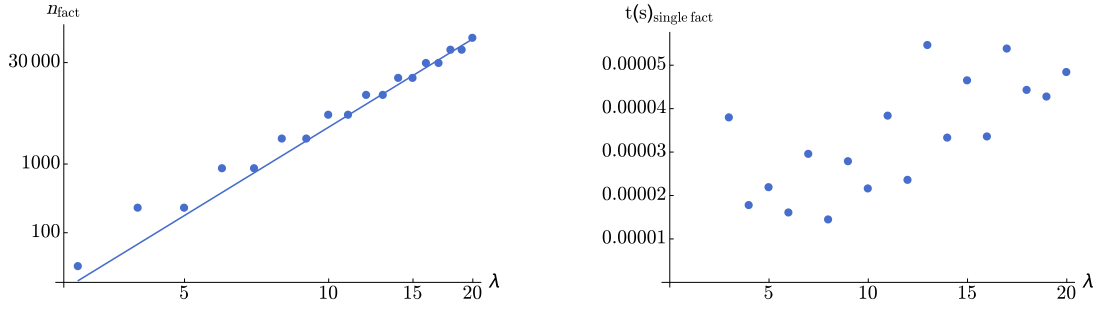
Figure 3.8: *Left panel:* We show the number of factors $\#_{fact}$ to be cycled over to compute a single 4-simplex with boundary spins, intertwiners equal to λ, and $\Delta = 0$. The power law is given by $a = 0.2$ and $b = 4.3$ *Right panel:* Evaluation time of a single factor in a computation with all boundary spins and intertwiners equal to λ. Each factor takes $\sim 10^{-5}$ s. Memory data access using `khash` works at $\sim 10^{-7}$s: we have to retrieve data for four B4, two "fixed" $\{6j\}$ and for a sum of three $\{6j\}$, converting data to `MPFR` variables and then assembly the amplitude.This leads us to $\sim 10^{-5}$s of evaluation time for a single factor of the l_f, k_e sum. If we would be able in the future to directly store $\{9j\}$ symbols we could save one order of magnitude in time.
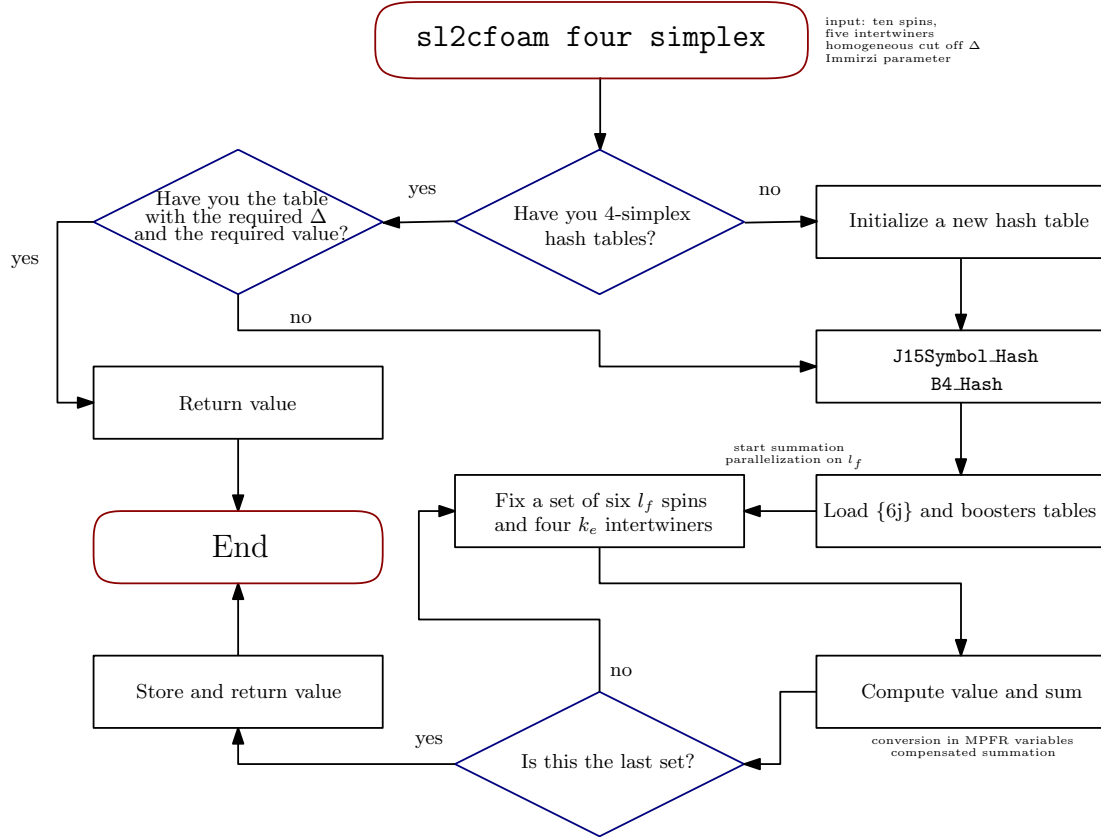
Figure 3.9: *sl2cfoam_four_simplex is the main function to compute and store EPRL vertex amplitudes*

28

3.2 Limitations and possible updates

Many technical improvements are necessary to unlock the full potential of this code. In analogy to what we do for the $\{6j\}$ symbols, we would need to implement hash tables for $\{9j\}$ symbols. This upgrade would speed up the computation of almost an order of magnitude, trading at low spins memory usage with faster access to data. Moreover, we want to explore the possibility of computing booster functions with the Kerimov formula, as explained in [31], for which recursion relations are available, simplifying the summation over the auxiliary spins l_f. A new version of the library has been released since [30], in which we implement recursion relations for $SU(2)$ Clebsch-Gordan coefficients and for three valent booster functions. Unfortunately, a formula for the four valent case it is still not known. This would improve a lot the computational time overall, at the present stage the computation of many B_4 is a strong time-consuming process. To perform the computation of transition amplitudes with many vertices, it is also crucial to improve our parallelization process, using `MPI` and `POSIX` threads enabling many servers calculations. A similar improvement will be reached by finding selection rules to restrict the summation to only the important terms. Our lack of analytical insight into the booster functions will force us to use new techniques like, for example, machine learning or Monte Carlo techniques.

For a quick reference, we report in Table 3.1 the timing of the various functions in `sl2cfoam` .

	$j_f = i_4 = 7$		$j_f = i_4 = 15$		$j_f = 1,\, i_4 = 1,\, \Delta = 5$	$j_f = 1,\, i_4 = 1,\, \Delta = 10$
$15j$	$0.1s$	6.8Mb	$6.1s$	218Mb	$1.4s$	0.8Mb	$62.0s$	6.8Mb
	$a = 2.9 \cdot 10^{-6}s$		$b = 5.4$		$a = 4 \cdot 10^{-4}s$	$b = 5.0$
B_4	$99.0s$		$642.1s$		$2433s$	$49214s$
	$a = 0.7s$		$b = 2.5$		$a = 2.7s$	$b = 4.3$
A_v	$0.03s$		$0.08s$		$2.0s$	$69.7s$
	$a = 2.0 \cdot 10^{-6}s$		$b = 4.8$		$a = 4 \cdot 10^{-4}s$	$b = 5.2$

Table 3.1: Summary of the computational time of the functions *J15Symbol_Hash, B4_Hash,* and *sl2cfoam_four_simplex*. We report some examples of computational time for configuration with all spins equal to 7 and 15 in the first two columns and the parameters of the power law behavior aj^b. In the last two columns we report some examples of computational time for configuration with all spins equal to 1 as a function of the cutoff and the parameters of the power law behavior $a\Delta^b$. All the computations are performed with a single processor.

A major problem is the following. Computations with many vertices have to be properly designed to be efficient. For instance, see Chapter 8 and the related numerical code [61]. From a memory point of view, the main obstacle is represented by the storage of many $\{6j\}$ symbols to be used in `J15Symbol_Hash`. On the other side, `B4_Hash`, and `sl2cfoam_four_simplex` are mostly time consuming functions due to integrations in the booster functions and resummation in the 4-simplex amplitude over l_f and over intertwiners k_e and i_e. Often, when computing an amplitude with many vertices, one has to find a balance between these two sides. One needs to store as much data as possible in memory to have a code working around clock speed. Sometimes this is not possible, depending on the machine used, and a better rearrangement of the terms in the summation has to be found. At the present stage, these functions are basic building blocks that have to be carefully used for a code to work fast. It would be useful to develop our framework further and to make the library `sl2cfoam` more user-friendly and available for users who do not know C well.

Chapter 4

Conclusive Overview

In the previous Chapters, we explored the theoretical and numerical tools that we will use in the proceedings. An interested reader can use these introductions as a reference. In the next Chapters, we present four out of the six papers written during this Ph.D. We start in Chapter 5, analyzing the numerical large spin limit of the coherent $SL(2,\mathbb{C})$ EPRL vertex amplitude 2.91. First of all, it is a fundamental test for the tools developed in [30] and briefly reported in Chapter 3. This result is also important because it confirms the semiclassical relation between the vertex amplitude 2.91 and the Regge action 2.25 of a euclidean 4-simplex. In the case of a lorenzian 4-simplex however, we were not able to obtain a satisfactory result. In fact, the number of shells to be summed over depends on the boundary data and, for a lorenzian 4-simplex, exceeded the numerical resources available to us at the time. It could be worth to design a better strategy to tackle the problem for that particular case, mainly thanks to the advances made in `sl2cfoam` and using more powerful servers. We then move to exploit new computations within the generalized sector of the EPRL model, presented in Chapter 6. We systematically study the transition amplitudes between two dipole spin networks up to two vertices. Generalized booster functions form the resulting amplitudes while $SU(2)$ invariants are not present. We understand some of their decay's properties when increasing the number of vertices, edges, and faces in the dual complex $\Delta^\star$. We discover that there are no asymptotic Regge actions at the order considered, even if the amplitudes still induce non-trivial correlations between boundary states. Also, spin correlations computed within a mini-superspace description appear only when one internal face is present in the foam. We think that the generalized sector can be used as an arena to test different ideas on how the sum of foams should be organized and could provide an interesting insight into the continuum limit of the theory. However, the lack of connections with Regge Calculus makes it hard to advocate for any physical interpretations in this domain. Moreover, the simplicity of the numerical evaluation of these non-simplicial spin foams has a payoff in the loose combinatorics of the faces. The proliferation of possible amplitudes is relevant, and the scaling power law can not be a priori determined by looking at the number of vertices, edges and faces.

We then move back to focus again on simplicial amplitudes. In Chapter 7, we propose a new algorithm to numerically identify stationary phase points in multi-vertices highly oscillating transition amplitudes at fixed boundary data. Our strategy is based on the numerical study of the stationary phase points in an amplitude's internal faces. This proposal is powerful. First of all, it is generalizable to many vertices and many internal faces and can detect an arbitrary number of stationary phase points. The algorithm can, in principle, be used to investigate any triangulation. Moreover, the numerical computation of the amplitude's scaling in the large spin limit has many limitations. On the contrary, this new procedure is much more feasible from a computational point of view since it requires to compute an amplitude at fixed boundary spins. We test our idea in the 3-dimensional Ponzano Regge model 2.2.2, analyzing the amplitude formed by three tetrahedra glued together on one internal length. We recover the semiclassical geometries dominating the spin foam. Stationary phase points in the bulk spin match the classical internal lengths allowed at given boundary data. This paper is particularly interesting

because it shows that computations in spin foam theories can be done from a different perspective, in a new and easier way. Our algorithm could be useful also for people in other fields dealing with the critical behavior of highly oscillating functions. Finally, in Chapter 8, we apply our methods to the 4-dimensional $SU(2)$ BF model. By computing the amplitude formed by three 4-simplices glued together, the so-called Δ_3, we can detect stationary phase points that are compatible with flat and curved boundary geometries. This result clashes with the claims of flatness in spin foam present in literature that, even if developed for the EPRL model, can be applied to this simpler case. The flatness problem argues that the partition function of the EPRL model is dominated in the semiclassical limit by flat geometries. The same arguments can be directly applied to $SU(2)$ BF spin foam theory, and they indicate that curved geometries should be suppressed in the large boundary spins limit. Our numerics prove that this is not the case.

Our work and the papers here presented, aimed to address some crucial questions in spin foam theories. We found some partial answers so far, which suggest a way forward to proceed.

In [63, 27] there are two different estimates of the divergence called "self-energy" diagram. An extensive set of power-law divergences are compatible with these two analyses. A better understanding of its properties would help to correctly regularize the theory without introducing a cosmological constant, following a prescription similar to the one studied in [64]. `sl2cfoam` allows the numerical computation of this amplitude, and it could be useful to clarify the problem.

Another pressing issue is the renormalization group flow of the EPRL vertex amplitude. Since the discretization breaks the diffeomorphism invariance of the continuous theory, we need to understand what mechanism can restore it. It would be helpful to find a fixed point in the renormalization group flow and to identify phase transitions. An interesting insight on this topic is provided in [23, 65, 66] and in [67, 68, 69, 70, 29]. In this last series of works, the authors perform a numerical investigation of the flow of the euclidean EPRL model on a hypercubic lattice and a large number of vertices. The calculations are possible thanks to some strong but vital approximations: they work with the euclidean version of the theory, they restrict to a specific form of the intertwiners, and instead of using the full vertex amplitude they replace it with its asymptotic formula. At present, `sl2cfoam` cannot directly attack analog computation since the number of vertices needed for a lattice computation is probably out of our reach. Still, we do not exclude to be able to do it soon after all the proposed upgrades are implemented, and we have access to more processing power (for the moment we are limited to a 32 cores machine). Nevertheless, if we restrict our computations to a purely quantum region characterized with relatively small spins, probably up to order 10, we can now compute transition amplitudes with a few vertices.

Concerning the flatness problem, there are two interesting opportunities to finally settle the dispute. From a numerical standpoint, an important step would be to apply the algorithms in 7 and 8 to the $SL(2, \mathbb{C})$ EPRL model and to explore more refined triangulations in which the Regge equations are not trivial, as it is the case for the 4-dimensional Δ_3. We should then be able to compare BF and EPRL directly. In the topological case, in principle, all deficit angles are allowed in the semiclassical limit of a given boundary state. Instead, if the EPRL aims to be a 4-dimensional analogous of the Ponzano-Regge model, then the quantum simplicity constraints 2.62 should select only stationary phase points corresponding to solutions of the Regge equations of motion. At the present stage, this is not clear at all: the semiclassical limit of amplitudes with multiple vertices could lead to a different discrete version of classical General Relativity then Regge Calculus. Or the simplicity constraints could not be correctly imposed at the quantum level. In this sense, numerics can help us in understanding the theory. A calculation involving bulk lengths can be set up. Using our algorithms, it is feasible from a computational point of view, both in the EPRL and in the BF model, and we think it should be carried out as soon as possible.

Analytically, we are currently exploring a different path. In [19], Hellmann and Kaminski studied the wave front set of the partition function of the $SO(4)$ EPRL model. They argue that analyzing the properties of the distributions involved in the spin foam amplitudes, one can recover the holonomies dominating the partition function's integrals 2.70 (and the classical equations for bivectors). They then

interpret these holonomies with classical variables, and they argue for the flatness of the model. Their geometrical interpretation is not entirely convincing since it should also lead to flatness for the BF case. However, we are intrigued by their ideas. We are currently computing the wave front set of the $SL(2,\mathbb{C})$ EPRl partition function, and we hope it could help us to shed some light on the spin foam semiclassical limit for an extended triangulation from an analytic point of view.

Are the simplicity constraints 2.23 imposed correctly in the EPRL model? Do we recover the solution of Regge equations 2.26 in a specific limit of the theory? And if not, what is the semiclassical limit in the case of an extended triangulation? These questions still do not have a clear answer. At the same time, we think that the work we have been done in Marseille in the last years can be rightly considered an important step ahead, to explore spin foam theories and to start filling the gap between computations and physical speculations. Is the EPRL model a good, or at least consistent, theory for quantum gravity? We can not answer this fundamental question yet, but we like to think that we are heading in the right direction to solve the puzzle.

Bibliography

[1] C. Rovelli, "Quantum gravity," Cambridge University Press, Cambridge (UK), 2004.

[2] T. Thiemann, "Modern Canonical Quantum General Relativity," Cambridge University Press, Cambridge (UK), 2007.

[3] Jonathan Engle, Etera Livine, Roberto Pereira, and Carlo Rovelli. LQG vertex with finite Immirzi parameter. *Nucl. Phys.*, B799:136–149, 2008.

[4] Etera R. Livine and Simone Speziale. A New spinfoam vertex for quantum gravity. *Phys. Rev.*, D76:084028, 2007.

[5] Etera R. Livine and Simone Speziale. Consistently Solving the Simplicity Constraints for Spinfoam Quantum Gravity. *EPL*, 81(5):50004, 2008.

[6] Laurent Freidel and Kirill Krasnov. A New Spin Foam Model for 4d Gravity. *Class. Quant. Grav.*, 25:125018, 2008.

[7] Wojciech Kaminski, Marcin Kisielowski, and Jerzy Lewandowski. Spin-Foams for All Loop Quantum Gravity. *Class. Quant. Grav.*, 27:095006, 2010. [Erratum: Class. Quant. Grav.29,049502(2012)].

[8] John W. Barrett, R. J. Dowdall, Winston J. Fairbairn, Henrique Gomes, and Frank Hellmann. Asymptotic analysis of the eprl four-simplex amplitude. *J. Math. Phys.*, 50:112504, 2009.

[9] John W. Barrett, R. J. Dowdall, Winston J. Fairbairn, Frank Hellmann, and Roberto Pereira. Asymptotic analysis of Lorentzian spin foam models. *PoS*, QGQGS2011:009, 2011.

[10] T. Regge, "General Relativity Without Coordinates," Nuovo Cim. **19**,

[11] G. Ponzano, T. Regge, Semiclassical limit of Racah coefficients *Spectroscopic and group theoretical methods in physics* (1968), 1-58 pp.

[12] Eugenio Bianchi, Leonardo Modesto, Carlo Rovelli, and Simone Speziale. Graviton propagator in loop quantum gravity. *Class. Quant. Grav.*, 23:6989–7028, 2006.

[13] Simone Speziale. Background-free propagation in loop quantum gravity. *Adv. Sci. Lett.*, 2:280–290, 2009.

[14] Eugenio Bianchi, Elena Magliaro, and Claudio Perini. LQG propagator from the new spin foams. *Nucl. Phys.*, B822:245–269, 2009.

[15] Eugenio Bianchi and You Ding. Lorentzian spinfoam propagator. *Phys. Rev.*, D86:104040, 2012.

[16] Florian Conrady and Laurent Freidel. On the semiclassical limit of 4d spin foam models. *Phys. Rev.*, D78:104023, 2008.

[17] Valentin Bonzom. Spin foam models for quantum gravity from lattice path integrals. *Phys. Rev.*, D80:064028, 2009.

[18] M. Han, "Semiclassical Analysis of Spinfoam Model with a Small Barbero-Immirzi Parameter," *Phys. Rev. D*, vol. 88, p. 044051, 2013.

[19] Frank Hellmann and Wojciech Kaminski. Holonomy spin foam models: Asymptotic geometry of the partition function. *JHEP*, 10:165, 2013.

[20] José Ricardo Oliveira. EPRL/FK Asymptotics and the Flatness Problem. *Class. Quant. Grav.*, 35(9):095003, 2018.

[21] J. Engle and W. Kaminski, private communications and ILQGS seminar "Panel on the status of the vertex"

[22] B. Dittrich, S. Mizera and S. Steinhaus, "Decorated tensor network renormalization for lattice gauge theories and spin foam models," New J. Phys. **18** (2016) no.5, 053009

[23] B. Dittrich, "The continuum limit of loop quantum gravity - a framework for solving the theory," in *Loop Quantum Gravity*, vol. Volume 4 of *100 Years of General Relativity*, pp. 153–179.

[24] B. Bahr and S. Steinhaus, "Investigation of the Spinfoam Path integral with Quantum Cuboid Intertwiners," Phys. Rev. D **93** (2016) no.10, 104029

[25] V. Bonzom, R. Gurau and V. Rivasseau, "Random tensor models in the large N limit: Uncoloring the colored tensor models," Phys. Rev. D **85** (2012), 084037

[26] D. Benedetti and R. Gurau, "Phase Transition in Dually Weighted Colored Tensor Models," Nucl. Phys. B **855** (2012), 420-437

[27] P. Donà, "Infrared divergences in the EPRL-FK Spin Foam model," Class. Quant. Grav. **35** (2018) no.17, 175019

[28] V. Bayle, F. Collet and C. Rovelli, Short-scale Emergence of Classical Geometry, in Euclidean Loop Quantum Gravity

[29] B. Bahr, G. Rabuffo and S. Steinhaus, Renormalization of symmetry restricted spin foam models with curvature in the asymptotic regime *Phys. Rev. D **98**, no.10*, 106026 (2018)

[30] P. Dona and G. Sarno, "Numerical methods for eprl spin foam transitionamplitudes and lorentzian recoupling theory," *Gen. Rel. Grav.*, vol. 50, p. 127, 2018.

[31] Simone Speziale. Boosting wigner's nj-symbols. *J. Math. Phys.*, 58(3):032501, 2017.

[32] Pietro Dona, Marco Fanizza, Giorgio Sarno, and Simone Speziale. SU(2) graph invariants, Regge actions and polytopes. *Class. Quant. Grav.*, 35(4):045011, 2018.

[33] P. Donà, M. Fanizza, G. Sarno and S. Speziale, "Numerical study of the Lorentzian Engle-Pereira-Rovelli-Livine spin foam amplitude," Phys. Rev. D **100** (2019) no.10, 106003

[34] J. W. Barrett, W. J. Fairbairn and F. Hellmann, "Quantum gravity asymptotics from the SU(2) 15j symbol," Int. J. Mod. Phys. A **25** (2010), 2897-2916

[35] Giorgio Sarno, Simone Speziale, and Gabriele V. Stagno. 2-vertex Lorentzian Spin Foam Amplitudes for Dipole Transitions. *Gen. Rel. Grav.*, 50(4):43, 2018.

[36] E. Bianchi, C. Rovelli and F. Vidotto, "Towards Spinfoam Cosmology," Phys. Rev. D **82** (2010), 084035 doi:10.1103/PhysRevD.82.084035

[37] P. Donà, F. Gozzini and G. Sarno, "Searching for classical geometries in spin foam amplitudes: a numerical method," Class. Quant. Grav. **37** (2020) no.9, 094002

[38] P. Dona, F. Gozzini and G. Sarno, "Numerical analysis of spin foam dynamics and the flatness problem,"

[39] Carlo Rovelli and Francesca Vidotto. *Covariant loop quantum gravity: an elementary introduction to quantum gravity and spinfoam theory.* Cambridge University Press, Cambridge (UK), 2015.

[40] P. Dona and S. Speziale, "Introductory lectures to loop quantum gravity"

[41] Alejandro Perez. The spin foam approach to quantum gravity. *Living Rev. Rel.*, 16:3, 2013.

[42] R. De Pietri and L. Freidel, "so(4) Plebanski action and relativistic spin foam model," Class. Quant. Grav. **16** (1999), 2187-2196

[43] R. M. Williams, "Discrete quantum gravity: The Regge calculus approach," Int. J. Mod. Phys. B **6** (1992), 2097-2108

[44] D. A. Varshalovich, A. N. Moskalev, and V. K. Khersonskii. *Quantum Theory of Angular Momentum.* World Scientific, Singapore, 1988.

[45] A. P. Yutsis, I. B. Levinson, and V. V. Vanagas. *Mathematical apparatus of the theory of angular momentum.* 1962.

[46] P. Martin-Dussaud, "A Primer of Group Theory for Loop Quantum Gravity and Spin-foams," Gen. Rel. Grav. **51** (2019) no.9, 110

[47] Werner Ruhl. *The Lorentz group and harmonic analysis.* The Mathematical physics monograph series. New York: W. A. Benjamin, 1970.

[48] Jonathan Engle and Roberto Pereira. Regularization and finiteness of the Lorentzian LQG vertices. *Phys. Rev.*, D79:084034, 2009.

[49] M.A. Naimark and H.K. Farahat. *Linear Representations of the Lorentz Group.* International Series in Pure and Applied Mathematics. Elsevier Science, 2014.

[50] M. A. Rashid. Boost Matrix Elements of the Homogeneous Loretz Group. *J. Math. Phys.*, 20:1514–1519, 1979.

[51] A. Perelomov, "Generalized coherent states and their applications,"

[52] Torbjorn Granlund and the GMP development team. GNU multiple precision arithmetic library 6.1.2, December 2016. `https://gmplib.org/`.

[53] Laurent Fousse, Guillaume Hanrot, Vincent Lefèvre, Patrick Pélissier, and Paul Zimmermann. MPFR: A Multiple-Precision Binary Floating-Point Library With Correct Rounding, 2018.

[54] Andreas Enge, Patrick Pélissier, and Paul Zimmermann. *MPC: Multiple Precision Complex Library.* INRIA, 1.1.0 edition, 2018. `http://www.multiprecision.org/mpc/`.

[55] William Kahan. *Pracniques: Further Remarks on Reducing Truncation Errors, Commun. ACM* 8, (1965) 40,

[56] H. T. Johansson and C. Forssen. Fast and accurate evaluation of Wigner 3j, 6j, and 9j symbols using prime factorisation and multi-word integer arithmetic. *SIAM J. Sci. Statist. Comput.*, 38:A376–A384, 2016.

[57] J. Rasch and A. C. H. Yu. Efficient storage scheme for precalculated wigner 3j, 6j and gaunt coefficients. *SIAM J. Sci. Comput.*, 25(4):1416–1428, April 2003.

[58] Open Source. Klib. `https://github.com/attractivechaos/klib/`, 2016.

[59] François Collet. A (simple) expression of the unitary-irreducible SL(2,C) representations as a finite sum of exponentials. *In Preparation.*

[60] Jacek Puchta. Asymptotic of Lorentzian Polyhedra Propagator. 2013.

[61] The code to compute the $SU(2)\Delta_3$amplitude is available here.

[62] J. W. Barrett, M. Rocek and R. M. Williams, "A Note on area variables in Regge calculus," Class. Quant. Grav. **16** (1999), 1373-1376 doi:10.1088/0264-9381/16/4/025

[63] Aldo Riello. Self-energy of the Lorentzian Engle-Pereira-Rovelli-Livine and Freidel-Krasnov model of quantum gravity. *Phys. Rev.*, D88(2):024011, 2013.

[64] L. Freidel and D. Louapre, Diffeomorphisms and spin foam models. *Nucl. Phys.* B **662** (2003) 279 doi:10.1016/S0550-3213(03)00306-7

[65] B. Dittrich, E. Schnetter, C. J. Seth and S. Steinhaus, Coarse graining flow of spin foam intertwiners. *Phys. Rev. D* **94**, no. 12, 124050 (2016) doi:10.1103/PhysRevD.94.124050

[66] C. Delcamp and B. Dittrich, Towards a phase diagram for spin foams. *Class. Quant. Grav.* **34** (2017) no.22, 225006 doi:10.1088/1361-6382/aa8f24

[67] Benjamin Bahr. On background-independent renormalization of spin foam models. *Class. Quant. Grav.*, 34(7):075001, 2017.

[68] Benjamin Bahr and Sebastian Steinhaus. Numerical evidence for a phase transition in 4d spin foam quantum gravity. *Phys. Rev. Lett.*, 117(14):141302, 2016.

[69] Benjamin Bahr and Sebastian Steinhaus. Hypercuboidal renormalization in spin foam quantum gravity. *Phys. Rev.*, D95(12):126006, 2017.

[70] Benjamin Bahr, Sebastian Kloser, and Giovanni Rabuffo. Towards a Cosmological subsector of Spin Foam Quantum Gravity. *Phys. Rev.*, D96(8):086009, 2017.

Chapter 5

Numerical study of the Lorentzian Engle-Pereira-Rovelli-Livine spin foam amplitude

Numerical study of the Lorentzian Engle-Pereira-Rovelli-Livine spin foam amplitude

Pietro Donà[a], Marco Fanizza[b], Giorgio Sarno[c] and Simone Speziale[c]

[a] IGC & Physics Department, Penn State, University Park, PA 16802, USA

[b] NEST, Scuola Normale Superiore and Istituto Nanoscienze-CNR, I-56126 Pisa, Italy

[c] CPT, Aix Marseille Univ., Univ. de Toulon, CNRS, Marseille, France

June 25, 2020

Abstract

The Lorentzian Engle-Pereira-Rovelli-Livine spin foam amplitude for loop quantum gravity is a multi-dimensional noncompact integral of highly oscillating functions. Using a method based on the decomposition of Clebsch-Gordan coefficients for the unitary infinite-dimensional representations of SL(2,C) in terms of those of SU(2), we are able to provide for the first time numerical evaluations of the vertex amplitude. The values obtained support the asymptotic formula obtained by Barrett and collaborators with a saddle point approximation, showing, in particular, a power law decay and oscillations related to the Regge action. The comparison offers a test of the efficiency of the method. Truncating the decomposition to the first few terms provides a qualitative matching of the power law decay and oscillations. For vector and Euclidean Regge boundary data, a qualitative matching is obtained with just the first term, which corresponds to the simplified EPRL model. We comment on future developments for the numerics and extension to higher vertices. We complete our work with some analytic results: We provide an algorithm and explicit configurations for the different geometries that can arise as boundary data, and explain the geometric consequences of the decomposition used.

Contents

1 Introduction

We report on numerical studies of the Lorentzian Engle-Pereira-Rovelli-Livine (EPRL) vertex amplitude for spin foam quantum gravity [1, 2] (for reviews, see [3, 4]). These are aimed in particular at testing its large spin asymptotic behavior, as derived by Barrett et al. [5]. The asymptotics can be interpreted as a semiclassical limit for the vertex amplitude and shows the presence of the Regge action, for a suitable choice of boundary data. It establishes an important relation to (discrete) general relativity that is at the heart of most of the physical applications of the EPRL model, thereby the interest in numerical verifications.

Our numerical work is based on the code `sl2cfoam` developed in [6] and publicly available at [7], optimized here for the specifics of the vertex amplitude. The code implements the method of [8] to compute Lorentzian Clebsch-Gordan coefficients and spin foam amplitudes. Our goal is twofold: on the one hand, to provide the first numerical test of Barrett's Lorentzian asymptotics results [5], thus verifying the saddle point approximation underpinning it, as well as estimating its validity. On the other hand, to examine the robustness of `sl2cfoam` and test its performances. This means being able to compute Lorentzian spin foam amplitudes in the deep quantum regime, a necessary step for the spin foam formalism.

The results we found are encouraging, albeit not completely satisfactory. The numerics confirm Barrett's formula for boundary data corresponding to vector geometries or to Euclidean 4-simplices. In these cases, the asymptotics is reached fast, with an error below 10% at spins of order 10. This confirms the validity of the saddle point approximation already at small spins, a situation similar to the much more extensively studied case of asymptotics of SU(2) invariants, see e.g. [9, 10]. In parallel, it shows the accuracy and robustness of `sl2cfoam`. To give an idea of the heavy computational load required to achieve these results, the plot used to confirm the Euclidean asymptotics at spins of order 10 needed the evaluation of 10^{11} configurations, each of which is determined by up to 10^4 one-dimensional unbounded integrals of oscillating functions. We used a server provided by the CPT with 32 Intel® Xeon® CPUs E5-2687W v2 at 3.40GHz with 264 gigabytes of RAM. The evaluation times depend on the boundary data, as we will explain in the next sections. For an Euclidean 4-simplex, the main plot of section 5.3 took approximately 3 weeks. For vector geometries the two plots in section 5.2 took about 30h each. Lorentzian 4-simplices are even more demanding, and a bottleneck in our computational precision restricted the number of data points accessible to us. These are shown in section 5.4, which took about 2 days. These were enough to provide evidence of a critical behavior with the predicted power law falloff, as well as nonmonotonic behavior depending on the Immirzi parameter. But a more significative agreement with the asymptotic formula, in particular seeing the predicted oscillations, was not obtained, and will require more computational work. Our results also show that the simplified model

introduced in [8] captures the key features of the full EPRL asymptotics for vector and Euclidean Regge geometries, but fails to do so, and instead decays exponentially, for Lorentzian geometries.

The increased difficulty of Lorentzian 4-simplices has partially to do with the fact that one cannot resort to an equispin configuration. The best we found was a certain isosceles configuration, but even then one has to deal with individual spins that are much higher than the value of the rescaling parameter controlling the asymptotics. Furthermore, the internal sums introduced by the method of [8] turn out to converge more slowly than for a Euclidean 4-simplex. This fact actually has a geometric origin, which explains how the Lorentzian 4-simplex is reconstructed from many Euclidean 4-simplices compatible with the SU(2) $\{15j\}$ symbol, and whose tetrahedra are suitably transformed thanks to the half-edge booster functions. This discussion also clarifies the critical behavior observed for the simplified model.

To obtain the numerical results presented, it proved necessary to develop an efficient algorithm to construct the boundary data. This is a spin-off of our work, and we devote a section of the paper to explain how this problem can be solved and provide in the same online repository [7] the relevant pieces of code. For the vector geometries, we used the explicit parametrization worked out in [10]. For the Regge geometries, we used a "deconstruction" algorithm, whereby we start from a geometric 4-simplex identified by its vertices, and derive the 3D data associated with it by the EPRL model's Y map. This procedure exposes some useful properties of the 3D data and was helpful for us to better understand the details of the saddle point analysis of [5]. We provide some more explicit formulas for the Hessian at the saddle point, needed for the numerical comparison of the analytic formula with the data points.

Barring the increased computational power to confirm precisely the analytic formula for Lorentzian 4-simplices, our work confirms the validity of this crucial result for the semiclassical limit of the EPRL model, but more importantly supports the robustness of the method [8] and code `sl2cfoam` [6], which can now be used to perform more ambitious calculations. To that end, we point out the heavy cost of using coherent intertwiners. These are needed for the asymptotic formula, but many physical applications of the EPRL spin foam model can be done in the much cheaper orthonormal basis of intertwiners. Some of us presented calculations with two nonsimplicial vertices in [11]. The present code is much more performing than the one there used, and we hope to apply it in future work to calculations with a few simplicial vertices and orthonormal intertwiners.

With the intent to make the paper concise and its technical results easier to appreciate, we refer to the existing literature for the necessary background. In particular, to [1, 12, 2] for the analytic background on the EPRL model, to [5] for its saddle point approximation (see also [13, 14, 15, 16, 17] for related work), to [8] for the method used for the exact evaluation, and to [6] for the numerical code, describing its details, functioning scheme, and generic performance tests. Section 2 contains the minimal information about the vertex amplitude for the paper to be self-contained and gives an overview of the approach used for the calculation. Section 3 describes our algorithm to identify boundary data with the required properties, and the explicit configurations used in the numerical calculations. Section 4 discusses the central point of the convergences of the internal sums and presents a useful approximation that we use to shorten significantly the numerical time of some numerical evaluations. Section 5 contains our main results, a selection of data and their comparison with the analytic asymptotic behavior. Section 6 contains a discussion on the role of the booster functions in mapping Lorentzian 4-simplices from the Euclidean ones associated with the SU(2) $\{15j\}$ symbol, as well as a summary of the numerical situation and future developments. After our conclusions, we supplement the paper with two Appendices. In one we provide explicit formulas to fix our conventions. In the second we summarize the asymptotic analysis of the EPRL vertex [5] and report on the form of the Hessian at the critical point.

2 EPRL vertex amplitude and its asymptotic limit

The (coherent) vertex amplitude for the Lorentzian EPRL spin foam model [1, 2] is an SL(2, ℂ) invariant associated to the boundary graph of a 4-simplex,

$$A_v(j_{ab}, \vec{n}_{ab}) := \int \prod_{a=2}^{5} dh_a \prod_{a<b} D^{(\gamma j_{ab}, j_{ab})}_{j_{ab}, -\vec{n}_{ab}, j_{ab}, \vec{n}_{ba}}(h_a^{-1} h_b), \tag{1}$$

where $h_a \in \mathrm{SL}(2,\mathbb{C})$, and $D^{(\rho,k)}(h)$ are infinite-dimensional unitary representations of the principal series, labeled by $\rho \in \mathbb{R}$ and $k \in \mathbb{Z}/2$. The irreducible representations (irreps) are restricted to satisfy $\rho_{ab} = \gamma k_{ab}$, where γ is the Immirzi parameter, and expressed using Naimark's canonical basis with minimal spin eigenvalues $j_{ab} = k_{ab}$, and unit vectors $\vec{n}_{ab}$ used to build coherent intertwiners [18, 12]. Conventions and explicit formulas are reported in Appendix A. The minus sign in the vectors appearing as rows is for later convenience. The indices $a, b = 1, \ldots 5$ stand for the nodes of the graph, and notice that one redundant integration has been removed, which is necessary to ensure finiteness [19, 20] (see also the discussion in [11]).

The boundary data of the amplitude are ten spins $j_{ab} = j_{ba}$ and twenty unit vectors $\vec{n}_{ab} \neq \vec{n}_{ba}$. Four different subsets of data play an important role, see Fig. 1: First, closed twisted geometries, defined by the following closure conditions,

$$\sum_{b \neq a} j_{ab} \vec{n}_{ab} = 0, \qquad \forall a = 1. \tag{2}$$

This means that the spins and normals data around each node define a tetrahedron.[1]

Within the space of closed twisted geometries, we can distinguish two disconnected subsets. One is vector geometries, if furthermore there exist five rotations $R_a \in \mathrm{SO}(3)$ such that the two normals associated to each face can be made opposite to one another:

$$R_a \vec{n}_{ab} = -R_b \vec{n}_{ba}. \tag{3}$$

These rotations are determined by h_a at the corresponding critical point. Clearly, the simplest possible case is when the normals are pairwise antiparallel,

$$\vec{n}_{ab} = -\vec{n}_{ba}, \tag{4}$$

which plays a useful role in choosing data. It is a remarkable fact that all Euclidean Regge geometries, namely all Euclidean 4-simplices in this context, are a subset of vector geometries. They are characterized by additional shape-matching constraints on top of Eq. 3, which can be described either using bivectors [5, 25] or spherical cosine laws [26, 10]. Their neat implication is to guarantee that the five tetrahedra determined by the closure conditions coincide with those determined as the boundary of a 4-simplex having the spins as areas.[2] What happens in the simplest case 4 is that there is always one critical point with all holonomies at the identity, and only when the shape-matching conditions are further satisfied does one find a second non trivial critical point that allows the reconstruction of the Euclidean 4-simplex.

The second disconnected subset of the closed twisted geometries are the Lorentzian Regge geometries, for which the boundary data coincide with those determined by a Lorentzian 4-simplex with all tetrahedra spacelike. The subset can again be characterized by shape-matching constraints in terms of bivectors [5, 25] or Lorentzian spherical cosine laws [27, 28]. Furthermore, while in this subset 3 are not satisfied, it is still true that the 3D normals are related by five *complex* transformation H_a such that

$$H_a \vec{n}_{ab} = -H_b \vec{n}_{ba}. \tag{5}$$

These unimodular complex matrices are non unitary 3D representations of Lorentz boosts. They are again determined by the h_a at the corresponding critical point.

---

[1]To be more precise, twisted geometries have additional 'twist' angle variables, denoted ξ_{ab} and canonically conjugated to the spins [21, 22]. These angles do not show up in the coherent amplitude 1, defined by eigenvectors of the Casimir spin operator. They would appear in amplitudes where also the areas are semiclassical and not quantum, like in the graviton propagator calculations, see e.g. [23, 24]. The boundary data of 1 are thus a subset of twisted geometries with $\xi_{ab} = 0$.

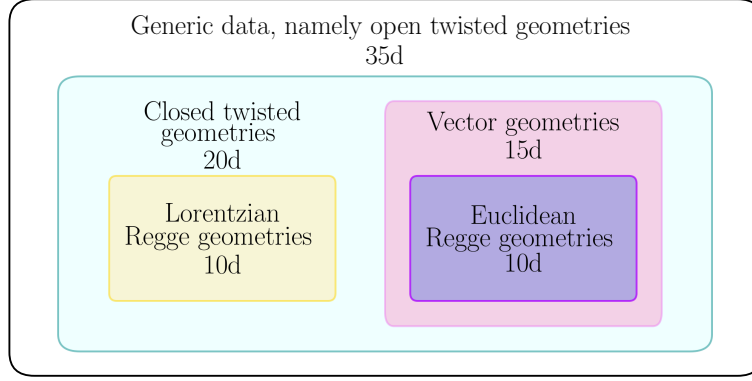[2]That this is compatible with Eq. 3 is not obvious, and one of the key results of the reconstruction.

Figure 1: *Classification of the boundary data. It is interesting to compare the situation with SU(2) BF theory [16, 10] and with the Euclidean EPRL model [29, 2, 12]. All three models have the same boundary states and thus some boundary data $(j_{ab}, \vec{n}_{ab})$ in the coherent amplitudes. What changes are the group elements being integrated over [which belong to $\mathrm{SL}(2, \mathbb{C})$, $\mathrm{SU}(2)$ and $\mathrm{SO}(4)$ respectively] and therefore the existence of critical points for a given set. For instance, Lorentzian Regge data only admit critical points for the $\mathrm{SL}(2, \mathbb{C})$ model.*

How these conditions allow the embedding of the boundary data in a flat Euclidean or Lorentzian 4-simplex will be explained in detail below. It is in the meantime useful to remark that the areas alone suffice to characterize a 4-simplex and distinguish whether it is Euclidean or Lorentzian. Data with areas compatible with a Euclidean 4-simplex can be either a vector geometry or a Euclidean Regge geometry depending on the compatibility or lack thereof of the normals with the Euclidean 4-simplex. This requirement can be expressed in terms of the shape-matching conditions reducing a twisted geometry to a Regge geometry [26, 10].

The coherent amplitude 1 is a complex number, and it is important to make a remark about its phase before continuing. The original formulation of the model [1] uses the standard basis of orthonormal inter-twiners, which are labeled by a spin number i_a per vertex, instead of the coherent intertwiners, labeled by unit vectors $\vec{n}_{ab}$. The resulting vertex amplitude $A_v(j_{ab}, i_a)$ is a real number, provided a certain phase convention for the Lorentz irrep matrices is chosen [8]. The interest in using the complex coherent amplitude 1 comes from the finer characterization of the boundary data and the clearer geometric interpretation that it permits. However, while the original amplitude is SU(2) invariant, Eq. 1 is only SU(2) covariant: A rotation of the 4-normals on a node preserves the amplitude only up to a phase.[3] This phase is irrelevant for geometric considerations because the coherent states themselves are only defined up to a phase, thus for any chosen boundary configuration, one can suitably tune the coherent state phase to have a real amplitude. Accordingly, we can neglect this phase and factor out the rotational gauge freedom at each node in our geometric considerations. Up to rotations, the boundary data span a 35-dimensional space. The closed twisted geometries are a 20-dimensional subset, 10 areas and $2 \times 5 = 10$ shape parameters, the vector geometries a 15-dimensional subset, ten areas and five angles [10], and the Regge geometries a ten dimensional subset, ten lengths or ten areas (up to some discrete ambiguity in the Euclidean case).

Thanks to properties of the coherent states, integrands like Eq. 1 can be written in exponential form with a linear dependence on the spins [18]. In particular, under a homogeneous rescaling $j_{ab} \mapsto \lambda j_{ab}$ we can write the integrand as $\exp \lambda S(g_a; j_{ab}, \vec{n}_{ab})$. This gives the possibility of evaluating the amplitude with a saddle point approximation in the homogeneous large spin limit, $\lambda \mapsto \infty$. This approximation was studied in [5],[4] and it was found that the leading order asymptotics of the coherent amplitude 1 has the following dependence on the boundary data:

---

[3]As for full Lorentz invariance, this is broken by the Y-map identifying $k = j$. Nonetheless, it can be shown that the vertex amplitude transforms covariantly under Lorentz transformations of the boundary data, and when various vertex amplitudes are glued together to form an extended spin foam, Lorentz invariance is restored in the bulk [30].

[4]The definition of the coherent vertex amplitude used here differs from the one in [5] by an overall phase, given for $\gamma > 0$ by

$$\exp\{i \sum_{a<b} (2j_{ab}(\pi + \Phi_{ab}) + \arctan \gamma)\}.$$

This is due to a phase difference between the Wigner matrices and the antilinear pairing of two unitary representations, as well as to our use of the antipodal map instead of the complex structure in associating coherent states to the target nodes. See Appendix A for details.

1. For generic open or closed twisted geometries: exponential decay in λ;

2. For vector geometries: power law decay λ^{-12};

3. For Regge geometries: power law decay λ^{-12} with nonambiguous real oscillations, and frequency given by the Regge action. The Regge action is independent of γ for Euclidean data and depends linearly on it for Lorentzian data.

Our goal in this paper is to test numerically these saddle point approximations, in particular the power law decays and the frequency of the oscillations. Such a numerical evaluation is not an easy task: The formula for the amplitude contains 12 unbounded integrations, and a complex and rapidly oscillating integrand built out of sums of products of hypergeometric functions. A direct approach using for instance adaptive Monte Carlo methods[5] appears daunting, and we are not aware of any results even for the much simpler Lorentzian Barrett-Crane integrals. Facing these difficulties, the idea of [8] was to reduce as much as possible the unbounded integrations, taking advantage of the known factorization of $\mathrm{SL}(2,\mathbb{C})$ Clebsch-Gordan coefficients into $\mathrm{SU}(2)$ ones. Applied to Eq. 1, the method in [8] splits the expression into a convolution between an $\mathrm{SU}(2)$ $\{15j\}$ symbol and one-dimensional boost integrals, called booster functions and denoted B_4^γ:

$$A_v\left(j_{ab}, \vec{n}_{ab}\right) = \sum_{l_{ab}\geq j_{ab}} \sum_{k_a,i_a} \{15j\} \prod_{a=2}^{5} d_{k_a} B_4^\gamma(j_{ab}, l_{ab}; i_a, k_a) \prod_{a=1}^{5} c_{i_a}(\vec{n}_{ab}) \quad (6)$$

$$= \sum_{l_{ab},k_a,i_a} \quad (7)$$

Here $d_j := 2j + 1$. The $\{15j\}$ symbol is labeled by internal spins l_{ab} and intertwiners k_a, except at the node 1 without group integration, where it is labeled directly by the boundary spins and intertwiners. The unbounded sums over l_{ab} go from j_{ab} to infinity, whereas the sums over the intertwiner labels k_a, i_a are bounded by the usual $\mathrm{SU}(2)$ triangle inequalities. We define the simplified EPRL model consistently with [8, 6, 11] as the truncation of the EPRL amplitude (7) where only the first term in the summation $l_{ab} = j_{ab}$ is considered.
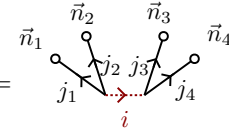
The booster functions depend both on the internal and the boundary data, and to obtain the coherent amplitude 1, they are contracted with the coefficients c_i of the coherent intertwiners determined by the normals $\vec{n}_{ab}$. The graphical notation used in the second line helps to keep track of which links carry internal spins, as well as of the orientation of the normals. The booster functions encode the details of the Y-map defining the EPRL model, and are defined as follows,

$$B_4^\gamma(j_f, l_f; i, k) = d_i d_k \sum_{m_f} \begin{pmatrix} j_f \\ m_f \end{pmatrix}^{(i)} \begin{pmatrix} l_f \\ m_f \end{pmatrix}^{(k)} \frac{1}{4\pi} \int_0^\infty dr \sinh^2 r \prod_{f=1}^{4} d_{j_f l_f m_f}^{(\gamma j_f, j_f)}(r) = \quad (8)$$

in terms of generalized four-legged $(4jm)$ Wigner symbols and boost matrix elements $d^{(\rho,k)}(r)$, see [8] for explicit formulas. To not be confused with d_i and d_k the dimension of the $\mathrm{SU}(2)$ irrep of spin i and k, see

Appendix A for more details on our conventions. For all links outgoing, the coherent intertwiner coefficients are

$$c_i(\vec{n}_f) := \sum_{m_f} \left(\begin{array}{c} j_f \\ m_f \end{array} \right)^{(i)} \prod_{f=1}^{4} D^{(j_f)}_{m_f j_f}(\vec{n}_f) = \quad \raisebox{-1em}{} \quad , \tag{9}$$

where

$$D^{(j)}(\vec{n}) = e^{-i\Phi J_z} e^{-i\Theta J_y} e^{i\Phi J_z} \tag{10}$$

is a Wigner matrix with Θ and Φ the zenithal and azimuthal angles of $\vec{n}$. If one of the links is incoming one multiplies the above formula by $\epsilon^{(j)}_{mn} = (-1)^{j-m} \delta_{m,-n}$.

In spite of its complexity, the vertex amplitude 6 is in a form suitable for numerical evaluations. The unbounded integrations have been limited to the booster functions, that are accessible numerically, but at the price of introducing infinite summations, the sums over the internal spins l, or "internal sums" for short. These may be just as hard to deal with numerically if they cannot be efficiently truncated. We will discuss this point below in detail. Let us first examine the different ingredients required in setting up the algorithm.

The first is evaluating the $\{15j\}$. Optimized algorithms exist in the literature for the simpler $\{6j\}$ and $\{9j\}$ symbols, but the $\{15j\}$ can be significantly more complicated. In fact, the problem would be intractable if one had to compute it starting from its definition as ten $(3jm)$ symbols, contracted following the graph drawn in Eg. 7. We can instead exploit the invariance of the sum over intertwiners under recoupling moves to trade the irreducible $\{15j\}$ appearing in Eq. 7 with a reducible one, a strategy successfully applied in [10] to compute numerically the semiclassical limit of the coherent $\{15j\}$ symbol. The simplest choice is a reducible $\{15j\}$ given by one sum of five $\{6j\}$ symbols. The $\{6j\}$ symbols can then be very efficiently computed thanks to the libraries `wigxjpf` developed in [32], based on smart storage of factorials used to compute the symbols. With this procedure, computing a single $\{15j\}$ for spins of order 10 takes about 10^{-6} s. We refer to the original paper for a detailed discussion of the library's performances, accuracy, and memory management.

The second is the booster functions. Here and in `sl2cfoam` we use the definition 8 with a polynomial expression for the boost matrix elements in e^{-r} derived in [33], which is more efficient to implement numerically than the usual expression as hypergeometric functions.[6] This expression is then amended with the phase conventions of [8] to make the booster functions and vertex amplitudes with orthonormal intertwiners real. We compute the numerical integrals at fixed magnetic labels m_f, then resum over the $(4jm)$ coefficients. This gives an upper estimate of $4\lambda^3$ integrals, since only three magnetic labels are linearly independent. The results are then stored using a hash table. With this procedure, computing a booster for spins of order 10 takes approximately 6 minutes on a single core, and needs to be computed only once. The main limitation of this method is that numerical instabilities become important at spins of order 50. These instabilities prevent the convergence of the boost integrals and are presumably due to the algebraic manipulations of very large numbers in the integrand. We worked with the GNU MPFR library for multiple-precision floating-point computations. See [6] for explicit formulas and more details. This makes the boosters the most delicate part of our code, and an obvious target for improvements, as we will discuss below in Sec. 6.2.

The third is the coherent intertwiner coefficients (9). This is the simplest part of the code, obtained contracting the Wigner matrices (10) with $(4jm)$ symbols computed with `wigxjpf`. The evaluation time of a single coherent state coefficient in `sl2cfoam` , is negligible with respect to the other computation times.

Finally one has to tabulate all these quantities and combine them to compute the amplitude. This is a delicate task that is performed using the hash-table algorithm described in detail in [6]. The resulting code is available in [7], and can be downloaded and used to independently rederive the results presented here, or push them forward using more powerful computers.

---

[6]The expression of [33] is very similar to the one previously derived in [34], but with the crucial difference that it only has finite sums. It is obtained starting from the integral representation, whereas the one of [34] starts from the infinite power series for the hypergeometric functions.

3 Constructing the boundary data

Our code allows us to compute the vertex amplitude for any boundary data, in principle. However, some choices are more efficient than others: for instance, symmetric configurations maximize the number of data points with a given maximal value of the rescaling parameter λ, thus optimizing the numerical effort. This is simply a consequence of the discreteness of the areas, and the fact that the numerical costs are strongly determined by the highest spin in the amplitude. For twisted, vector and Euclidean Regge geometries, one has access to the most symmetric configuration with all equal spins $j_{ab} \equiv j$, and this is the one we focused on.

For Lorentzian Regge geometries, it is not possible to take all spins as equal since an equilateral Lorentzian 4-simplex does not exist. We then devised a Mathematica code to span Lorentzian 4-simplices with all tetrahedra spacelike, and we scanned the space of configurations with integer or half-integer areas. We found that the case with minimal highest spin is a configuration with six spins equal to 2, and four spins equal to 5, which can then be rescaled by an integer multiple (but not a half-integer). The four highest spins can all be associated to the same tetrahedron, and it is then best to choose to gauge fix the $SL(2,\mathbb{C})$ integration on the same tetrahedron, so to avoid having to compute the heaviest booster function.

In all cases, we define the homogeneous rescaling parameter λ as an integer multiplying the smallest allowed configuration, hence $j_{ab} = \lambda/2$ for equispin data, and $j_{ab} = (2\lambda, 5\lambda)$ for Lorentzian boundary data. The two spin configurations are summarized in Table 1. From a purely numerical perspective, these configurations are rather generic, in the sense that they test generic structures of the numerical code.

Twisted, vector, Euclidean data	All spins:	$\lambda/2$	$= \frac{1}{2}, 1, \frac{3}{2}, 2, \ldots$
Lorentzian data	Four spins in gauge-fixed tetrahedron:	5λ	$= 5, 10, \ldots$
	Remaining six spins:	2λ	$= 2, 4, \ldots$

Table 1: *The two configurations used for boundary Regge data throughout the paper. The equispin data used for the Euclidean Regge geometries can also be used for twisted and vector geometry data: It is the choice of normals that distinguish the three cases.*

The information just given suffices to follow the numerical analysis in the paper. On the other hand, the actual construction of the boundary data turned out to be a nontrivial part of our analysis, and for the interested reader, we explain in the rest of this section how it can be done, and provide more details on the specific configurations we chose. The online repository [7] contains the Mathematica notebooks that we used to construct the boundary data we used in our asymptotic analysis. The notebook can be used to generate the boundary data for any spin foam vertex amplitude.

The first thing to keep in mind is that the amplitude's boundary data $(j_{ab}, \vec{n}_{ab})$ are purely 3-dimensional: j_{ab} label irreps of the canonical $SU(2)$ matrix subgroup corresponding to rotations preserving the time direction $t^I := (1,0,0,0)$, and $\vec{n}_{ab}$ are unit vectors in $\mathbb{R}^3$. We then have both an algebraic and a geometric mapping of the data into four-dimensional structures. The algebraic mapping is straightforward: The stabilizer of t^I is also the canonical $SU(2)$ subgroup of $SL(2,\mathbb{C})$ used in Naimark's basis of the unitary representation of the principal series (ρ, k) used in the EPRL model. Then the mapping is given by the map $Y : j \mapsto (\gamma j, j)$, and $|j, \vec{n}\rangle \mapsto |\gamma j, j; j, \vec{n}\rangle$. See [1, 5, 35] for more details. The geometric mapping is based on looking at the 3D geometry described by the data, and studying when and how it can be taken as the boundary of a flat 4-simplex. This mapping is finer and allows the classification of the data reported in Fig. 1. Given a set of data $(j_{ab}, \vec{n}_{ab})$, it can be directly tested whether it describes one of the special geometric classes. For our purposes though, we are interested in the reverse, "deconstructing" problem: start from a geometric object of interest, like a Euclidean or Lorentzian 4-simplex, and deduce the 3D data to be used as boundary states.

3.1 A closed twisted geometry

To generate the data of a closed twisted geometry it is convenient to start with five tetrahedra with areas matching along the graph of the 4-simplex. Each one can be characterized by the four areas and

two independent 3D dihedral angles, $\phi_e \equiv \phi_{bc}^{(a)}$ at the edge e of the tetrahedron a identified as the one shared with the tetrahedra b and c in the graph. An alternative parametrization consists in using one dihedral angle and the twist angle τ_e between the edge e and the opposite edge, see Fig. 2. The latter parametrization is closely related to the Kapovich-Millson [36, 37] conjugate variables (τ_e, μ_e), where $\mu_e = (j_{ab}^2 + j_{ac}^2 - 2j_{ab}j_{ac}\cos\phi_{bc}^{(a)})^{1/2}$.
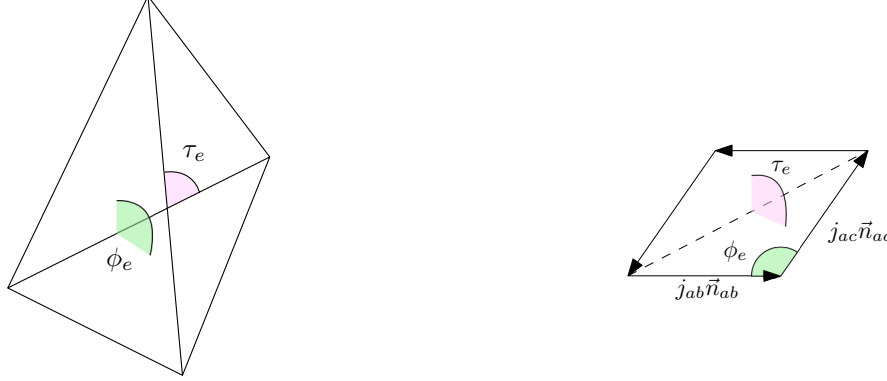

Figure 2: Left panel: *Parametrization of the tetrahedron with given areas in terms of a dihedral angle ϕ_e and the corresponding twist angle τ_e.*
Right panel: *The dihedral angle $\phi_e = \phi_{bc}^{(a)}$ and the corresponding twist angle τ_e in the Kapovich-Millson polygon made with the scaled normals $j_{ab}\vec{n}_{ab}$ and $j_{ac}\vec{n}_{ac}$. The variable μ_e is the length of the dashed line.*

In terms of these variables, we considered the following set of equiarea tetrahedra:

$$
\begin{array}{lllll}
\phi_{23}^{(1)} = \pi/2 & \phi_{12}^{(2)} = \pi/3 & \phi_{12}^{(3)} = 4\pi/5 & \phi_{12}^{(4)} = 5\pi/6 & \phi_{12}^{(5)} = 2\pi/3 \\
\tau_{23}^{(1)} = \pi/2 & \tau_{12}^{(2)} = 2\pi/3 & \tau_{12}^{(3)} = 5\pi/8 & \tau_{12}^{(4)} = 3\pi/8 & \tau_{12}^{(5)} = 5\pi/7
\end{array}
$$

These data correspond to five tetrahedra that, although all have the same areas, cannot be assembled to form a 4-simplex. As a result, we also have a certain freedom in picking up how to orient them in space. To keep things as simple as possible, we choose to orient all tetrahedra aligning a normal to a face with the x axis. We further fix the rotational gauge by assuming that a normal to a second face lies in the xy plane. The resulting normals are summarized in Table 2, and it can be explicitly checked that it is not possible to find local rotations so that all pairs at a given face satisfy the orientation equations (3).

$\vec{n}_{ab}$ b / a	1	2	3	4	5
1		$(1,0,0)$	$(0,1,0)$	$(-0.5,-0.5,0.70)$	$(-0.5,-0.5,-0.70)$
2	$(1,0,0)$		$(0.5,0.87,0)$	$(-0.62,-0.65,0.43)$	$(-0.88,-0.22,-0.43)$
3	$(1,0,0)$	$(-0.81,0.59,0)$		$(0.25,-0.41,0.88)$	$(-0.44,-0.18,-0.88)$
4	$(1,0,0)$	$(-0.87,0.5,0)$	$(-0.42,-0.15,0.89)$		$(0.29,-0.35,-0.89)$
5	$(1,0,0)$	$(-0.5,0.87,0)$	$(0.22,-0.70,0.68)$	$(-0.72,-0.17,-0.68)$	

Table 2: *Choice of normals for the closed twisted geometry described in the text. The gauge is fixed so that for every tetrahedron there is one normal in the x direction, and a second normal in the xy plane. The additional alignment $\vec{n}_{23} = (0,1,0)$ is a consequence of the straight angle $\phi_{23} = \pi/2$ among the shape parameters.*

3.2 A vector geometry

Vector geometries were originally characterized in [38], and an explicit parametrization was recently provided in [10]: One gives the ten areas, one dihedral angle $\phi_{bc}^{(a)}$ in four different tetrahedra, plus one additional angle

between two normals belonging to different tetrahedra; the latter angle is not gauge invariant and has to satisfy an inequality. It is convenient to choose the gauge 4 with all normals pairwise antiparallel. A simple configuration following this construction, with all areas equal and not giving a Regge geometry, is the following:

$$\phi_{34}^{(2)} = \frac{6}{15}\pi, \qquad \phi_{25}^{(3)} = \frac{8}{15}\pi, \qquad \phi_{25}^{(4)} = \frac{7}{15}\pi, \qquad \phi_{34}^{(5)} = \frac{8}{15}\pi, \qquad \phi_{53,42} = \frac{9}{15}\pi, \tag{11}$$

where $\phi_{53,42} := \arccos\left(\vec{n}_{53} \cdot \vec{n}_{42}\right)$ is the gauge-dependent angle. The resulting normals are summarized in Table 3.

$\vec{n}_{ab}$ b / a	1	2	3	4	5
1		$(0.82, -0.45, -0.35)$	$(-0.96, 0.05, 0.28)$	$(-0.76, 0.54, -0.34)$	$(0.9, -0.15, 0.41)$
2	$(-0.82, 0.45, 0.35)$		$(0.31, 0.21, -0.93)$	$(1, 0, 0)$	$(-0.49, -0.66, 0.57)$
3	$(0.96, -0.05, -0.28)$	$(-0.31, -0.21, 0.93)$		$(-0.34, -0.69, -0.64)$	$(-0.31, 0.95, 0)$
4	$(0.76, -0.54, 0.34)$	$(-1, 0, 0)$	$(0.34, 0.69, 0.64)$		$(-0.1, -0.14, -0.98)$
5	$(-0.9, 0.15, -0.41)$	$(0.49, 0.66, -0.57)$	$(0.31, -0.95, 0)$	$(0.1, 0.14, 0.98)$	

Table 3: *Choice of normals for the vector geometry 11 described in the text. The gauge is fixed so that all normals are pairwise antiparallel, $\vec{n}_{ab} = -\vec{n}_{ba}$.*

3.3   A Euclidean Regge geometry

By Euclidean Regge geometry we refer to boundary data that can be embedded in $\mathbb{R}^4$ to form a Euclidean flat 4-simplex. To construct such data, we start from a flat Euclidean 4-simplex, as the convex envelope of its five vertices. Using the freedom to do SO(4) transformations, we can always put a vertex in the origin of $\mathbb{R}^4$, one on the x axis, a third one in the xy plane, and a fourth one in the xyz hyperplane. This exhausts the rotational freedom, and the position of the last vertex is free. From the vertices we compute the edge vectors ℓ_e^I, with $I = 0, 1, 2, 3$ a Cartesian coordinate index. Their lengths $\ell_e := \|\ell_e^I\| := \sqrt{\ell_e^I \ell_e^J \delta_{IJ}}$ provide ten numbers that characterize uniquely the 4-simplex up to SO(4) transformations. From the edge vectors we can also define a simple bivector to each triangle t of the 4-simplex, given by $B_t^{IJ} := 2\ell_e^{[I} \ell_{e'}^{J]}$, where ee' is any pair of edges in t. Then from $A^2 := \|B^{IJ}\|^2 = B_{IJ} B^{IJ}/2$, or equivalently using Heron's formula from the edge lengths, we obtain the ten areas of the 4-simplex.[7]

The amplitude's boundary data are areas and 3D normals in the time-gauge frame. Therefore the next step is to find the transformation that takes all tetrahedra of our 4-simplex to the time-gauge, then compute the resulting 3D normals to the faces. Only then we can identify the SO(4)-invariant geometric area with the SU(2) irrep label j. To do so, we take as reference frame the $t = 0$ hyperplane to which the first tetrahedron belongs (the one determined by the first four vertices fixed earlier). Its 4D normal is already the canonical one for the time-gauge, $t^I = (1, 0, 0, 0)$. Hence we can directly compute the areas and 3D normals of this tetrahedron from the edge vectors, and take them as the first set of boundary data. For each of the remaining four tetrahedra, the procedure is not as straightforward. First, we determine the 4D normal from the triple product of edges with a common vertex, $e = 1, 2, 3$,

$$N_{aI} = \frac{\epsilon_{IJKL} \ell_{a1}^J \ell_{a2}^K \ell_{a3}^L}{\|\epsilon_{IJKL} \ell_1^J \ell_2^K \ell_3^L\|}, \tag{12}$$

ordered so that it is outgoing.[8] The SO(4) transformations mapping these vectors to t^I can be found with

---

[7]Note that the resulting function from vertices (or equivalently from lengths) to areas is always injective and generically bijective; it fails to be bijective in special cases, like precisely for all equal areas, that can correspond to either an equilateral 4-simplex, or a 4-simplex with seven equilateral triangles and three isosceles. The 3D normals then distinguish the two cases.

[8]This is determined computing the Euclidean scalar product between the 4D normal and the vector connecting the chosen vertex to the center of the 4-simplex. Throughout the paper, we always work with outgoing normals, both 3D and 4D, and accordingly all dihedral angles are external.

a formula similar to Rodrigues's 3D rotation formula,

$$\Lambda_a{}^I{}_J = \delta_J^I - \frac{1}{1 + N_a \cdot t} \left(N_a^I N_{aJ} + t^I t_J + N_a^I t_J - (1 + 2N \cdot t) t^I N_{aJ} \right),$$ (13)

$$\Lambda_a{}^I{}_J N_a^J = t^I, \qquad \det \Lambda_a{}^I{}_J = 1.$$

The 4D normals define the 4D dihedral angles $\theta_{ab} = \arccos(N_a \cdot N_b)$, and provide alternative expressions for the face bivectors as well. Using the Hodge dual $\star := (1/2)\epsilon_{IJKL}$, we have in fact

$$B_{ab} = \|B_{ab}\| \frac{\star N_a \wedge N_b}{\| \star N_a \wedge N_b \|} = -B_{ba}.$$ (14)

The simplicity of the bivectors is now manifest in that

$$N_{aI} B_{ab}^{IJ} = 0 = N_{bI} B_{ab}^{IJ},$$ (15)

and sums on the triangles in the same tetrahedron close,

$$\sum_{b \neq a} B_{ab} = 0 \qquad \forall a.$$ (16)

Using Eq. 13 we map each tetrahedron to the time-gauge and define the rotated bivectors in the frame of the reference tetrahedron,

$$\mathring{B}_{ab}^{IJ} := \Lambda_{aK}^I B_{ab}^{KL} \Lambda_{aL}^J.$$ (17)

This is simple in the time-gauge frame, i.e. $t_I \mathring{B}_{ab}^{IJ} = 0$. Therefore its magnetic part vanishes, $\mathring{B}_{ab}^{0i} = 0$, and we can identify a 3D vector with its electric part,

$$j_{ab} n_{ab}^k := \epsilon^k{}_{ij} \mathring{B}_{ab}^{ij}, \qquad \|\mathring{B}_{ab}\| = j_{ab}.$$ (18)

Equation 18 defines the remaining boundary data for the tetrahedra 2 to 5. Notice that we can also give a covariant formula for all 3D normals,

$$n_{ab}^I := (0, \vec{n}_{ab}) = \frac{2}{\|\star \mathring{B}_{ab}\|} t_J (\star \mathring{B}_{ab})^{IJ} = \Lambda_a{}^I{}_J \frac{N_b^J - N_a^J (N_a \cdot N_b)}{\sqrt{1 - (N_a \cdot N_b)^2}},$$ (19)

where the case $a = 1$ has $\Lambda_1 = \mathbb{1}$ and $N_1 = t$. The covariant equations are actually more convenient to implement in the numerical algorithm because they use only the 4D normals, and bypass the explicit reconstruction of the bivectors.

Pictorially, we can describe the above procedure as the 4-simplex being opened up by SO(4) rotations of four tetrahedra to the same $\mathbb{R}^3$ frame of the first tetrahedron. The resulting 3D object was called a *spike* in [10], to which we refer the reader for explicit figures. Since the data $(j_{ab}, \vec{n}_{ab})$ defined by Eq. (18) or Eq. 19 come from a Euclidean 4-simplex, we expect that they satisfy the saddle point conditions 2 and 3 of the vertex amplitude asymptotic analysis. Indeed, the closure conditions 2 are satisfied since Eq. 16 is $SO(4)$-invariant, thus it applies to $\mathring{B}_{ab}$ as well and in turn to the 3D normals. As for the orientation conditions 3, they follow from Eqs. 14 and 17. To see this, one notices that the 3D vector 18 also coincides with the electric part of the self-dual part of $\mathring{B}_{ab}$, and that under Eq. 17 the self-dual part transforms like a rotation.

It is convenient to perform these rotations, so to have a configuration with pairwise-opposite normals 4. This configuration was called *twisted spike* in [10]. It was there shown that the required rotations have directions $\vec{n}_{1a}$ and angles given precisely by the 4D dihedral angle $\theta_{1a} = \arccos(N_1 \cdot N_a)$. In other words, the twisted spike twists the axis of the tetrahedra by an amount corresponding to the original 4D dihedral angle, and in doing so one achieves the condition of pairwise-opposite normals 4. See [10] again for illuminating pictures. The twisted spike has a computational advantage because all holonomies at one of the two critical points are the identity.

We implemented the algorithm described above in the Mathematica code `EuclideanBoundaryDataMaker` in [7], which can be used to generate data corresponding to arbitrary Euclidean 4-simplices. For our numerics, we chose an equilateral 4-simplex. The main advantage is that having all areas equal, we can obtain a maximal number of data points for a fixed maximal numerical effort. The resulting normals corresponding to the twisted spike are summarized in Table 4.

$\vec{n}_{ab}$ $\diagdown$ b a	1	2	3	4	5
1		$(0,0,1)$	$(0.94,0,-0.33)$	$(-0.47,0.82,-0.33)$	$(-0.47,-0.82,-0.33)$
2	$(0,0,-1)$		$(-0.24,-0.91,0.33)$	$(0.91,0.25,0.33)$	$(-0.67,0.66,0.33)$
3	$(-0.94,0,0.33)$	$(0.24,0.91,-0.33)$		$(0.09,-0.66,-0.75)$	$(0.62,-0.25,0.75)$
4	$(0.47,-0.82,0.33)$	$(-0.91,-0.25,-0.33)$	$(-0.09,0.66,0.75)$		$(0.53,0.41,-0.75)$
5	$(0.47,0.82,0.33)$	$(0.67,-0.66,-0.33)$	$(-0.62,0.25,-0.75)$	$(-0.53,-0.41,0.75)$	

Table 4: *Choice of normals for the Euclidean Regge data, corresponding to the twisted spike. These are reconstructed from an equilateral 4-simplex using the algorithm described in the text.*

As a final comment it is useful to understand the relation between our "deconstruction" of the 4-simplex and the reconstruction that one does in the saddle point approximation, the critical point equations for the Euclidean spike admit the following four solutions (see Appendix B),

$$ h_a^{(c)} = \pm \exp\left(\frac{i}{2}\theta_{1a}\vec{n}_{1a}\vec{\sigma}\right), \qquad h_a^{(\text{P}c)} = \pm \exp\left(-\frac{i}{2}\theta_{1a}\vec{n}_{1a}\vec{\sigma}\right) = h_a^{(c)\dagger}, \tag{20} $$

all with $h_a \in \text{SU}(2) \subset \text{SL}(2,\mathbb{C})$. These group elements are precisely the Λ_a appearing in our procedure, namely one can show that

$$ \Lambda_a{}^I{}_J = \frac{1}{2}\text{Tr}\left(\sigma^I h_a^{(c)} \sigma_J h_a^{(c)\dagger}\right) , \tag{21} $$

where $\sigma^I = (\mathbb{1},\vec{\sigma})$, and σ_I is lowered with the Euclidean metric.

3.4   A Lorentzian Regge geometry

To obtain the Lorentzian boundary data, we follow the same strategy as the previous case, but some additional care will be needed to take into account the presence of future pointing and past pointing timelike vectors. We start from a Lorentzian 4-simplex with all tetrahedra spacelike[9], and derive the corresponding 3D data in the time-gauge from it. We consider the five vertices in $\mathbb{R}^4$ with metric $\eta = \text{diag}(-+++)$, and use the SO(1,3) freedom to place them as before, a vertex in the origin, one on the x axis, a third one in the xy plane, and a fourth one in the xyz hyperplane, with the last one completely free. The tetrahedron described by the first four vertices will always be spacelike, whereas the nature of the other four tetrahedra depends on the location of the fifth vertex. We derive as before the edge vectors ℓ_e^I, bivectors B_{ab}^{IJ}, and 4D normals N_a^I. The norms and scalar products are now given by η, and for the epsilon symbol we take the convention $\epsilon_{0123} = 1$.

To find a convenient choice of data, notice first that a Lorentzian 4-simplex cannot be equilateral, just like a triangle in 2D. Just like in 2D, the most regular 4-simplex with all spacelike sub-simplices is isosceles, with one equilateral tetrahedron and four equal isosceles ones, so in the simplest configuration we have four areas of one value and six of a different one. To find suitable ones, we need both values to be integers or half-integers. Recall also that the numerical algorithm becomes the more costly the higher the spins involved. Therefore to optimize the numerical calculations we want a configuration in which the ratio between the two areas is maximal, while at the same time minimizing the smallest integer or half integer realization of each area value. Using the algorithm `FromAreasToVericesLorentzian` in [7], we scanned the space of admissible

---

[9]A tetrahedron on the boundary of a Lorentzian 4-simplex is spacelike if its four-dimensional normal N_a is timelike, $N_a^I N_{aI} = -1$. Conversely, the tetrahedron is said to be timelike if its four normal is spacelike.

configurations, and settled on the ratio $2/5$ anticipated above.[10] This is a 4-1 configuration, namely four of the timelike normals are future pointing and one past pointing, or vice versa.

Let us choose the gauge-fixed tetrahedron 1 to be past-pointing, i.e. $N_1 = -t$. The remaining 4 normals are all future pointing, and can be computed from the edge vectors as in 12. To determine the 3D normals we proceed as in the Euclidean case, with $\Lambda_a \in \mathrm{SO}(1,3)$ this time. To transform the future pointing 4-normals to t we select the pure boost in the plane determined by t and N_a, which can be computed to be

$$\Lambda_a{}^I{}_J = \delta^I_J + \frac{1}{1 - N_a \cdot t}\left(N_a^I N_{aJ} + t^I t_J + N_a^I t_J - (1 - 2N_a \cdot t)t^I N_{aJ}\right), \qquad a \neq 1, \tag{22}$$
$$\Lambda_a{}^I{}_J N_a^J = t^I, \qquad \det \Lambda_a{}^I{}_J = 1.$$

We then have the expression 14 for the bivectors and Eq. 17 for the time-gauge bivectors as before, and define again the 3D normals via Eq. 18. The only difference is at the level of the covariant formula, which now reads

$$n_{ab}^I := (0, \vec{n}_{ab}) = \frac{2}{\| \star \mathring{B}_{ab}\|} t_J (\star \mathring{B}_{ab})^{IJ} = -\Lambda_a{}^I{}_J \frac{N_b^J + N_a^J (N_a \cdot N_b)}{\sqrt{(N_a \cdot N_b)^2 - 1}}, \qquad a \neq 1. \tag{23}$$

The 3D normals of the tetrahedron 1 are already in the chosen reference $\mathbb{R}^3$, and can then be directly computed from the vertices (or equally from 23 but with now $\Lambda_1 = -\mathbb{1}$, due to the fact that the normal to this tetrahedron is past-pointing). The resulting 3D object can be referred to as an antispike, because the tetrahedra boosted in the frame of the first will be "sitting inside" it, see Fig. 3 for a $1+1$ example. And notice that the normals of the faces shared with the first tetrahedron will be aligned, and not antialigned. While this configuration is a good representation of a Lorentzian 4-simplex in 3D, it will *not* feed a critical point to the coherent amplitude 44, because of the minus signs in front of half of the vectors, which were chosen for convenience in dealing with the vector and Euclidean geometries.[11] This can be fixed if we turn around the reference tetrahedron applying an inversion, namely the composition $\hat{T}\hat{P} \notin \mathrm{SL}(2, \mathbb{C})$ of a time reversal and a parity transformation. Doing so we obtain again a picture with all tetrahedra outside, which we call the Lorentzian spike. Pictorially, it can be distinguished from a Euclidean spike because the tetrahedra spiking out are too "short" to allow the mapping to a closed Euclidean 4-simplex, see again Fig. 3 to get some intuition.
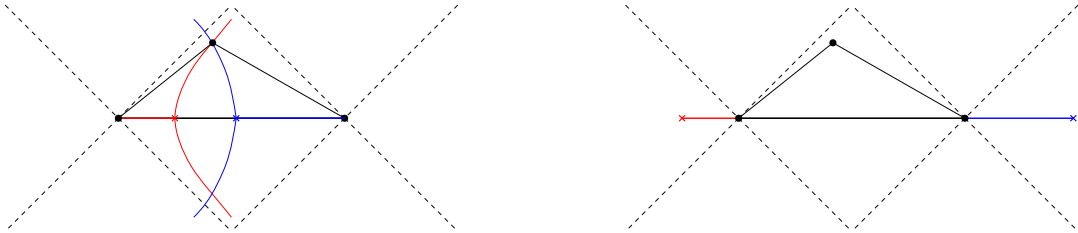

Figure 3: *Left panel: $1+1$ spacelike Lorentzian simplex and its antispike configuration, obtained boosting two sides in the 1D frame of the base. Two normals are future pointing and one is past pointing. The two hyperbolae are the points you obtain boosting the two sides.*
Right panel: The same simplex and the spike configuration, obtained acting with a $\hat{T}\hat{P}$ transformation after the antispike boosts. All normals are now pointing in the same direction.

For the Lorentzian spike, all 4-normals are future pointing, and the 3D normals of the first tetrahedron are each antialigned with the corresponding one of the tetrahedron sharing that face, as in the Euclidean case. On the other hand, there is not now a set of five rotations so that Eq. (3) holds, because the Λ_a are

---

[10]Limiting ourselves to numerators and denominators smaller than 40, we identified the following 32 possible ratios, in decreasing order:

$$\frac{2}{5}, \frac{15}{38}, \frac{13}{33}, \frac{11}{28}, \frac{9}{23}, \frac{7}{18}, \frac{12}{31}, \frac{5}{13}, \frac{13}{34}, \frac{8}{21}, \frac{11}{29}, \frac{14}{37}, \frac{3}{8}, \frac{13}{35}, \frac{10}{27}, \frac{7}{19}, \frac{11}{30}, \frac{4}{11}, \frac{13}{36}, \frac{9}{25}, \frac{14}{39}, \frac{5}{14}, \frac{11}{31}, \frac{6}{17}, \frac{13}{37}, \frac{7}{20}, \frac{8}{23}, \frac{9}{26}, \frac{10}{29}, \frac{11}{32}, \frac{12}{35}, \frac{13}{38}.$$

We found an upper bound at $1/\sqrt{6} \simeq .41 > 2/5 = .4$ for which the 4-simplex becomes degenerate, and a lower bound at $1/3$ for which the isosceles tetrahedra become null.

[11]The same would be true had we worked with the antipodal spinor conventions of [5] instead of the antipodal vectors.

pure boosts for $a \neq 1$. This means that there is no twisted spike configuration, and no configuration with all critical holonomies at the identity. The 3D normals satisfy instead Eq. (5), namely they can be antialigned by a set of five complex rotations.

The Mathematica code implementing this algorithm is called `LorentzianBoundaryDataMaker` in [7]. The normals obtained for the 2/5 ratio 4-simplex are summarized in Table 5 below.

$\vec{n}_{ab}$ b a	1	2	3	4	5
1		$(1, 0, 0)$	$(-0.33, 0.94, 0)$	$(-0.33, -0.47, 0.82)$	$(-0.33, -0.47, -0.82)$
2	$(-1, 0, 0)$		$(0.83, 0.55, 0)$	$(0.83, -0.28, 0.48)$	$(0.83, -0.28, -0.48)$
3	$(0.33, -0.94, 0)$	$(0.24, 0.97, 0)$		$(-0.54, 0.69, 0.48)$	$(-0.54, 0.69, -0.48)$
4	$(0.33, 0.47, -0.82)$	$(0.24, -0.48, 0.84)$	$(-0.54, 0.068, 0.84)$		$(-0.54, -0.76, 0.36)$
5	$(0.33, 0.47, 0.82)$	$(0.24, -0.48, -0.84)$	$(-0.54, 0.068, -0.84)$	$(-0.54, -0.76, -0.36)$	

Table 5: *Choice of normals for the Lorentzian Regge data. These are reconstructed from the chosen isosceles 4-simplex with area ratio 2/5, using the algorithm described in the text, and correspond to the spike configuration.*

In determining the analytic asymptotic formula to be compared with this configuration, let us recall the definition of the Lorentzian dihedral angles $\theta_{ab}^{L} \geq 0$. Following [5], the case with both timelike normals inside the same causal patch is called thick wedge, and the case with the timelike normals inside opposite causal patches is called thin wedge. With signature $-+++$, the scalar product of normals is negative in the first case, and positive in the second. Accordingly, we define

$$\text{thick wedge} \qquad N_a \cdot N_b = -\cosh \theta_{ab}^{L}, \tag{24}$$

$$\text{thin wedge} \qquad N_a \cdot N_b = \cosh \theta_{ab}^{L}. \tag{25}$$

The 4-simplex of Table 5 is of type 4-1, and we have four thin angles θ_{1a}^{L} and six thick ones θ_{ab}^{L} for $a, b \neq 1$.

The solutions of the critical point equations for the Lorentzian spike are

$$h_a^{(c)} = \pm \exp\left((\theta_{1a}^{L} + i\pi)\vec{n}_{1a} \cdot \frac{\vec{\sigma}}{2} \right), \qquad h_a^{(Pc)} = \pm \exp\left((-\theta_{1a}^{L} + i\pi)\vec{n}_{1a} \cdot \frac{\vec{\sigma}}{2} \right) = h_a^{(c)-1}. \tag{26}$$

They are a combination of a boost given by the thin angle and an additional rotation by π in the same direction. The origin of this rotation is the inversion performed to have the data describing a spike, so that the 3D normals in the reference tetrahedron are the opposite of the corresponding ones in the adjacent tetrahedra, and not parallel as in the antispike configuration with the reference tetrahedron being past pointing. To recover the pure boost 22 we remove this additional rotation, and indeed one can check that

$$\Lambda_a{}^{I}{}_J = \frac{1}{2}\text{Tr}\left(\sigma^I \hat{h}_a^{(c)} \sigma_J \hat{h}_a^{(c)\dagger} \right), \qquad \hat{h}_a^{(c)} = \pm \exp\left(\theta_{1a}^{L} \vec{n}_{1a} \cdot \frac{\vec{\sigma}}{2} \right) , \tag{27}$$

where $\sigma^I = (\mathbb{1}, \vec{\sigma})$, and where σ_I is lowered with the Minkowski metric.

4 Methods: Shelled sums and a useful approximation

The finiteness of the vertex amplitude [19] guarantees that the internal sums in Eq. (7) converge. However, the speed of the convergence depends on the boundary data considered, since for different configurations, both the booster functions and the $\{15j\}$ symbol can decrease either exponentially or polynomially. This speed determines crucially the efficiency of our numerical method: If the convergence is fast we can keep the lowest order terms only, but if the convergence is slow one has to add up more and more terms, and the numerical algorithm becomes slower and slower.

To study the convergence, we introduce a homogeneous integer cutoff Δ on the range of the internal spins,

$$\sum_{l_{ab}=j_{ab}}^{\infty} \rightarrow \sum_{l_{ab}=j_{ab}}^{j_{ab}+\Delta} \tag{28}$$

51

and we compare the value of the amplitude for successive truncations. Notice that each of these truncated sums, or *shelled* sums to use the terminology of [6], can have a priori arbitrarily high internal spins l. It is only the difference with the boundary spins j that is being truncated, namely the number of terms being summed over in Eq. 6. The truncation $\Delta = 0$ gives the simplified EPRL model defined in [8].

Let us estimate the number of terms in a given truncation, for the equispin case $j_{ab} = j$. The l configurations compatible with Eq. 28 are $(\Delta + 1)^6$. For each l's configuration, we have to sum over the internal intertwiners k. Notice from the graphical representation 7 that each internal intertwiner always has at least one external spin. Hence increasing l has the effect of tightening the triangular inequalities for the intertwiners. Consequently, the external triangular inequalities from the j spins provide an upper bound to the number of k configurations, which is $(2j)^4$ when all j's are equal. To complete the estimate we have to include the $2j$ terms coming from the sum defining the reducible $\{15j\}$ symbol used. Overall, this gives an upper bound of

$$(\Delta + 1)^6 \times (2j)^5 \tag{29}$$

configurations for the amplitude defined by boundary spins and intertwiners. For the coherent amplitude (6), one also has to sum over the external intertwiners i, which gives an additional $(2j)^5$ terms. Recall that for this configuration $\lambda = 2j$, the final upper bound estimate is

$$\#_\Delta \le (\Delta + 1)^6 \times \lambda^{10}. \tag{30}$$

An exact numerical counting confirms this estimate, see the Euclidean data in Fig. 4. A numerical fit reported there shows that the neat effect of the triangular inequalities is to remove a bit more than half of the configurations.
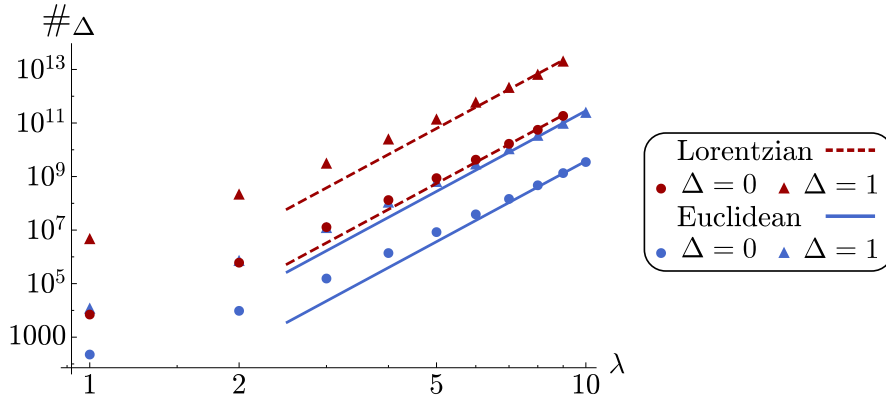

Figure 4: *Total number of terms to be summed over at a given λ, for Euclidean (blue) and Lorentzian (red) boundary data, for the simplified model (circles) and the first shelled sum (triangles). The lines are obtained through a numerical fit with the $(\Delta + 1)^6 \lambda^{10}$ estimate from 29. For Euclidean data, the fitted coefficients give .38 at $\Delta = 0$ and .45 at $\Delta = 1$. These numbers give an indication of the percentage of configurations removed by the triangle inequalities. For Lorentzian data, we cannot apply the counting leading to the estimate 29 because the spin configurations are isosceles. Nonetheless, the numerical fit shown in the figure is also with slope $(\Delta+1)^6\lambda^{10}$, and it is in qualitative agreement (a numerical fit with free exponent gives $\lambda^{9.96}$ for $\Delta = 0$ and $\lambda^{9.12}$ for $\Delta = 1$). This counting shows that for the same λ (and thus same number of data points in the asymptotic plots), the Lorentzian configurations are numerically much heavier. Generating this plot took about 24h on a standard laptop.*

To give an idea of the complexity of the numerics involved, the amplitude for Euclidean data with $\lambda = 16$ and $\Delta = 2$ contains 10^{14} configurations, each of which requires the evaluation of 10^4 integrals and five $\{6j\}$ symbols. The evaluation of this data point alone took three weeks on our server.

For Lorentzian boundary data, the situation is worse, since one cannot use equal spins. Therefore for the same value of the rescaling parameter λ, higher individual spins will enter, increasing the number of terms to be cycled over. For the 2/5 ratio used as Lorentzian boundary data, we are limited at $\lambda = 9$, which corresponds to highest spins 45, beyond which we encounter numerical instabilities in the booster functions. We counted numerically all the configurations allowed by triangular inequalities, and the results are shown

in Fig. 4. The most expensive data point we bought for Lorentzian data has $\lambda = 9$ and $\Delta = 1$, and 10^{13} configurations to be evaluated.

These estimates show the high price of increasing the cutoff Δ on the internal sums, making configurations for which the convergence is fast much more affordable. We also point out the λ^5 numerical cost coming from the use of coherent states in the boundary, which requires the additional summations over intertwiners. Hence our methods are much faster for calculations requiring orthogonal intertwiners and not coherent ones.

4.1 Convergence of the shells

Having discussed the numerical costs of the evaluations, let us now present some investigations on the convergence of the internal sums. We restricted attention to the four types of boundary data presented earlier, which will be relevant to study the asymptotic scaling. Figure 5 shows examples of convergence for $\gamma = 1.2$, and $\lambda = 1$. At this λ the convergence is quite fast for all four cases, with differences of 1% or less when increasing the truncation from $\Delta = 4$ to $\Delta = 5$.
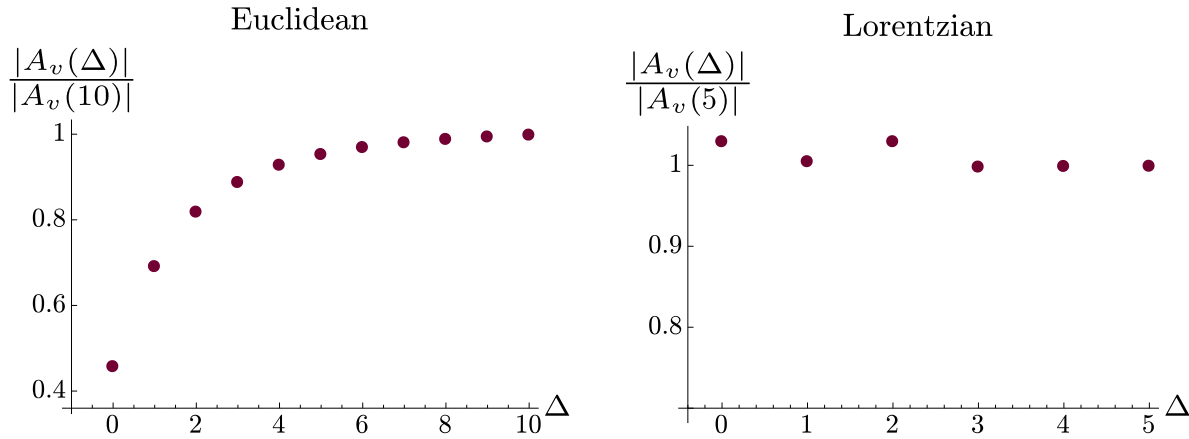

Figure 5: *Convergence of the internal sums at $\lambda = 1$ for Euclidean (left panel) and Lorentzian (right panel) data. Closed twisted and vector geometries give plots undistinguishable from the one on the left panel, with numerical differences typically at 4 digits.*

The convergence can, however, change quite significantly for different configurations or different values of γ. More importantly for our scopes, it can also change as we increase λ. An analysis like Fig. 5 for higher λ is unfortunately too costly and could not be performed. As a cheaper alternative, we looked at the gap $\Delta_1 - \Delta_0$ between the first shelled sum and the simplified model. This is reported in Fig. 6. We see that for Euclidean data the gap remains bounded at 30% of the $\Delta = 1$ amplitude. If the same happens for the other differences $\Delta_2 - \Delta_1$, etc, it would mean that the speed of convergence is constant in λ. This possibility is supported by the full asymptotic study presented in the next section. In that context, we will also explain the oscillation seen in (the right panel of) Fig. 6 as the rephasing of the asymptotic formula performed by the shells.

For Lorentzian data, on the other hand, we observe a generic growth of the gap. This suggests that while the convergence was (very) fast at $\lambda = 1$, it will likely slow down as λ increases. This slower convergence for Lorentzian data as λ is increased will also be confirmed by the full asymptotic study of the next section, and suggests that the simplified model will miss important aspects of the full model for such boundary configurations.
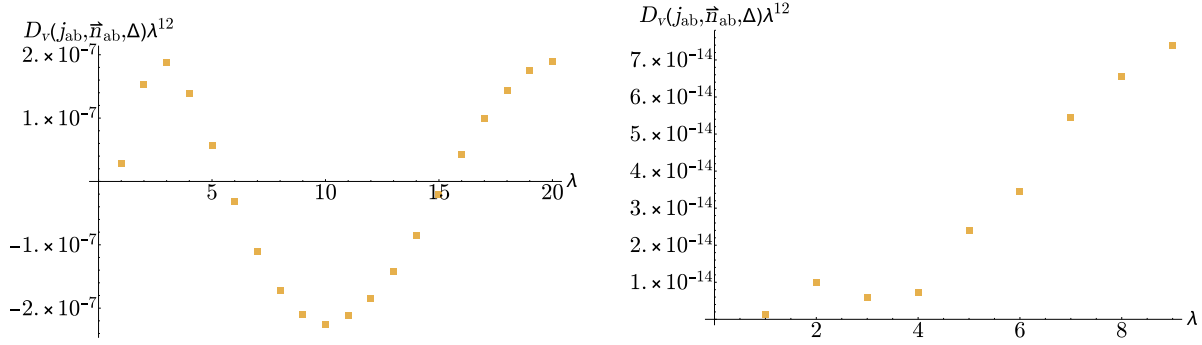
Figure 6:   *Behavior of the difference* $D_v(j_{ab}, \vec{n}_{ab}, \Delta) = A_v(j_{ab}, \vec{n}_{ab}, \Delta = 1) - A_v(j_{ab}, \vec{n}_{ab}, \Delta = 0)$, *for Euclidean (on the left) and Lorentzian (on the right) boundary data. The oscillating behavior in the Euclidean case is the Regge asymptotic behavior, as explained in the next Section. The growing behavior in the Lorentzian case is a clear indication that the simplified model is becoming subdominant with respect to the first shell as λ increases. This will be clarified in the next Section, where it will be shown that the simplified model misses the critical behavior and decays exponentially, while the first shell decays at power law.*

Summarizing, our investigations indicate that convergence is fast at very small spins for all types of data considered, but that while it remains fast for twisted, vector and Euclidean Regge geometries, it slows down for Lorentzian Regge geometries.

4.2   Approximating the coherent states

In an effort to reduce the numerical cost of the coherent amplitude, we studied the effect of truncating the sums over the boundary intertwiners i. In fact, $c_i(\vec{n}_f)$ is roughly a Gaussian distribution in i [18, 39], see e.g. Fig. 7, the more accurate and the sharper for larger spins, and one can explore the impact of cutting the tails. An analytic study of the Gaussian width shows that it depends on both the spins and the normals [39]. However the use of those formulas is not easy beyond the equilateral case. For our purposes it is more practical to estimate $\sigma(j_f, \vec{n}_f)$ numerically, as explained in the caption of Fig. 7.
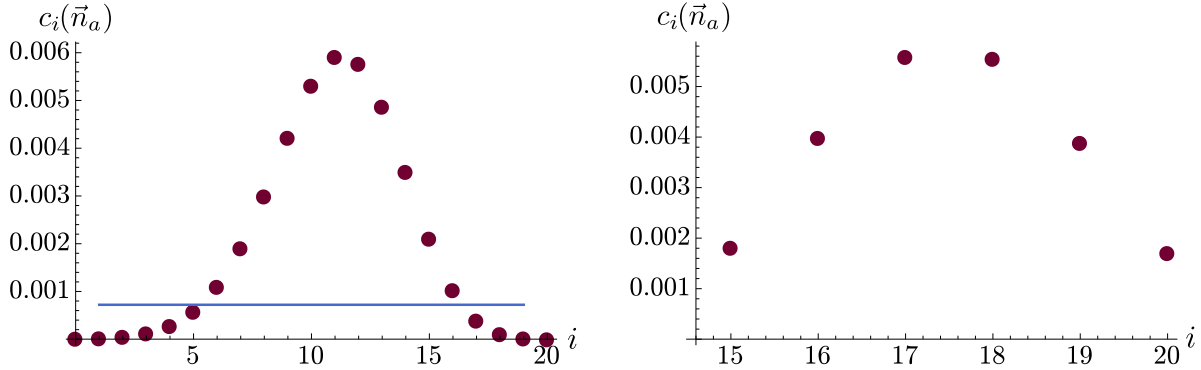

Figure 7:   Left panel: *The distribution of a coherent state with $j_{ab} = 10$ and normals corresponding to an equilateral tetrahedron, as a function of the intertwiner label $i = j_{12}$. To estimate numerically the width we interpolate the data points with a Gaussian, and use the function* `gsl_stats_sd` *of the* `GNU Scientific Library` *[40]. Numerically it is then convenient to define a cutoff α excluding terms for which $c_i(\vec{n}_f) \leq \sigma(j, \vec{n})/\alpha$. This means cutting the tails at $\sqrt{1 + 2\log\alpha}\,\sigma(j, \vec{n})$. The horizontal line in the figure corresponds to $\alpha = 3$, namely 1.79σ for which 93% of the Gaussian is covered.*
Right panel: *The distribution of an isosceles coherent state with three spins equal to 10 and one equal to 25. For this configuration there are only 6 intertwiner spins allowed, and the spread is too broad to allow any reliable truncation. These are the tetrahedra entering the most numerically economical Lorentzian boundary data.*

There is however no guarantee that truncating the tails of the Gaussians gives a valid approximation for the vertex amplitude because the intertwiner dependence of the $\{15j\}$ symbol can compensate for the

Gaussian damping. This happens for instance in the equilateral configurations used for Euclidean boundary data, where the coherent state distribution is roughly peaked around the middle value of the intertwiner label,[12] whereas the $\{15j\}$ is peaked on extremal intertwiners 0 or $2j$. In this case, it turns out that cutting the tails even just a bit introduces large errors. For the simplified model and λ around 10, one needs at least 5σ in the Gaussians to reduce the error on the full amplitude below 5%. This makes the approximation basically useless and pushed us to devise an alternative scheme. Instead of truncating all five Gaussians of the vertex amplitude, we kept two Gaussians exact and truncated only the other three (it does not matter which because of the symmetry of the problem). Using the simplified model as trial, we found that truncating three Gaussians at 1.79σ (namely covering 93%) we reduce drastically the number of terms included in the summation, see Fig. 8, while introducing a small error $\leq 3\%$. This reduces the required computational time to roughly $1/20$, for the simplified model and spins of order 10.
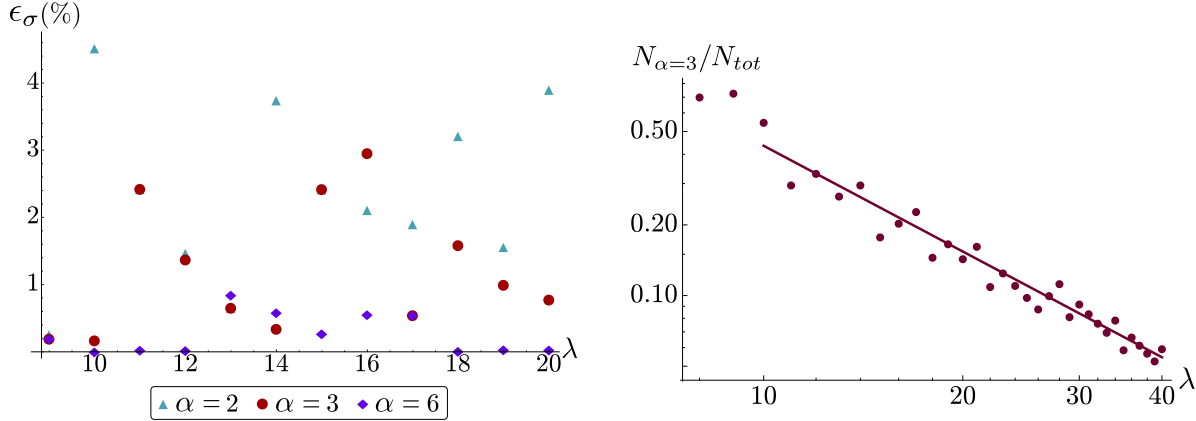

Figure 8: *Study of the impact of truncating three of the five coherent states distributions, for the simplified model with Euclidean equilateral boundary data, and $\gamma = 1.2$.*
Left panel, The error introduced: *We compute the relative error ϵ_σ between the exact amplitude and various truncations corresponding to different values of α – defined in the previous figure, the smaller α the bigger the truncation – as a function of the rescaling parameter λ. Setting ourselves an error tolerance of 3%, we truncate at $\alpha = 3$.*
Right panel, the improvement on the evaluation times: *We compute the ratio between the number of terms $N_{\alpha=3}$ surviving in a truncation with $\alpha = 3$ and the total number N_{tot}. The impact of the truncation grows roughly linearly in λ (the solid line is $13.6\lambda^{-3/2}$), and we see that for instance at $\lambda = 20$ only 5% of the terms survive.*

The advantage of such a truncation becomes even more important when adding the internal sums. To make sure that the error introduced is not significantly different than in the simplified model, we performed an analog study for $\Delta = 1$ and $\lambda \sim 10$, reported in Fig. 9. It confirms that $\alpha = 3$ is a good compromise between cutting as many terms as possible and keeping the error small.

_____

[12]More precisely slightly after, at $\bar{\imath} = (2/\sqrt{3})j \simeq 1.15j$ [18].
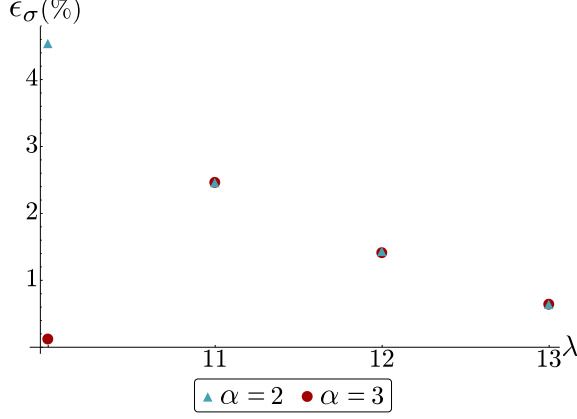
Figure 9: *The truncation relative error in the $\Delta = 1$ contribution of the shelled summation and Euclidean boundary data.*

Having so chosen the truncation $\alpha = 3$, we apply it to higher spins where the evaluation times are the longest. We have no quantitative estimate of the error made, but the coherence of the plots shown in the next section reassures us that we are not deviating significantly from the few percentage points established for $\lambda \sim 10$, and the evaluation times are very conveniently shortened.

On the other hand, a similar truncation does not work for Lorentzian boundary data because of the isosceles tetrahedra there used. For the isosceles configuration there is a smaller range of intertwiners and the Gaussians are more spread out, see Fig. 10. We found that any truncation in this case introduces large errors. Therefore for Lorentzian data we contented ourselves to truncate the only equilateral coherent intertwiner, again with $\alpha = 3$. This gives an improvement of roughly $1/4$ of the computational time for $\lambda = 9$. On the other hand, we can introduce the truncation already at $\lambda = 3$, something that with three Gaussians truncated as for Euclidean data was introducing a bigger error.
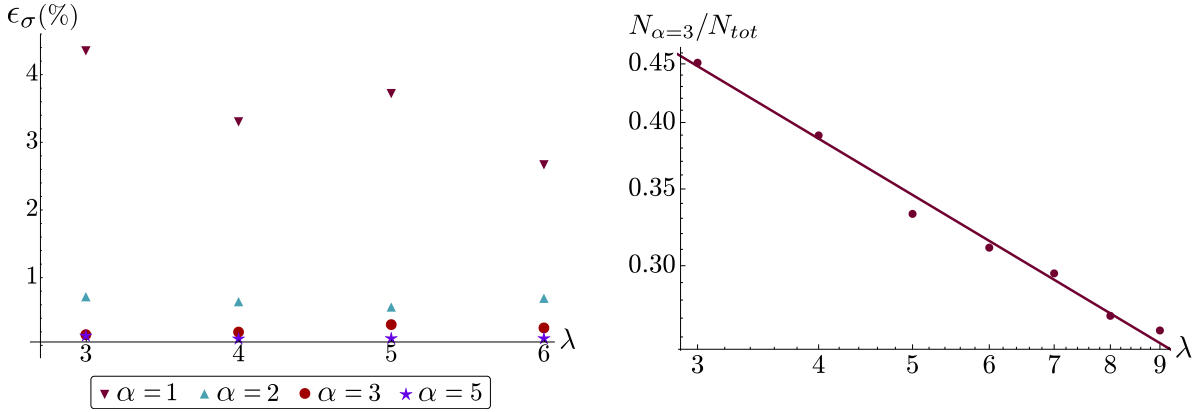

Figure 10: *The improvement of the evaluation times obtained truncating one of the Gaussians.* Left panel: *We perform the same test as shown in Fig. 8 for the Lorentzian configuration, truncating only on one coherent state (the equilateral one). We can cut only a single tetrahedron due to the fact that, for low rescaling parameters, the isosceles tetrahedra do not approximate a Gaussian, as shown in Fig. 7. In this case, the fit gives $0.8\lambda^{-1/2}$.*
Right panel: *The truncation relative error in the simplified model contribution for Lorentzian boundary data, used in Section 5.4.*

Summarizing, in the numerics we used the Gaussian truncation with $\alpha = 3$ on three coherent intertwiners for vector and Euclidean Regge data, starting at $\lambda = 8$; and a similar truncation with $\alpha = 3$ but on the unique equilateral coherent intertwiner for Lorentzian data, starting at $\lambda = 3$. This approximation enters the plots shown in Fig. 6, etc. An estimated error bar of 3% could be added but would not be visible.

56

5 Numerical analysis of the asymptotic formula

In this section, we present a selection of our numerical data. We consider the four different types of boundary geometries constructed in Sec. 3, plus a completely random configuration not satisfying even closure, to test the different possible asymptotic behaviors derived in [5].

1. For arbitrary areas and normals, or for the closed twisted geometry: the data confirm the exponential decay;

2. For the vector geometry: The data confirm a power law decay λ^{-12} and no oscillations;

3. For the Euclidean Regge geometry: The data confirm a power law decay λ^{-12} and an oscillation with a frequency given by the Regge action;

4. For the Lorentzian Regge geometry: The data indicate a power law decay λ^{-12} and an oscillation with a frequency depending on γ, but more conclusive results will require additional computational power.

5.1 Generic data, open and closed twisted geometry

5.1.1 Open boundary data

For generic data we expect from [5] an exponential decay, namely

$$A_v = o(\lambda^{-K}) \qquad \forall \text{ nonnegative integer } K. \tag{31}$$

To confirm this numerically, we took all spins to be equal, but the normals were randomly generated. We did not truncate the coherent states, since the Gaussian profile of Fig. 7 is lost for open configurations.[13] We evaluate the amplitude in the simplified model, $\Delta = 0$, and the first shelled summation, $\Delta = 1$. The vertex amplitude is exponentially suppressed, see Fig. 11.
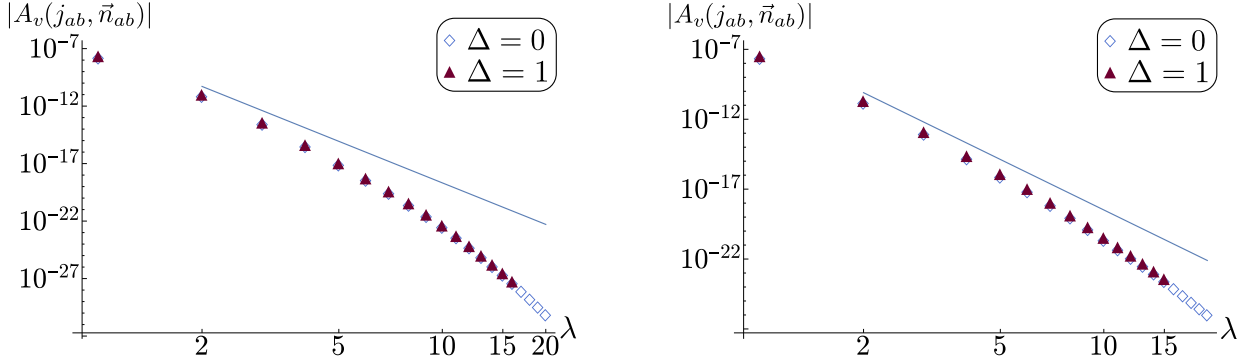

Figure 11: *The amplitude for generic boundary data not admitting critical points, showing an exponential falloff. Both log-log plots showing the absolute value of the amplitude for the simplified model ($\Delta = 0$) and the first shelled sum ($\Delta = 1$), with $\gamma = 1.2$. Each plot took roughly 2h for the simplified model, and 36h for $\Delta = 1$.*
Left panel: *Open data, with spins equal and random normals not satisfying closure. The line is $2.1 \times 10^{-7} \lambda^{-12}$, added to help the eye identifying the exponential falloff.*
Right panel: *Closed twisted geometries data, with the normals satisfying closure but not the vector geometry conditions. The line is $3.2 \times 10^{-12} \lambda^{-12}$, added to help the eye identifying the exponential falloff.*

---

[13] The reader may wonder why we can use open configurations in the boundary states, since these represent coherent intertwiners and closure is the classical counterpart of the quantum gauge invariance. The answer is that the normals are just classical labels, therefore one can have gauge invariant states with nonclosed normals. These states are on the other hand over-redundant, and can be effectively removed without losing coherence. The result is a family of coherent states depending only on the cross ratio parametrizing the intrinsic shape of the tetrahedron [39]. This family was used for numerical calculations of the volume operator in [37], but we refrain from using it here to keep the treatment as simple as possible.

5.1.2 Closed twisted geometry

A closed configuration is enough to have a critical point for the norm of the coherent intertwiners [18], but not for the full amplitude 6, and [5] predicts again an exponential falloff (31). We computed numerically the amplitude using the configuration constructed in Sec. 3.1, and verified the exponential suppression for the simplified model and the first shelled sum, see Fig. 11. In generating these data, we did not use any truncation on the coherent states. The coherent state distributions are in fact too broadly spread for this configuration, and it is thus not possible to efficiently truncate them for the values of spins considered.

5.2 Vector geometry

For vector geometries, namely data satisfying both closure (2) and orientation (3) constraints, there is one critical point (doubly degenerate), and one finds the following power law asymptotic behavior [5]

$$A_v = \frac{1}{\lambda^{12}} N_c e^{i\lambda \Phi_c} + O(\lambda^{-13}). \tag{32}$$

Here N_c contains the (inverse square root of the) Hessian determinant, the integration measure evaluated at the critical point, and the factors of 2 and π coming from the critical point degeneracies and the Gaussian integrations. The action at the critical point is purely imaginary, hence the phase Φ_c in Eq. 32. See [5] and our appendixes for details and explicit formulas. With the vector geometry constructed in Sec. 3.2 one finds

$$N_c = 7.86 \times 10^{-7}. \tag{33}$$

The value of the Φ_c is irrelevant because of the global phase ambiguity discussed earlier, and we restrict attention to the absolute value of the amplitude.

For the numerical evaluation of the amplitude, we fixed $\gamma = 1.2$, and evaluated first the simplified model, $\Delta = 0$, and then the first shelled sum, $\Delta = 1$. In both cases we included a truncation on three Gaussians, for reference, on tetrahedra 2, 3 and 4. Even if the configurations are not equilateral, equal area is enough to have sufficiently peaked Gaussians.

The results are reported in Fig. 12, together with the analytic prediction. We find excellent agreement for the power law. As for the numerical coefficient, the simplified model comes out a bit short, and the first shell gives an order-one contribution approaching the predicted analytical value. Notice also the short scale nonmonotonic behavior, which is introduced by the higher order corrections to the saddle point. Presumably the first shell is already converging quite well to the analytic value 33, and the contributions from the second and higher shells will be small. This would mean that the behavior observed at $\lambda = 1$ in Fig. 5 (left panel) is maintained at higher λ's.
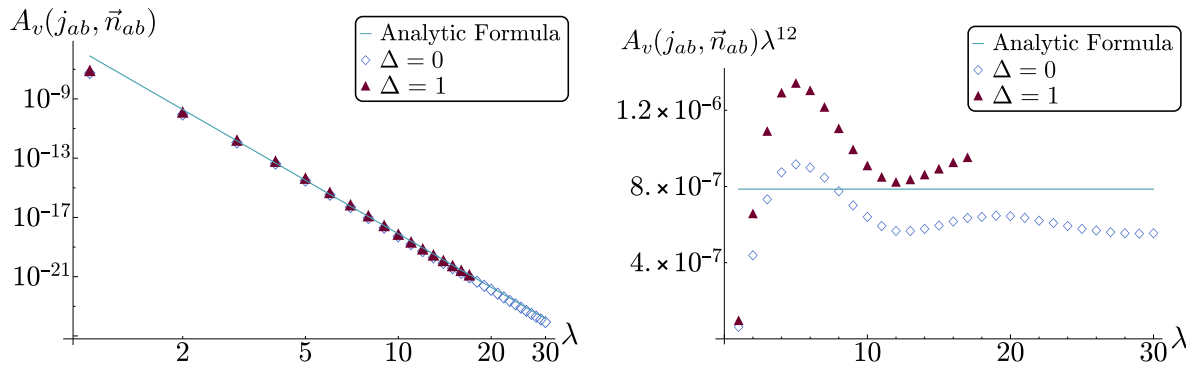
Figure 12: *Asymptotics of vector geometries, $\gamma = 1.2$.*
Left panel: *The absolute value of the vertex amplitude with a vector geometry boundary for an homogeneous rescaling of the spins in log scale. The amplitude is following the power law (32). We plot the value of the amplitude in the simplified model ($\Delta = 0$) with empty diamonds, and the first shelled summation ($\Delta = 1$) with full triangles. Here we used the cutoff on the coherent states discussed earlier, and the whole plot took roughly 30h. The line plotted is the analytical formula.*
Right panel: *The absolute values rescaled by λ^{12}, showing a short scale nonmonotonic behavior, coming from the higher order saddle point corrections.*

5.3 Euclidean Regge geometry

For Euclidean Regge data, the integral has two distinct critical points, and the asymptotic formula given in [5] reads

$$A_v = \frac{(-1)^\chi}{\lambda^{12}} e^{i\lambda\Phi_c} \left(N_c e^{i\lambda S_R} + N_{Pc} e^{-i\lambda S_R} \right) + O(\lambda^{-13}). \tag{34}$$

Here χ is an integer depending on the eventual braiding of the intertwiners; c and Pc the two critical points, at which the action is purely imaginary and equal up to sign, up to a global phase Φ_c;[14] N_c contains the (inverse square root of the) Hessian determinant, but also a contribution from the integration measure at the critical point which is not trivial, and for convenience also the various factors of 2 and π coming from the twofold degeneracy of the critical points and the Gaussian integrations; and most importantly,

$$S_R(j_{ab}, \vec{n}_{ab}) := \sum_{a<b} j_{ab} \theta_{ab}(\vec{n}_{ab}), \tag{35}$$

is the Regge action. Here θ_{ab} are the 4D dihedral angles between tetrahedra, which can be reconstructed from the 3D normals using the spherical cosine laws.

It is always worthwhile to remind the reader that the actual Regge action is a function of edge lengths, unlike 35. Nonetheless, the bivector reconstruction theorem [25] used in [5] to derive Eq. 34 guarantees that the data span all Euclidean 4-simplices, and therefore Eq. 35 is equivalent to the Regge action. One can also give a different proof that does not rely on the bivector reconstruction theorem [10]. To that end, notice first that due to the rotational invariance at each node of the functions θ_{ab}, the independent variables of 35 are areas and angles between the 3D normals. It is known from [26] that the area-angle action 35 is equivalent to the Regge action based on edge lengths provided closure and shape-matching conditions are satisfied, a result that holds for a generic triangulation and not only a single 4-simplex. In the case at hand of a single 4-simplex, closure is guaranteed by the critical point condition 2. And it can be shown explicitly [10] that the conditions for the existence of two distinct critical points is precisely the shape-matching conditions, in the form of consistency of spherical cosine laws.[15]

If $N_c = \bar{N}_{Pc}$, the asymptotics can be written as a cosine of λS_R, with a λ-independent phase offset given by the argument of N_c,

$$A_v = \frac{(-1)^\chi}{\lambda^{12}} 2|N_c| e^{i\lambda\Phi_c} \cos\left(\lambda S_R - \frac{1}{2}\arg H_c \right) + O(\lambda^{-13}). \tag{36}$$

We are not aware of an analytic proof of this property, but we verified it in all cases numerically checked. To avoid confusions between the phases Φ_c and $\arg H_c$, we will refer to the first as the global phase and to the second as the cosine phase offset.

For our numerical simulations, we considered the equilateral twisted spike configuration described in Sec. 3.3. Assigning the normals to the intertwiners according to the geometric picture of a 4-simplex, we have no braiding and $\chi = 0$. For the Hessian, we use the explicit formulaq in Appendix B.1, and the Mathematica algorithm `EuclideanHessian` of [7] to evaluate it at the chosen configuration. The result is real and identical at both critical points, and fixing for example $\gamma = 1.2$, we find

$$N_c = N_{Pc} = 2.65 \times 10^{-7}. \tag{37}$$

Furthermore, using our phase convention for the coherent amplitude (which is not the same as the one in [5], see Appendix A) and the conventional phase convention for the coherent states [41], we numerically found that $\Phi_c = S_R$. Removing this phase (redefining for instance the phase of the coherent states), the analytic prediction is

$$A_v = \frac{5.13 \times 10^{-7}}{\lambda^{12}} \cos\left(5\lambda \arccos\left(-\frac{1}{4} \right) \right). \tag{38}$$

---

[14]The two critical points are related by a parity transformation, hence the notation Pc. Then one finds $S_c = i\lambda(S_R + \Phi_c)$ and $S_{Pc} = i\lambda(-S_R + \Phi_c)$, leading to Eq. 34.

[15]More precisely, one gets *angle-matching* conditions. However, for triangular faces with the areas already matching by construction, matching angles imply matching shapes. This is not the case for general polytopes with nontriangular faces, and in fact the large spin asymptotics of nonsimplicial vertices contains not just Regge geometries, but more general *conformal* twisted geometries, see the discussion in [10].

We recall that for these boundary data $\lambda = 2j$. Notice that there is no phase offset in the argument of the cosine, unlike for SU(2) asymptotics [9, 42, 10]. This fact will play a role below.

In the numerics we used the approximation truncating three of the Gaussians, for reference the tetrahedra 2, 3 and 4. We evaluated first the simplified model, then added the internal sums, with truncations at $\Delta = 1$ and $\Delta = 2$. This increases progressively the cost of the numerics. We were able to reach $\lambda = 40$ for the simplified model, 20 for the first shell, and 18 for the second shell. We did not push our analysis to a third shell, because we would have been forced to stop at spins too small to test the asymptotic behavior. The data obtained are complex, but since we identified the global phase, we can remove it a posteriori and obtain real data points.

The first result we found is that the numerical data are in excellent agreement with the λ^{-12} power law, see Fig. 13. The agreement is achieved already at small spins, and holds for both the simplified model and the first shelled sum. We plot also the difference $\Delta_1 - \Delta_0$ to show that it follows the same power law: not only does the simplified model see the critical behavior, but so do (at least some of) the individual higher l configurations.
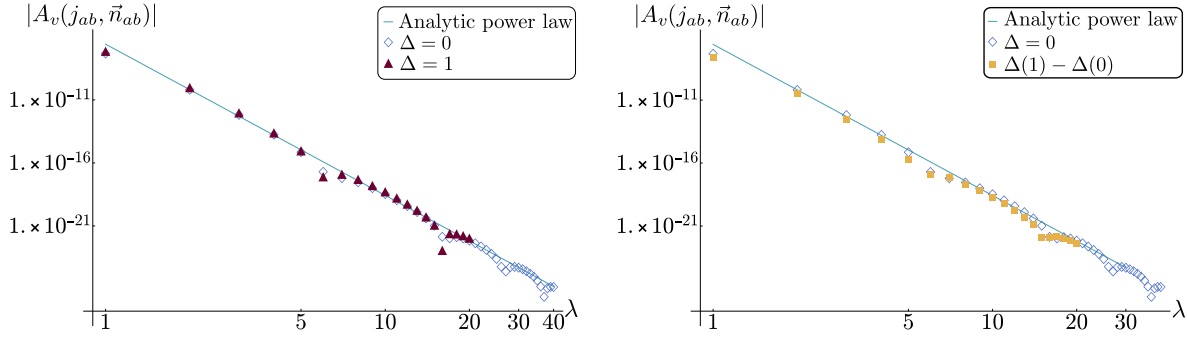

Figure 13: *Numerical data versus the analytic asymptotics 38, for Euclidean Regge data, $\gamma = 1.2$. Log-log plots, absolute values of the amplitude, versus the analytic scaling $5.13 \times 10^{-7} \lambda^{-12}$.*
Left panel: *Simplified model and first shelled sum. Both scale according to the predicted power law, and feature oscillations.*
Right panel: *The simplified model and the difference between the first shelled sum and the simplified model; namely, all contributions with one nonminimal l. This difference also scales with the predicted power law and features oscillations, showing that individual higher l contributions see the critical behavior.*

We found the same λ^{-12} scaling also for the second shell $\Delta_2 - \Delta_1 - \Delta_0$, with includes individual terms with two $l = j + 1$ or one $l = j + 2$. We deduce from these numerical results that the simplified model captures the right scaling, and so do individual shells. This means that the convergence of the internal sums for higher λ is still qualitatively similar to the extended study that was possible to make for $\lambda = 1$ (see Fig. 5), and also that the the analytic behavior 34 must be the result of adding up all the relevant contributions of different l's. These are of order one initially, but we expect them to suitably decrease as guaranteed by the convergence.

Next, let us zoom in on the palatable oscillations already visible in Fig. 13. We rescale the data and asymptotic formula by λ^{12} and report the result in Fig. 14, the highlight plot of our paper. It shows a beautiful agreement between the numerical evaluation of the vertex and the analytic asymptotic formula in particular, a confirmation of the frequency of the oscillations determined by the Regge action, its most important feature.[16]

---

[16]A word of caution to avoid possible confusion: If one plots the asymptotic formula as a real function, the real frequency given by S_R is much higher than the frequency of oscillations that can be deduced interpolating the (half-)integer sampling, a situation familiar from the study of SU(2) asymptotics. Hence when we speak of matching frequency of oscillations between the numerical data and the analytic formula, we refer to the "effective" frequency of the (half-)integer oscillations, which is not the Regge cation, but a function thereof.
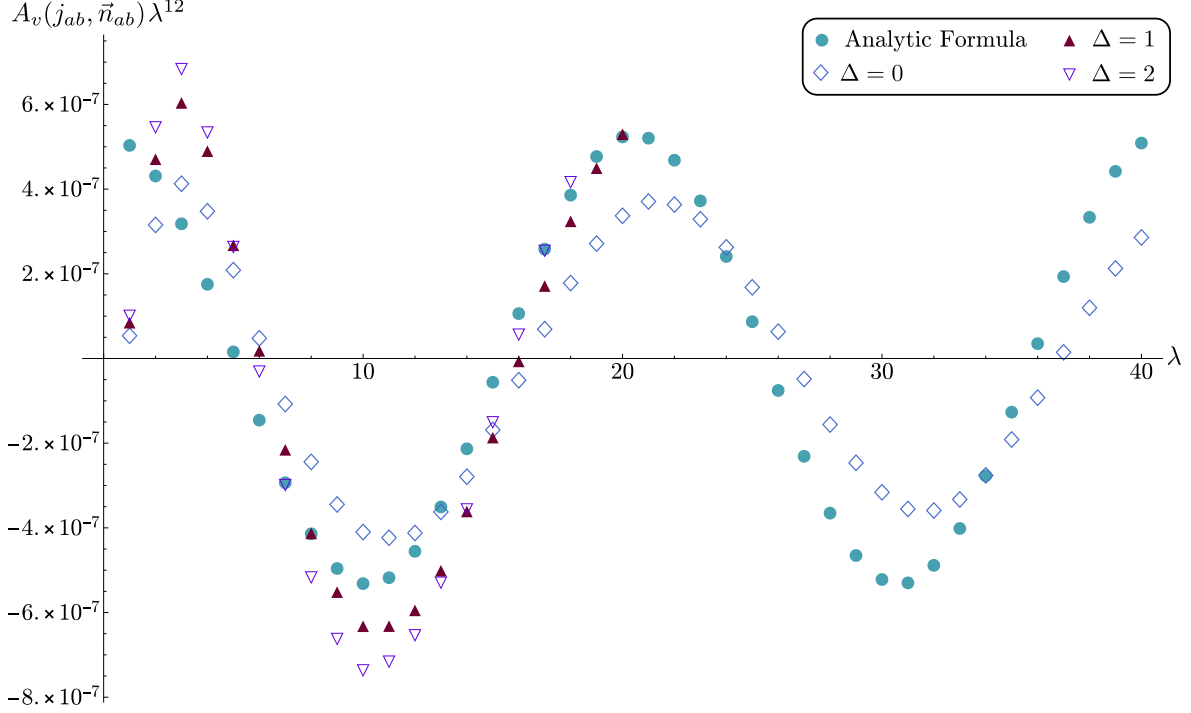
Figure 14: *Rescaled numerical data versus the analytic asymptotics 38, for Euclidean Regge data and $\gamma = 1.2$, for the simplified model and internal summations with cutoffs $\Delta = 1$ and 2. The simplified model alone already sees the Regge oscillations of the analytic formula. The two shelled sums maintain the same frequency, but give contributions of order one to the magnitude and the phase offset.*

In more details, we observe the following situation. First, the simplified model captures already the right frequency of oscillations. What is missing is the precise magnitude and cosine phase offset. The first and second shells have the same frequency of oscillations, and different magnitude and cosine phase offset, which lead to a better qualitative match with the asymptotic formula. A more precise quantitative improvement will likely require pushing to higher spins where the asymptotic formula becomes more accurate. As for the crude numerical values, we see that at $\lambda \sim 20$ (which means spins $j \sim 10$, recall half-integers are also being computed here) the simplified model and shelled sums agree with one another and with the analytic formula with a 10% error.

From these data we deduce that individual l's see the same critical behavior for Euclidean Regge data, including the simplified model, and that the asymptotic formula 34 is the result of summing all the relevant contributions. However the power law and frequency of oscillations are well described by the simplified model, with the internal sums only contributing to the overall magnitude and phase offset. Given the much faster evaluation times of the simplified model, this is an interesting property, whose origin will be explained in the next section.

The data presented in the figures of this section have $\gamma = 1.2$. For double checking, we performed further numerical investigations with the different value $\gamma = 0.1$, leading to similar plots. In particular, we found the same frequency of oscillations as predicted by Eq. 34.

We conclude from the numerics that the power law and frequency of the asymptotic formula can be confirmed already at spins of order 10, to a 10% error. A better match requires changes in the amplitude and the phase offset, for which one needs more shells and/or higher spins.

5.4 Lorentzian Regge geometry

For Lorentzian Regge data, we have two distinct critical points, and the oscillating power law decay [5]

$$A_v = \frac{(-1)^{\chi + M}}{\lambda^{12}} e^{i\lambda\Phi_c} \left(N_c e^{i\lambda S_c} + N_{Pc} e^{-i\lambda S_c} \right) + O(\lambda^{-13}). \tag{39}$$

61

The crucial difference is that this time the action at the critical point depends linearly on γ,

$$S_c = \gamma \sum_{a<b} j_{ab} \theta_{ab}^{\mathrm{L}}(\vec{n}_{ab}). \tag{40}$$

The Lorentzian 4D dihedral angles θ_{ab}^{L} are defined from the Lorentzian spherical cosine laws in terms of the 3D normals, or from the 4D normals as recalled in Sec. 3.4 above. They are boosts between the timelike normals if the latter are both future or past pointing, and in the mixed case (called the thin wedge configuration) one has to add a shift by a factor $i\pi$. These shifts result in the additional $(-1)^M$ phase, where

$$M = \sum_{\text{thin wedges}} j_{ab}. \tag{41}$$

We remark that Eq. 40 is a Lorentzian Regge action with areas are given by γj, which is in agreement with the area spectrum of loop quantum gravity in the large spin limit. As for the shape-matching and equivalence of Eq. 40 to the Regge action based on lengths, the same considerations of the Euclidean case apply.

For our numerical simulations, we considered the isosceles configuration described in Sec. 3.4. Assigning the normals to the intertwiners according to the geometric picture of a 4-simplex, we have no braiding and $\chi = 0$. Further, we have four thin wedges all associated with $j_{ab} = 5\lambda$, thus $M = 20\lambda$ with integer λ and this phase drops out as well. For the Hessian, we use the explicit formulas in Appendix B.1, and the Mathematica algorithm `LorentzianHessian` of [7] to evaluate it at the chosen configuration. Taking $\gamma = 0.1$, we find

$$N_c = \overline{N_{Pc}} = 1.76 \times 10^{-13} + i1.87 \times 10^{-14}, \tag{42}$$

thus Eq. 39 is a cosine up to a global phase. Reabsorbing the global phase in the definition of the coherent states and computing the corresponding Regge action, we obtain the analytic asymptotic formula

$$A_v = \frac{3.53 \times 10^{-13}}{\lambda^{12}} \cos\left(0.01\lambda + 0.106\right). \tag{43}$$

In running the numerical code, we used the Gaussian truncation on only one coherent intertwiner, the equispin gauge-fixed tetrahedron 1. The data obtained are complex, and their λ-dependent phase this time is not simply the Regge action. We spent a considerable amount of time going through the conventions and technical details that determine this anyway irrelevant global phase, for the sake of having real data points. In the end the simplest solution was to determine the λ-dependent phase through a numerical fit, then remove it from the numerical data. A more brutal removal by taking absolute values would have deprived us of the numerical sign, which is important in comparing data and analytic formulas.[17]

The code works fine also for Lorentzian boundary data, and we were able to evaluate the amplitude for the simplified model and first shell. The numerical results we were able to obtain are however less satisfying than for the previous configurations, in terms of comparing with the analytic asymptotic formula. The main problem is the numerical instability in the booster functions, which limits us to $\lambda = 9$, before the $j = 50$ instability of the boosters is reached. Furthermore, the numerical cost of the calculation limits us to $\Delta = 1$. We can, on the other hand, take advantage of the expected linear dependence of the oscillations on γ, and evaluate numerically the vertex amplitude at different values of γ, to try to establish different aspects of the asymptotics. We considered three different values of γ, chosen to have qualitatively different behaviors in the accessible $\lambda \in [1,9]$ range: a rather flat plateau with no oscillations, and visible oscillations but with a different frequency. The resulting asymptotic formulas needed to match the numerics in the three cases are reported in Table 6.

---

[17]We shamelessly admit that we actually *failed* to reproduce the observed numerical global phase from our analytic calculations – Ref. [5] does not compute it, given its irrelevance. Appendix A collects all explicit formulas and all numerous places where a global phase arises, as well as a careful comparison between the conventions here used based on [43, 41, 44], and the ones of [5]. Albeit an overlooked phase lurking there and open to inspection, we suspect that the origin of the problem lies in a mismatch in the conventions for the orientation of the links of the reducible $\{15j\}$ between the numerical code and our analytic description of the amplitude.

γ	$N_c = \overline{N}_{Pc}$	$\lambda^{12} A_v$
0.1	$1.76 \times 10^{-13} + i1.87 \times 10^{-14}$	$3.53 \times 10^{-13} \cos\left(0.963 \times 10^{-2}\lambda + 0.106\right)$
1.2	$2.82 \times 10^{-16} + i5.7 \times 10^{-16}$	$1.27 \times 10^{-15} \cos\left(0.116\lambda + 1.111\right)$
7	$8.86 \times 10^{-25} - i3.67 \times 10^{-25}$	$1.92 \times 10^{-24} \cos\left(0.674\lambda - 0.392\right)$
8	$1.48 \times 10^{-25} - i4.32 \times 10^{-26}$	$3.08 \times 10^{-25} \cos\left(0.770\lambda - 0.284\right)$

Table 6: *Asymptotics for Lorentzian boundary data at different values of γ.*

Not having enough points for a significative log-log plot, we present directly the data rescaled by the predicted λ^{12} falloff, versus the rescaled asymptotic formula. The first plot shown in Fig. 15 is for $\gamma = 0.1$. The effective frequency of oscillations is low, giving a roughly constant behavior in the accessible range. The first consideration to be deduced from the data is that the simplified model appears to fall off significantly faster than the analytic power law decay of the EPRL model. We interpret this to mean that the simplified model does not have a critical behavior for Lorentzian Regge geometries. The data points of the first shell on the other hand roughly stabilize in parallel to the asymptotic formula. This indicates that the first shell is already enough to capture the critical behavior, even though with its actual magnitude being too small, we expect nearby shells to still give order-one contributions, and thus a slow convergence.
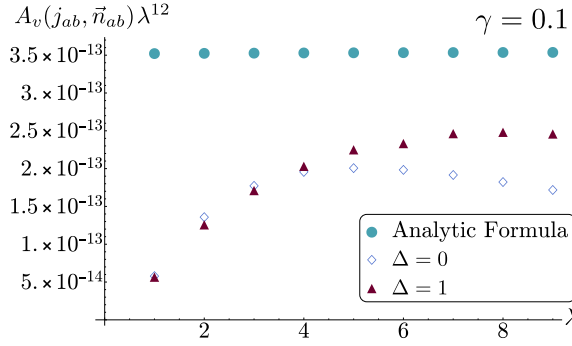

Figure 15: *Rescaled numerical data for Lorentzian Regge geometry, versus the analytic asymptotics 39, for $\gamma = 0.1$. The bottleneck is the numerical instabilities of the booster functions at spins of order 50, which even for the optimal isosceles configuration we identified, occur already at $\lambda = 10$. With the caveat of the few points obtained, the simplified model is decaying faster than the first shell, indicating that it lacks the critical behavior, and will likely decay exponentially. The first shell, on the other hand, is well in line with the power law decay. Its magnitude falls short of the asymptotic formula by a factor of order one: this could be completed by higher order shells, accordingly with the previous indications that convergence is slow for Lorentzian Regge geometries.*

Next, we increase the expected frequency looking at larger values of γ. Taking $\gamma = 7$ and $\gamma = 8$ allows us to fit roughly one full period of analytic oscillations within the accessible range, and with different frequencies, to see whether the data offer a compatible nonmonotonic behavior. The results are plotted in Fig. 16. The behavior of the first shell is again compatible with the power law scaling, and we clearly observe nonmonotonic behavior and dependence on γ. This is nice evidence in support of the numerical evaluation of the vertex amplitude and of the validity of the asymptotic formula. The data points at disposal are however too few and at too small λ to draw any conclusions about the frequency of oscillations like we could do for the Euclidean Regge geometry. As a somewhat optimistic remark, as we increase γ from 7 to 8 the (interpolated) analytic zero with positive slope moves to the left, and so does the (interpolated) zero of the numerical data.
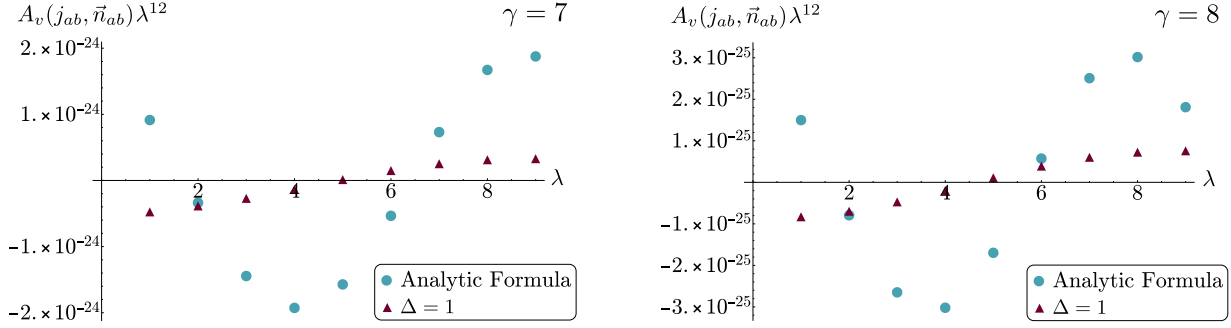
Figure 16: *Rescaled numerical data versus the analytic asymptotics 39, for Lorentzian Regge data and $\gamma = 7$ and 8. These values are chosen so that the analytic formula has a visible oscillation within the range numerically accessible. The faster frequency of the $\gamma = 8$ case can be inferred comparing the eyesight interpolation of the positive slope through the x axis. The data points for the first shell are well in line with the analytic power law, and show a nonmonotonic behavior qualitatively comparable with the predicted oscillations. Higher spins are needed for a better match, as well as increasing the number of shells being summed over.*

In summary, the simplified model does not see the critical behavior for Lorentzian Regge data, but the first shell already does, and presumably all other shells. The power law decay observed confirms the asymptotic formula. There is a γ-dependent nonmonotonic behavior, qualitatively compatible with the oscillations predicted by the asymptotic formula. The convergence of the internal sums is slower than with Euclidean Regge data, and higher shells/higher spins are needed for a more quantitative confirmation of the asymptotic formula.

6 Outlook

6.1 Geometric meaning of the internal sums

The formula 6 and more generally the method of [8], introduce a factorization of Lorentzian spin foam amplitudes so that only SU(2) objects appear at the vertices, and all Lorentzian properties are in the booster functions localized at the edges. Since the vertices are dual to 4D structures and the edges to 3D structures, this raises the question of how the 4D Lorentzian structures are reconstructed by the internal sums. A second question concerns the simplified model, which we have shown to capture the EPRL asymptotics for vector and Euclidean Regge geometries. Since the simplified model has the advantage of much faster evaluation times, it is useful to understand why this is the case. These two questions are closely related, and can be answered by inspecting in more detail the role of the sums over the internal spins l_{ab}.

Let us look again at the decomposition 6, and consider the simplified model, for which the internal sums are removed.[18] The vertex amplitude reduces to the $\{15j\}$ symbol evaluated at the boundary spins, and the booster functions at their minimal configurations:

$$A_v^{\mathrm{EPRLs}}\left(j_{ab},\,\vec{n}_{ab}\right) = \sum_{k_a,i_a} \{15j\} \prod_{a=2}^{5} d_{k_a} B_4^{\gamma}(j_{ab},j_{ab};i_a,k_a) \prod_{a=1}^{5} c_{i_a}(\vec{n}_{ab}). \tag{44}$$

The internal intertwiners are still being summed over, but in the large spin limit the booster functions are Gaussians peaked on equal intertwiners, and to lowest order [45, 8, 11]

$$B_4^{\gamma}(j_{ab},j_{ab};i_a,k_a) \simeq \frac{b(\gamma,j_{ab})}{\lambda^{3/2}\, d_{i_a}} \delta_{i_a k_a}. \tag{45}$$

The simplified vertex amplitude 44 is thus in first approximation proportional to a single coherent $\{15j\}$

---

[18]This is achieved through a further imposition of the Y map inside the product $h_a^{-1}h_b$ in Eq. 6, see [8] for details and motivations.

symbol, which we recall is the vertex amplitude for SU(2) BF theory:

$$A_v^{\mathrm{EPRLs}}(j_{ab}, \vec{n}_{ab}) \simeq \frac{1}{\lambda^6} \left(\prod_{a=2}^{5} b(\gamma, j_{ab}) \right) A_v^{\mathrm{SU(2)}}(j_{ab}, \vec{n}_{ab}), \qquad A_v^{\mathrm{SU(2)}}(j_{ab}, \vec{n}_{ab}) := \sum_{i_a} \{15j\} \prod_{a=1}^{5} c_{i_a}(\vec{n}_{ab}). \quad (46)$$

This approximation shows that the simplified model has the same critical points of SU(2) BF theory, and λ^{-6} times its scaling. The SU(2) coherent vertex amplitude has no critical behavior for Lorentzian Regge data and thus decays exponentially; whereas for Euclidean Regge data it admits two distinct critical points and oscillations with exactly the same frequency 35 of the EPRL model [16],

$$A_v^{\mathrm{SU(2)}}(j_{ab}, \vec{n}_{ab}) = \frac{1}{\lambda^6} \frac{1}{2^6 \pi^2} \frac{e^{i\lambda\Psi_c}}{|\det H_c^{\mathrm{SU(2)}}|^{1/2}} \cos \left(\lambda S_{\mathrm{R}} - \frac{1}{2} \arg H_c^{\mathrm{SU(2)}} \right) + O(\lambda^{-7}). \tag{47}$$

Here $H_c^{\mathrm{SU(2)}}$ is the Hessian determinant at the critical point, and Ψ_c a global phase determined by the action at the critical point, which is purely imaginary, and which depends in turn on the gauge choice and the phase of the coherent states exactly as for the EPRL model.

From this analysis we understand why the simplified model has no critical behavior for Lorentzian Regge data, and the same critical behavior of SU(2) BF for vector and Euclidean Regge data. In particular, for Euclidean Regge data, inserting Eq. 47 into Eq. 46 we find that the simplified model has the same λ^{-12} power law decay and the same γ-independent frequency of oscillations S_{R} of the full EPRL model. This explains why the simplified model captures the right scaling and frequency of oscillations of the EPRL asymptotics 34, as was shown in Fig. 14.

It also explains why it does *not* capture the right cosine phase offset: The simplified model sees the SU(2) phase offset $-\frac{1}{2} \arg H_c^{\mathrm{SU(2)}} = -0.324$ for the equilateral configuration, which is absent in the asymptotic formula for the EPRL model, since the Hessian is in that case real. Consider then a modified asymptotic formula

$$A_v^s(\text{Euclidean data}) = \frac{5.13 \times 10^{-7}}{\lambda^{12}} \cos \left(5\lambda \arccos \left(-\frac{1}{4} \right) - 0.324 \right), \tag{48}$$

where we added by hand the offset of the SU(2) BF amplitude. This formula correctly matches the cosine phase offset of the simplified model, see Fig. 17. As a consequence, the internal sums pile up to the SU(2) Hessian to give the right magnitude of the EPRL amplitude, but also contribute to the phase offset of the cosine, creating an interference pattern that changes Eq. 47 to Eq. 34.
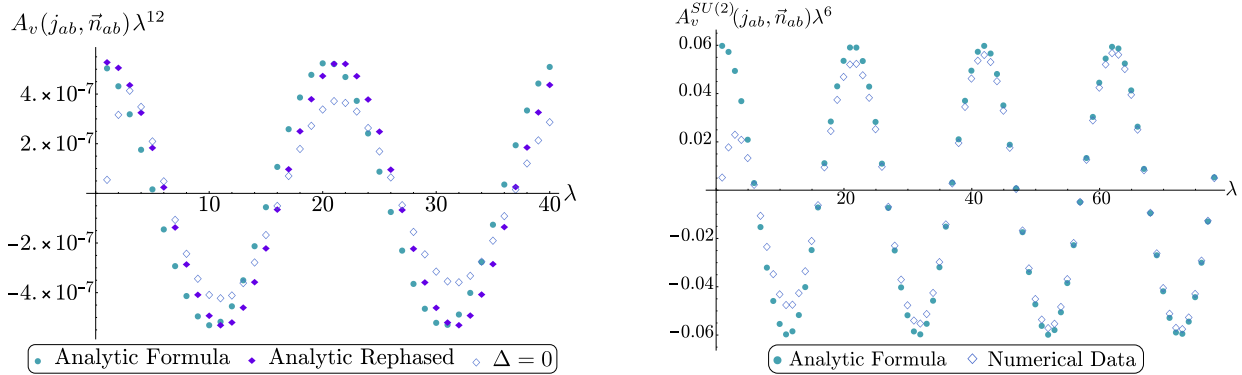

Figure 17: Left panel: *Comparison of the simplified model with the EPRL asymptotics and the modified asymptotics with the SU(2) offset 48. The improved agreement shows that the right asymptotics of the simplified model is to first approximation the same of SU(2) BF theory, and implies that the role of the internal sums in this case is to contribute to the re-phasing of the offset to match the EPRL asymptotics - as well as contributing to the magnitude.*
Right panel: *Evauation of the SU(2) BF asymptotics for an equilateral Euclidean 4-simplex, and comparison with the analytic formula 47 (It updates the plot of [10] which stopped at $\lambda = 50$ - or $\lambda = 25$ in that notation). It shows how while the frequency is captured early on, the magnitude requires higher spins. At $\lambda = 79$ the data for the $\{6j\}$ required weighted 230 gigabytes and saturated our server's capacity.*

We take this opportunity to provide in the same figure an updated plot of the SU(2) BF asymptotics with respect to the one presented in [10]. It allows us to highlight that the frequency of the asymptotic

formula is matched early on by the exact evaluation, but the magnitude only at higher spins. We expect a similar situation for the EPRL model.

Let us now consider Lorentzian boundary data. As already stated, the SU(2) vertex amplitude is exponentially suppressed for such data and thus also the simplified model should be, in agreement with the indication of exponential decay in Fig. 15. Only the l-shells can see the critical behavior. If we look at the factorization 6, we need both booster functions and the $\{15j\}$ symbol to individually have critical behavior. The $\{15j\}$ has critical behavior only for Euclidean Regge configurations, or vector geometries. The booster functions must then admit a critical behavior precisely at those configurations for which the j's correspond to a spacelike Lorentzian 4-simplex, and the l's to a Euclidean one, or a vector geometry. A saddle point approximation of the booster function will appear in [46], and shows that critical behavior appears when the two sets of spins and coherent intertwiners correspond to tetrahedra that can be boosted into one another. The action of the boosts is defined embedding each 3D normal as the electric part of a γ-simple bivector. Hence there are a priori an infinite number of admissible l's contributing to the critical behavior, characterized by the existence of a certain classical boost mapping the j tetrahedra to the l tetrahedra, and then a critical point of the $\{15j\}$ symbol at that configuration. There are a priori infinitely many Euclidean 4-simplices for which this construction works, and we had fun exploring the ones with smallest l's in a reconstruction algorithm depicted in Fig. 18.

According to this argument, all shells should contribute to the asymptotic formula, and Eq. 39 should only be reproduced accurately when sufficiently many shells are summed over. One can reasonably hope that a limited number of shells will suffice to most applications, and in the luckiest cases, the single first shell and its qualitative matching to the asymptotic behavior. For situations where one needs to sum many shells, the method [8] here used becomes less efficient and may have to leave way for alternative approaches, like for instance adaptive Monte Carlo.
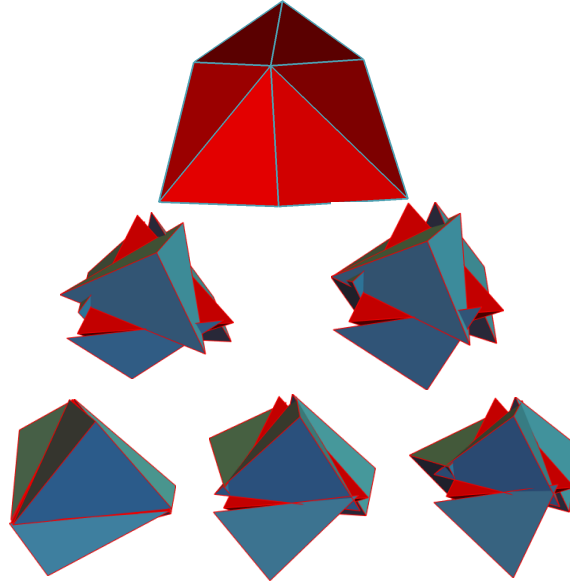

Figure 18: Top panel: *A pictorial representation of the spike of the Lorentzian 4-simplex used in our numerical analysis. One tetrahedron is equilateral with areas 5, the other four are isosceles with base area 5 and the others 2.*
Middle panel: *Twisted spike for the Euclidean 4-simplices with areas compatible with the spins in the first shell. The 4-simplex on the left has one equilateral tetrahedron with areas 5, one isosceles tetrahedron with base area 5 and the other 3 and three tetrahedra with one area 5, one area 3 and the other two areas 2. The one on the right has one equilateral tetrahedron with areas 5, and four isosceles tetrahedra with base area 5 and the others 3 .*
Bottom panel: *Twisted spike for the Euclidean 4-simplices with areas compatible with the spins in the second shell. The 4-simplex on the left has one equilateral tetrahedron with areas 5, one isosceles tetrahedron with base area 5 and the other 4 and three tetrahedra with one area 5, one area 4 and the other two areas 2. The one in the middle is similar but with areas 5, 4, and 3. The one on the right has one equilateral tetrahedron with areas 5, and four isosceles tetrahedra with base area 5 and the others 4.*

6.2 Numerical improvements

6.2.1 Improved server

A few of the numerics presented in this paper can be performed on a simple laptop, like computing the simplified model at spins below 10, our counting of the number of configurations compatible with the triangle inequalities. For the rest, we used a server with 32 cores at the CPT. While this enormously improves with respect to a single laptop, it is effectively very small with respect to the computing power used in other branches of theoretical physics. The CPT is in the process of acquiring a server with 128 cores. When it will come on line, it will cut our evaluation times by a factor of 4, and push forward current computing and RAM limits. To fully take advantage of this additional power however, one will need to improve the part of the code that computes the booster functions, to eliminate the numerical instabilities plaguing it at spins of order 50. Once this is done, a more powerful server will no doubt be able to fully test the asymptotics with Lorentzian boundary data, and show at which spins it is reached, and for which cutoff Δ, answering the questions left open here.

A more powerful server will also allow numerical evaluations for extended triangulations. In particular for calculations not requiring the use of coherent states, computational times may be reasonable for a triangulation with a handful or more of 4-simplices. Beyond that, one may likely need simplification schemes, like for instance the minisuperspace models used for a numerical study of renormalization in the Euclidean EPRL [47], or approximations. To that end, let us briefly comment on one approximation and two variations that could be considered in future work.

6.2.2 Cutting the boosters

Cutting the coherent boundary states is the only approximation used in some of the calculations of this paper. A second approximation that should be considered is to cut the booster functions, as it could turn out to be more efficient. The boosters are decreasing functions of the l's, typically power law but in many cases exponentially decreasing. If one could identify a priori which ones, then one could cut the l sums. The numerical investigations we performed do not suggest any easy way in which this can be done. We found for example cases in which most of the boosters within a shell are one to 3 orders of magnitude smaller than the few dominant ones, yet the total sum of the subdominant ones is of the same order as the sum of the dominant ones, thus forestalling any truncation. Some light over this possibility could be shed by analytic studies of the boosters' asymptotic behavior [45, 46].

6.2.3 Alternative expressions for the boosters

Our code computes the booster functions using numerical integration with the trapezoidal method, and the expression of the boost matrix elements d as finite sums derived in [33]. This expression contains ratios of Euler's gamma functions with both real and complex arguments. We spent a significative amount of time optimizing this part of the code and running tests and debugs. The instabilities we found arising at spins of order 50 are the results of very small numbers constructed from ratios of very large numbers, and it is the part of our code that we should, and we plan to, improve next.

On the other hand, there are alternative expressions that could be considered in future work. One is the alternative formula derived in [8], where the r integrals are solved analytically but at the price of introducing a new integral over a virtual ρ label. The ρ integrand has a nice Gaussian-like behavior,[19], which can be exploited in numerical evaluations.

Another possibility is to implement the recursion relations for the $SL(2, \mathbb{C})$ Clebsch-Gordan coefficients derived in [48]. For a simpler model with three-valent boosters and no intertwiners, this approach is extremely powerful, and one can push the internal sums to order $\Delta \sim 100$ [49].

6.2.4 Alternative form of the coherent states

The coherent state coefficients $c_i(\vec{n}_{ab})$ are a fast part of the numerical code. However, since an enormous number of these coefficients is needed, it could be interesting to explore alternative definitions that could speed up this procedure. One possibility is the cross ratio coherent states [39], and the analytic expressions

---

[19]With a peak when the virtual ρ label takes value γj, thus showing a certain type of simplicity off-shellness in the model.

studied in [50]. This basis has more economical features and proved advantageous in numerical evaluations of the coherent state volume operator defined in [37]. We hope to be able to investigate its implementation in future work.

As we estimated in Sec. 4, the use of coherent states can require up to an additional λ^5 terms, which has a strong impact on the numerical cost of the amplitude. Coherent states are necessary for the asymptotic formula, but many spin foam calculations can be done in the more economical orthonormal basis of intertwiners. This can be an important trade-off when moving to consider amplitudes on many 4-simplices. We have seen that the number of terms for a single equilateral 4-simplex with coherent states scales like λ^{10}. This is the same number of terms needed to compute, with orthonormal intertwiners, the equispin amplitude with three 4-simplices glued together and one internal sum. This Δ_3 amplitude is relevant for a discussion of the flatness problem [51, 52], and will be the object of future work. More in general, avoiding coherent states and increasing the number of cores, we expect to be able to make calculations on a few vertices. Going beyond that will probably require some deeper optimization of the method, or reduction to minisuperspace models.

7   Conclusions

We presented for the first time a numerical evaluation of the Lorentzian EPRL vertex amplitude. Obtaining this result proved to be a challenging task, and the work presented in this paper took more than two years to complete. Preliminary, more qualitative results were presented at the conference Loops '17. Making them quantitatively precise was complicated by the many technical details to be worked out. The challenges were twofold. The main one was clearly to setup the numerical code, which includes evaluating the booster functions, the $\{15j\}$ symbols, the coherent states, and assembling them via hash tables. All making sure that there were no numerical instabilities or inconsistent conventions. A bit more surprisingly, we also faced some analytical challenges, concerning the way the boundary data were to be constructed and fed to the computer, and computing the overall phase and Hessian of the asymptotic formula. While these quantities were well defined in principle, precise explicit formulas and reconstruction algorithms were missing. We devoted part of the paper to explaining how this can be done explicitly, and the online repository [7] contains explicit Mathematica codes to answer these questions. We hope that our paper and this repository can provide a reference point for future work in this direction, so that one does not have to spend time again on this background material.

On the analytic side, we provided useful formulas and explicit configurations for the boundary data to be used in the amplitude. We shed light on the geometric meaning of the internal sums, explaining in particular why the simplified model asymptotes to the Regge action for Euclidean configurations but not for Lorentzian ones.

On the numerical side, our main conclusion is that precise numerical evaluations of the complete Lorentzian EPRL model are currently possible, and it is worthwhile to invest computational capabilities to address explicit physical questions. The method of [8] and its implementation developed in [6] have been successfully tested. Including only a few terms of the internal shells appears sufficient to most applications, avoiding the need to develop a full Monte Carlo approach of the amplitude. The codes for the geometric reconstruction of the data and the numerical evaluation of the vertex amplitudes are publicly available at [7]. More specifically to the asymptotic large spin behavior of the vertex amplitude, our conclusions confirm the analytic formula of [5] already at spins of order 10 for vector and Euclidean Regge data. Higher spins are required for a good match in the case of Lorentzian Regge data, but the power law decays and γ-dependence of the oscillations are already evident at spins of order 10.

The computational resources it takes to compute the vertex amplitude in the coherent basis are considerable but at the same time affordable. A natural and indeed crucial question is how to extend the numerical calculations to many vertices. We performed computations using 32 parallel cores, but let us not forget that in other areas of physics, computations are done with hundreds or thousands of cores. What will be computed in the future depends on the resources available, as well as on numerical improvements and optimizations that can still be done. Finally, we would like to stress that while our methods and results were motivated by the EPRL model, they can be applied or adapted to other spin foam models based on or related to SL(2, $\mathbb{C}$) [53, 52, 54, 55, 56, 57, 58], their physical applications, e.g., [59], to applications involving many vertices through intertwiner renormalization as in [60] or minisuperspace renormalization as in [47],

as well as to calculations of tensorial and graph invariants regardless of their quantum gravity applications.

Acknowledgments

A   Conventions and explicit formulae

In this appendix we fix our conventions and notation, and provide the explicit relation between our version 6 of the coherent amplitude and the one in [5]. The difference is just in the phase and a complex conjugation of the spinors, but it has multiple origins due to the many conventional choices involved. Our conventions follow those of [41, 44, 43].

A.1   SU(2) coherent states and spinors

SU(2) coherent states

The uncertainty in the direction of a state $|j, m\rangle$ in the SU(2) irrep j is minimized by the lowest and highest weights $m = \pm j$. Acting with a rotation $g \in$ SU(2) on $|j, \pm j\rangle$ defines two alternative families of coherent states. Orbits of the isotropy subgroup U(1) $\subset$ SU(2) generate an irrelevant global phase in the coherent states, and it is sufficient to consider two-parameters group elements in the form [41]

$$n(\zeta) := \frac{1}{\sqrt{1 + |\zeta|^2}} \begin{pmatrix} 1 & \zeta \\ -\bar{\zeta} & 1 \end{pmatrix}, \qquad \zeta = -\tan \frac{\Theta}{2} e^{-i\Phi} \in \mathbb{C}P^1. \tag{A.1}$$

This is also known as the Hopf section for the SU(2) $\simeq S^2 \times S^1$ fibration, and we parametrized ζ as the stereographical projection of the sphere from the south pole, with (Θ, Φ) the zenith and azimuth angles. In terms of Wigner's matrices as $D(\alpha, \beta, \gamma) = e^{-i\alpha J_z} e^{-i\beta J_y} e^{-i\gamma J_z}$ [43] (caveat in reading the files in [7], Wolfram's Mathematica uses opposite sign conventions for this parametrization),

$$n(\zeta) = D^{(1/2)}(\Phi, \Theta, -\Phi). \tag{A.2}$$

The standard choice is to define coherent states starting from the lowest weight [41],

$$|j, \zeta\rangle := n^{(j)}(\zeta)|j, -j\rangle, \qquad \langle j, m|j, \zeta\rangle = D^{(1/2)}_{m,-1/2}(\Phi, \Theta, -\Phi). \tag{A.3}$$

They satisfy

$$\langle j, \zeta|\vec{J}|j, \zeta\rangle = -j\vec{n}, \qquad \vec{n} := (\sin \Theta \cos \Phi, \sin \Theta \sin \Phi, \cos \Theta), \tag{A.4}$$

and the important factorization property

$$\langle j, \zeta_1|j, \zeta_2\rangle = \langle \tfrac{1}{2}, \zeta_1|\tfrac{1}{2}, \zeta_2\rangle^{2j}. \tag{A.5}$$

The phase ambiguity associated with the U(1) subgroup, namely with choosing a different section than Hopf's, is the one that can be used to make the coherent amplitude real for any boundary data configuration, as discussed in [5] and in the main text.

It is often convenient to use also the second family, the one constructed from the highest weight. To distinguish it, we use a different ket notation,

$$|j, \zeta] := n^{(j)}(\zeta)|j, j\rangle, \qquad \langle j, m|j, \zeta] = D^{(1/2)}_{m,1/2}(\Phi, \Theta, -\Phi). \tag{A.6}$$

It satisfies

$$[j, \zeta | \vec{J} | j, \zeta] = j\vec{n}, \tag{A.7}$$

namely the state points in the antipodal direction on the sphere. The two families are in fact related by a parity transformation realized by the complex structure

$$J^{(j)} \triangleright |j, \zeta\rangle := \epsilon^{(j)} |j, \bar{\zeta}\rangle = |j, \zeta], \qquad J^{(j)2} = (-1)^{2j}. \tag{A.8}$$

Here $\epsilon_{mn}^{(j)} := (-1)^{j-m}\delta_{m,-n} = D_{mn}^{(j)}(i\sigma_2)$ is the spinorial metric. Another useful operation is the antipodal map

$$\vec{n} \mapsto -\vec{n} \quad \Leftrightarrow \quad (\Theta, \Phi) \mapsto (\pi - \Theta, \pi + \Phi) \quad \Leftrightarrow \quad \zeta \mapsto \zeta^{\mathrm{AP}} = -\frac{1}{\bar{\zeta}}. \tag{A.9}$$

We observe that

$$|j, \zeta\rangle = e^{2ij(\pi+\Phi)} |j, \zeta^{\mathrm{AP}}\rangle, \qquad |j, \zeta^{\mathrm{AP}}] = e^{2ij\Phi} |j, \zeta\rangle, \tag{A.10}$$

so the antipodal map has the effect of changing family without preserving the Hopf section because of the additional phase. This will play a role below.

Coherent intertwiners

Group averaging the tensor product of coherent states defines the coherent intertwiners [18],

$$\int_{\mathrm{SU}(2)} dg \otimes_f D^{(j_f)}(g) |j_f, \zeta_f\rangle = \sum_{i_{12}} d_{i_{12}} \, c_{i_{12}}(\vec{n}_f) \, |j_1, \ldots j_4, i_{12}\rangle, \tag{A.11}$$

where i_{12} is the standard orthonormal intertwiner basis, here taken in the 12 recoupling channel. The coherent intertwiner coefficient $c_{i_{12}}(\vec{n}_f)$ is given by Eq. 9 in terms of Wigner's four-legged symbol

$$\begin{pmatrix} j_f \\ m_f \end{pmatrix}^{(i_{12})} = \begin{pmatrix} j_1 & j_2 & j_3 & j_4 \\ m_1 & m_2 & m_3 & m_4 \end{pmatrix}^{(i_{12})} = \sum_{m_{12}} (-1)^{j_{12}-m_{12}} \begin{pmatrix} j_1 & j_2 & j_{12} \\ m_1 & m_2 & m_{12} \end{pmatrix} \begin{pmatrix} j_{12} & j_3 & j \\ -m_{12} & m_3 & m \end{pmatrix}.$$

In Eq. 9 we used $\vec{n}$ to label the argument of the Wigner matrices, instead of Eq.A.2. This was done so to reduce at most the technical details needed to read the main text. This coherent intertwiner is directly applicable to the tetrahedron labeled 5 in Eq. 7. In the other cases, one or more kets are replaced by bras, and simultaneously we put an antipodal map in the normal labeling the coherent states, like in Eq. 1. Where we have a bra, the intertwiner needs to be multiplied by the epsilon matrix $\epsilon^{(j)}$ to take into account the link's orientation. For a tetrahedron with only one bra, say in the first position of the graphic symbol, the resulting coefficient is

$$c_{i_{12}}^{(1)}(\vec{n}_f) := \begin{pmatrix} j_1 & j_2 & j_3 & j_4 \\ -m_1 & m_2 & m_3 & m_4 \end{pmatrix}^{(i_{12})} (-1)^{j_1-m_1} \overline{D_{m_1,j_1}^{(j_1)}(-\vec{n}_1)} \prod_{f=2}^{4} D_{m_f,j_f}^{(j_f)}(\vec{n}_f). \tag{A.12}$$

For the numerical code, it was convenient to rewrite this expression in terms of the intertwiner with all four legs outgoing. This can be achieved by recalling that

$$\overline{D_{m,n}^{(j)}(g)} = (-1)^{m-n} D_{-m,-n}^{(j)}(g), \tag{A.13}$$

which applied to Eq. A.12 leads to

$$c_{i_{12}}^{(1)}(\vec{n}_f) = \begin{pmatrix} j_1 & j_2 & j_3 & j_4 \\ m_1 & m_2 & m_3 & m_4 \end{pmatrix}^{(j_{12})} D_{m_1,-j_1}^{(j_1)}(-\vec{n}) \prod_{f=2}^{4} D_{m_f,j_f}^{(j_f)}(\vec{n}_f). \tag{A.14}$$

These are the expressions used in `sl2cfoam`.

70

Spinors

The fundamental irrep $j = 1/2$ is isomorphic to $\mathbb{C}^2$, and the relation of the coherent states to spinors is very useful to study properties of the $\mathrm{SL}(2, \mathbb{C})$ unitary irreps. We denote a spinor with $z^A \in \mathbb{C}^2$, $A = 0, 1$, and use

$$\epsilon_{AB} = \begin{pmatrix} 0 & 1 \\ -1 & 0 \end{pmatrix} = \epsilon^{AB} \tag{A.15}$$

to raise and lower indices. We equip $\mathbb{C}^2$ with a complex structure J and define the dual spinor

$$(Jz)^A := J \triangleright z^A := \begin{pmatrix} \bar{z}^1 \\ -\bar{z}^0 \end{pmatrix}, \qquad J^2 = (-1)^{2j}. \tag{A.16}$$

Notice that so defined, the complex structure is consistent with Eq. A.8 for $j = 1/2$. ϵ_{AB} gives an $\mathrm{SL}(2, \mathbb{C})$-invariant bilinear coupling, and we can introduce an Hermitian norm given by complex conjugation (book kept by dotting the indices) and the identity matrix $\delta_{A\dot{A}}$, which is nothing but a choice of canonical timelike vector in Penrose's abstract index notation. With a Dirac-like notation for spinors [61], the relations between spinors and their dual can be compactly written

$$|z\rangle = \begin{pmatrix} z^0 \\ z^1 \end{pmatrix} = -\epsilon|\bar{z}] = -J \triangleright |z] = -|Jz], \qquad |z] = J \triangleright |z\rangle = |Jz\rangle = \epsilon|\bar{z}\rangle = \begin{pmatrix} \bar{z}^1 \\ -\bar{z}^0 \end{pmatrix}, \tag{A.17}$$

with $\epsilon = i\sigma_2$, and the Hermitian and Lorentz-invariant bilinear are

$$\langle z|w\rangle = \delta_{A\dot{A}}\bar{z}^{\dot{A}}w^A = \langle Jw|Jz\rangle = [w|z], \qquad [z|w\rangle = \epsilon_{AB}w^A z^B \equiv \langle Jz|w\rangle. \tag{A.18}$$

Finally, for the norm we use

$$\|z\|^2 := \langle z|z\rangle = |z^0|^2 + |z^1|^2. \tag{A.19}$$

Coming back to the $\mathrm{SU}(2)$ coherent states, the lowest-weight ones define spinors

$$|\zeta\rangle := |\tfrac{1}{2}, \zeta\rangle = \begin{pmatrix} -\sin\frac{\Theta}{2}e^{-i\Phi} \\ \cos\frac{\Theta}{2} \end{pmatrix} \tag{A.20}$$

of unit norm and $\arg z^1 = 0$. The map $z^0 = -\sin\frac{\Theta}{2}e^{-i\Phi}, z^1 = \cos\frac{\Theta}{2}$ provides a choice of section for the $\mathbb{C}^2 \simeq \mathbb{C}P^1 \times \mathbb{C}P^1$ fibration. Conversely, an arbitrary spinor defines a coherent state for the fundamental irrep which is redundantly parametrized by an additional norm and phase,

$$|z\rangle = \|z\|e^{i\arg z^1}|\tfrac{1}{2}, \zeta\rangle, \qquad \zeta = \frac{z^0}{z^1}, \qquad |z^1| = \frac{\|z\|}{(1 + |\zeta|^2)^{1/2}}. \tag{A.21}$$

The additional phase corresponds to the phase ambiguity in the coherent states previously discussed, whereas the norm can be eliminated by working always with normalized spinors. Spinorial $\mathrm{SU}(2)$ coherent states feature prominently in spin foam models and their applications, see e.g. [62, 63, 61, 64, 65, 66]. An immediate advantage of their use is to write the resolution of the identity as Gaussian integrals.

For the highest weight,

$$|\zeta] := |\tfrac{1}{2}, \zeta] \equiv J \triangleright |\zeta\rangle = \begin{pmatrix} \cos\frac{\Theta}{2} \\ \sin\frac{\Theta}{2}e^{i\Phi} \end{pmatrix} = e^{i\Phi}|\tfrac{1}{2}, \zeta^{\mathrm{AP}}\rangle. \tag{A.22}$$

Again, an arbitrary dual spinor defines a redundant coherent state with an additional norm and phase,

$$|z] = \|z\|e^{i\arg z^1}|\tfrac{1}{2}, \zeta]. \tag{A.23}$$

The expressions A.21 and A.23 can be generalized to an arbitrary irrep j, to provide spinorial coherent states for $\mathrm{SU}(2)$. To that end, we consider the matrix

$$g(z^A) := \frac{1}{\|z\|}\Big(|z], |z\rangle\Big) = \frac{1}{\|z\|}\begin{pmatrix} \bar{z}^1 & z^0 \\ -\bar{z}^0 & z^1 \end{pmatrix} = n(\zeta)e^{-i\arg z^1 \sigma_3}, \qquad \zeta = \frac{z^0}{z^1}, \qquad n(\zeta) \equiv g_{\mathrm{R}}(\zeta, 1). \tag{A.24}$$

We then define the spinorial coherent states

$$|j, z^A\rangle := \|z\|^{2j} D^{(j)}\big(g_\mathrm{R}(z^A)\big)|j, -j\rangle = \sum_m \binom{2j}{j+m}^{1/2} (z^0)^{j+m}(z^1)^{j-m}|j,m\rangle \equiv \|z\|^{2j} e^{2ij\,\arg z^1}|j,\zeta\rangle, \quad (\mathrm{A.25})$$

$$|j, z^A] := \|z\|^{2j} D^{(j)}\big(g_\mathrm{R}(z^A)\big)|j, j\rangle = \sum_m \binom{2j}{j+m}^{1/2} (-\bar{z}^0)^{j-m}(\bar{z}^1)^{j+m}|j,m\rangle \equiv \|z\|^{2j} e^{-2ij\,\arg z^1}|j,\zeta], \quad (\mathrm{A.26})$$

where in the second equality we used the following properties of the Wigner matrices:

$$D^{(j)}_{m,-j}(g) = \binom{2j}{j+m}^{1/2}(g_{12})^{j+m}(g_{22})^{j-m}, \qquad D^{(j)}_{mj}(g) = \binom{2j}{j-m}^{1/2}(-\bar{g}_{12})^{j-m}(\bar{g}_{22})^{j+m}. \qquad (\mathrm{A.27})$$

These expressions reduce to Eqs. A.21 and A.23 for $j = 1/2$.

Finally, we note the factorization properties

$$[j, w|j, z\rangle = \sum_m \binom{2j}{j+m}(w^1 z^0)^{j+m}(-w^0 z^1)^{j-m} = [z|w\rangle^{2j}, \qquad (\mathrm{A.28})$$

$$\langle j, w|j, z\rangle = \sum_m \binom{2j}{j+m}(\bar{w}^0 z^0)^{j+m}(\bar{w}^1 z^1)^{j-m} = \langle w|z\rangle^{2j}. \qquad (\mathrm{A.29})$$

A.2 $\mathrm{SL}(2,\mathbb{C})$ unitary irreps of the principal series

Homogeneous representation

We follow the conventions of [44], with the notational difference

$$\rho = \frac{1}{2}\rho_\mathrm{Ruhl}, \qquad k = -\frac{1}{2}m_\mathrm{Ruhl}. \qquad (\mathrm{A.30})$$

Unitary irreps of the principal series of $\mathrm{SL}(2,\mathbb{C})$ are labeled by a pair $(\rho \in \mathbb{R}, k \in \mathbb{Z}/2)$ [67, 68, 44], and can be represented on a space of homogeneous functions of two complex variables,

$$F^{(\rho,k)}(\lambda z^A) = \lambda^{k-1+i\rho}\bar{\lambda}^{-k-1+i\rho} F^{(\rho,k)}(z^A), \qquad \lambda \in \mathbb{C}, \qquad A = 0, 1. \qquad (\mathrm{A.31})$$

The scalar product is defined choosing any section of the $\mathbb{C}^2 \simeq \mathbb{C}P^1 \times \mathbb{C}P^1$ fibration,

$$(F, F') := \int_{\mathbb{C}P^1} d\mu(z^A)\overline{F(z^A)}F'(z^A), \qquad d\mu(z^A) := \frac{i}{2} z_A dz^A \wedge \bar{z}_{\dot{A}} d\bar{z}^{\dot{A}}. \qquad (\mathrm{A.32})$$

The scaling of the Lorentz-invariant measure $d\mu(z^A)$ guarantees that the whole integrand is homogeneous of degree zero, and thus the integration is independent of the choice of section.

For the EPRL model with spacelike tetrahedra we pick Naimark's orthonormal basis, labeled by the eigenfunctions of L^2 and L_z and given in the conventions of [44] by

$$F^{(\rho,k)}_{jm}(z^A) := e^{i\Psi^\rho_j}\sqrt{\frac{d_j}{\pi}}\frac{1}{\|z\|^{2(1-i\rho)}}D^{(j)}_{m,-k}\big(g(z^A)\big), \qquad j \ge |k|, \qquad j \ge m \ge -j. \qquad (\mathrm{A.33})$$

Here $D^{(j)}$ are Wigner matrices, and $g(z^A)$ is the same matrix defined in Eq. A.24.

The function Ψ^ρ_j parametrizes a freedom in choosing the phase of the basis elements. This is set to zero in [44] and [5]. This economical choice however leads to complex Clebsch-Gordan coefficients. An alternative choice is to take [8]

$$e^{i\psi^\rho_j} = (-1)^{-\frac{j}{2}} \frac{\Gamma(j+i\rho+1)}{|\Gamma(j+i\rho+1)|}, \qquad (\mathrm{A.34})$$

which guarantees reality of the Clebsch-Gordan coefficients, and as a consequence also of all EPRL amplitudes $A_v(j_{ab}, i_a)$ in the orthogonal intertwiner basis. This is the convention used in our numerical code, but this phase difference goes away in the expression of the coherent amplitude.

We introduce next the antilinear map $\mathcal{J}$, the infinite-dimensional analog of the complex structure J for spinors, given by

$$\mathcal{J}F(z^A) := \overline{\mathcal{A}F(z^A)}, \tag{A.35a}$$

$$\mathcal{A}F(z^A) := \frac{\sqrt{\rho^2 + k^2}}{\pi} \int_{\mathbb{C}P^1} d\mu(w^A)[w|z\rangle^{-k-1-i\rho}\overline{[w|z\rangle}^{k-1-i\rho}F(w^A). \tag{A.35b}$$

It satisfies

$$\mathcal{J} \; : \; (\rho, k) \mapsto (\rho, k), \qquad (\mathcal{J}F, \mathcal{J}F') = (F', F), \qquad \mathcal{J}^2 = (-1)^{2k}. \tag{A.36}$$

Using this map we can define the bilinear pairing

$$\epsilon(F, F') := (\mathcal{J}F, F') = (-1)^{2k}\epsilon(F', F), \qquad (F, F') = \epsilon(F', \mathcal{J}F). \tag{A.37}$$

This is the infinite-dimensional analog of the spinorial bilinear A.18.

Group elements and vertex amplitude

The $\mathrm{SL}(2,\mathbb{C})$ group action in the homogeneous representation is given by matrix multiplication on the spinor argument, $h \triangleright F(z^A) = F(h^{\mathrm{T}}z^A)$. The matrix elements can be equally written as the Hermitian or the bilinear products,

$$D_{jmln}^{(\rho,k)}(h) := \langle \rho, k; j, m|h|\rho, k; l, n\rangle = \left(F_{jm}^{(\rho,k)}, h \triangleright F_{ln}^{(\rho,k)} \right) = \epsilon\left(h \triangleright F_{ln}^{(\rho,k)}, \mathcal{J}F_{jm}^{(\rho,k)} \right). \tag{A.38}$$

For the EPRL model, we are only interested in the "minimal" weights

$$\rho = \gamma k, \qquad j = l = k, \tag{A.39}$$

and for group elements in the form $h = h_a^{-1}h_b$. Using the invariance of the integration measure, we can write these group elements as

$$D_{jmjn}^{(\gamma j, j)}(h_a^{-1}h_b) = \int_{\mathbb{C}P^1} d\mu(z^A)\overline{F_{jm}^{(\gamma j, j)}(h_a^{\mathrm{T}}z^A)}F_{ln}^{(\gamma j, j)}(h_b^{\mathrm{T}}z^A). \tag{A.40}$$

The vertex amplitude in the orthonormal basis is simply the tensor associated to the complete five-valent graph,

$$A_v(j_{ab}, m_{ab}) = \int \prod_{a=2}^{5} dh_a \prod_{a<b} D_{j_{ab},m_{ab},j_{ab},m_{ba}}^{(\gamma j_{ab}, j_{ab})}(h_a^{-1}h_b). \tag{A.41}$$

Because of its $\mathrm{SU}(2)$ invariance it can be contracted for free with the four-legged Wigner's symbol to define the amplitude in the intertwiner basis $A_v(j_{ab}, i_a)$.

A.3   Definition of the $\mathrm{SL}(2,\mathbb{C})$ coherent amplitude

Since the maximal isotropy group of $\mathrm{SL}(2,\mathbb{C})$ is the same as of $\mathrm{SU}(2)$, coherent states are a direct embedding of the $\mathrm{SU}(2)$ ones into the unitary irreps used. For the EPRL irreps in the homogeneous representation A.33, we define the (lowest-weight) family of coherent states

$$F_{j\zeta}^{(\gamma j, j)}(z^A) := \sum_m F_{jm}^{(\gamma j, j)}(z^A)\langle j, m|j, \zeta\rangle = \sqrt{\frac{d_j}{\pi}} \|z\|^{2(i\gamma j - 1 - j)}\langle \bar{z}|\zeta\rangle^{2j}, \tag{A.42}$$

where the last step follows from the factorization properties of coherent states.[20] It is useful to define also a dual basis associated with the highest weight A.6,

$$F_{jJ\zeta}^{(\gamma j, j)}(z^A) := \sum_m F_{jm}^{(\gamma j, j)}(z^A)\langle j, m|j, \zeta] = \sqrt{\frac{d_j}{\pi}} \|z\|^{2(i\gamma j - 1 - j)}\langle \bar{z}|\zeta]^{2j}. \tag{A.43}$$

---

[20]The complex conjugation in $\langle \bar{z}|$, which could be avoided by defining the coherent states as $\sum_m F_{jm}^{(\rho,j)}(z^A)\langle j, \zeta|j, m\rangle$, is actually all right, and familiar from (holomorphic) representations generated by (unnormalized) coherent states, e.g. $f_n(z) := \langle \bar{z}|n\rangle = z^n/n!$ for the harmonic oscillator.

This is related to the antipodal map by the same phase shift A.10 of the $SU(2)$ case, namely

$$F_{jJ\zeta}^{(\gamma j,j)}(z^A) = e^{2ij(\pi+\Phi)} F_{j\zeta^{\mathrm{AP}}}^{(\gamma j,j)}(z^A). \tag{A.44}$$

The map $\zeta \mapsto J\zeta$ from one family to the other can also be induced using the infinite-dimensional complex structure A.35. An explicit calculation gives in fact

$$\mathcal{J} F_{j\zeta}^{(\gamma j,j)}(z^A) = e^{-i\arctan\gamma}\sqrt{\frac{d_j}{\pi}}\,\|z\|^{2(i\gamma j-1-j)}[\zeta|z)^{2j} = e^{-i\arctan\gamma} F_{jJ\zeta}^{(\gamma j,j)}(z^A), \tag{A.45}$$

$$\mathcal{J} F_{jJ\zeta}^{(\gamma j,j)}(z^A) = (-1)^{2j} e^{i\arctan\gamma} F_{j\zeta}^{(\gamma j,j)}(z^A), \tag{A.46}$$

where we fixed $\gamma > 0$ for convenience.

When defining the coherent vertex amplitude, it is convenient to have an antipodal map on the coherent state at the target of each link, so that the vectors can be interpreted consistently as outgoing (or incoming, if one prefers) normals. From the previous formulas, we know three different ways to apply the antipodal map: via ζ^{AP}, via $J \triangleright |\zeta\rangle$, or via $\mathcal{J}F$. The resulting amplitudes differ by an overall phase. To keep the notation as simple as possible in the main text, we used the first option, so as to be able to refer only to unit vectors and bypass spinors. The coherent basis elements used in Eq. 1 are defined as follows,

$$D_{j_{ab},-\vec{n}_{ab},j_{ab},\vec{n}_{ba}}^{(\gamma j_{ab},j_{ab})}(h_a^{-1}h_b) := D_{j_{ab},j_{ab},j_{ab},j_{ab}}^{(\gamma j_{ab},j_{ab})}\big(n^\dagger(\zeta_{ab}^{\mathrm{AP}})h_a^{-1}h_b n(\zeta_{ba})\big) = e^{-2ij_{ab}\Phi_{ab}} D_{j_{ab}\zeta_{ab}j_{ab}J\zeta_{ba}}^{(\gamma j_{ab},j_{ab})}(h_a^{-1}h_b)$$

$$= e^{-2ij_{ab}\Phi_{ab}} \int_{\mathbb{C}P^1} d\mu(z_{ab}^A) \overline{F_{j_{ab}\zeta_{ab}}^{(\gamma j_{ab},j_{ab})}(h_a^{\mathrm{T}}z_{ab}^A)} F_{j_{ab}J\zeta_{ba}}^{(\gamma j_{ab},j_{ab})}(h_b^{\mathrm{T}}z_{ab}^A)$$

$$= e^{-2ij_{ab}\Phi_{ab}} \frac{d_{j_{ab}}}{\pi} \int_{\mathbb{C}P^1} d\mu(z_{ab}^A) \frac{\exp S_{ab}}{\|h_a^{\mathrm{T}}z_{ab}\|^2 \|h_b^{\mathrm{T}}z_{ab}\|^2}, \tag{A.47}$$

where in the last step we defined the action

$$S_{ab} := j_{ab} \ln \frac{\langle h_a^{\mathrm{T}}z_{ab}|\bar{\zeta}_{ab}\rangle^2 [\bar{\zeta}_{ba}|h_b^{\mathrm{T}}z_{ab}\rangle^2}{\|h_a^{\mathrm{T}}z_{ab}\|^2 \,\|h_b^{\mathrm{T}}z_{ab}\|^2} + i\gamma j_{ab} \log \frac{\|h_b^{\mathrm{T}}z_{ab}\|^2}{\|h_a^{\mathrm{T}}z_{ab}\|^2}. \tag{A.48}$$

Therefore our definition 1 of the coherent vertex amplitude is

$$A_v(j_{ab},\vec{n}_{ab}) = \int \prod_{a=2}^{5} dh_a \prod_{a<b} D_{j_{ab},-\vec{n}_{ab},j_{ab},\vec{n}_{ba}}^{(\gamma j_{ab},j_{ab})}(h_a^{-1}h_b) =$$

$$= e^{-2i\sum_{a<b} j_{ab}\Phi_{ab}} \left(\prod_{a<b} \frac{d_{j_{ab}}}{\pi}\right) \int \prod_{a=2}^{5} dh_a \int_{\mathbb{C}P^1} \prod_{a<b} \frac{d\mu(z_{ab}^A)}{\|h_a^{\mathrm{T}}z_{ab}\|^2 \|h_b^{\mathrm{T}}z_{ab}\|^2} \exp S, \tag{A.49}$$

with

$$S = \sum_{a<b} S_{ab}. \tag{A.50}$$

At this point we can follow the saddle point approximation developed in [5], but not before explaining the different conventions used.

Phase ambiguity and the conventions of [5]

The basis of homogeneous functions used in [5] differs from Eq. A.33 in choosing k instead of $-k$ and a different spinorial parametrization,

$$F_{jm}^{\mathrm{B}(\rho,k)}(z^A) := \sqrt{\frac{d_j}{\pi}} \frac{1}{\|z\|^{2(1-i\rho)}} D_{m,k}^{(j)}\big(g_{\mathrm{B}}(z^A)\big), \qquad g_{\mathrm{B}}(z^A) := \frac{1}{\|z\|} \begin{pmatrix} z^0 & -\bar{z}^1 \\ z^1 & \bar{z}^0 \end{pmatrix}. \tag{A.51}$$

In spite of this generic difference, the two choices coincide for the minimal weights used in the EPRL model, since

$$D_{m,j}^{(j)}\big(g_{\mathrm{B}}(z^A)\big) \equiv D_{m,-j}^{(j)}\big(g(z^A)\big). \tag{A.52}$$

74

So there is no difference at this level. The choices however reflect that [5] takes as fundamental family of coherent states the highest weights, and furthermore the spinorial complex structure A.16 is defined with an opposite sign. The spinorial bilinear in [5] is $[w, z] = [z|w\rangle$.

The coherent basis is defined from the highest weights, and denoted

$$\mathcal{I}\phi_\xi(z^A) := \sqrt{\frac{d_j}{\pi}} \|z\|^{2(i\gamma j - 1 - j)} [\xi|z\rangle^{2j} \equiv F_{j\overline{J\xi}}^{(\gamma j, j)}(z^A). \tag{A.53}$$

Then,

$$\mathcal{JI}\phi_\xi(z^A) = (-1)^{2j} e^{-i\arctan\gamma} \sqrt{\frac{d_j}{\pi}} \|z\|^{2(i\gamma j - 1 - j)} \langle\xi|z\rangle^{2j} \equiv (-1)^{2j} e^{-i\arctan\gamma} F_{j\overline{\xi}}^{(\gamma j, j)}(z^A), \tag{A.54}$$

consistent with A.45, since we have the same sign convention for $\mathcal{J}$.

The link "propagator" is defined in [5] from the infinite-dimensional bilinear A.37 (there denoted $\beta(F, F')$ but otherwise identically defined). This is the same as a coherent unitary representation matrix up to a phase,

$$P_{ab} := \epsilon(h_a \triangleright \mathcal{I}\phi_{ab}, h_b \triangleright \mathcal{I}\phi_{ba}) \equiv (h_a \triangleright \mathcal{JI}\phi_{ab}, h_b \triangleright \mathcal{I}\phi_{ba}) = (-1)^{2j_{ab}} e^{i\arctan\gamma} D_{j_{ab}\overline{\xi}_{ab}j_{ab}\overline{J\xi}_{ba}}^{(\gamma j_{ab}, j_{ab})}(h_a^{-1}h_b)$$

$$= (-1)^{2j_{ab}} e^{i\arctan\gamma} \int_{\mathbb{C}P^1} d\mu(z^A) \overline{F_{j_{ab}\overline{\xi}_{ab}}^{(\gamma j_{ab}, j_{ab})}(h_a^\mathrm{T} z^A)} F_{j_{ab}\overline{J\xi}_{ba}}^{(\gamma j_{ab}, j_{ab})}(h_b^\mathrm{T} z^A). \tag{A.55}$$

Hence our expression A.47 for the link propagator differs from the one of [5] by the overall phase $\exp\{i \sum_{a<b}(2j_{ab}(\pi + \Phi_{ab}) + \arctan\gamma)\}$ reported in footnote 4, and by the identification

$$\zeta_{ab} = \bar{\xi}_{ab}. \tag{A.56}$$

With this map, and the renaming $h_a \mapsto \bar{h}_a$, the action becomes

$$S_{ab} := j_{ab} \ln \frac{\langle h_a^\dagger z_{ab}|\xi_{ab}\rangle^2 \langle J\xi_{ba}|h_b^\dagger z_{ab}\rangle^2}{\|h_a^\dagger z_{ab}\|^2 \|h_b^\dagger z_{ab}\|^2} + i\gamma j_{ab} \log \frac{\|h_b^\dagger z_{ab}\|^2}{\|h_a^\dagger z_{ab}\|^2}, \tag{A.57}$$

which coincides with [5] (with our definition of J of opposite sign, but this is irrelevant because of the squares). Alternatively, we can reproduce the action of [5] keeping the same spinors $\zeta_{ab} = \xi_{ab}$ and the same group elements h_a if we take a global complex conjugate and map $\gamma \to -\gamma$.

B   EPRL critical point equations and Hessian

We can at this point recall briefly the key steps of the saddle point approximation of [5], and complete it with the explicit calculation of the Hessian. We look for critical points defined by the vanishing of the gradient of Eq. A.57 with respect to the variables integrated over, the spinors z_{ab}, and the group elements h_a. Vanishing of the spinor gradient gives

$$|\xi_{ab}\rangle = \frac{e^{iv_{ab}}}{\|h_a^\dagger z_{ab}\|} h_a^\dagger |z_{ab}\rangle, \qquad |J\xi_{ba}\rangle = \frac{e^{iv_{ba}}}{\|h_b^\dagger z_{ab}\|} h_b^\dagger |z_{ab}\rangle, \tag{B.58}$$

which can be combined to

$$(h_a^\dagger)^{-1}|\xi_{ab}\rangle = \frac{\|h_b^\dagger z_{ab}\|}{\|h_a^\dagger z_{ab}\|} e^{i(v_{ab}-v_{ba})} (h_b^\dagger)^{-1}|J\xi_{ba}\rangle, \tag{B.59a}$$

as well as

$$h_a|\xi_{ab}\rangle = \frac{\|h_a^\dagger z_{ab}\|}{\|h_b^\dagger z_{ab}\|} e^{i(v_{ab}-v_{ba})} h_b|J\xi_{ba}\rangle. \tag{B.59b}$$

Here v_{ab} are phases to be determined. Because of the homogeneity of the action, these are only four independent real equations per link. Two fix z_{ab} up to the irrelevant choice of section, and the remaining

ones fix the group element and v_{ab} phases. On-shell of these equations, the vanishing of the h_a gradient gives the closure conditions

$$\sum_{b \neq a} j_{ab} \vec{n}_{ab} = 0. \tag{B.60}$$

These are not equations for the integration variables, but directly a restriction on the boundary data. On the other hand, also Eq. B.59 cannot be solved in general for z_{ab} and h_a, but only if the boundary data satisfy special conditions, which leads us to the classification recalled in Sec.2.

In the first subset satisfying Eq. 3, let us further specialize the boundary data to the twisted spike configuration 4, where all normals are pairwise antiparallel. Plugging this condition into Eq. B.59 and looking at the norms, we find equations for the 3D representation matrices $H_a := D^{(1)}(h_a)$,

$$H_a \vec{n}_{ab} = -H_b \vec{n}_{ba} = H_b \vec{n}_{ab}. \tag{B.61}$$

These have a trivial solution with $h_a = \pm\mathbb{1}$ $\forall a$. This corresponds in general to a vector geometry in the twisted spike gauge. However if additionally the shape-matching conditions are satisfied, it is possible to find a second, nontrivial solution, given by $h_1^{(c)} = \mathbb{1}$ and

$$h_a^{(c)} = \pm \exp\left(\theta_{1a} \vec{n}_{1a} \cdot \vec{\sigma}\right) \tag{B.62}$$

for $a \neq 1$. This is the second critical point for Euclidean Regge data in the twisted spike. As for the spike configuration, one rotates back the tetrahedra so that all edges are aligned, and in that case the two critical points are Eq. 20 in the main text. See also Fig. 8 of [10]. Then to evaluate the action at the critical point, we plug the solutions back in Eq. B.59 and determine the v_{ab} phases.

In the second subset, the solutions are not in the SU(2) subgroup, and their derivation is more involved, see [5]. Again we can simplify the analysis choosing judiciously the boundary data. Fixing the spike configuration described in the main text, and using the freedom to gauge fix $h_1 = \mathbb{1}$, we can solve the system with Mathematica, finding the set of four solutions 26. Notice the presence of the $i\pi$: this is due to the inversion required by the fact that the first tetrahedron is past pointing, whereas all the others are future pointing. Plugging them back into Eq. B.59 we determine the v_{ab} phases entering the action at the critical point.

For vector geometries in the twisted spike, $v_{ab} = 0$. For the Regge geometries with two critical points, the v_{ab} contribute not only to the Regge action oscillation but also to the overall phase of the amplitude. Their value for the configurations used in this paper are computed in the Mathematica files in [7]. However, the overall phase is the only part of the analytic calculation that does not fit our numerical data. This could be due to an overlooked phase in the previous appendix, or to a mismatch between the analytic definition and the numerical implementation that we were not able to identify. This is of limited harm, since the global phase is irrelevant to the model, and we determined it from a numerical fit for the sake of plotting real data points.

B.1 Hessian

The Hessian H is the matrix of second derivatives of the action (A.57) with respect to the group elements h_a and the spinors z_{ab}. It is a 44×44 matrix of the form

$$H = \begin{pmatrix} H_{hh} & H_{hz} \\ H_{zh} & H_{zz} \end{pmatrix}. \tag{B.63}$$

The generic structure of the Hessian is presented in [5], however not in a form explicit enough for numerical evaluations. Here we close this gap, and provide the explicit expressions for all the blocks.

The top left block is a 24×24 block diagonal matrix

$$H_{h_a h_b} = \delta_{ab} H_{h_a},$$

where each block is a 6×6 matrix given by

$$H_{h_a} = \frac{1}{2} \sum_{b \neq a} j_{ab} \begin{pmatrix} -(\mathbb{1} - \vec{n}_{ab} \otimes \vec{n}_{ab}) & -i\epsilon_{ab}(\mathbb{1} - \vec{n}_{ab} \otimes \vec{n}_{ab}) + (\epsilon_{ab} + i\gamma) \star \vec{n}_{ab} \\ -i\epsilon_{ab}(\mathbb{1} - \vec{n}_{ab} \otimes \vec{n}_{ab}) - (\epsilon_{ab} + i\gamma) \star \vec{n}_{ab} & -(1 + 2i\epsilon_{ab}\gamma)(\mathbb{1} - \vec{n}_{ab} \otimes \vec{n}_{ab}) \end{pmatrix}$$

where $\epsilon_{ab} = \text{sign}\,(b - a)$ and $\star$ is the Hodge dual in the 3D internal space. The bottom right block of Eq. B.63 is a 20×20 block diagonal matrix

$$H_{z_{ab}z_{cd}} = \delta_{ac}\delta_{bd}H_{z_{ab}z_{ab}}$$

where each block is a 2×2 matrix

$$
H_{z_{ab}} = j_{ab}(i\gamma + 1)\begin{pmatrix} e^{i4v_{ab}}\langle\xi_{ab}|h_a h_a^\dagger|J\xi_{ab}\rangle^2 & |\langle J\xi_{ab}|h_a h_a^\dagger|\xi_{ab}\rangle|^2 - \langle J\xi_{ab}|(h_a h_a^\dagger)^2|J\xi_{ab}\rangle \\ |\langle J\xi_{ab}|h_a h_a^\dagger|J\xi_{ab}\rangle|^2 - \langle J\xi_{ab}|(h_a h_a^\dagger)^2|J\xi_{ab}\rangle & -e^{-2i(2v_{ba}+\arctan\gamma)}\langle J\xi_{ab}|h_a h_a^\dagger|\xi_{ab}\rangle^2 \end{pmatrix}
$$
$$
+ j_{ab}(i\gamma - 1)\begin{pmatrix} e^{i2(2v_{ba}+\arctan\gamma)}\langle J\xi_{ba}|h_b h_b^\dagger|\xi_{ba}\rangle^2 & \langle\xi_{ba}|(h_b h_b^\dagger)^2|\xi_{ba}\rangle + |\langle\xi_{ba}|h_b h_b^\dagger|\xi_{ba}\rangle|^2 \\ \langle\xi_{ba}|(h_b h_b^\dagger)^2|\xi_{ba}\rangle + |\langle\xi_{ba}|h_b h_b^\dagger|\xi_{ba}\rangle|^2 & -e^{-i4v_{ba}}\langle\xi_{ba}|h_b h_b^\dagger|J\xi_{ba}\rangle^2 \end{pmatrix}.
$$

The off-diagonal block of Eq. B.63 is a 24×20 matrix defined with sparse blocks

$$
H_{hz} = \begin{pmatrix} H_{h_1 z_{12}} & H_{h_1 z_{13}} & H_{h_1 z_{14}} & H_{h_1 z_{15}} & 0 & 0 & 0 & 0 & 0 & 0 \\ H_{h_2 z_{12}} & 0 & 0 & 0 & H_{h_2 z_{23}} & H_{h_2 z_{24}} & H_{h_2 z_{25}} & 0 & 0 & 0 \\ 0 & H_{h_3 z_{13}} & 0 & 0 & H_{h_3 z_{23}} & 0 & 0 & H_{h_3 z_{34}} & H_{h_3 z_{35}} & 0 \\ 0 & 0 & H_{h_4 z_{14}} & 0 & 0 & H_{h_4 z_{24}} & 0 & H_{h_4 z_{34}} & 0 & H_{h_4 z_{45}} \end{pmatrix}
$$

where each block is the following 6×2 matrix,

$$
H_{h_c z_{ab}} = \delta_{cb}k_{ab}\begin{pmatrix} ie^{i2v_{ba}}\vec{v}_{ba} & 0 \\ i\gamma e^{i2v_{ba}}\vec{v}_{ba} & (i\gamma - 1)e^{-i2v_{ab}}\overline{\vec{v}_{ba}} \end{pmatrix} + \delta_{ca}k_{ab}\begin{pmatrix} 0 & ie^{-i2v_{ab}}\vec{w}_{ab} \\ (i\gamma + 1)e^{i2v_{ab}}\overline{\vec{w}_{ab}} & i\gamma e^{-i2v_{ab}}\vec{w}_{ab} \end{pmatrix}
$$

defined in terms of the 3D complex vectors

$$\vec{v}_{ba} = \langle J\xi_{ba}|\vec{\sigma}h_b h_b^\dagger|\xi_{ba}\rangle - \vec{n}_{ba}\langle J\xi_{ba}|h_b h_b^\dagger|\xi_{ba}\rangle\,, \quad \text{and} \quad \vec{w}_{ab} = \langle J\xi_{ab}|h_a h_a^\dagger\vec{\sigma}|\xi_{ab}\rangle + \vec{n}_{ab}\langle J\xi_{ab}|h_a h_a^\dagger|\xi_{ab}\rangle\,.$$

By symmetry, the block H_{zh} is a 20×24 matrix that can be obtained by transposition of H_{hz}.

The expression reported here must be evaluated at the critical point, and since we know that $h_a h_a^\dagger$ is a boost along $\vec{n}_{1a}$, everything can be written as a function of dihedral angles, 3D normals, and phases v_{ab}. The result is rather cumbersome and we do not write it here, but we refer to the Mathematica notebook `SL2Cderivatives` in [7] that generates the symbolic expression of the Hessian starting from the action, where this final step is made.

If we revert to our action A.48 (or **??** in the main text), we have

Finally, let us review the various numerical factors that contribute to N_c in the asymptotic formula. This includes the inverse square root of the Hessian determinant, as well as the integration measure at the critical point. For the spinor measure $\Omega_{ab} := \|h_a^\dagger z_{ab}\|^{-2}\|h_b^\dagger z_{ab}\|^{-2}d\mu(z_{ab}^A)$, one needs to make a choice of section of the tautological spinor bundle, the same made in evaluating the (inverse square root of the) Hessian at the critical point. Only their product is independent from this choice. The section we chose is $\|z_{ab}\| = 1$ and $v_{ab} = 0$ for $a < b$, and the result can be read from `SL2Cderivatives`. For the group integrals, we use the normalization of the $SL(2,\mathbb{C})$ Haar measure given in [44]. This gives a factor $1/(2^8\pi^4)^4$ in both the numerical code and the value of the group measure at the critical point. We then have a factor $(2\pi)^{22}$ from the Gaussian integrations, a factor 2^4 from the double multiplicity of the solutions $h_a = \pm h^{(c)}$ for $a \neq 1$, and a factor $(2/\pi)^{10}$ from the normalization of the coherent states in the amplitude. This gives the factor $2^{36}\pi^{12}$ of [5] times the factor $2^{-32}\pi^{-16}$ from the Haar measure. Putting everything together,

$$N_c = \frac{2^4}{\pi^4}\frac{1}{\sqrt{-\det H_{|\sigma}}}\prod_{a<b}\Omega_{ab|c}. \tag{B.64}$$

References

[1] J. Engle, E. Livine, R. Pereira and C. Rovelli, *LQG vertex with finite Immirzi parameter*, Nucl.Phys. **B799** (2008) 136–149 [0711.0146].

[2] L. Freidel and K. Krasnov, *A New Spin Foam Model for 4D Gravity*, Class.Quant.Grav. **25** (2008) 125018 [0708.1595].

[3] A. Perez, *The Spin Foam Approach to Quantum Gravity*, Living Rev.Rel. **16** (2013) 3 [1205.2019].

[4] C. Rovelli and F. Vidotto, *Covariant Loop Quantum Gravity*. Cambridge Monographs on Mathematical Physics. Cambridge University Press, 2014.

[5] J. W. Barrett, R. Dowdall, W. J. Fairbairn, F. Hellmann and R. Pereira, *Lorentzian spin foam amplitudes: Graphical calculus and asymptotics*, Class.Quant.Grav. **27** (2010) 165009 [0907.2440].

[6] P. Dona and G. Sarno, *Numerical methods for EPRL spin foam transition amplitudes and Lorentzian recoupling theory*, Gen. Rel. Grav. **50** (2018) 127 [1807.03066].

[7] The code `sl2cfoam` is public and available at the address: `bitbucket.org/giorgiosarno/sl2cfoam-1.0`.
The code adapted for the computation of asymptotics, and the notebooks used in this work are public and available at the address: `bitbucket.org/giorgiosarno/sl2cfoam-asym-1.0`.

[8] S. Speziale, *Boosting Wigner's nj-symbols*, J. Math. Phys. **58** (2017), no. 3 032501 [1609.01632].

[9] G. Ponzano and T. E. Regge, *Semiclassical limit of Racah coefficients*, (1968).

[10] P. Donà, M. Fanizza, G. Sarno and S. Speziale, *SU(2) graph invariants, Regge actions and polytopes*, Class. Quant. Grav. **35** (2018), no. 4 045011 [1708.01727].

[11] G. Sarno, S. Speziale and G. V. Stagno, *2-vertex Lorentzian Spin Foam Amplitudes for Dipole Transitions*, Gen. Rel. Grav. **50** (2018), no. 4 43 [1801.03771].

[12] E. R. Livine and S. Speziale, *Consistently Solving the Simplicity Constraints for Spinfoam Quantum Gravity*, Europhys.Lett. **81** (2008) 50004 [0708.1915].

[13] J. W. Barrett and L. Crane, *A Lorentzian signature model for quantum general relativity*, Class.Quant.Grav. **17** (2000) 3101–3118 [gr-qc/9904025].

[14] J. W. Barrett, R. Dowdall, W. J. Fairbairn, H. Gomes and F. Hellmann, *Asymptotic analysis of the EPRL four-simplex amplitude*, J.Math.Phys. **50** (2009) 112504 [0902.1170].

[15] F. Conrady and L. Freidel, *On the semiclassical limit of 4D spin foam models*, Phys.Rev. **D78** (2008) 104023 [0809.2280].

[16] J. W. Barrett, W. J. Fairbairn and F. Hellmann, *Quantum gravity asymptotics from the SU(2) 15j symbol*, Int. J. Mod. Phys. **A25** (2010) 2897–2916 [0912.4907].

[17] M. Han and M. Zhang, *Asymptotics of Spinfoam Amplitude on Simplicial Manifold: Lorentzian Theory*, Class. Quant. Grav. **30** (2013) 165012 [1109.0499].

[18] E. R. Livine and S. Speziale, *A New spinfoam vertex for quantum gravity*, Phys.Rev. **D76** (2007) 084028 [0705.0674].

[19] J. Engle and R. Pereira, *Regularization and finiteness of the Lorentzian LQG vertices*, Phys.Rev. **D79** (2009) 084034 [0805.4696].

[20] J. C. Baez and J. W. Barrett, *Integrability for relativistic spin networks*, Class. Quant. Grav. **18** (2001) 4683–4700 [gr-qc/0101107].

[21] L. Freidel and S. Speziale, *Twisted geometries: A geometric parametrisation of SU(2) phase space*, Phys. Rev. **D82** (2010) 084040 [1001.2748].

[22] L. Freidel and S. Speziale, *From twistors to twisted geometries*, Phys. Rev. **D82** (2010) 084041 [1006.0199].

[23] E. Bianchi, L. Modesto, C. Rovelli and S. Speziale, *Graviton propagator in loop quantum gravity*, Class.Quant.Grav. **23** (2006) 6989–7028 [gr-qc/0604044].

[24] S. Speziale, *Background-free propagation in loop quantum gravity*, Adv.Sci.Lett. **2** (2009) 280–290 [0810.1978].

[25] J. W. Barrett and L. Crane, *Relativistic spin networks and quantum gravity*, J. Math. Phys. **39** (1998) 3296–3302 [gr-qc/9709028].

[26] B. Dittrich and S. Speziale, *Area-angle variables for general relativity*, New J.Phys. **10** (2008) 083006 [0802.0864].

[27] F. Anzà and S. Speziale, *A note on the secondary simplicity constraints in loop quantum gravity*, Class. Quant. Grav. **32** (2015), no. 19 195015 [1409.0836].

[28] P. Dona and S. Speziale, *Asymptotics of nonsimplicial Lorentzian EPRL-KKL vertex amplitudes*, in preparation (2019).

[29] J. Engle, R. Pereira and C. Rovelli, *The Loop-quantum-gravity vertex-amplitude*, Phys.Rev.Lett. **99** (2007) 161301 [0705.2388].

[30] C. Rovelli and S. Speziale, *Lorentz covariance of loop quantum gravity*, Phys.Rev. **D83** (2011) 104029 [1012.1739].

[31] J. D. Christensen, E. R. Livine and S. Speziale, *Numerical evidence of regularized correlations in spin foam gravity*, Phys. Lett. **B670** (2009) 403–406 [0710.0617].

[32] H. T. Johansson and C. Forssén, *Fast and accurate evaluation of wigner 3j, 6j, and 9j symbols using prime factorisation and multi-word integer arithmetic*, SIAM J. Sci. Statist. Comput. **38** (2016) A376–A384 [1504.08329].

[33] F. Collet, *A (simple) expression of the unitary-irreducible SL(2,C) representations as a finite sum of exponentials*, in preparation.

[34] M. A. Rashid, *Boost Matrix Elements Of The Homogeneous Lorentz Group*, J. Math. Phys. **20** (1979) 1514–1519.

[35] P. Martin-Dussaud, *A Primer of Group Theory for Loop Quantum Gravity and Spin-foams*, 1902.08439.

[36] M. Kapovich and J. Millson, *The symplectic geometry of polygons in euclidean space*, J. Differential Geom **44** (1996), no. 3 479–513.

[37] E. Bianchi, P. Dona and S. Speziale, *Polyhedra in loop quantum gravity*, Phys. Rev. **D83** (2011) 044035 [1009.3402].

[38] J. W. Barrett and C. M. Steele, *Asymptotics of relativistic spin networks*, Class.Quant.Grav. **20** (2003) 1341–1362 [gr-qc/0209023].

[39] L. Freidel, K. Krasnov and E. R. Livine, *Holomorphic Factorization for a Quantum Tetrahedron*, Commun.Math.Phys. **297** (2010) 45–93 [0905.3627].

[40] G. P. Contributors, "GSL - GNU scientific library - GNU project - free software foundation (FSF)." http://www.gnu.org/software/gsl/, 2010.

[41] A. M. Perelomov, *Generalized coherent states and their applications*. Springer, 1986.

[42] I. Esterlis, H. M. Haggard, A. Hedeman and R. G. Littlejohn, *Maslov indices, Poisson brackets, and singular differential forms*, EPL **106** (2014), no. 5 50002 [1402.0786].

[43] D. A. Varshalovich, A. N. Moskalev and V. K. Khersonsky, *Quantum Theory of Angular Momentum: Irreducible Tensors, Spherical Harmonics, Vector Coupling Coefficients, 3nj Symbols*. World Scientific, Singapore, 1988.

[44] W. Ruhl, *The Lorentz Group and Harmonic Analysis*. W. A. Benjamin, 1970.

[45] J. Puchta, *Asymptotic of Lorentzian Polyhedra Propagator*, `1307.4747`.

[46] M. Fanizza, P. Martin-Dussaud and S. Speziale, *Asymptotics of SL(2,C) tensor invariants*, in preparation (2019).

[47] B. Bahr and S. Steinhaus, *Hypercuboidal renormalization in spin foam quantum gravity*, Phys. Rev. **D95** (2017), no. 12 126006 [`1701.02311`].

[48] R. L. Anderson, R. Raczka, M. A. Rashid and P. Winternitz, *Recursion and symmetry relations for the clebsch-gordan coefficients of the homogeneous lorentz group*, J. Math. Phys. **11** (1970) 1059–1068.

[49] P. Dona, F. Gozzini and G. Sarno, *Searching for classical geometries in spin foam amplitudes: a numerical method*, arXiv:1909.07832 [gr-qc].

[50] V. Bonzom and E. R. Livine, *Generating Functions for Coherent Intertwiners*, Class. Quant. Grav. **30** (2013) 055018 [`1205.5677`].

[51] V. Bayle, F. Collet and C. Rovelli, *Short-scale Emergence of Classical Geometry, in Euclidean Loop Quantum Gravity*, `1603.07931`.

[52] F. Hellmann and W. Kaminski, *Holonomy spin foam models: Asymptotic geometry of the partition function*, JHEP **1310** (2013) 165 [`1307.1679`].

[53] W. Kaminski, M. Kisielowski and J. Lewandowski, *Spin-Foams for All Loop Quantum Gravity*, Class.Quant.Grav. **27** (2010) 095006 [`0909.0939`].

[54] H. M. Haggard, M. Han, W. Kamiski and A. Riello, *SL(2,C) ChernSimons theory, a non-planar graph operator, and 4D quantum gravity with a cosmological constant: Semiclassical geometry*, Nucl. Phys. **B900** (2015) 1–79 [`1412.7546`].

[55] J. Engle and A. Zipfel, *Lorentzian proper vertex amplitude: Classical analysis and quantum derivation*, Phys. Rev. **D94** (2016), no. 6 064024 [`1502.04640`].

[56] J. Engle, I. Vilensky and A. Zipfel, *Lorentzian proper vertex amplitude: Asymptotics*, Phys. Rev. **D94** (2016), no. 6 064025 [`1505.06683`].

[57] W. Kaminski, M. Kisielowski and H. Sahlmann, *Asymptotic analysis of the EPRL model with timelike tetrahedra*, `1705.02862`.

[58] H. Liu and M. Han, *Asymptotic analysis of spin foam amplitude with timelike triangles*, `1810.09042`.

[59] M. Christodoulou, C. Rovelli, S. Speziale and I. Vilensky, *Planck star tunneling time: An astrophysically relevant observable from background-free quantum gravity*, Phys. Rev. **D94** (2016), no. 8 084035 [`1605.05268`].

[60] B. Dittrich, S. Mizera and S. Steinhaus, *Decorated tensor network renormalization for lattice gauge theories and spin foam models*, New J. Phys. **18** (2016), no. 5 053009 [`1409.2407`].

[61] S. Speziale and W. M. Wieland, *The twistorial structure of loop-gravity transition amplitudes*, Phys. Rev. **D86** (2012) 124023 [`1207.6348`].

[62] M. Dupuis and E. R. Livine, *Holomorphic Simplicity Constraints for 4D Spinfoam Models*, Class.Quant.Grav. **28** (2011) 215022 [`1104.3683`].

[63] M. Dupuis, L. Freidel, E. R. Livine and S. Speziale, *Holomorphic Lorentzian Simplicity Constraints*, J. Math. Phys. **53** (2012) 032502 [`1107.5274`].

[64] J. Hnybida, *Spin Foams Without Spins*, Class. Quant. Grav. **33** (2016), no. 20 205003 [`1508.01416`].

[65] A. Banburski, L.-Q. Chen, L. Freidel and J. Hnybida, *Pachner moves in a 4D Riemannian holomorphic Spin Foam model*, Phys. Rev. **D92** (2015), no. 12 124014 [`1412.8247`].

[66] V. Bonzom, F. Costantino and E. R. Livine, *Duality between Spin networks and the 2D Ising model*, Commun. Math. Phys. **344** (2016), no. 2 531–579 [`1504.02822`].

[67] I. M. Gelfand, R. A. Minlos and Z. Y. Shapiro, *Representations of the rotation and Lorentz groups and their applications*. Pergamon Press, Oxford, 1963.

[68] M. A. Naimark, *Linear representations of the Lorentz group*. Elsevier, 2014 (1st Ed. Pergamon Press, 1964).

Chapter 6

2-vertex Lorentzian Spin Foam Amplitudes for Dipole Transitions

2-vertex Lorentzian Spin Foam Amplitudes for Dipole Transitions

Giorgio Sarno[1], Simone Speziale[1] and Gabriele V. Stagno[1,2]

[1] Aix Marseille Univ., Univ. de Toulon, CNRS, CPT, UMR 7332, 13288 Marseille, France

[2] Sapienza University of Rome, P.le Aldo Moro 5, (00185) Roma, Italy

June 25, 2020

Abstract

We compute transition amplitudes between two spin networks with dipole graphs, using the Lorentzian EPRL model with up to two (non-simplicial) vertices. We find power-law decreasing amplitudes in the large spin limit, decreasing faster as the complexity of the foam increases. There are no oscillations nor asymptotic Regge actions at the order considered, nonetheless the amplitudes still induce non-trivial correlations. Spin correlations between the two dipoles appear only when one internal face is present in the foam. We compute them within a mini-superspace description, finding positive correlations, decreasing in value with the Immirzi parameter. The paper also provides an explicit guide to computing Lorentzian amplitudes using the factorisation property of SL(2,C) Clebsch-Gordan coefficients in terms of SU(2) ones. We discuss some of the difficulties of non-simplicial foams, and provide a specific criterion to partially limit the proliferation of diagrams. We systematically compare the results with the simplified EPRLs model, much faster to evaluate, to learn evidence on when it provides reliable approximations of the full amplitudes. Finally, we comment on implications of our results for the physics of non-simplicial spin foams and their resummation.

Contents

6 Spin Correlations

7 Conclusions

1   Introduction

The spin foam formalism offers a covariant approach to the dynamics of loop quantum gravity, see [1] for an introduction. The state of the art is well described by the EPRL model [2, 3, 4, 5], which includes the Immirzi parameter, can be extended to provide transition amplitudes to all spin network states [6, 7], and admits a quantum group deformation conjectured to describe the case of non-vanishing cosmological constant [8]; Most importantly, the large spin asymptotics of the 4-simplex vertex amplitude contains exponentials of the Regge action [9, 10]. On the other hand, a systematic evaluation of spin foam transition amplitudes for given boundary data is hindered by their sheer complexity. For instance, numerical calculations of spin correlations have been performed so far only with a single 4-simplex and with the old Barrett-Crane model [11, 12]. The situation is even worse for Lorentzian signature, because of the unbounded group integrations in the vertex amplitude. Testing the EPRL Regge asymptotics is numerically very hard [13, 14], and spin correlations are out of reach for the time being.[1] In this respect, the extension of the EPRL model to arbitrary vertices [6, 7] can be used to simplify the problem of explicit evaluations, by considering foams which are combinatorially simpler than the simplicial ones. For instance, one can consider boundary graphs in the form of a 'flower' (a single node with links starting and ending on it), or of a 'dipole' (two nodes and all links connecting one node to the other): the lowest-order spin foams are then much simpler than the simplicial ones, and one can hope to evaluate them explicitly with analytic and numerical methods. This is what we do in this paper: we choose a simple boundary given by two dipoles with 4-links, and study a dozen different spin foam amplitudes with up to two vertices and one internal face.

Schematically, we compute amplitudes for the following spin foam expansion:

$$ \qquad\qquad\qquad + \lambda \qquad\qquad\qquad + \lambda^2 \qquad\qquad\qquad + \lambda^2 \qquad\qquad\qquad\qquad (1) $$

Here λ is a bookkeeping 'coupling constant' of the vertex expansion. The method we use to evaluate the Lorentzian amplitudes is the factorization introduced in [18], together with Wolfram's Mathematica and C++ codes to compute the boost integrals and SU(2) Clebsch-Gordan coefficients. The explicit evaluations are very costly, and we limited detailed computations to those foams that we identified as the most interesting ones.

Non-simplicial transition amplitudes have been used in preliminary work in spin foam quantum cosmology based on a dipole boundary graph [19, 20, 21, 22, 23, 24] or on a flower one [25]. Similar simple graphs appear also in symmetry-reduced models of quantum cosmology using the canonical framework [26, 27, 28].[2] Apart from mini-superspace applications, simpler graphs also provide a case study to gain control over

---

[1]There is on the other hand a growing literature on results using approximate numerical methods for toy models or symmetry reduced models, e.g. [15, 16, 17].

[2]These canonical models are different from the main loop quantum cosmology approach (see e.g. [29] for a review), in which the graph structure effectively disappears; and from [30, 31], where a regular 6-valent graph is used.

the structure of the spin foam expansion. Being able to compute the explicit value of the amplitudes, or even just the large spin scaling or the divergence structure, are crucial ingredients to understand how to organize them, be it for resumming them or taking their continuum limit. To begin with, we are interested in questions of the following type: *(i)* at fixed boundary graph, how do the different foams scale in a large spin expansion? *(ii)* which foams dominate at large spins? *(iii)* what correlations between initial and final states are introduced by the foam? In the case of 1 we found the following answers: The foams become quickly sub-dominant as their complexity increases; The large spin scaling is not simply a function of the number of vertices, edges and faces of the foam. There are non-trivial correlations even in the absence of the Regge asymptotic behaviour; Only in the presence of an internal face (but not always) the correlations couple spins on the two dipoles, otherwise the amplitudes factorize and only spins and intertwiners within each connected part of the graph are correlated.

The paper is organized as follows. First, we provide a summary of our main results and the consequences that can be drawn from them in Section 1.1 at the end of the Introduction, for the benefit of the reader already familiar with spin foams, and who wants to quickly identify the methods and results closest to her interests. In the main body of the paper we provide an explicit guide on how to compute the EPRL Lorentzian amplitudes for generalized (non-simplicial) foams. In Section 2 we briefly recall the definition of the vertex amplitude; We discuss the existence of non-integrable graphs, and introduce a face criterion to partially limit the proliferation of diagrams, the hardest issue in using non-simplicial spin foams. The criterion we use, of faces as minimal cycles only, basically makes the 2-complex rigidly determined by its 1-skeleton. The exclusion of non-integrable graphs and non-minimal faces significantly reduce the number of foams to be computed. For instance at one vertex, graph integrability eliminates 16 of the 20 possible vertex graphs listed in [24] for the Euclidean theory; our face criterion eliminates 3 more, leaving only one, which is the one considered in [20]. With two vertices and one edge we have again a single admissible type of vertex graph. With two edges and an internal face we have seven topologically distinct vertex graphs. The graphs and associated foams are presented in Section 3. A complementary Appendix C contains the complete list relaxing our face criterion. In Section 4.1 we review the factorization property introduced in [18], and explain how we use it to provide analytical and numerical studies of the amplitudes. It provides us also with a simplified version of the amplitude (denoted EPRLs in [18]), which provides a good approximation in certain cases, and can be used to compute some analytic estimates and much faster numerical evaluations. One of the results of this paper is that we tested that for most foams of 1 the simplified model gives correct estimates of both scaling and correlations. This result and all exact numerical evaluations and approximate analytic estimates we performed of the EPRL amplitudes are reported in Section 5. In Section 5.4 we focus on the dominant non-factorized foam with one internal face, and discuss and compute in some details the spin correlations it induces. The final Section contains our conclusions with the implications of our results, and a perspective on future work, explaining the limits we face at the moment at the numerical level, and what could be improved. Two additional Appendices contain the recoupling theory rules used for the evaluations of the spin foams, a summary of scaling properties of the booster functions, and the results of evaluating the 3 one-vertex foams left out by our face criterion.

We follow the conventions of [32] for SU(2) and its recoupling theory, and those summarised in [18] for $SL(2, \mathbb{C})$. We refer to the nomenclature of [33] for spin foams: the boundary graph is characterised by nodes connected by links, and as the boundary of a 2-complex, each node is the boundary of an edge (and one only), each link the boundary of a face (and one only).

1.1 Summary of the main results

The notation for 1 is as follows: we use thin lines for the links of the boundary dipole graphs, and round dots for their nodes; thick lines for the edges of the foams and (red) crosses for their vertices; we call j_a the spins of the lower dipole ($a = 1 \ldots 4$) and (i, t) its left and right intertwiners, and similarly but with primed letters for the upper dipole. Then 1 is a function $W(j_a, j'_a; i, t; i', t')$ (ignoring the dependence on λ) determined by the Lorentzian EPRL model.

- Aware of the risk of an uncontrollable proliferation of non-simplicial spin foams, we introduced a strong criterion to select the 2-complexes: we admit only faces corresponding to minimal cycles. With this choice, to be motivated and detailed below, there is only one admissible vertex graph at one vertex;

only one at two vertices and one edge; seven topologically distinct vertex graphs for foams with one internal face.

- As shown already in [23], the one-vertex foam factorizes in two contributions each depending only on lower or upper spins. There are thus no correlations between lower and upper graphs, but only within each connected component. We find that also the two-vertex-one-edge foam factorizes in the same manner. Non-factorized amplitudes appear only in the presence of an internal face, and thus lower-upper spin correlations.

- The spin correlations we found do not have an immediate geometric interpretation. In fact, most of the foams considered do not contain non-trivial nj-symbols, but only (generalized) θ-graphs, and Regge actions do not appear in the asymptotics. We numerically computed the spin correlations, using for cost sustainability the simplest non-factorized amplitude and a mini-superspace approach with all spins fixed to be equal. We found positive correlations between lower and upper spins, with a monotonical decrease in γ. We also considered spin correlations in the general boundary framework with a unit-width Gaussian state peaked on a background geometry j_0. The resulting correlations peak near the Planck scale at γ-dependent value, and have a γ-dependent power-law tail in j_0.

- The large-spin leading order of each foam decreases as the complexity of the foam increases. The power of the large spin scaling depends on the explicit combinatorics of the faces, and it is not simply a function of the number of vertices V, edges E and faces F of the 2-complex. This is unsurprising given the non-topological nature of the EPRL model, however one could have still hoped for a dependence on the three numbers (V, E, F) alone. We discuss this point and what we can learn for power counting of scalings from the foams here considered.

- Numerical estimates show that the foam with one vertex (DVD, for dipole-vertex-dipole) scales like N^{-3} in the homogeneously large spin limit; the foam with two vertices and one edge (DED, for dipole-edge-dipole) scales like N^{-6}; the simplest non-factorized foam with an internal face (DLD, for dipole-loop-dipole) scales like N^{-9}. Using both analytical and numerical methods, we found that the large spin behaviour of 1 has the following structure:

$$
\begin{aligned}
W(Nj_a, Nj_a'; i, i'; t, t') = \delta_{j_a, j_a'}\delta_{i,i'}\delta_{t,t'} + \lambda \frac{f(j_a)f(j_a')}{N^3}\delta_{it}\delta_{i't'} \\
+ \lambda^2 \frac{g^2(j_a)g^2(j_a')}{N^6}\delta_{it}\delta_{i't'} + \lambda^2 \frac{h(j_a, j_a', i, t, i', t')}{N^9},
\end{aligned}
\tag{2}
$$

where the functions f, g and h will be presented below.

- We systematically compared the EPRL evaluations with those of the simplified EPRLs model introduced in [18], corresponding to additional impositions of the primary simplicity constraints (via the Y-map): this is much faster to evaluate, and furthermore analytic estimates of the scalings are known.

  For the first two foams (DVD and DED) the EPRLs provides an exact evaluation of the full model; for the simplest foam with an internal face it does not, but it still captures the right large spin scaling and the spin correlations, hence providing a valid approximation for most questions. There are 3 additional foams of the 7 with an internal face that have non-factorized amplitudes. For these the simplified model amplitudes differ significantly from the complete EPRL model. They could have slower decay behaviour than N^{-9} (by one or two powers, a priori) because of the presence of unbounded summations, and may thus dominate the correlations in the large spin limit; but we do not know at present.

- Our results can also be immediately applied to a nothing-to-dipole expansion,

$$
W_D = \lambda \quad \bigvee \quad + \lambda^2 \quad \prod \quad \cdots
\tag{3}
$$

There are three principal lessons that can be drawn from these results. The first is that Lorentzian amplitudes are explicitly computable, in spite of their complexity. We were limited to small foams, but with improved

codes for the booster functions and the guidance from the simplified model here learned to estimate the scalings, the analysis can be pushed significantly further. The second is that large spin decays speed up with the complexity of the foam, allowing a naive hierarchical organization of the expansion. The power of the decay depends explicitly on the routing of the faces and not just on their number. This complicates power-counting arguments even with our criterion to restrict the faces, and show the dominance of disconnected vertex graphs. The third is that there are non-trivial spin correlations even in absence of asymptotic Regge actions. Such correlations do not show a squared-inverse power law as in the 4-simplex graviton calculations (see e.g. [34, 11, 12, 35]), but a non-trivial dependence on the Immirzi parameter. It is a priori possible to compute spin correlations on larger graphs and study whether they fall off with the graph distance or background distance, but that would definitively require much more numerical power than currently available to us, or find better approximation schemes.

2   Lorentzian EPRL model for general complexes

In this Section we briefly review the definition of the Lorentzian EPRL model [3], its factorization introduced in [18], and discuss its extension to non-simplicial complexes. The two aspects that require attention are the presence of non-integrable graphs and the proliferation of foams. We assume the reader to be familiar with the basics of loop quantum gravity and the spin foam model, and refer to the cited literature [2, 3, 4, 5] and to the monographs [1, 33] for details. Conventions and notations follow [18].

2.1   Boundary states, spin foam amplitudes and correlations

We work with abstract oriented graphs colored by spins j_l on every link l, and a set of intertwiner labels $\vec{\imath}_n$ on every node n: these are $v_n - 3$ half-integers for a node of valence v_n, corresponding to the spins along virtual links once a recoupling scheme is chosen. We define an SU(2) spin network state by

$$\langle g_l | \Gamma, j_l, \vec{\imath}_n \rangle = \prod_l D^{(j_l)}_{m_{s(l)} m_{t(l)}}(g_l) \prod_n \left(\begin{array}{c} j_l \\ m_l \end{array} \right)^{(\vec{\imath}_n)}, \tag{4}$$

with $s(l)$ and $t(l)$ the source and target nodes of the link l, and summations over magnetic indices m implicitly assumed. Here $D^{(j)}(g)$ are Wigner matrices, and the right-most symbol a short-hand notation for generalized Clebsch-Gordan coefficients, see Appendix A for definitions. These functions provide a basis of the Hilbert space of square-integrable gauge-invariant functions with respect to the SU(2) Haar measure, schematically

$$\mathcal{H}_\Gamma = L^2 \left[SU(2)^L / SU(2)^N, d\mu_{\text{Haar}} \right],$$

where we denoted by L and N the total number of links and nodes of the graph. Because of standard conventions in the definition of the Wigner matrices and $\{nj\}$-symbols, the basis 4 is not normalized. That requires multiplying each state by $(\prod_l d_{j_l} \prod_n d_{\vec{\imath}_n})^{1/2}$, where $d_j := 2j + 1$ is the dimension of the SU(2) irrep j, and $d_{\vec{\imath}} = (2i^{(1)} + 1)...(2i^{(v_e - 3)} + 1)$ is the dimension of the virtual links irreps.

Consider next an open 2-complex $\mathcal{C}$ whose boundary is Γ: it consists of vertices, edges and faces, such that to each node and link of Γ there correspond a unique edge and face of the boundary of $\mathcal{C}$. We color it with spins j_f on the faces and intertwiners $\vec{\imath}_e$ on the edges, such that $j_f = j_l$ and $\vec{\imath}_e = \vec{\imath}_n$ for each face and edge on the boundary. The spin foam formalism [36, 37, 1, 33] assigns an amplitude to each pair $(|s\rangle = |\Gamma, j_l, \vec{\imath}_n\rangle, \mathcal{C})$ in the form of a state sum model,

$$\langle W_\mathcal{C} | \Gamma, j_l, \vec{\imath}_n \rangle = \sum_{\{j_f, \vec{\imath}_e\}} \prod_f d_{j_f} \prod_e d_{\vec{\imath}_e} \prod_v A_v(j_f, \vec{\imath}_e), \tag{5}$$

where the summations are at fixed boundary values, and face and edge weights are internal only.[3] The vertex amplitude A_v is model-dependent and carries the core of the dynamics of the theory.

---

[3]In other words, the weight for a boundary face and edge is 1. This is a consequence of our choice of basis 4. If we work instead with normalized boundary spin networks, the boundary face and edge weights would be the square roots of the internal ones. Notice also that in the literature the edge weights are often absorbed in the definition of the vertex amplitude. We choose not to do so, so that the vertex amplitudes are given by the conventional $\{nj\}$-symbols.

The physical interpretation of $W_\mathcal{C}$ is to provide a dynamical amplitude for the (quantum) 3-geometry $|s\rangle$. The total transition amplitude was historically defined as the sum over all possible 2-complexes compatible with the boundary graph, and conjectured to implement the projector over physical states in the kernel of the Hamiltonian constraint [36, 37]. Hopes to control the sum and make sense of it mathematically were put on the group field theory approach [38, 39], and work of the last few years (see e.g. [40, 41, 42]) is starting to bear fruits: for simplicial complexes and simpler models at least (typically topological BF theory) it is now possible to establish convergence or renormalizability of the sum. Extending these results to the Lorentzian EPRL is a key open question. The study presented in this paper contributes by evaluating individual foams and assessing their relative scaling weights in the non-simplicial case.[4]

To give physical content to the amplitudes at fixed foam, one can define dynamical expectation values following the general boundary framework [34]. For an observable $\hat{\mathcal{O}}$ and a state $|\Psi\rangle \in \mathcal{H}_\Gamma$, we consider the quantity

$$\frac{\langle W_\mathcal{C}| \hat{\mathcal{O}} |\Psi\rangle}{\langle W_\mathcal{C}| \Psi\rangle} \tag{6}$$

as the '$\mathcal{C}$-representative' of the dynamical projection on $|\Psi\rangle$. In this construction, $|\Psi\rangle$ is required to be a semiclassical state peaked on a classical discrete geometry q_Γ associated to the boundary. One often works with Gaussian states (see however [44]), with width kept as a free parameter or fixed by dynamical requirements [45]. In special circumstances, the linear map $\langle W_\mathcal{C}|$ is normalizable; or alternatively it can be suitably regularized. Then it is also possible to look at the spin foam expectation values

$$\frac{\langle W_\mathcal{C}| \hat{\mathcal{O}} |W_\mathcal{C}\rangle}{\langle W_\mathcal{C}| W_\mathcal{C}\rangle}. \tag{7}$$

In both cases, a simple choice of observables are those diagonalized by the spin network basis 4, for which

$$\langle W_\mathcal{C}| \hat{\mathcal{O}} |\Psi\rangle = \sum_{j_l, \vec{\imath}_n} W_\mathcal{C}(j_l, \vec{\imath}_n) \mathcal{O}(j_l, \vec{\imath}_n) \Psi(j_l, \vec{\imath}_n). \tag{8}$$

In particular, we will compute below correlations among spins, defined as

$$\langle j_l j_{l'} \rangle_{(\mathcal{C}, \Psi)} := \frac{\langle W_\mathcal{C}| \hat{J}_l \hat{J}_{l'} |\Psi\rangle}{\langle W_\mathcal{C}| \Psi\rangle} - \frac{\langle W_\mathcal{C}| \hat{J}_l |\Psi\rangle}{\langle W_\mathcal{C}| \Psi\rangle} \frac{\langle W_\mathcal{C}| \hat{J}_{l'} |\Psi\rangle}{\langle W_\mathcal{C}| \Psi\rangle}. \tag{9}$$

2.2 EPRL vertex amplitude

For the EPRL model in Lorentzian signature [3], the vertex amplitude A_v is built from $\mathrm{SL}(2, \mathbb{C})$ unitary irreducible representations (irreps) of the principal series, see [46]. These are labelled by a pair ($\rho \in \mathbb{R}, k \in \mathbb{Z}/2$), and Naimark's canonical basis is chosen diagonalizing the operators L^2 and L_z of the matrix subgroup $\mathrm{SU}(2)$, with eigenvalues $j(j+1)$ and m. The group elements in this basis are represented by infinite-dimensional unitary matrices

$$D_{jmln}^{(\rho, k)}(g), \qquad (j, l) \geq k, \quad -j \leq m \leq j, \quad -l \leq n \leq l, \qquad g \in \mathrm{SL}(2, \mathbb{C}). \tag{10}$$

Only a certain subset of irreps is used, that we refer to as γ-*simple* representations; they satisfy

$$\rho = \gamma k, \qquad k = j. \tag{11}$$

This restriction defines an embedding of $\mathrm{SU}(2)$ irreps in unitary $\mathrm{SL}(2, \mathbb{C})$ ones called Y-map.

The explicit form of the vertex amplitude A_v depends on both the valence of the vertex (i.e. the number of edges attached to it) and the combinatorics of the faces. The combinatorics can be most easily visualized if we draw a sphere around the vertex: each edge projects to a point on the sphere, each face to a line connecting two points. The spherical graph so obtained is referred to as the *vertex graph*, see Fig. 1 for an example. Points and lines of the vertex graph are in 1-to-1 correspondence with edges and faces of the spin foams, and we adapt the labelling accordingly.

---

[4]An alternative definition of the dynamics is to view spin foams as amplitudes cut-off at a finite number of degrees of freedom, to be studied in the continuum limit instead of being summed over. See e.g. [43] and [15, 16] for recent results in this directions.
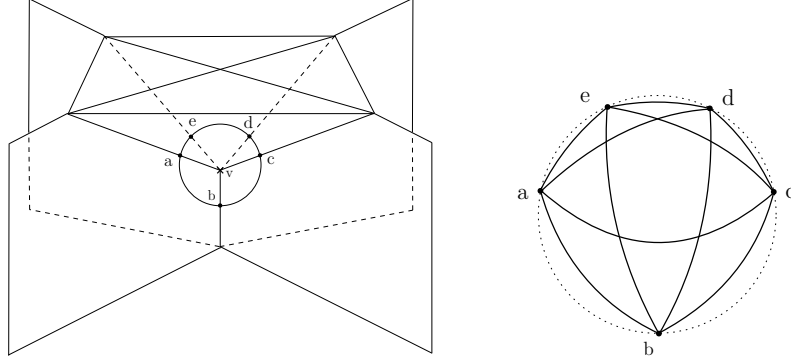
Figure 1: *On the left the complex for a single 4-simplex together with a little sphere surrounding the vertex v. On the right the vertex graph associated to it (the pentagon graph) as explained in the text.*

The amplitude is then defined by the evaluation of a γ-simple $\mathrm{SL}(2,\mathbb{C})$ spin network on the vertex graph, namely

$$A_v(j_f, \vec{\iota}_e) := \int_{\mathrm{SL}(2,\mathbb{C})^{E_v-1}} \prod_{e=1}^{E_v-\#} dg_e \prod_f D^{(\gamma j_f, j_f)}_{j_f m_{s(e)} j_f m_{t(e)}}(g_{s(e)}^{-1} g_{t(e)}) \prod_e \begin{pmatrix} j_f \\ m_f \end{pmatrix}^{(\vec{\iota}_e)}, \tag{12}$$

with the summation over magnetic indices implicitly assumed as in 4. Here E_v is the valence of the vertex graph and $\#$ the number of connected components of the vertex graph. Although in the definition we assign a group element to each node of the vertex graph, we need to remove one integration per connected part of the graph: left-right invariance of the Haar measure makes it redundant, and it would lead to a diverging amplitude because of the non-compactness of the group. This is an important difference from Euclidean models where removing or not the redundant integration does not affect the amplitude. However, even once the redundancy has been taken care of, not all vertex graphs are integrable. Examples of graphs for which 12 is not well-defined are reported in Fig. 2. The amplitude of a graph with a uni-valent node diverges trivially
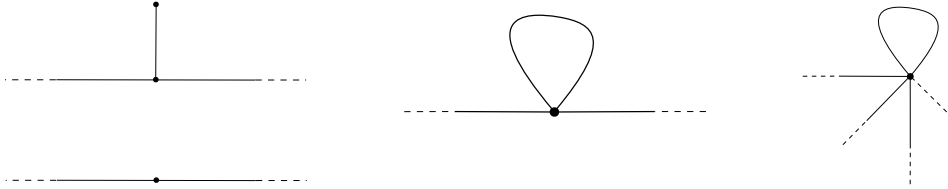

Figure 2: Left: *Vertex graph with uni-valent or bi-valent nodes: divergent amplitudes.* Right: *Vertex graph with a petal: the associated amplitude diverges in the case of two legs, and converges for three or more legs.*

because it contains the integration

$$\int_0^\infty dr\,(\sinh r)^2\, d^{\rho,k}_{jlm}(r) = \infty. \tag{13}$$

For a graph with a bi-valent node, the amplitude contains the integration

$$\int dg\, D^{(\rho_1,k_1)}_{j_1 m_1 l_1 n_1}(g) D^{(\rho_2,k_2)}_{j_2 m_2 l_2 n_2}(\bar{g}) = \frac{\delta(\rho_1 - \rho_2)\delta_{k_1 k_2}}{4(\rho_1^2 + k_1^2)}\, \delta_{j_1 j_2}\delta_{l_1 l_2}\delta_{m_1 m_2}\delta_{n_1 n_2}. \tag{14}$$

The right-hand side, a consequence of the orthogonality of the matrix representations, gives a distributional divergence for general irreps; and gives always infinite for the simple ones 11 used in the EPRL model. A

related example is a vertex graph containing a closed loop, or 'petal'. Using the following 'sliding' identity from graphical calculus (see Appendix A),
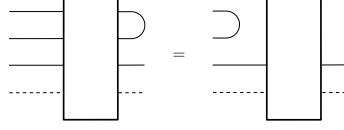
petals factorize in the evaluation of the amplitude, leaving behind an intertwiner with two lesser links. For a petal with two legs, or tadpole, this gives 14 and the same divergence as before; whereas for higher-valence petals with three or more legs the amplitude is finite.

The existence of divergent graph introduces a necessary restriction on the admissible foams unlike in the Euclidean case. We are not aware of a necessary condition for graph integrability. A *sufficient* condition is 3-link-connectivity, meaning any bi-partition of the nodes cannot be disjointed by cutting only two links [47, 48]. One could then decide to restrict attention to such vertex graphs, for which convergence of 12 is guaranteed. The criterion is however based on very loose bounds, and one can find many vertex graphs that are not 3-link-connected and yet finite: We will encounter some examples below. For this reason, we will remove in our analysis only vertex graphs with uni- and bi-valent nodes, and two-legged petals, and keep non-3-link-connected ones – at least a priori.[5]

The fact that not all vertex graphs are integrable reduces the number of admissible foams with respect to Euclidean amplitudes. For instance, out of the 20 possible vertex graphs considered in [24], only 4 do not contain tadpoles, and only 3 satisfy the triple-connectivity criterion. See Appendix C for details. Nonetheless, the proliferation of generalized spin foams remains a severe problem of this approach, as compared for instance to the use of simplicial ones. To have any hope of taming it, it is quite likely that one needs to supplement the definition of the theory with some notion of class of complexes to be considered.[6] For the purposes of this paper, we work with a single but strong restriction on the assignment of the faces in the 2-complex:

Definition: The faces of the 2-complex are defined as all minimal cycles of its 1-skeleton, namely minimal closed sequences of edges (for internal faces), or edges and links (for external faces).

This definition means that the 2-complex is uniquely specified by its 1-skeleton and the boundary graph, thus imposing a strong restriction on the foams to be considered. Two important consequences are the following:

- There are no minimal cycles without a face assigned; nor multiple faces can be assigned to the same minimal cycle. The latter forbids trivial infinite proliferations like adding ad libitum rolled-up faces or 'pillow-like' faces to the bulk edges, which corresponds to adding petals or additional links between the same two nodes to vertex graphs.

- It also forbids the 'intermediate static foam' construction used in [49] to freely associate arbitrary vertex graphs to a given boundary graph. It implies in particular that petals in vertex graphs can only appear if induced by petals in the boundary graph.

This definition appears to us natural in order not to be irremediably swamped by the problem of proliferation of non-simplicial foams. Whether it is sufficient to truly tame the combinatorics, and whether it can be relaxed is an interesting but also very difficult question. With the ensuing restriction imposed, there are still two additional configurations unusual from the simplicial setting worth to be pointed out:

1. Disconnected vertex graphs: these can lead to factorizations of the transition amplitudes that limit their relevance.

2. Spin foam faces with two or more boundary links in them: these force the boundary spins on the shared links to match, leading to trivial pieces in the amplitudes. Such 'face-rigidity' limits as well the relevance of such amplitudes.

With these considerations in mind, we discuss next our choice of boundary graphs.

---

[5]A related open question is whether the simplified model, see below, allows one to sharpen this sufficient condition. At first sight it looks like removing uni- and bi-valent nodes may be enough for this model, which sits at an intermediate place between the complete EPRL and a pure SU(2) theory. We leave it as an open question for future work.

[6]A radically opposite philosophy has been proposed in [49, 24], whereby one tries to accommodate *all possible vertex graphs* to all boundaries. This removes combinatorial constraints on the vertex graph, thus simplifying the problem of listing all admissible foams with a given boundary graph; but at the price of largely increasing their number.

3   Minimal boundary graphs and lowest-order interpolating foams

In its original formulation, the EPRL model was defined on simplicial foams, i.e. 2-complexes dual to simplicial decompositions of spacetime. Since the boundary of a simplicial manifold is again a simplicial manifold of co-dimension one, these can be used to compute transition amplitudes only for spin networks with 4-valent graphs dual to a 3d simplicial manifold. A reason to be interested in non-simplicial foams is that one can then look at simpler boundary graphs, and interpolate them with simpler foams. The computational advantage of simpler foams is immediate from 15: we get simpler $\{nj\}$ symbols whose evaluation is faster. In the context of abstract spin networks, the simplest possible boundary graphs are flower graphs with a single node, or a dipole graph with two nodes, see Fig. 3. Between these two types, dipole graphs have

Figure 3: *The 4-petal graphs and the 4-link dipole.*

simpler interesting lowest-order spin foams, and have a more intuitive geometric interpretation that makes them preferable for applications.

3.1   Flower Graphs

Flower graphs appear often in the discussion of gauge fixing, see e.g. [50]. By gauge-invariance, the algebra of observables on any abstract closed graph is isomorphic to that associated with a flower graph, were the number of 'petals' matches the number $L - N + 1$ of independent loops of the initial graph. The isomorphism depends on a choice of maximal tree on the initial graph, along which all holonomies can be gauge-fixed to the identity. Although flower graphs are very simple, they are not so natural as boundaries of spin foams: each face touching the boundary is rolled-up on itself, meaning it touches twice the same edge. This does not forbid the definition of (non-simplicial) spin foam amplitudes, however it leads to peculiar combinatorics: either a rolled-up face shares both boundaries, or one of the spin foam vertices must have at least one petal in its vertex graph, to absorb the 'rolling-up'. This is for instance the case of [51]: there the authors considered a three-petal flower boundary graph, and a single-vertex foam in the bulk. The vertex graph is identical to the boundary graph, and the contribution of the spin foam amplitude is trivial. Considering two disconnected flowers for transitions, it is easy to see that our face criterion leads to factorized amplitudes for simple 2-complexes. Using flower boundary graphs leads to subtle combinatorics and not particularly rewarding from the perspective of simplifying the analysis. In the exploratory spirit of this paper, we find it more suitable to work with less peculiar foam structures.

3.2   Dipole Graphs

The next simplest graph is a 'dipole', namely two nodes connected by a set of L links. It can be associated to a partially gauge-fixed abstract extended graph, where one fixes to the identity all but one of the holonomies on a maximal tree, and it admits a more intuitive geometric interpretation as two atoms of space connected by all faces: the dual graph to a (degenerate) tessellation of the 3-sphere by two L-faced polyhedra. For the sake of concreteness and simplicity, we restrict attention to 4-valent dipoles, as in Fig. 3. We can consider two different types of transition amplitudes: 'nothing-to-dipole' or 'dipole-to-dipole'. If Γ has a single closed connected component, it is a 'nothing-to-Γ' amplitude similar in spirit to the Hartle-Hawking 'no-boundary' proposal [52, 53]. If the boundary graph has two closed disconnected components, $W_{\mathcal{C}}$ provides a transition amplitude between two 3-geometries associated with the two S^3 boundaries of a 4d hyper-spherical shell. This set-up was proposed in [20], and it is the one we focus on. It shows very neatly the advantage of working with non-simplicial spin foams: were we to use a simplicial discretization, the minimal configuration would be five tetrahedra for each boundary S^3 and a 2-complex with 30 vertices! Whereas with the dipole, one can get transitions with as little as a single vertex. We list here all possible vertex graphs associated

with the expansion 1 and the restrictions given by finiteness and our face criterion. For completeness, we report in Appendix C the complete list of vertex graphs relaxing our face criterion. With reference to 1, we refer to foams with one vertex as DVD (for dipole-vertex-dipole), two vertices and one edge as DED (for dipole-edge-dipole), two vertices and two edges as DLD (for dipole-loop-dipole).

DD complex

The first term in 1 is a foam with no vertices, and corresponds to the trivial transition amplitude.

DVD complex

Using our definition of faces, we only have 1 admissible vertex graph, see Fig.4, which is the one originally considered in [20, 23]. It is disconnected, and thus manifestly leads to a factorized amplitude between initial and final states.
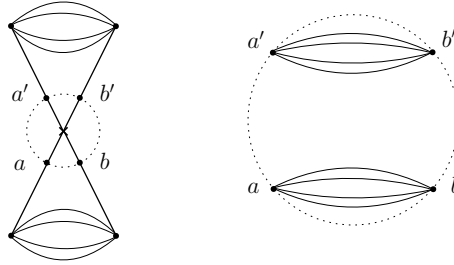

Figure 4: *DVD complex and the admissible vertex graph.*

Vertex graph for DED

The smallest foam with two vertices has a single edge connecting them, and the two vertex graphs are necessarily equal and specular from our definition of faces. There is again a single admissible choice, shown in Fig. 5: all other routings of the strands would produce faces corresponding to non-minimal cycles.
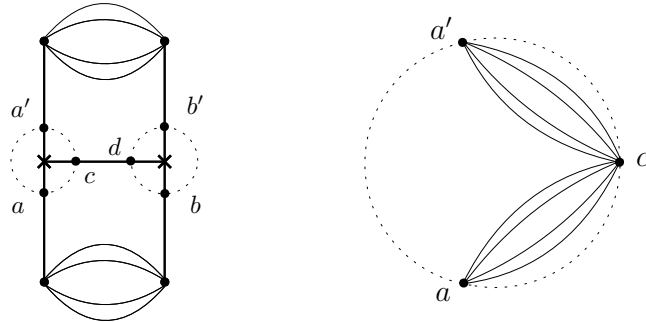

Figure 5: *DED complex and the admissible vertex graph.*

Although the vertex graph is not disconnected, it still leads to a factorized amplitude. As we will show explicitly below, this simply comes from the fact that we can remove the $SL(2, \mathbb{C})$ integration at the middle vertex, thus effectively 'disconnecting' the evaluation in two pieces.

Vertex graphs for DLD

With two internal edges we have more than just one admissible foam. By our criterion, we can have one internal face only; but the boundary links can be routed in topologically distinct ways without violating the minimal-cycle rule for the faces. This leads to seven different possibilities compatible with our definition of

faces, shown in Fig. 6. Again the two vertex graphs must be equal and specular, so we show only one of them.
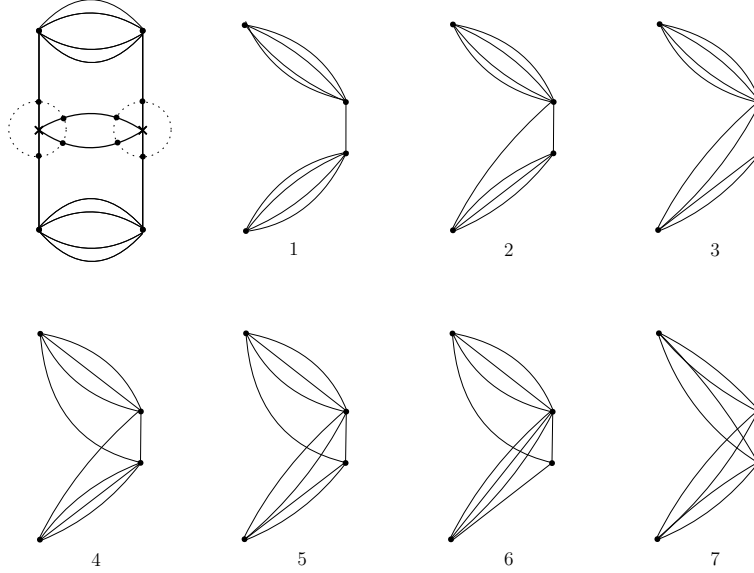

Figure 6: *DLD complex with the seven topologically distinct admissible vertex graphs. Each can give different foams by permutations of the spin labels or by flipping the two internal edges; The graphs 2, 3, 5, and 6 are not symmetric if we flip the internal edges, thus both configurations give two independent spin foam amplitudes. Graphs 1, 2 and 3 lead to factorized amplitudes, although 1 and 2 are not 3-link-connected, so their amplitude are not guaranteed to be finite. Graph 6 is the non-factorized amplitude easiest to evaluate, and the one we will study in more details below.*

Anticipating on the results presented below, the first three diagrams factorize, but not the remaining four. These are thus the first ones with non-trivial bulk dynamics, and correlations between initial and final spins.

If we were to allow for faces corresponding to non-minimal cycles, we would have 4 topologically distinct vertex graphs for DVD, 3 for DED, and 13 for DLD, see Appendix C.

4   Evaluation of Lorentzian diagrams

4.1   Amplitude factorization and booster functions

Having listed the foams we are interested in, we now move to their explicit evaluation. The key to do so is the factorization of the amplitudes introduced in [18]. We observe that the vertex amplitude defined in 12 is an $SL(2, \mathbb{C})$ tensor invariant, and as such can be represented in terms of Clebsch-Gordan coefficients. For the unitary irreps of the principal series, these can be written as (infinite) sums of Clebsch-Gordan coefficients for the canonical SU(2) matrix subgroup weighted by 1-dimensional boost integrals. See [18] for details. The result gives

$$A_v(j_f, i_e) = \sum_{l_f, k_e} \{nj\}(l_f, k_e) \prod_{e=1}^{E_v - \#} B_{v_e}^{\gamma}(j_f; l_f; \vec{i}_e, \vec{k}_e), \tag{15}$$

where $\{nj\}(l_f, k_e)$ is the SU(2) nj-symbol associated to the vertex graph, labelled by spins l_f and k_e; v_e is the valence of the edge e (namely the number of faces it bounds), and

$$B_n^{\gamma}(j_a, l_a; \vec{i}, \vec{k}) = \frac{1}{4\pi} \int_0^{\infty} dr \sinh^2 r \sum_{p_a} \left(\begin{array}{c} j_a \\ p_a \end{array} \right)^{(\vec{i})} \left(\begin{array}{c} l_a \\ p_a \end{array} \right)^{(\vec{k})} \prod_{a=1}^{n} d_{j_a l_a p_a}^{(\gamma j_a, j_a)}(r). \tag{16}$$

The boost matrix elements $d^{(\rho,k)}(r)$ for simple irreps are reported in Appendix A. The summations over k_e in 15 are bounded by Clebsch-Gordan conditions, and those over l_f by $l_f \geq j_f$.

The factorization result 15 has the neat effect of minimizing the number of unbounded integrations over boost directions, and reduce the evaluation of the Lorentzian amplitude to an exercise in recoupling theory of SU(2), with the boost contributions as weights localised on the edges, see Fig. A.12. The fact that only $E_v - \#$ boosters appear per vertex reflects the redundancy of one group integration in 12. The freedom to arbitrarily choose the redundant integration can be used at one's advantage to eliminate the booster function with the highest valence n_e, a simplification that we will use systematically below.

For the purposes of using graphical calculus for the recoupling theory, we follow the conventions of [32] for the SU(2) part (briefly summarized in Appendix A), and the following graphical representations for 16,

$$B_3^\gamma(j_a; l_a) = \quad \quad \quad \quad B_4^\gamma(j_a; l_a; i, k) = \quad \quad \quad \quad (17)$$

$$B_5^\gamma(j_a; l_a; i_1, i_2, k_1, k_2) = \quad \quad \quad \quad (18)$$

and so on for higher n. Here the convention is that both lower and upper sets of spins are assigned from left to right in the $4jm$ symbols.[7] Because of this diagrammatic expression, the boost integrals were referred to as 'dipole amplitudes' in [18]. We refrain from using this expression here to avoid confusion with the dipole spin network graph, and call them *booster functions* instead.

In spite of the simplicity achieved by 15, the explicit evaluation is still a very complex task: first of all, only for $n = 3$ there exist a closed expression for 16 in terms of finite sums of Γ functions, see [54, 18]; for $n \geq 4$ one has to rely on numerical methods to perform the integrals.[8] The difference is important, since using Mathematica we are able to reliably evaluate B_3^γ for spins up to 100 within few seconds, whereas for B_4 we are limited to spins of order 30 by numerical instabilities on hypergeometric functions, and at those spins each value of B_4 can take hours to compute. Some numerical calculation times are reported in Fig. 15 in the Appendix, based on a standard laptop computer with core speed of 2.5 GHz and 8 Gb of RAM. To perform the calculations of spin foam amplitudes in this paper we used the server maintained by our lab, featuring 32 processors with 3.4 GHz CPU and 24 Gb of RAM.

Secondly, the factorization has introduced infinite sums over the l's, which play the role of 'magnetic numbers' from the $SL(2,\mathbb{C})$ viewpoint. These can be very slow to converge and hinder the numerical efficiency. This is for instance the reason why it is difficult to test Barrett's asymptotic formula [10] with Lorentzian boundary data [14]. For some of the foams considered in this paper, the sums turn out to be quickly converging, in which case they can be handled with a controllable cutoff.

Hence, exact evaluations of Lorentzian EPRL amplitudes are possible but limited, and very costly. One important information that we are interested in is the large spin scaling of the amplitudes. For such estimates the factorization 15 is very useful because we can use known results from the asymptotics of SU(2) nj-symbols [55, 56] and combine them with scalings of the booster functions and estimates for the sums. To that end, let us briefly review some scaling properties of the booster functions. Plots showing the behaviours and

---

[7]This means that all lower (upper) nodes have clockwise (anticlockwise) orientation, see Appendix A. As shown in Appendix B, the booster functions are independent of orientation of the strands. For this reason we omit the arrows on the strands in the picture.

[8]Also for $n \geq 4$ it is possible to analytically perform the r integrals, see [18]; however the results involves new integrations which at present are still of comparable numerical complexity.

claims of this section, as well as more details and expressions for the booster functions and their numerical evaluations can be found in Appendix B.

4.2 Boosters' scalings

1. Minimal spins, homogeneous large spin asymptotics (see [18] and Fig. 16.):

$$B_3^\gamma(Nj_a; Nj_a) \sim \begin{cases} N^{-3/2} & \text{if} \quad \sum_a j_a \text{ odd} \\ N^{-1} & \text{if} \quad \sum_a j_a \text{ even} \end{cases}, \qquad B_{n\geq 4}^\gamma(Nj_a; Nj_a; \vec{\imath}, \vec{k}) \sim N^{-3/2}. \qquad (19)$$

In the second expression, the leading order scaling is the same irrespectively of the intertwiners. However, seen as a function of the intertwiners at fixed spins, it is strongly peaked at equal values. The precise shape and width of the peak depends on the spins considered, but the drop is measured in orders of magnitude already one step away from equal values. Hence, it is qualitatively fair to complete the estimate with a Kronecker delta $\delta_{\vec{\imath}\vec{k}}$. There exist also an analytic estimate for the leading order, given by [57]:

$$B_n^\gamma(Nj_a; Nj_a; i, k) \sim \frac{1}{(4\pi)^2} \left[\frac{6\pi}{(1+\gamma^2)N \sum_a j_a} \right]^{3/2} \frac{\delta_{\vec{\imath}\vec{k}}}{d_{\vec{\imath}}}. \qquad (20)$$

This correctly reproduce the power law decay, and numerical tests (see e.g. [18] or App. B) confirm also the γ and $\sum_a j_a$ dependence. On the other hand, the numerical factor is not very accurate (the error is of order 1), nor the dependence on the intertwiners. Indeed as mentioned above configurations with non-equal intertwiners also decay like $N^{-3/2}$ and not faster as 20 would suggest.

2. Minimal spins, inhomogeneous large spin asymptotics with one spin small (see Fig. 17):

$$B_3^\gamma(Nj_{\bar{a}}, j_3; Nj_b, j_3) \sim N^{-1}, \qquad B_4^\gamma(Nj_{\bar{a}}, j_4; Nj_b, j_4; Ni, Nk) \sim N^{-5/2}, \qquad (21a)$$

$$B_5^\gamma(Nj_{\bar{a}}, j_5; Nj_b, j_5; Ni_1, Nk_1, Ni_2, Nk_2) \sim N^{-7/2}, \qquad (21b)$$

where in the above $\bar{a} = 1, \ldots, n-1$.

3. Non-minimal spin decay, homogeneous (see [18] and Fig. 18):

$$B_3^\gamma(j_a; j_a + \Delta l) \sim \frac{1}{\sqrt{\Delta l}}, \qquad B_4^\gamma(j_a; j_a + \Delta l; i, k) \sim \frac{1}{\Delta l} \qquad (22)$$

4. Non-minimal spin decay, inhomogeneous: an exponential decay if we rescale a single l label, see Fig. 19.

4.3 Simplified model and scaling estimates

The non-minimal spin decays described in points 3 and 4 just above suggest that for some configurations good estimates of the EPRL model can be obtained looking at the minimal configurations only, $l_a = j_a$. This restriction defines a simplified version of the EPRL model, called EPRLs in [18], s for simplified. Since the EPRLs amplitudes are much faster to evaluate, it is useful to get a hand on when the simplification gives a good approximation of the full EPRL model. There are three possibilities, depending on the foam:

(i) The summations over l's are truncated to the minimal value by Clebsch-Gordan inequalities: this can happen for particular configurations, and if it happens for all ls, we refer to such amplitudes as *EPRLs-exact*.

(ii) The summations are bounded, or unbounded but quickly converging: EPRLs gives different numerical values than EPRL, nonetheless it provides precise estimates of the large spin scalings and of correlations' properties.

(iii) The summations are unbounded and slowly converging: the EPRLs differs strongly from the EPRL, and does not provide good estimates.

Because of the intricate structure of the amplitudes, it is not easy to give a general criterion to identify a priori which ones are well approximated by the simplified model. One of the results of this paper is to show for which of the considered foams it happens. The interest in this is that the simplified model is much faster to evaluate, and furthermore, it allows us to use the analytic estimate 20.

5 Dipole-to-dipole spin foam amplitudes

In this Section we present the explicit form of the amplitudes for the foams listed in Section 3. For an SU(2) BF theory, the evaluation of the various spin foam amplitudes associated to the above diagrams is a straightforward, if somewhat tedious, exercise in recoupling theory. It is very similar for the EPRL model, using the factorization reviewed above. We use graphical calculus for SU(2) with the conventions of [32], briefly reported in Appendix A, and the notation 17 for the booster functions. In the diagrams below, every strand represents a face and every box an integration over $SL(2,\mathbb{C})$ assigned for each half-edge. One has to choose a face orientation, but the result is independent of this choice (not of the orientation of the boundary links, on the other hand).

5.1 DD foam

The first term of 1 is a trivial foam, with no internal vertices and faces bounded by a lower and an upper link. The corresponding 'face-rigid' amplitude is the identity,

$$W^{DD}(j_a, j_a'; i, t, i', t') = \delta_{j_a, j_a'} \delta_{i, i'} \delta_{t, t'}. \tag{23}$$

5.2 DVD foam

The vertex graph is disconnected (see Fig. 4), leading to an exact factorization of the amplitude into lower and upper contributions. Each connected component has a single $SL(2,\mathbb{C})$ integration after gauge-fixing, and the amplitude reads

$$W^{DVD}(j_a, j_a'; i, t, i', t') = d_i d_{i'} d_t d_{t'} \int dg_1 dg_2 \prod_{a=1}^{4} D^{\gamma j_a, j_a}_{j_a m_a j_a n_a}(g_1) D^{\gamma j_a', j_a'}_{j_a' m_i' j_a' n_i'}(g_2) \begin{pmatrix} j_a \\ m_a \end{pmatrix}^{(i)} \begin{pmatrix} j_a \\ n_a \end{pmatrix}^{(t)} \begin{pmatrix} j_a' \\ m_a' \end{pmatrix}^{(i')} \begin{pmatrix} j_a' \\ n_a' \end{pmatrix}^{(t')}$$

$$= d_i d_{i'} d_t d_{t'}$$

where in the graphical notation we used a box with an identity I to flag the group integrations we removed. The arrows on the box keep track of the edge orientations, and the signs of the spin ordering chosen for the $4jm$ symbols, see Appendix A.[9]

To proceed with the graphical evaluation we use A.12 to split the boxes in terms of intertwiners. This results in one booster function and one SU(2) 4-valent θ graphs per edge. The θ graph gives a dimensional factor, see A.5, and we get

$$W^{DVD}(j_a, j_a'; i, t, i', t') = d_i d_{i'} d_t d_{t'} \quad \text{} . \tag{24}$$

---

[9]In the literature the signs in the graphical calculus are often discarder under the assumption of fixing a convention once and for all, say anticlockwise. We prefer to keep track of them so that we can use an unique algebraic $4jm$ symbol and have a easier mnemonic rule for the boundary spins (j_a goes to j_a' with the same a)

The amplitude factorizes as anticipated, and we see that there are no summations over the magnetic spins l: In the DVD case the simplified model coincides with the complete model, or in other words, this diagram is EPRLs-exact. We can then use the estimate 20 for the large spin scaling, finding

$$W_{DVD}(Nj_a, Nj_a'; i, t, i', t') \sim \frac{1}{N^3} \frac{27}{32\pi} \frac{1}{(1+\gamma^2)^3} \frac{d_i d_{i'} \delta_{it} \delta_{i't'}}{(\sum_a j_a)^{3/2} (\sum_a j_a')^{3/2}}. \tag{25}$$

We have an N^{-3} power law, peaked on configurations with equal intertwiners for each connected component of the boundary graph. The only correlations introduced by the amplitude are within spins and intertwiners within each connected component of the boundary graph.

In Appendix C we study the other 3 integrable vertex graphs with non-minimal faces. We do so to get a first understanding of what is excluded by our face criterion, but also because they provide simple examples of some interesting features: diagrams non 3-link-connected yet integrable; diagrams with unbounded l summations but which are nonetheless well approximated by the simplified model; presence of non-trivial $6j$ symbols and thus oscillation in the large spin limit.

5.3 DED foam

For the vertex graph in Fig. 5, the associated spin foam amplitude is (here and in the following we omit the first, trivial step of listing the matrix elements, and use directly the graphical calculus)

$$W^{DED}(j_a, j_a'; i, t, i', t') = d_i d_{i'} d_t d_{t'}$$

Notice that, by choosing judiciously the integration to be removed, we can avoid the presence of booster functions with 8 legs. This choice further shows manifestly that the vertex graph reduces to two connected components, although this would be true with any other gauge-fixing chosen. Hence, the amplitude is again factorized, and no mixing of lower and upper spins occurs.

Proceeding as before with A.12 and the normalization of the SU(2) generalized θ graphs we get

$$W^{DED}(j_a, j_a'; i, t, i', t') = d_i d_{i'} d_t d_{t'} \sum_k d_k$$

$$\times \sum_{k'} d_{k'}$$

$$\tag{26}$$

Again only minimal spins enter, and the diagram is EPRLs-exact. The estimate 20 gives the asymptotic behaviour

$$W^{DED}(j_a, j_a'; i, t, i', t') \sim \frac{1}{N^6} \frac{1}{(4\pi)^8} \left[\frac{6\pi}{(1+\gamma^2)} \right]^6 \frac{\delta_{it} \delta_{i't'}}{(\sum_a j_a)^3 (\sum_a j_a')^3}. \tag{27}$$

97

This foam order λ^2 is thus suppressed with respect to the one of order λ by three powers in the large spin limit. As for correlations, the situation is identical to the previous one: the amplitude factorizes, and the only non-trivial correlations are within each connected component of the graph.

5.4 DLD foams

Foams with an internal face give more interesting amplitudes. First of all, these foams turn out to contain sums over the magnetic l's, hence the EPRL amplitudes differ from the simplified ones. Secondly, the presence of an internal face can couple lower and upper spins. This does not happen for all foams: the first three vertex graphs of Fig. 22 still give factorized amplitudes: to see this, notice that all spins of a connected part of the boundary go through the same internal edge. If we choose to remove the group integral associated with that edge on both vertices, we immediately see that those spins completely decouple from the rest of the diagram. The remaining four are all coupled. Among them, the simplest to evaluate is number 6: it has a six-valent node, whose integration can be removed by gauge-fixing, leaving only 3-valent and 4-valent strands behind. We study this one first and in more details, and report some properties of the others in the next Section. Unless otherwise stated, the reference value for the Immirzi parameter in the numerical calculations is $\gamma = 6/5$.

The amplitude of DLD_6 is given by

$$W^{DLD_6}(j_a, j'_a; i, t; i', t') = d_i d_{i'} d_t d_{t'}$$

where we used the internal SU(2) gauge invariance to route the faces within each boxes in a convenient way. Permuting spin labels or flipping the internal edges gives trivially related amplitudes. We further use the freedom to remove one group integral by vertex to remove the highest valent ones, marked with I in the picture. The internal lines without the Y-map are magnetic l's. However those that hit an I-box are also projected by the Y-map to their minimal value. This leaves us with four free l's only, those going through the g_5 and g_6 boxes. Splitting the boxes as in A.12 and using the orthogonality A.6, the l's must be pairwise equal and the SU(2) symbols reduce to generalized θ graphs. The amplitude is then equivalent to

$$W^{DLD_6}(j_a, j'_a; i, t; i', t') = d_i d_t d_{i'} d_{t'} \sum_{l,l'k,k'} \frac{d_k d_{k'}}{d_l d_{l'}} \left[\sum_{j_f} d_{j_f} \left(\begin{array}{c} \text{[}\theta\text{ graph]} \end{array} \right)^2 \right]$$

$$\times \quad \text{[four } \theta \text{ graphs]} \quad . \tag{28}$$

With respect to the previous diagrams, we have two new features: the first is a coupling of lower and upper

98

labels, thanks to the internal face function

$$C_{l,l'}(j_4, j_4') := \sum_{j_f=\max\{|j_4-j_4'|,|l-l'|\}}^{\min\{j_4+j_4'|,l+l'\}} d_{j_f}\Big(B_3^\gamma(j_4, j_4', j_f; l, l', j_f)\Big)^2, \tag{29}$$

where we made the extremes of the sum explicit with respect to 28. The second is the summations over the magnetic-l numbers: this amplitude differs then from the one computed with the simplified model.

In order to study the large spin beahviour of 28, we begin within the simplified model: namely we cut the two l-summations to their first contribution: $l = j_4$, $l' = j_4'$, and define in this way the EPRLs amplitude $W_s^{DLD_6}(j_a, j_a'; i, t; i', t')$ and its internal face correlation as

$$C_s(j, j') := C_{j,j'}(j, j'). \tag{30}$$

Using the inhomogeneous scaling $B_3^\gamma(Nj_1, Nj_2, j_3) \sim N^{-1}$, see 17, and the boundness of the summation in j_f, we can infer the power laws

$$C_s(Nj, j') \sim N^{-1}, \qquad C_s(Nj, Nj') \sim N^{-1}. \tag{31}$$

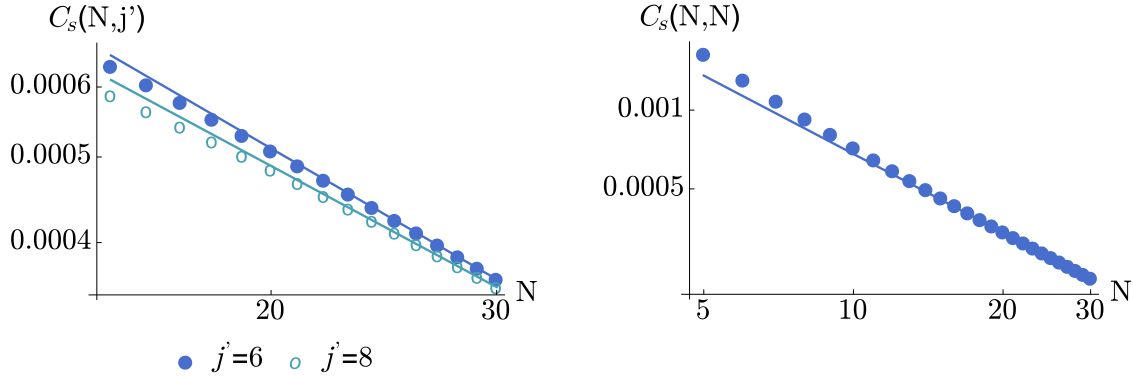Both are confirmed with good accuracy by numerical analysis, see Fig. 7.

Figure 7: *Numerical confirmation of the asymptotics 31 of the face correlation function for the simplified model. The dots are the numerical data, the lines fits obtained assuming a power law N^{-1}.*

Using this result and 19 for the scaling of B_4^γ, we estimate the EPRLs contribution to 28 to be

$$W_s^{DLD_6}(Nj, Nj'; i, t; i', t') \sim N^{-9}. \tag{32}$$

We further expect peakedness on equal intertwiners as before, $\delta_{it}\delta_{i't'}$.

From the simplified to the full EPRL model there are only a finite number of extra terms: the sum over l is bounded by j_3 and k, which in turn is bounded by j_1 and j_2; and similarly for l'. We thus expect the same scaling,

$$W^{DLD_6}(Nj, Nj'; i, t; i', t') \sim N^{-9}. \tag{33}$$

We performed numerical tests of both estimates 32 and 33 at spins of order 10, finding a qualitative agreement, see Fig.8. This could be made sharper pushing to higher spins, since at such low spins, even the individual B_4^γ is still not precisely at its asymptotic power law behaviour, see Fig. 16. However we lack at present the numerical power to do so, because Mathematica has instabilities in evaluating and integrating hypergeometric functions starting from around spins $j = 30$. Given the extremes of 29, this puts our numerical limits at spins of order 10.[10]

---

[10]We can go beyond only for diagrams having only three-valent booster functions, since for these we can use a finite sum expression without hypergeometric functions [18].
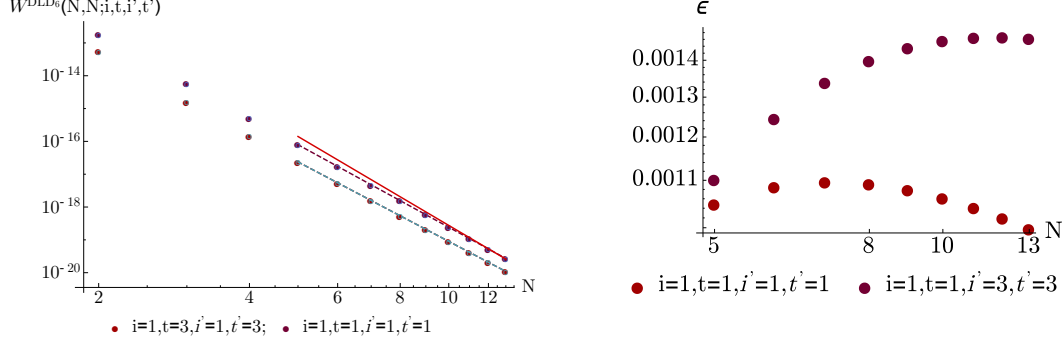
Figure 8: Left panel: *Large spin scaling of $W^{DLD_6}(N, N; i, t; i', t')$ in 28 for equal spins and two different configurations of interwiners. The dots are the numerical data, and the continuous lines the expected N^{-9} decay derived in 33. The dashed lines are the actual fits at the spins we can access. Using the last 5 points, the fits give $N^{-8.4}$ and $N^{-8.1}$ respectively. The discrepancy can be imputed to the slow spins, at which already the indivudal booster function is not yet at asymptotic behaviour, see Fig. 16 in the Appendix. Data points for the simplified model are indistinguishable, the difference is in the per thousands and shown in the right panel.* Right panel: *Numerical studies of the relative error between the EPRL model and the simplified one, $\epsilon := |W^{DLD_6} - W_s^{DLD_6}|/W^{DLD_6}$.*

This means that even if this foam is not EPRLs exact, the difference is very small. The simplified model captures the correct scaling, and also the spin correlations, as we will see in Section 6.

5.5 DLD foams: additional vertex graphs

As we have seen, integrability and our face criterion do not single out a unique amplitude diagram for the DLD complex. Next to DLD_6 studied in the previous Section, there are 3 additional types of vertex graphs leading to non-factorized amplitudes, those numbered 4,5 and 7. As before, these graphs give raise to different foams by considering permutations of spin labels, and swapping the routing through the internal edges. We consider here only one representative of these possible permutations.

In order of numerical complexity, the next non-factorized amplitude is the one with vertex graphs number 5, which only contains 4-stranded boosters. Proceeding as in the previous Section, we have

$$W^{DLD_5}(j_a, j'_a; i, t, i', t') = d_i d_{i'} d_t d_{t'}$$

$$= d_i d_t d_{i'} d_{t'} \sum_{\substack{l_a, \bar{l}_a, l'_4 \\ k, k', h}} \frac{d_k d_{k'} d_h}{d_{l_4} d_{l'_4}} \left(\sum_{j_f} d_{j_f} \right. \quad \text{(34)}$$

100
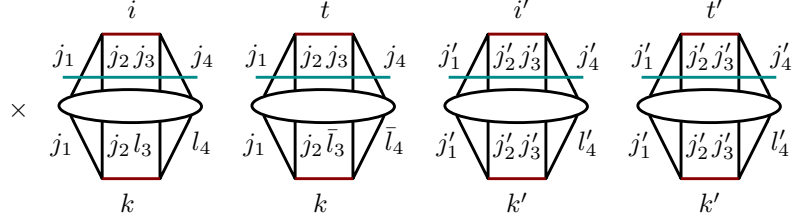
There are five l summations (the SU(2) symbol associated with the internal face identifies two initially different l'_4 and $\bar{l}'_4$), only one bounded. This EPRL amplitude differs thus from the simplified model by an infinite number of terms, decreasing in magnitude with a power law in the ls. The quantity in round brackets identifies the face correlation function coupling lower and upper spins. It is again a square of boosters, 4-stranded this time.

As before, let us first estimate the scaling of the simplified model. The first thing to notice is the dependence of the face correlation function on the intertwiner labels. If we let the boundary spins grow, Clebsch-Gordan inequalities quickly reduce to zero the number of terms in the sum over the internal spin, unless we let the intertwiners also grow. Hence, the dominating contribution comes from large bulk intertwiners. But since in the simplified model the boundary booster functions (in the last line of 34) are sharply peaked on equal intertwiners, this means that the whole amplitude scales differently for different values of the boundary intertwiners, with dominant contribution coming from the largest intertwiners. This is quite different from the previous foam considered, where the scaling was homogeneous in the intertwiners. To estimate the power law associated with this dominant scaling, we look at the inhomogeneous scaling of B_4^γ with one small spin, see 21a. Then, since the number of terms to be summed over grows linearly with the spins, we estimate

$$\sum_{j_f} d_{j_f} B_4^\gamma(Nj_{\bar{a}}, j_f; Nj_{\bar{a}}, j_f; Nh, Nk) B_4^\gamma(Nj_{\bar{a}}, j_f; Nj_{\bar{a}}, j_f; Nh, Nk') \sim N(N^{-5/2})^2 = N^{-4}, \qquad (35)$$

where the extremes of the summations are

$$[\max\{N|j'_4 - h|, N|j'_4 - k|, N|j_4 - k'|\}, \min\{N(j'_4 + h), N(j'_4 + k), N(j_4 + k')\}].$$

This function is hard to evaluate numerically, and we were able to compute it explicitly up to spins of order 10 only. At those value, a numerical fit gives a power law $N^{-3.2}$. This is in qualitative agreement with the estimate 35, since at the same values the inhomogeneous B_4^γ only scales like $N^{-2.1}$ instead of $N^{-2.5}$. With this numerical support, we use 35 to estimate the whole amplitude. The summations over the intertwiners are all cut down by the Gaussian peak in the boosters. Putting 35 together with the dimensional factors of the intertwiners and the homogeneous scalings of the boosters in the last line of the amplitude, and taking into account the fact that also the boundary intertwiners must be rescaled to get the dominant contribution, we get for the simplified model

$$W_s^{DLD_5}(Nj_a, Nj'_a; Ni, Nt, Ni', Nt') \sim N^4 N N^{-4}(N^{-5/2})^4 = N^{-9}. \qquad (36)$$

This is the same scaling estimated for the previous foam. At spins of order 10, a linear fit of the exact numerical data gives $N^{-8.1}$, same qualitative agreement as expected from 35.

For the complete model, our results are more limited. The numerical evaluation is significantly harder because of the many l-summations, and out of reach of our current numerical power. This is unfortunate because unlike for the previous foam, the two scalings could differ this time. Indeed, the presence of unbounded summations of slow convergence (the booster functions now have a power-law decay in the ls, as opposed to the exponential one of the previous foam) means that the complete EPRL model could have a *slower* decay. Consider in fact the following example:

$$f(j) = \frac{1}{j^x} \sum_{\Delta l=0}^{\infty} \frac{1}{(j + \Delta l)^y} \sim \frac{1}{j^{x+y-1}} \frac{1}{y-1} \qquad (37)$$

where in the last step we approximated the sum with an integral. This suggests that an unbounded sum can slow by one power the large spin decay. If this is the case, then this foam dominates and the overall

expansion 1 should be completed with an intermediate scaling, and spin correlations between the boundary dipoles would appear at a stronger power than N^{-9}. Since there are only two independent summations, the boosters decay and the example 37 suggest that the scaling would be at most two powers slower, that is N^{-7}.

The remaining two non-factorized amplitudes have a more complicated structure, with 5-stranded booster functions. Their expression is, respectively,

$$W^{DLD_4}(j_a, j'_a; i, t, i', t') = d_i d_{i'} d_t d_{t'}$$

$$= d_i d_t d_{i'} d_{t'} \sum_{\substack{l_a, \bar{l}_a, l'_a \\ k, k', s, h, h'}} \frac{d_k d_{k'} d_s d_h d'_h}{d_l d_{l'}} \left(\sum_{j_f} d_{j_f} \right. $$

and

$$W^{DLD_7}(j_a, j_a'; i, t, i', t') = d_i d_{i'} d_t d_{t'}$$

The best we can do for these two foams is to give the large spin scaling of the simplified amplitude. Proceeding in the same way as before, suing this time the inhomogeneous scaling 21a of the 5-stranded booster, we obtain the following estimates:

$$W_s^{DLD_4}(Nj_a, Nj_a'; Ni, Nt, Ni', Nt') \sim N^4 N^3 N^{-6}(N^{-5/2})^4 = N^{-9}, \tag{38}$$

$$W_s^{DLD_7}(Nj_a, Nj_a'; Ni, Nt, Ni', Nt') \sim N^4 N^2 N^{-6}(N^{-5/2})^4 = N^{-10}. \tag{39}$$

The presence of unbounded summations means again that the amplitudes for the complete EPRL model could decay slower.

Finally, we have the three vertex graphs 1,2 and 3 of Fig. 6, corresponding to factorized DLD amplitudes. Proceeding as above, we find that the amplitudes for the simplified model scale respectively as N^{-6}, N^{-7}, N^{-11}. As for the complete model, we did not invest numerical resources to study these diagrams, that give factorized amplitudes. Since the vertex graphs 1 and 2 are not 3-link-connected, we are not guaranteed that the associated amplitudes are ill-defined. We present in Appendix C an example with a similar structure in which the amplitude is finite.

The results of our estimates and comparisons with the simplified model are summarized in the following Table 1:

Foam	Factorization	LOs scaling	EPRLs=EPRL	Numerics
DVD	Y	N^{-3}	Y	✓
DED	Y	N^{-6}	Y	✓
DLD_1	Y	N^{-6}	N	
DLD_2	Y	N^{-7}	N	
DLD_3	Y	N^{-11}	N	
DLD_4	N	N^{-9}	N	
DLD_5	N	N^{-9}	N	
DLD_6	N	N^{-9}	N	✓
DLD_7	N	N^{-10}	N	

Table 1: *Summary of scalings and properties of the foams. The column Factorization refers to whether the amplitude factorizes in two terms associated with each connected part of the boundary graph; LOs scaling gives the scaling of the simplified model; the next column marks the foams for which EPRL and EPRLs give the amplitude (so in particular the scaling is the same); Numerics lists those foams for which we have numerical evaluations. In the three cases considered, the numerics confirm the scaling of the simplified model. For the other foams, we notice in particular that DLD_4, DLD_5 and DLD_7 contain slowly converging unbounded summations over ls and could likely give slower fall offs. The summary of different scalings shows manifestly that already for the simplified EPRLs model the large spin scaling is not a simple function of V, E and F.*

It goes without saying that we would have liked to perform numerical studies of (at least) the large spin scaling of all foams, especially for those like DLD_4, DLD_5 and DLD_7 that have non-factorized amplitudes and may have a slower power law decrease than the simplified model. This lays however beyond our current numerical means: Evaluating the booster functions is very slow and limited at spins of order 30, and the slow convergence of the sums over l makes it impossible to deduce any meaningful behaviour from our data.

One thing that can be nonetheless fruitfully learned from the estimates for the EPRLs is that the power of the leading scaling is not a simple function of the number of vertices, edges and faces. A priori, one has the following structure:

- Number of vertices and their valence = Number and type of $SU(2)$ symbols;

- Number of half-edges = Number of booster function;

- Number of faces per half-edge = Valence of booster functions.

Using 20 and the scalings of the SU(2) symbols one can use this structure to estimate the scaling of the amplitudes, at least for the simplified model. This works for simplicial foams, as explained in [18].[11] However for non-simplicial foams the situation is made more complicated by the large freedom in the routing of the faces and the valence of the edges. The routing in particular turns out to strongly influence the scaling, as shown in the Table above. As a particular example, the routing can lead to disconnected vertex graphs, which are always the dominant ones for given V, E, F: this is because gauge-invariance implies to remove one integral per connected component, and thus an additional booster power-law decay with it. Only if the routing of the faces is rigidly fixed, one can hope to find easy rules to estimates the power-law decay without writing down the explicit form of the amplitude. For the complete EPRL model we have two possibilities: either the same scaling of the simplified model, or a slower scaling. The first situation occurs for simple foams with no unbounded l summations, like DVD and DED above, or with fast convergent unbounded summations, like DLD_6 and the additional examples in Appendix C. The second situation is however more general, and to estimate the difference one can look at how many independent unbounded l-summations are present, see discussion around 37 for an example. The slower decays impact also the analysis of the amplitude divergences associated to internal bubbles, like for the self-energy spin foam or the Pachner 1-5 move, see [58]. The actual details on the behaviour of the complete EPRL model depend on the structure of the booster functions for non-minimal spins, and an improved analytic understanding of their large spin behaviour is certainly necessary if one wants to make progress in the evaluation of Lorentzian EPRL amplitudes. See [59] for work in this direction.

---

[11]The actual estimate there given does not take into account the removal of one integration per node and should accordingly be amended.

5.6 Higher vertices and Regge asymptotics

The next foams in the vertex expansion have two vertices with three internal edges and, according to our criterion, three internal faces, see Fig. 9. The vertices are now 5-valent: one may wonder whether $\{15j\}$ symbols appear in the amplitudes, and allow us to make some contact with simplicial spin foams and their geometric interpretation. The answer is in the negative, due to the combinatorial structure of the faces: a 4-simplex vertex graph would require one of the faces to have two external links (one upper and one lower). But for this specific foam that would mean a non-minimal cycle, thus violating our face criterion. $15j$ symbols will certainly appear with a high enough number of vertices, however it is hard to anticipate without a detailed analysis how much of their potential Regge-like behaviour will survive in the presence of so many non-simplicial symbols around them.

Although lacking a relation to Regge actions, the simple foams considered so far carry nonetheless non-trivial correlations, and we will look at some of them in the next Section.
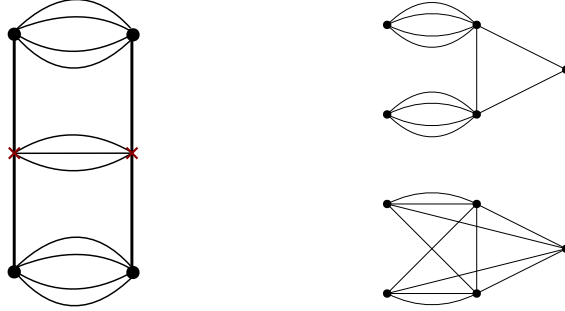

Figure 9: *An example of 2-complex with two pentavalent vertices, on the left, and two of its possible vertex graphs, on the right. The requirement of avoiding faces corresponding to non-minimal cycles excludes vertex graphs with the combinatorics of a $\{15j\}$ symbol.*

6 Spin Correlations

One of the most important properties of spin foam amplitudes is to introduce dynamical correlations among spin network states. These correlations have played an important role in the study of the 2-point function for simplicial foams [34], and the relation with the graviton propagator in the linearized expansion (see e.g. [45]).[12] For non-simplicial foams, we do not have a geometric interpretation of the correlations, but it is nonetheless important to study their structure if such amplitudes have to play a dynamical role in the theory. We focus here on the most interesting correlations encountered in our dipole-to-dipole transitions, those between spins associated with disconnected parts of the boundary graph. We have seen in the previous Section that such correlations appear only in the presence of an internal face and a routing mixing the boundary faces. The simplest foam for which this happens is DLD_6, and in this Section we present a more detailed analysis of the spin correlations. Our analysis will however be only indicative in nature, for the following reason: we do not have sufficient computer power and time to evaluate the twelve sums over boundary spins and intertwiners. We resorted to a strong simplification provided by a 'mini-superspace' model: we assume all lower and all upper spins to be equal, $j_a \equiv j$, $j'_a \equiv j'$, and study the amplitudes as probability distributions $W_{\text{mini}}^{DLD_6}(j, j')$ in this two-dimensional space, at fixed γ and intertwiners. This enormously reduces the contributions we need to sum over and makes numerical calculations an easy task. We hope that it still captures, at least qualitatively, the nature of the spin correlations of the true model. Using a Gaussian boundary state $|\Psi\rangle = \sum_{j,j'} \exp\{-(j - j_0)^2 - (j' - j_0)^2\} |j, j'\rangle$ as in the general boundary framework, we evaluate

$$\langle jj' \rangle_{\gamma, j_0} := \frac{\langle W_{\text{mini}}^{DLD_6} | \hat{J}_l \hat{J}_{l'} | \Psi \rangle}{\langle W_{\text{mini}}^{DLD_6} | \Psi \rangle} - \frac{\langle W_{\text{mini}}^{DLD_6} | \hat{J}_l | \Psi \rangle}{\langle W_{\text{mini}}^{DLD_6} | \Psi \rangle} \frac{\langle W_{\text{mini}}^{DLD_6} | \hat{J}_{l'} | \Psi \rangle}{\langle W_{\text{mini}}^{DLD_6} | \Psi \rangle}. \tag{40}$$

---

[12]For recent alternative ideas based on entanglement to select physically correlated states, see e.g. [60, 61, 62, 63].
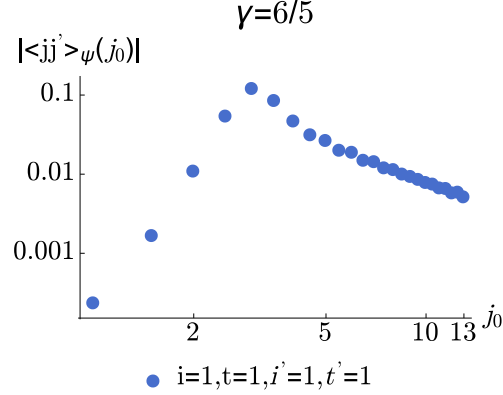
The results are reported in Fig. 10.

Figure 10: *Correlations 40 as functions of the background spin j_0 introduced by the boundary state. The value of the peak and of the power-law tail depend on γ, here taken to be 6/5. The intertwiners labels are all equal to 1.*

We see a peak and a power-law large j_0 decay. These two features are qualitatively reminiscent of the simplicial spin correlations (see e.g. [11]), although the details differ, notably the power law and the width of the Gaussian.

An important consequence of the minisuperspace model is that the amplitude is normalizable:

$$\langle W_{\text{mini}}^{DLD_6} | W_{\text{mini}}^{DLD_6} \rangle = \sum_{j,j'} W_{\text{mini}}^{DLD_6}(j,j')^2 < \infty. \tag{41}$$

Furthermore, convergence is achieved almost immediately, see Fig. 11. Hence, we can define the correlations
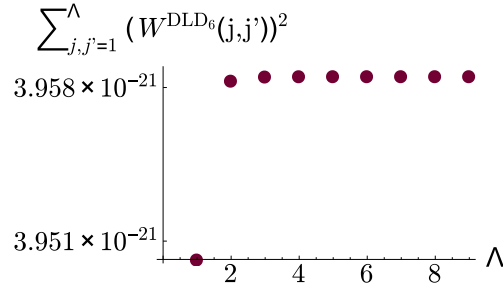
Figure 11: *Normalizability of the minisuperspace amplitude. The plot shows the convergence of 41 as a cut-off Λ on the summations is increased. Here we fixed all intertwiner labels to 1, and $\gamma = 1.2$.*

for this mini-superspace model also as in 7,

$$\langle jj'\rangle_{DLD_6} := \frac{\sum_{j,j'}^{\Lambda} jj' W_{\text{mini}}^{DLD_6}(j,j')^2}{\sum_{j,j'}^{\Lambda} W_{\text{mini}}^{DLD_6}(j,j')^2} - \frac{\sum_{j,j'}^{\Lambda} j W_{\text{mini}}^{DLD_6}(j,j')^2}{\sum_{j,j'}^{\Lambda} W_{\text{mini}}^{DLD_6}(j,j')^2} \frac{\sum_{j,j'}^{\Lambda} j' W_{\text{mini}}^{DLD_6}(j,j')^2}{\sum_{j,j'}^{\Lambda} W_{\text{mini}}^{DLD_6}(j,j')^2}, \tag{42}$$

where, since the sums over j and j' are infinite, we put an homogeneous cut-off Λ on them. The convergence in Λ is very fast, see left panel of Fig. 12, as it was for the normalization alone. The same plot shows that the EPRL and simplified model give basically the same correlations: the difference is of order 10^{-4}. Hence for this diagram the simplified model correctly captures both the scaling and the spin correlations.

Finally, we studied the dependence of 42 on the Immirzi parameter γ, see left panel of Fig. 12. The correlations are positive, and decrease as γ increases.

106
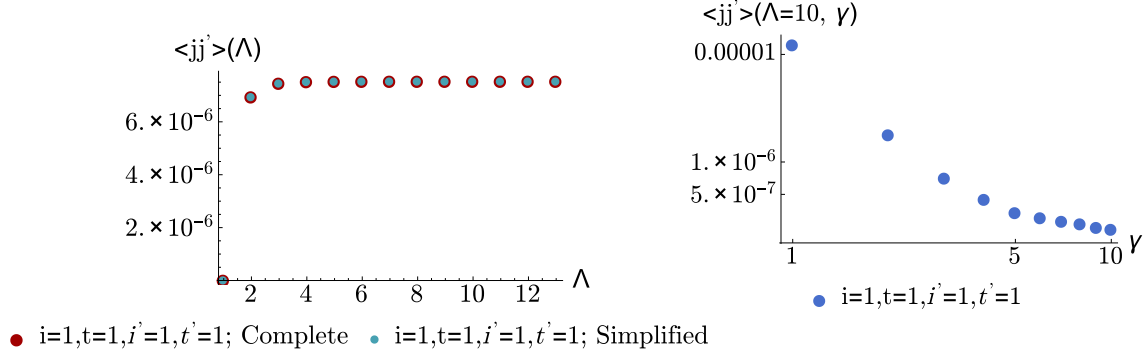
Figure 12: Left panel: *Spin correlation 42 for the complete and the simplified models, showing that convergence of the sum is achieved at small values of the cut-off* Λ. *The models give indistinguishable data points, the relative error being of order* 10^{-4}. *The same fast convergence is seen for all values of* γ *considered.* Right panel: *Spin correlation 42 as a function of the Immirzi parameter, using the simplified model and cut-off* $\Lambda = 10$.

Let us now look at the origin of the correlations, namely the internal face function 29 responsible for the coupling of upper and lower spins. The main contribution is the one for the simplified model, 30. As a distribution in the spins this function has an interesting behaviour, with a principal peak for equal spins and symmetric sub-leading peaks, see Fig. 13.
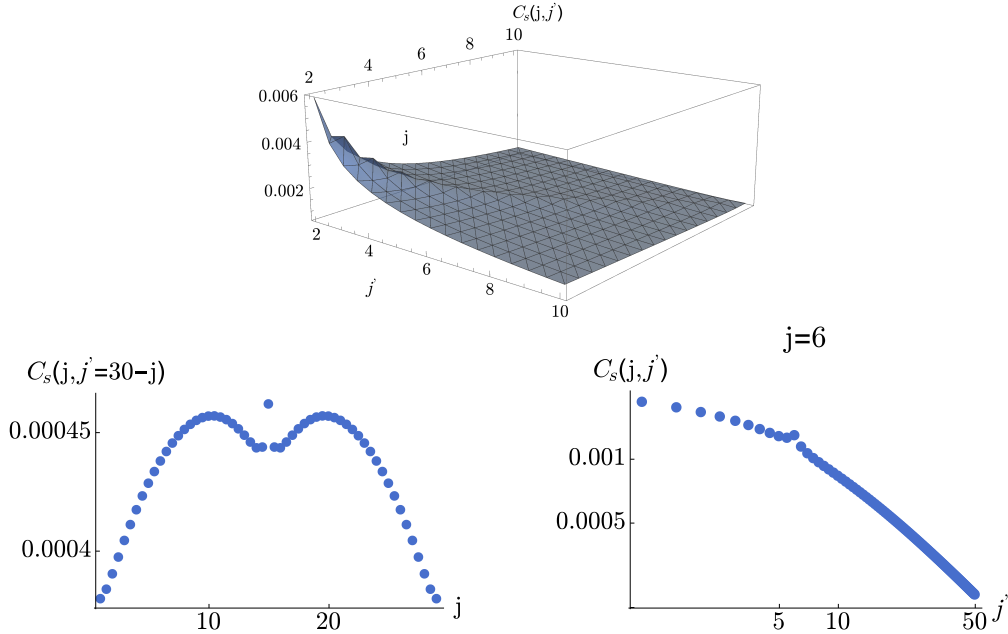
Figure 13: *Numerical studies of the internal face correlation function, for the simplified model and* $\gamma = 6/5$. Upper panel: *3d plot of* $C_s(j, j')$, *showing a power-law decay superimposed with a peak for equal spins and symmetric sub-leading peaks.* Lower panels: *2d sections of* $C_s(j, j')$, *showing more details about the peaks. The peak in the fixed-j cut may amusingly remind the reader of a resonance in particles scattering, like the famous Higgs-diphoton bump, however the background typically has opposite concavity.*

Adding the l contributions of the complete EPRL model gives stronger correlations, although by a very

small amount. For the internal face function, we can look at a cut-off summation,

$$C_{\Delta l}(j, j') = \sum_{l=j}^{j+\Delta l} \sum_{l'=j'}^{j+\Delta l} C_{l,l'}(j, j').$$ (43)

Each new term added enhances the peak, as shown in Fig. 14. However, the l, l' to be summed over in 28 are convoluted with booster functions, that has seen previously decrease as we increase the l labels. This has the effect of damping the peak enhancement, and as anticipated above, the final correlations only differ by an order 10^{-4}.

The resummed $C_{\Delta l}$ only gives a qualitative picture of the effect in the complete model, in particular it overestimate it since the B_4 convoluted over are also decaying functions in Δl. Indeed, the correct result can be seen by looking at the complete amplitude as a function of final (say all equal) spins at fixed initial (all equal) spins. That is the reason why, also for the correlation of the present foam and not only for the scaling behaviour, the simplified model offers a good approximation.
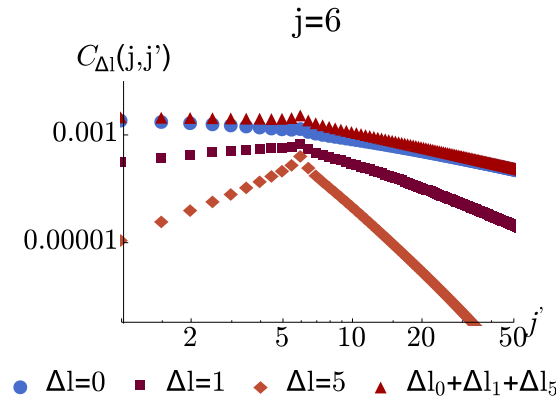
Figure 14: *Peak enhancement for the cut-offed sums 43.*

As a final comment, let us point out that the simplicity constraints play an important role in generating the correlations. Had Had we worked with SU(2) BF theory alone, in fact, the internal face function would simply be

$$C_{BF}(j, j') = \sum_{j_f=|j-j'|}^{j+j'} d_{j_f}.$$ (44)

There is no more coupling of the spins in the summand, and the only almost-trivial correlations come from the extremes of the sum. Hence these correlation are a good test of the dynamics of the EPRL model, within the limit of the simple foams and mini-superspace setup here considered.

7   Conclusions

Numerical calculations of spin foam amplitudes are notoriously difficult, especially for Lorentzian signature. In this paper we have considered amplitudes for a boundary graph with two 4-link dipoles, originally considered in [20, 23] for cosmological applications. We have extended that analysis to foams with two vertices, and showed how the amplitudes can be computed explicitly using the method introduced in [18]. Our results show that the decoupling of the boundary dipoles present at one vertex [20] is still present at two vertices with a single connecting edge. In order to couple the spins on the two dipole one needs an internal face. This is however not sufficient, as some foams with an internal face also can give factorized amplitudes, depending on the routing of the faces. For the simplest foam with a non-factorized amplitude we performed numerical studies of its scaling and spin correlations. The amplitude is suppressed by six powers in the large spin limit with respect to that with a single vertex, and the correlations between lower and upper spins, studied with

a mini-superspace model, are positive and monotonically decreasing with γ. The origin of the correlations can be isolated in a specific function associated to the internal face, which features a non-trivial structure with multiple peaks. This study of correlations can be considered as a first step to understand the dynamics induced by the spin foam for the two dipoles, and it is relevant for the development of spin foam cosmology. Indeed, one of our main motivations to undertake the present analysis was to take a look at cosmological applications using spin foams [19, 20, 21, 22, 23, 24, 25, 17], with the specific question of seeking evidence of the famous Big Bounce predicted by loop quantum cosmology [64]. We are not there yet with our approach, partly because the path proved rich and complicated, partly because our current numerical power is significantly limited. We thus content ourselves for the time being with presenting the results obtained so far, and postpone a study of cosmological applications to future work.

For all foams considered, the spin sum over the internal face is convergent, and the amplitudes have a power law decay in the large spin limit. The power increases with the complexity of the foam, thus introducing a hierarchical scheme on top of the vertex coupling expansion. However, the exact scaling depends in a complicated way on the combinatorics of the foam, and cannot be easily established just looking at the number of vertices, edges and faces of the 2-complex. For instance a routing of faces leading to a disconnected vertex graphs always gives a dominant amplitude with respect to a connected routing, because of the extra group integrations to be removed. These results leave us with a mixed feeling. Exposing the large spin hierarchy of the foams allows one to play around with expansions like 1 as an arena to test different ideas on how the sum should be organized, or a continuum limit taken, and how different questions may be sensitive to different orders. On the other hand, the (relative) simplicity of the numerical evaluation of these non-simplicial spin foams has a payoff in the loose combinatorics of the faces. Even introducing a very strong criterion as we did, the proliferation is still important, and most unsatisfactorily, the scaling power law can not be a priori determined simply looking at the number of vertices, edges and faces, not even for the simplified EPRLs model.

In the course of presenting these results we also discussed detailed aspects of the evaluations, the guiding role that the simplified model can play, and what are our current numerical limits. In particular, we were able to numerically evaluate only one – and the simplest – non-factorized foam for the complete EPRL model. Both types of results, on the scalings and the correlations, concern the very limited setting 1 with at most two vertices and a single internal face, and it is necessary to push our analysis further before more meaningful conclusions can be drawn. The numerical evaluations are very costly, and we are furthermore limited by instabilities of hypergeometric functions in Mathematica to compute the booster functions at spins beyond 30. Our analysis tells us that we need to improve these instabilities and parallelize the code so to speed up the l summations. Work is currently in progress in this direction, and these improvements will be crucial to testing the Regge asymptotic of the simplicial amplitude [14]. Once this is achieved, the factorization method of [18] put the Lorentzian amplitudes on the same tractability level as SU(2) amplitudes. This is non-trivial progress, but far from saying that the hardest part of the work is done: it is actually at that point that one can face the true hard problem, namely the summations over internal j spins for many-vertex foams. So from the numerical perspective our results are both good and bad: good because we were able to do explicit numerics at two vertices, bad because they showed how much more improvement is needed, in methods and numerical codes and/or approximation schemes.

Let us conclude with a comment on the dynamical meaning of the amplitudes here considered. Most of the literature on spin foams focuses on simplicial amplitudes, for their natural geometric interpretation and relation to Regge calculus. Nonetheless, non-simplicial amplitudes have been put forward as a mean to provide transition amplitudes to spin networks on arbitrary graphs [6]. One can go out of the simplicial setting in two opposite directions: on the one, considering simpler foams, with lower-valence vertices and simple boundary states. This is the set up proposed in [20, 23] for cosmological applications and considered here. On the other one, considering higher-valence vertices, which could be interesting from a coarse-graining perspective for instance, and has also been considered for cosmological applications [17]. In the first case, the connection with Regge calculus and that geometric interpretation of the dynamics is lost, as we have seen in this paper no Regge actions enter the dynamics of the leading foams in the expansion. In the second case, the analysis of [13] (which is restricted to SU(2) theory, but already points out what the story is like for the EPRL model, see also [65] on this) shows that while it is possible in principle to get a Regge-like dynamics based on flat 4d polytopes instead of 4-simplices, the EPRL model as it is now allows for more general non-flat polytope configurations at the saddle point, corresponding to 3d data describing a class of

conformal twisted geometries in which areas and angles match, but not the diagonal of the polygonal faces.

The lack of a simple connection with Regge calculus, and of a simple rule to identify the large spin scaling of each diagram, are for us indications that more work is needed to assess the viability of non-simplicial EPRL amplitudes for quantum gravity.

Acknowledgements

We are grateful to Pietro Donà and Marco Fanizza for many helpful discussions about numerical aspects and to Marcin Kisielowski and Thomas Krajewski about generalised spin foams, and to Francesca Vidotto for initial motivations and a reading of the manuscript. Simone thanks Daniele Oriti for discussions on spin foam expectation values.

A $SU(2)$ and $SL(2,\mathbb{C})$ graphical calculus

For the graphical calculus used to explicitly compute the amplitudes, we refer the reader to the monography [32], whose conventions we use here.

A.1 SU(2) Symbols

We represent Wigner's $3jm$ symbol as

$$
\left(\begin{array}{ccc} j_1 & j_2 & j_3 \\ m_1 & m_2 & m_3 \end{array} \right) = \quad \raisebox{-1em}{$\vphantom{x}$} \quad = \quad \raisebox{-1em}{$\vphantom{x}$} \quad , \tag{A.1}
$$

where the signs $\pm$ on the nodes keep track of the assignment of spins in the symbol, respectively anticlockwise/clockwise.

The contraction of two $3jm$ symbols via an intertwiner gives

$$
\raisebox{-1.5em}{$\vphantom{x}$} = \raisebox{-1.5em}{$\vphantom{x}$} = \sum_{m_i} (-1)^{i-m_i} \left(\begin{array}{ccc} j_1 & j_2 & i \\ m_1 & m_2 & m_i \end{array} \right) \left(\begin{array}{ccc} i & j_3 & j_4 \\ -m_i & m_3 & m_4 \end{array} \right)
$$

$$
=: \left(\begin{array}{cccc} j_1 & j_2 & j_3 & j_4 \\ m_1 & m_2 & m_3 & m_4 \end{array} \right)^{(i)} \tag{A.2}
$$

which we used to define a $4jm$ symbol with four external legs. From now on we forget to use dots for nodes and we discard signes assuming they are always minus if not otherwise stated. These symbols satisfy orthogonality properties such as

$$
\sum_{m_1,m_2} \left(\begin{array}{ccc} j_1 & j_2 & j_3 \\ m_1 & m_2 & m_3 \end{array} \right) \left(\begin{array}{ccc} j_1 & j_2 & l_3 \\ m_1 & m_2 & n_3 \end{array} \right) = \frac{\delta_{j_3 l_3}\delta_{m_3 n_3}}{d_{j_3}}, \tag{A.3}
$$

$$
\sum_{m_a} \left(\begin{array}{cccc} j_1 & j_2 & j_3 & j_4 \\ m_1 & m_2 & m_3 & m_4 \end{array} \right)^{(j_{12})} \left(\begin{array}{cccc} j_1 & j_2 & j_3 & l_4 \\ m_1 & m_2 & m_3 & n_4 \end{array} \right)^{(l_{12})} = \frac{\delta_{j_{12}l_{12}}}{d_{j_{12}}} \frac{\delta_{j_4 l_4}\delta_{m_4 n_4}}{d_{j_4}}. \tag{A.4}
$$

Unlike the $3jm$ symbol, the $4jm$ symbol we defined is not normalized.[13]

---

[13]A normalised $4jm$-symbol is obtained multiplying the right-hand side of A.2 by $\sqrt{d_{j_{12}}}$. We chose the non-normalised convention because it is the one that corresponds to a 4-valent node in the SU(2) graphical calculus, and because it is more convenient to work with in order to reconstruct the invariants $\{nj\}$-symbols associated to graphs.

In the graphical notation of the $4jm$ symbol we distinguish one spin, j_{12}, which corresponds to an intertwiner label in the recoupling channel 12. Graphically, tracing over the free magnetic indices the orthogonality relations A.3 and A.4 we obtain the evaluation of the θ graph and its generalized version with 4 links,

$$
j_2 \ \langle\!\!\!\!\begin{array}{c} j_1 \\ \\ j_3 \end{array}\!\!\!\!\rangle = 1; \qquad i \ \left|\!\!\!\!\begin{array}{c} j_1 \\ j_2 \\ j_3 \\ j_4 \end{array}\!\!\!\!\right| \ k \ = \frac{\delta_{i,k}}{d_i}. \tag{A.5}
$$

Above and everywhere we implicitly assumed that the Clebsch-Gordan inequalities are satisfied, else the evaluations vanish.

For the simple foams considered in this paper, the rule that we needed the most is the orthogonality relation (A.3), namely

$$
j_3 \ \bigcirc \ j_4 \quad = \quad d_{j_1}^{-1} \ \left|\begin{array}{c} j_1 \\ \\ j_3 \end{array}\right. \ \langle\!\!\!\!\begin{array}{c} j_4 \\ \\ j_2 \end{array}\!\!\!\!\rangle \tag{A.6}
$$

Other two useful rules are the node sign change, equation (6) in Section 8.5 of [32], and the $6j$ graph identity at the bottom of page 429.

Inverting the orientation of an internal line with spin j gives a $(-1)^{2j}$ phase. Inverting the orientation of an external line gives a parity map $\epsilon = i\sigma_2$. Depending on whether we are acting on a ket or a bra we get

$$
D_{mn}^{(j)}(i\sigma_2) = \epsilon_{mn}^{(j)} = \quad \longrightarrow\!\!\bullet\!\!\longleftarrow \quad = (-1)^{j+m}\delta_{m,-n}
$$

$$
\epsilon^{-1\,(j)mn} = \epsilon^{(j)nm} \quad \longleftarrow\!\!\bullet\!\!\longrightarrow \quad = (-1)^{j-m}\delta_{m,-n} \tag{A.7}
$$

So for instance

$$
\begin{array}{c} j_1 \ j_2 \ j_3 \ j_4 \\ \bigvee \\ i \end{array} = (-1)^{j_1-m_1} \left(\begin{array}{cccc} j_1 & j_2 & j_3 & j_4 \\ -m_1 & m_2 & m_3 & m_4 \end{array} \right)^{(i)}. \tag{A.8}
$$

Since $\sum_l j_l \in \mathbb{N}$ at a node, reversing all external lines has no effect:

$$
\begin{array}{c} j_1 \ j_2 \ j_3 \\ \bigvee \end{array} = \begin{array}{c} j_1 \ j_2 \ j_3 \\ \bigvee \end{array} \ , \qquad \begin{array}{c} j_1 \ j_2 \ j_3 \ j_4 \\ \bigvee \\ i \end{array} = \begin{array}{c} j_1 \ j_2 \ j_3 \ j_4 \\ \bigvee \\ i \end{array} . \tag{A.9}
$$

Changing the orientation of the virtual line gives a phase in agreement with the rule for internal lines:

$$
\begin{aligned}
& \;\; \text{(diagram with } j_1\ j_2\ j_3\ j \text{, label } i) \\
&= \sum_{m_i} \begin{pmatrix} j_1 & j_2 & i \\ m_1 & m_2 & m_i \end{pmatrix} (-1)^{i-m_i} \begin{pmatrix} i & j_3 & j \\ -m_i & m_3 & m \end{pmatrix} \\
&= \sum_{m_i} \begin{pmatrix} j_1 & j_2 & j_{12} \\ m_1 & m_2 & -m_i \end{pmatrix} (-1)^{i+m_i} \begin{pmatrix} i & j_3 & j \\ m_i & m_3 & m \end{pmatrix} \\
&= \sum_{m_i} (-1)^{2(i-m_i)} \begin{pmatrix} j_1 & j_2 & i \\ m_1 & m_2 & -m_i \end{pmatrix} (-1)^{i+m_i} \begin{pmatrix} i & j_3 & j \\ m_i & m_3 & m \end{pmatrix} \\
&= (-1)^{2i} \;\; \text{(diagram with } j_1\ j_2\ j_3\ j \text{, label } i) \, .
\end{aligned}
$$

A.2 Boxes and Integrations

We refer the reader to [10] for a more detailed description of graphical calculus for $SL(2,\mathbb{C})$. Here we just need two elements to complement the $SU(2)$ calculus. The $SL(2,\mathbb{C})$ integration boxes, and the booster functions. We represent every half-edge of a foam with a box, every face with a strand and the Y map with a blue line orthogonal to the strands. If e.g. four faces touch an half edge the corresponding box will have four strands. The Y map projects the 'magnetic spins' to their minimal value, which we always denote with a j in this paper. 'Magnetic spins' allowed to vary freely above their minimal value are always labeled with a l. Hence for a 4-stranded half-edge,

$$
\text{(box diagram with } g\text{)} = \int_{SL(2,\mathbb{C})} dg \bigotimes_{a=1}^{4} D^{(\gamma j_a, j_a)}_{j_a m_a l_a n_a}(g). \tag{A.10}
$$

The arrow under the box is needed to keep track of whether the group element to be integrated over is g or g^{-1}. For instance, following the same convention as before for outgoing and ingoing lines, we have

$$
\text{(box diagram with } g, h\text{)} = \int dh\, dg \sum_{l_1, r_1, l_2, r_2} D^{\gamma j_1, j_1}_{j_1 m_1 l_1 r_1}(g) D^{\gamma j_1, j_1}_{l_1 r_1 j_1 n_1}(h^{-1}) D^{\gamma j_2, j_2}_{j_2 m_2 l_2 r_2}(g^{-1}) D^{\gamma j_2, j_2}_{l_2 r_2 j_2 n_2}(h) .
$$

$$\tag{A.11}$$

Following [18], the $SL(2,\mathbb{C})$ integrals can be split in two $SU(2)$ Wigner's njm symbols summed over a booster function, for instance

$$
\text{(box diagram } \{j_a\}, g, \{l_a\}\text{)} = \sum_{i,k} d_i\, d_k \;\; \text{(diagram } \{j_a\}, i, k, \{l_a\}\text{)} . \tag{A.12}
$$

The graphical notation for the booster function is the one introduced in the main text. With this choice the signs of the nodes are alternating. We use this property also in the main text, to avoid keeping track of the signs on all diagrams: we assign + or - to the boundary states, then the signs of the internal nodes are implicitly assigned according to this alternate rule.

The booster functions do not depend on the strand orientations. To see this, notice that in a box with n lines we can have two possible configurations:

$$\begin{array}{cc} \raisebox{-1em}{\includegraphics{}} \;\; j & \raisebox{-1em}{} \end{array}$$

$$\square \downarrow \;\; = D^{\gamma j,j}_{lnjm}(g^{-1}) \qquad \square \downarrow \;\; = D^{\gamma j,j}_{jmln}(g), \tag{A.13}$$

with $g \in SL(2,\mathbb{C})$. On the first case the decomposition reads [18]

$$D^{\gamma j,j}_{lnjm}(g^{-1}) = \overline{D}^{\gamma j,j}_{jmln}(g) = (-1)^{j-l+m-n} D^{\gamma j,j}_{j-ml-n}(g)$$
$$= (-1)^{j-l+m-n} D^{j}_{-mp}(u) d^{\gamma j,j}_{jlp}(r) D^{l}_{p-n}(v), \tag{A.14}$$

while in the second case

$$D^{\gamma j,j}_{jmln}(g) = D^{j}_{mp}(u) d^{\gamma j,j}_{jlp}(r) D^{l}_{pn}(v). \tag{A.15}$$

In both cases we can split the $SL(2,\mathbb{C})$ group element without any phase depending on magnetic index p, thus the booster functions do not get any arrow.

B   Booster functions: numerical results

In this Appendix we collect numerical results for the booster functions 16. For $n = 3$ there is a fast and exact formula in terms of finite sums, see [18]. Using this we can go up to spins of order a hundred within seconds. For larger n we can do much less. A formula based on the finite sums for presented in [18], and in spite of promising properties, it presents numerical instabilities due to subtractions of ratios of large numbers. For this paper we then used the basic definition 16 with the boost matrix elements expressed in terms of hypergeometric functions. This gives reliable evaluations with Mathematica, although slow, up to spins of order 30 where numerical instabilities appear. Fig. 15 gives an idea of the evaluation times.
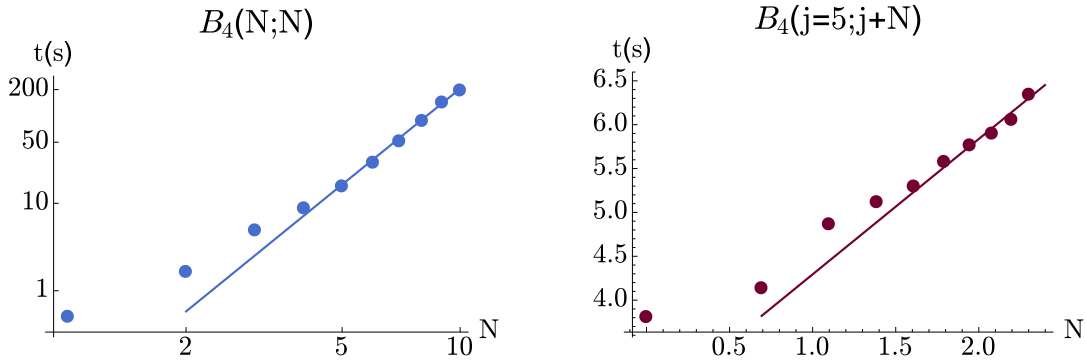

Figure 15: Left panel: *Time (in seconds) to evaluate a $B_4^\gamma(Nj, Nj)$ for minimal and equal spins for all possible intertwiners, the important contribution is given by numerical integration while, at low spins, 4j symbol calculation time is negligible using [66]* Right panel: *Calculation time for $B_4^\gamma(j, j + N\Delta l)$, for all intertwiners and with a homogeneous rescaling of magnetic spins.*

Spins of order 30 are enough to see convincingly the $N^{-3/2}$ scaling, although it is still a few per cents away with a fit, see Fig. 16. Experience from the 3-stranded boosters shows in fact that a 1% fit needs spins of order 60. The same figure also shows that the analytic estimate 20 is off by a numerical factor of order 1. Further studies show also that the decay with unequal intertwiners has the same power law, hence the Kronecker delta reported in 20 should be more precisely be replaced by a Gaussian.
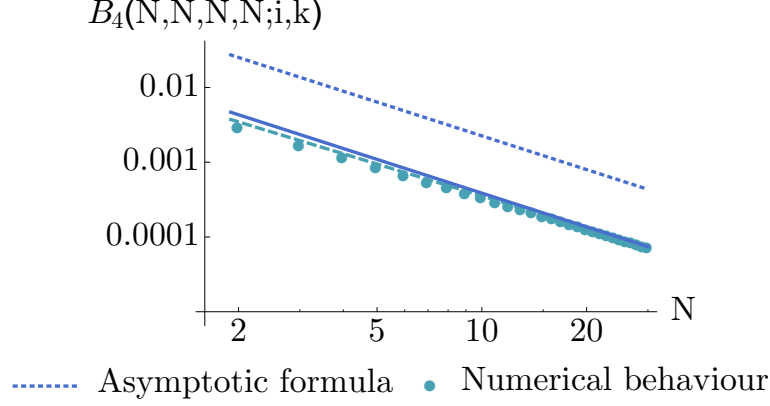
$B_4(\text{N,N,N,N;i,k})$

------- Asymptotic formula • Numerical behaviour

Figure 16: *Homogeneous large spin scaling of B_4^γ, with equal intertwiners $i = k = 1$ and $\gamma = 6/5$. Dots are the data points, and the continuous line is a numerical fit with power $N^{-3/2}$. The dashed line is a numerical fit with a free power, which gives a scaling $N^{-1.4}$ using the last 5 points. This is compatible with the $N^{-3/2}$, and suggests that the asymptotics is reached at spins of order 50 to 100, as it is for the B_3^γ, see [18]. Finally, the dotted line is the analytic formula 20, which captures the right scaling but not the numerical factor. Further analysis [18] shows that also the γ and j_i dependences are well captured, but not so well the intertwiner one which is a Gaussian rather than a Kronecker delta.*

Next, we report in Fig. 17 the studies of the inhomogeneous scalings, with a single small spin, and all other large.

$B_3(j_1,j_2,j_3)$

• j_1=1,j_2=N,j_3=N   ∘ j_1=3,j_2=N+2,j_3=N

$B_4(\text{1,N,N,N;i,k})$

• i=N, k=N

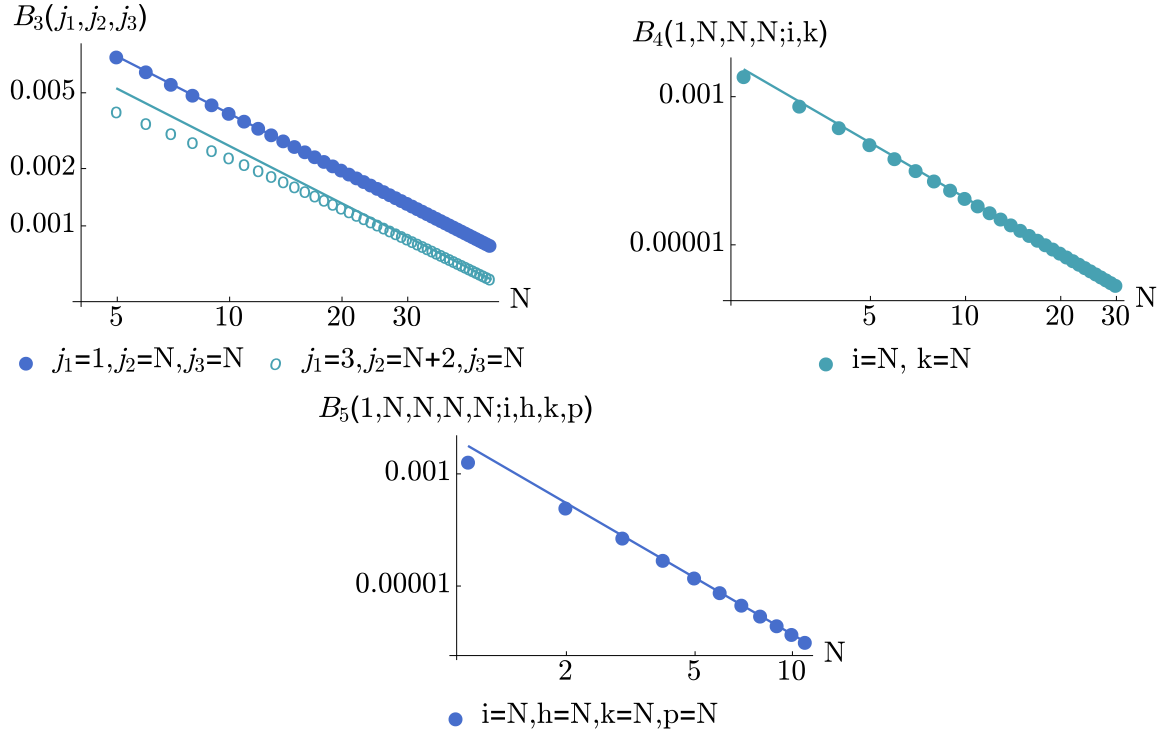$B_5(\text{1,N,N,N,N;i,h,k,p})$

• i=N,h=N,k=N,p=N

Figure 17: *Inhomogeneous large spin scalings of booster functions with a small spin, see 21 in the main text. The dots are data points, the lines numerical fits. We find a power law N^{-1} for B_3^γ (top left), $N^{-5/2}$ for B_4^γ with intertwiners equal and large (top right), $N^{-7/2}$ for B_5^γ with both intertwiners equal and large (bottom).*

Another important property of the booster functions is the way they decay as we increase the l 'magnetic numbers', starting from their minimal value j. This can be either a power law or an exponential decay.

Fig. 18 shows non-oscillating and oscillating power laws obtained increasing homogeneously all l's of B_4^γ for different spin configurations.
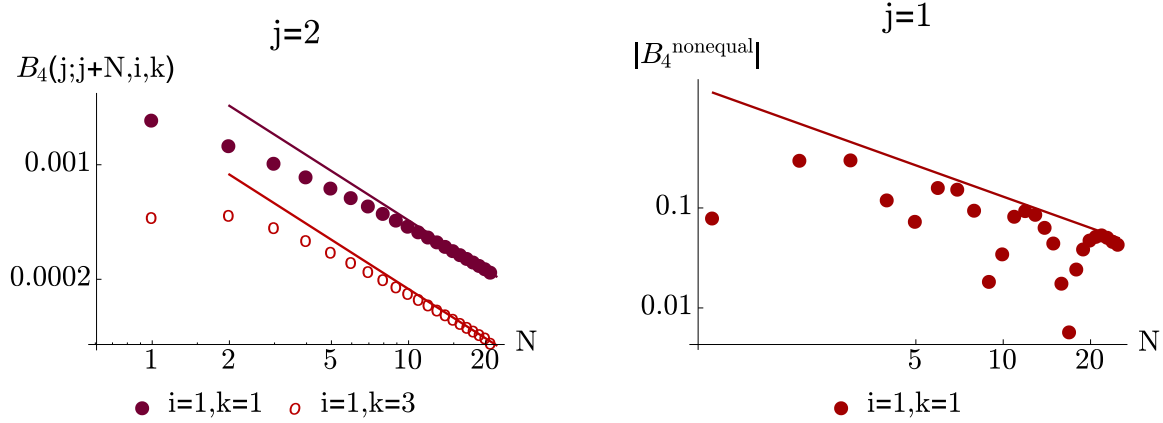

Figure 18: *Non-minimal spin decays, homgeneous.* Left panel: *Equal spins, equal and non-equal intertwiners. Numerical fits give a power law N^{-1} in both cases.* Right panel: *Configuration with non-equal spins, $B_4^{nonequal} = B_4(j, j, j+1, j+2; j+N, j+N, j+1+N, j+2+N; i, k)$, showing oscillatory behaviour with the same N^{-1} power law.*

The final Fig. 19 shows that allowing a single l to grow large with respect to its minimal value give an exponential decay.
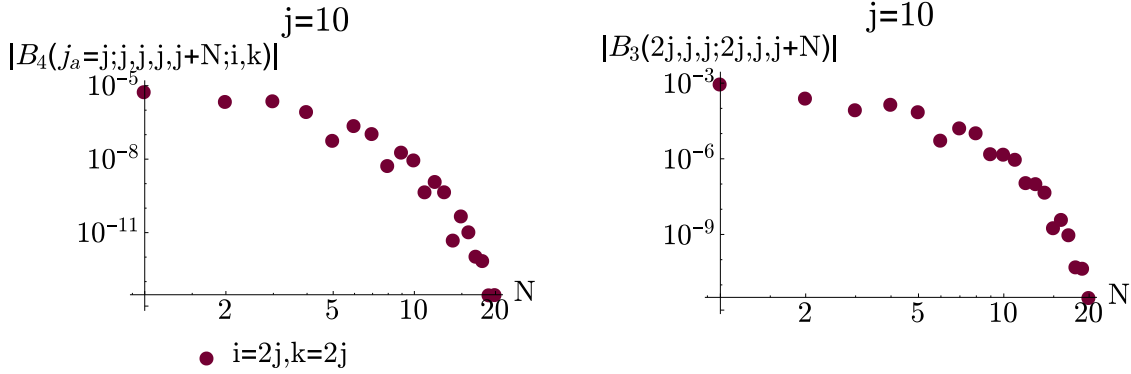

Figure 19: Left panel: *Decaying at $j=10$ for a B_4 while increasing one l. The difference between the first two points ($N = 0$ and $N = 1$) is one order of magnitude while between the first and the last point nine orders.* Right panel: *Decaying at $j=10$ for a B_3 while increasing one l.*

C Extended graph analysis

In the main body of the paper, we used two different types of arguments to reduce the number of vertex graphs to be studied. First, the existence of non-integrable Lorentzian spin networks; second, our criterion to define the spin foam faces as minimal cycles. In this Appendix we relax the second argument, and show what it would look like to take into account all possible graphs which are a priori integrable. Accordingly, we only exclude graphs containing uni-valent and bi-valent nodes, as well as tadpoles. We keep a priori also non-3-link-connected graphs: as explained in the main text, 3-link connectivity is only a sufficient criterion, and indeed we will see below examples of integrable non-3-link connected graphs.

Allowing for faces corresponding to non-minimal cycles, we have 4 possible vertex graphs for DVD, see Fig. 20, 3 for DED, see Fig. 21, and 13 for DLD, see Fig. 22. We have listed only the topologically distinct vertex graphs; to list the associated spin foams one has to take into account also label permutations and alternative but topologically equivalent routings (for these simple graphs, these can be captured by rotating the graph by $\pi/2$ and by flipping it vertically). Many of these diagrams lead to 'face-rigid' amplitudes for the dipole transitions: these can be easily identified as those with a link connecting the top and bottom nodes. It is also easy to identify those that would lead to factorized amplitudes, by using the criterion explained in the main text: if all the spins of a single boundary are linked to a unique node of the vertex graph then decoupling can be immediately seen choosing to remove the group integration at that node. This is the case for the first graph of 21 and for the first three graphs of 22.

The admissible graph analysis shown in these figures was performed by hand, using rules analogue to those explained in details in [24]. For more general graphs it is highly recommendable to switch to an automatic evaluation on Mathematica.
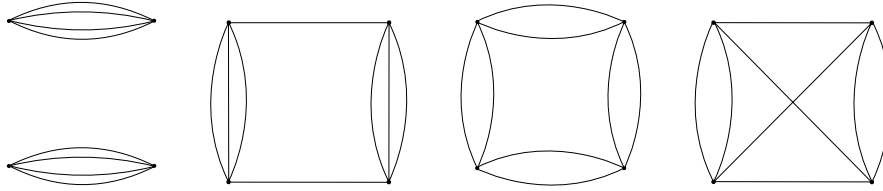

Figure 20: *Integrable graphs for a 4-valent vertex with 8 faces. The second is not 3-link-connected, yet it turns out to be integrable. The last one is the only one to contain a non-trivial symbol, a $6j$. When applied to the DVD foam, all but the first violate the minimal-cycle faces criterion; all non-minimal-cycle faces in this case lead to 'face-rigid' amplitudes, meaning one face has two boundary links thus imposing equality of those boundary spins.*
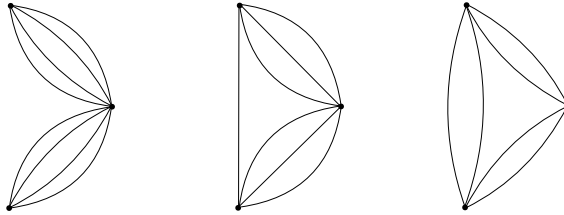

Figure 21: *Integrable graphs for a 3-valent vertex with 8 faces. When applied to DED the last two give 'face-rigid' amplitudes.*
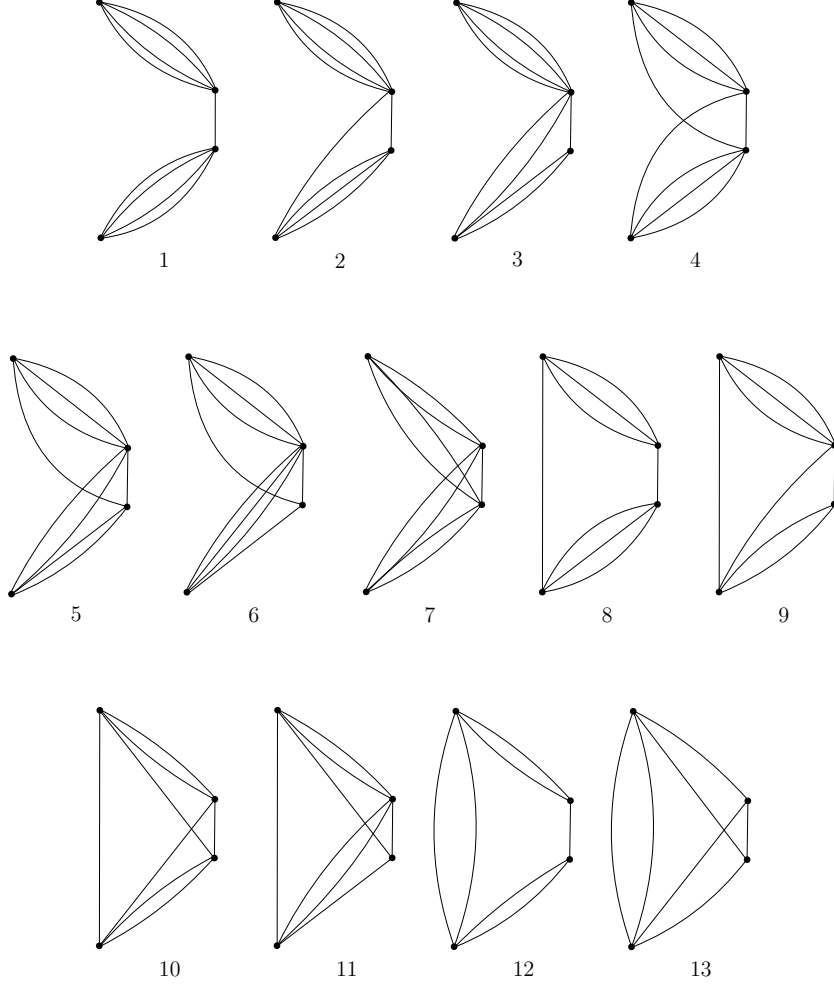
Figure 22: *Integrable graphs for a 4-valent vertex with 9 faces. Number 1,2 and 8 are not 3-link-connected. The simplified amplitude is finite, but we do not know whether the complete EPRL amplitude is finite or not.*

C.1   Evaluations of the 'face-rigid' DVD foams

We report here the explicit evaluation of the three additional vertex graphs of Fig. 20. These calculations, although not directly relevant to the main goal of the paper, allow us to highlight some properties of the EPRL model useful for more general evaluations. First, the fact the non-3-link connected graphs can have integrable Lorentzian amplitudes (in DVD_2). Second, the fact that even in the presence of unbounded 'magnetic l's' summations the simplified model can still provide precise leading order approximations of the EPRL model, if the sums quickly converge (in DVD_2 and DVD_3). Third, it allows us also to see a diagram in which a non-trivial $6j$ symbol appears (in DVD_4).

With reference to Fig. 20, the second vertex graph for DVD gives the following amplitude:

$$W^{DVD_2}(j_a, j'_a; i, t, i', t') = didi'dt \sum_{k', l_a} dk'(-1)^{2(k'+t')} \frac{\delta_{j'_3, l_4}}{d_{j'_3}} \delta_{j_1, j'_1} \delta_{j_2, j'_2} \delta_{j_3, j'_3}$$

$$(\text{C.16})$$

We see in the first line above the three 'face-rigid' conditions imposing equal spins between the lower and the upper dipole. The amplitude is not 3-link-connected, thus convergence of the l-summations is not guaranteed. Of the 4 l summations, 3 are unbounded due to triangular inequalities, and further the l's enter in 3 or 4 slots of the (last two) booster functions, whose decay is a slow power-law. Nonetheless, the summations quickly converge, and the amplitude is finite, see Fig. 23. The quick convergence of the summations indicates also that the simplified model can give a good scaling estimate, which is also confirmed numerically. Using 19 we estimate the large spin limit of the EPRLs amplitude to scale as $N^{-11/2}$, and the numerical fit on the right panel of Fig. 23 shows that already at spins of order 10 the power approaches this value.
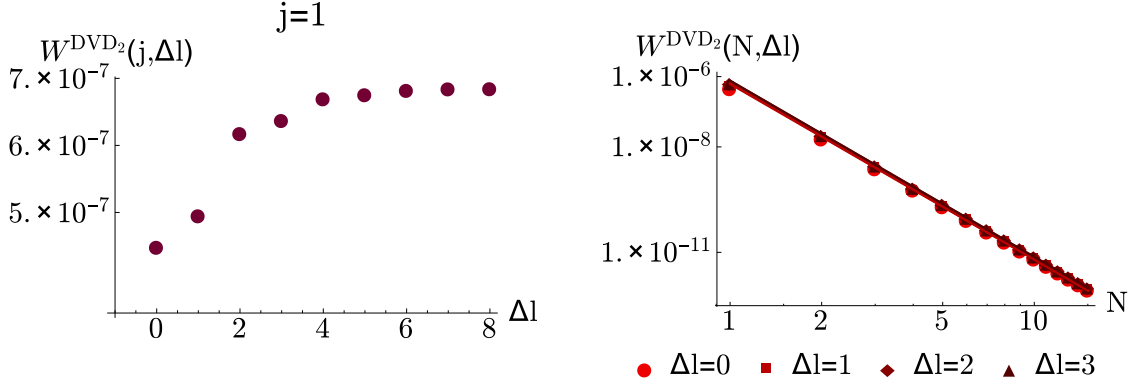

Figure 23: Left panel: *Convergence of the sums over l's in C.16 with an homogeneous cut off Δl. Boundary spins and intertwiner fixed to 1, $\gamma = 6/5$. The relative error between the first and the last point is of 35% while between the seventh and the last one is 0.03%* Right panel: *Scaling of W^{DVD_2} for different values of the cut off with all boundary's intertwiners fixed to 1. The roughly 10% differences are squashed by the scale of the y-axis. The continuous line is a numerical fit, which gives $N^{-5.01}$ for all of them, a value compatible with the EPRLs analytic estimate at this low spins at which the boosters have not yet reached asymptotic scaling.*

We have a similar story for DVD_3, whose unbounded l summations also quickly converge, making the EPRLs scaling coincide with the complete evaluations. The amplitude reads

$$W^{DVD_3}(j_a, j'_a; i, t, i', t') = didi'dt \sum_{l_a} \delta_{j_1, j'_1} \delta_{j_2, j'_2}$$

$$(\text{C.17})$$

with only two l summations unbounded. The simplified scaling is $N^{-9/2}$, and the numerical studies are reported in Fig. 24.
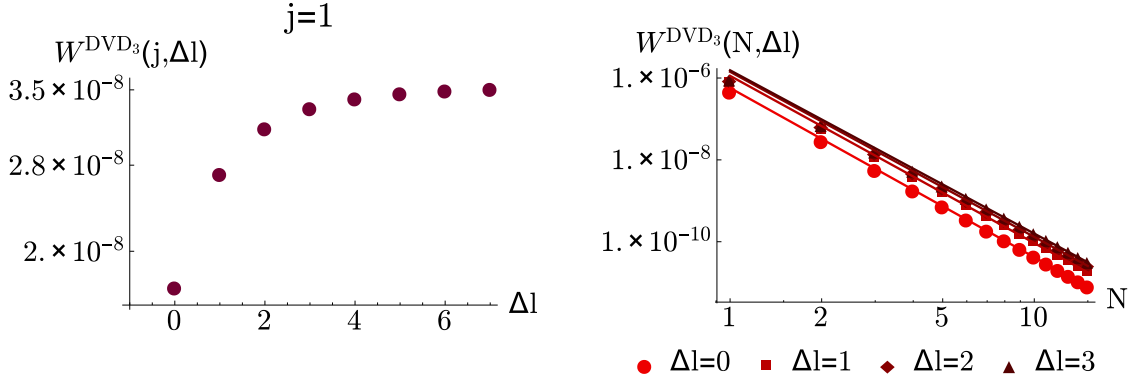
118

Figure 24: Left panel: *Convergence of the sums over l's in C.17 with an homogeneous cut off Δl. Boundary spins and intertwiner fixed to 1, $\gamma = 6/5$. The relative error between the first and the last point is of 50% while between the seventh and the last one is 0.4%.* Right panel: *Scaling of C.17 for different values of the cut off with all boundary's intertwiners fixed to 1. The convergence is now slower and we can tell the different cut-offs apart. The numerical fits in the continuous lines give $N^{-4.1}$, again compatible with the EPRLs estimates.*

These results show that the EPRLs captures well the scaling of the complete model, but with a caveat: it could happen that the quick convergence of the l summations, exposed in the numerics above at small spins (left panels of Figs. 23 and 24, is not preserved at high spins. This could result in larger contributions and slower decays. The fact that the numerical fits (in the right panels of the same figures) are unchanged shows that this should be true up to j of order 10, but we do not have stronger evidence beyond that.

Finally, DVD_4 carries a $\{6j\}$ symbol due to the crossing of two of the faces:

$$W^{DVD_4}(j_a, j_a'; i, t, i', t') = d i d i' d t \sum_{k, l_a} d k (-1)^{2t' + 3l_4 + j_1'} \delta_{j_1, j_1'} \delta_{j_2, j_2'} \delta_{j_3, j_3'}$$

$$\text{(C.18)}$$

For the simplified model with boundary intertwiners fixed, the involved $\{6j\}$ symbol has only four large entries, and scales like N^{-1}, see Fig. 25. The estimate for the simplified amplitude gives

$$W_s^{DVD_4}(Nj, Nj; i, t, i', t') \sim (N^{-3/2})^3 N^{-1} = N^{-11/2}. \tag{C.19}$$

The properties of the DVD foams studied in this Appendix are summarized in the following Table 2:

Foam	Factorization	LOs scaling	EPRLs=EPRL	Face-rigidity
DVD_1	Y	N^{-3}	Y	
DVD_2	N	$N^{-10/2}$	N	3-face rigid
DVD_3	N	$N^{-9/2}$	N	2-face rigid
DVD_4	N	$N^{-11/2}$	N	3-face rigid

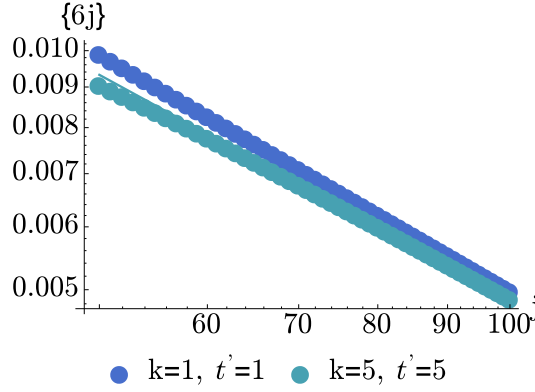Table 2: *Summary of scaling and some properties of the DVD foams.*

119

Figure 25: *Scaling of a {6j} symbol with 4 large entries. The dots are data points, the continuous line a N^{-1} fit.*

References

[1] A. Perez, *The Spin Foam Approach to Quantum Gravity*, Living Rev.Rel. **16** (2013) 3 [1205.2019].

[2] J. Engle, R. Pereira and C. Rovelli, *The Loop-quantum-gravity vertex-amplitude*, Phys.Rev.Lett. **99** (2007) 161301 [0705.2388].

[3] J. Engle, E. Livine, R. Pereira and C. Rovelli, *LQG vertex with finite Immirzi parameter*, Nucl.Phys. **B799** (2008) 136–149 [0711.0146].

[4] L. Freidel and K. Krasnov, *A New Spin Foam Model for 4d Gravity*, Class.Quant.Grav. **25** (2008) 125018 [0708.1595].

[5] E. R. Livine and S. Speziale, *Consistently Solving the Simplicity Constraints for Spinfoam Quantum Gravity*, Europhys.Lett. **81** (2008) 50004 [0708.1915].

[6] W. Kaminski, M. Kisielowski and J. Lewandowski, *Spin-Foams for All Loop Quantum Gravity*, Class.Quant.Grav. **27** (2010) 095006 [0909.0939].

[7] Y. Ding, M. Han and C. Rovelli, *Generalized Spinfoams*, Phys.Rev. **D83** (2011) 124020 [1011.2149].

[8] H. M. Haggard, M. Han, W. Kamiński and A. Riello, *Four-dimensional Quantum Gravity with a Cosmological Constant from Three-dimensional Holomorphic Blocks*, Phys. Lett. **B752** (2016) 258–262 [1509.00458].

[9] J. W. Barrett, R. Dowdall, W. J. Fairbairn, H. Gomes and F. Hellmann, *Asymptotic analysis of the EPRL four-simplex amplitude*, J.Math.Phys. **50** (2009) 112504 [0902.1170].

[10] J. W. Barrett, R. Dowdall, W. J. Fairbairn, F. Hellmann and R. Pereira, *Lorentzian spin foam amplitudes: Graphical calculus and asymptotics*, Class.Quant.Grav. **27** (2010) 165009 [0907.2440].

[11] J. D. Christensen, E. R. Livine and S. Speziale, *Numerical evidence of regularized correlations in spin foam gravity*, Phys. Lett. **B670** (2009) 403–406 [0710.0617].

[12] J. D. Christensen, I. Khavkine, E. R. Livine and S. Speziale, *Sub-leading asymptotic behaviour of area correlations in the Barrett-Crane model*, Class. Quant. Grav. **27** (2010) 035012 [0908.4476].

[13] P. Donà, M. Fanizza, G. Sarno and S. Speziale, *SU(2) graph invariants, Regge actions and polytopes*, Class. Quant. Grav. **35**, no. 4, 045011 (2018) 1708.01727.

[14] P. Donà, M. Fanizza, G. Sarno and S. Speziale, *Numerical studies of the Lorentzian EPRL vertex amplitude*, in preparation.

[15] C. Delcamp and B. Dittrich, *Towards a phase diagram for spin foams*, Class. Quant. Grav. **34** (2017), no. 22 225006 [1612.04506].

[16] B. Bahr and S. Steinhaus, *Numerical evidence for a phase transition in 4d spin foam quantum gravity*, Phys. Rev. Lett. **117** (2016), no. 14 141302 [1605.07649].

[17] B. Bahr, S. Kloser and G. Rabuffo, *Towards a Cosmological subsector of Spin Foam Quantum Gravity*, 1704.03691.

[18] S. Speziale, *Boosting Wigner's nj-symbols*, J. Math. Phys. **58** (2017), no. 3 032501 [1609.01632].

[19] C. Rovelli and F. Vidotto, *Stepping out of Homogeneity in Loop Quantum Cosmology*, Class. Quant. Grav. **25** (2008) 225024 [0805.4585].

[20] E. Bianchi, C. Rovelli and F. Vidotto, *Towards Spinfoam Cosmology*, Phys.Rev. **D82** (2010) 084035 [1003.3483].

[21] E. F. Borja, I. Garay and F. Vidotto, *Learning about quantum gravity with a couple of nodes*, SIGMA **8** (2012) 015 [1110.3020].

[22] E. Bianchi, T. Krajewski, C. Rovelli and F. Vidotto, *Cosmological constant in spinfoam cosmology*, Phys.Rev. **D83** (2011) 104015 [1101.4049].

[23] F. Vidotto, *Many-nodes/many-links spinfoam: the homogeneous and isotropic case*, Class. Quant. Grav. **28** (2011) 245005 [1107.2633].

[24] M. Kisielowski, J. Lewandowski and J. Puchta, *One vertex spin-foams with the Dipole Cosmology boundary*, Class. Quant. Grav. **30** (2013) 025007 [1203.1530].

[25] J. Rennert and D. Sloan, *A Homogeneous Model of Spinfoam Cosmology*, Class. Quant. Grav. **30** (2013) 235019 [1304.6688].

[26] M. V. Battisti and A. Marciano, *Big Bounce in Dipole Cosmology*, Phys. Rev. **D82** (2010) 124060 [1010.1258].

[27] E. F. Borja, J. Diaz-Polo, I. Garay and E. R. Livine, *Dynamics for a 2-vertex Quantum Gravity Model*, Class.Quant.Grav. **27** (2010) 235010 [1006.2451].

[28] E. R. Livine and M. Martin-Benito, *Classical Setting and Effective Dynamics for Spinfoam Cosmology*, 1111.2867.

[29] A. Ashtekar and P. Singh, *Loop Quantum Cosmology: A Status Report*, Class. Quant. Grav. **28** (2011) 213001 [1108.0893].

[30] E. Alesci and F. Cianfrani, *Quantum-Reduced Loop Gravity: Cosmology*, Phys. Rev. **D87** (2013), no. 8 083521 [1301.2245].

[31] E. Alesci, G. Botta and G. V. Stagno, *QRLG effective hamiltonians from a statistical regularization scheme*, 1709.08675.

[32] D. A. Varshalovich, A. N. Moskalev and V. K. Khersonsky, *Quantum Theory of Angular Momentum: Irreducible Tensors, Spherical Harmonics, Vector Coupling Coefficients, 3nj Symbols*. World Scientific, Singapore, 1988.

[33] C. Rovelli and F. Vidotto, *Covariant Loop Quantum Gravity*. Cambridge Monographs on Mathematical Physics. Cambridge University Press, 2014.

[34] E. Bianchi, L. Modesto, C. Rovelli and S. Speziale, *Graviton propagator in loop quantum gravity*, Class.Quant.Grav. **23** (2006) 6989–7028 [gr-qc/0604044].

[35] E. Bianchi and Y. Ding, *Lorentzian spinfoam propagator*, Phys. Rev. **D86** (2012) 104040 [1109.6538].

[36] M. P. Reisenberger and C. Rovelli, *'Sum over surfaces' form of loop quantum gravity*, Phys.Rev. **D56** (1997) 3490–3508 [`gr-qc/9612035`].

[37] J. C. Baez, *An Introduction to spin foam models of quantum gravity and BF theory*, Lect.Notes Phys. **543** (2000) 25–94 [`gr-qc/9905087`]. Published in in Geometry and Quantum Physics. Edited by H. Gausterer and H. Grosse. Springer, Berlin, 2000.

[38] R. De Pietri, L. Freidel, K. Krasnov and C. Rovelli, *Barrett-Crane model from a Boulatov-Ooguri field theory over a homogeneous space*, Nucl. Phys. **B574** (2000) 785–806 [`hep-th/9907154`].

[39] R. De Pietri and C. Petronio, *Feynman diagrams of generalized matrix models and the associated manifolds in dimension 4*, J. Math. Phys. **41** (2000) 6671–6688 [`gr-qc/0004045`].

[40] V. Bonzom, R. Gurau and V. Rivasseau, *Random tensor models in the large N limit: Uncoloring the colored tensor models*, Phys. Rev. **D85** (2012) 084037 [`1202.3637`].

[41] S. Carrozza, D. Oriti and V. Rivasseau, *Renormalization of a SU(2) Tensorial Group Field Theory in Three Dimensions*, Commun. Math. Phys. **330** (2014) 581–637 [`1303.6772`].

[42] D. Oriti, *Group Field Theory and Loop Quantum Gravity*, 2014. `1408.7112`.

[43] C. Rovelli, *On the structure of a background independent quantum theory: Hamilton function, transition amplitudes, classical limit and continuous limit*, `1108.0832`.

[44] E. R. Livine and S. Speziale, *Group Integral Techniques for the Spinfoam Graviton Propagator*, JHEP **11** (2006) 092 [`gr-qc/0608131`].

[45] B. Dittrich, L. Freidel and S. Speziale, *Linearized dynamics from the 4-simplex Regge action*, Phys.Rev. **D76** (2007) 104020 [`0707.4513`].

[46] W. Ruhl, *The Lorentz Group and Harmonic Analysis*. W. A. Benjamin, 1970.

[47] J. C. Baez and J. W. Barrett, *Integrability for relativistic spin networks*, Class. Quant. Grav. **18** (2001) 4683–4700 [`gr-qc/0101107`].

[48] W. Kaminski, *All 3-edge-connected relativistic BC and EPRL spin-networks are integrable*, `1010.5384`.

[49] M. Kisielowski, J. Lewandowski and J. Puchta, *Feynman diagrammatic approach to spin foams*, Class. Quant. Grav. **29** (2012) 015009 [`1107.5185`].

[50] C. Charles and E. R. Livine, *The Fock Space of Loopy Spin Networks for Quantum Gravity*, Gen. Rel. Grav. **48** (2016), no. 8 113 [`1603.01117`].

[51] J. Rennert and D. Sloan, *Anisotropic Spinfoam Cosmology*, Class. Quant. Grav. **31** (2014) 015017 [`1308.0687`].

[52] J. B. Hartle and S. W. Hawking, *Wave function of the universe*, Phys. Rev. D **28** (Dec, 1983) 2960–2975.

[53] J. B. Hartle, S. W. Hawking and T. Hertog, *The Classical Universes of the No-Boundary Quantum State*, Phys. Rev. **D77** (2008) 123537 [`0803.1663`].

[54] G. A. Kerimov and I. A. Verdiev, *Clebsch-Gordan Coefficients of the SL(2,c) Group*, Rept. Math. Phys. **13** (1978) 315–326.

[55] V. Bonzom, E. R. Livine, M. Smerlak and S. Speziale, *Towards the graviton from spinfoams: The Complete perturbative expansion of the 3d toy model*, Nucl. Phys. **B804** (2008) 507–526 [`0802.3983`].

[56] J. W. Barrett, W. J. Fairbairn and F. Hellmann, *Quantum gravity asymptotics from the SU(2) 15j symbol*, Int. J. Mod. Phys. **A25** (2010) 2897–2916 [`0912.4907`].

[57] J. Puchta, *Asymptotic of Lorentzian Polyhedra Propagator*, `1307.4747`.

[58] P. Donà, *Infrared divergences in the EPRL-FK Spin Foam model,* 1803.00835.

[59] M. Fanizza, P. Martin-Dussaud and S. Speziale, *Asymptotics of $SL(2,\mathbb{C})$ tensor invariants*, in preparation.

[60] A. Perez, *Statistical and entanglement entropy for black holes in quantum geometry*, Phys. Rev. **D90** (2014), no. 8 084015 [1405.7287]. [Addendum: Phys. Rev.D90,no.8,089907(2014)].

[61] E. Bianchi, J. Guglielmon, L. Hackl and N. Yokomizo, *Loop expansion and the bosonic representation of loop quantum gravity*, Phys. Rev. **D94** (2016), no. 8 086009 [1609.02219].

[62] A. Feller and E. R. Livine, *Quantum Surface and Intertwiner Dynamics in Loop Quantum Gravity*, Phys. Rev. **D95** (2017), no. 12 124038 [1703.01156].

[63] G. Chirco, F. M. Mele, D. Oriti and P. Vitale, *Fisher Metric, Geometric Entanglement and Spin Networks*, 1703.05231.

[64] A. Ashtekar, T. Pawlowski and P. Singh, *Quantum Nature of the Big Bang: Improved dynamics*, Phys. Rev. **D74** (2006) 084003 [gr-qc/0607039].

[65] B. Bahr and S. Steinhaus, *Investigation of the Spinfoam Path integral with Quantum Cuboid Intertwiners*, Phys. Rev. **D93** (2016), no. 10 104029 [1508.07961].

[66] H. T. Johansson and C. Forssén, *Fast and accurate evaluation of wigner 3j, 6j, and 9j symbols using prime factorisation and multi-word integer arithmetic*, SIAM J. Sci. Statist. Comput. **38** (2016) A376–A384 [1504.08329].

Chapter 7

Searching for classical geometries in spin foam amplitudes: a numerical method

Searching for classical geometries in spin foam amplitudes: a numerical method

Pietro Donà,[*]   Francesco Gozzini,[†]   Giorgio Sarno[‡]

CPT, Aix-Marseille Université, Université de Toulon, CNRS, 13288 Marseille, France

June 25, 2020

Abstract

We develop a numerical method to investigate the semiclassical limit of spin foam amplitudes with many vertices. We test it using the Ponzano-Regge model, a spin foam model for three-dimensional euclidean gravity, and a transition amplitude with three vertices. We study the summation over bulk spins, and we identify the stationary phase points that dominate it and that correspond to classical geometries. We complement with the numerical analysis of a four vertex transition amplitude and with a modification of the model that includes local curvature. We discuss the generalization of our results to the four-dimensional EPRL spin foam model, and we provide suggestions for new computations.

1   Introduction and Motivations

Spin foam theory is a Lorentz-covariant and background-independent formulation of the dynamics of loop quantum gravity. The state of the art is the EPRL-FK model, proposed independently by Engle et al [1, 2, 3] and by Freidel and Krasnov [4]. The spin foam partition function, defined on a simplicial triangulation, provides a regularized version of the quantum gravity path integral. The theory introduces transition amplitudes between spin network states on the boundary of the triangulation.

Spin foam theory leads to many interesting results: in the semiclassical limit the single vertex amplitude contains the Regge action, a discrete version of general relativity [5, 6]; the graviton n-point function exhibits the correct scaling [7, 8, 9, 10]; it has physical applications in the study of black hole-to-white hole tunneling processes [11] and quantum cosmological models [12, 13, 14].

With the fast development of computational techniques and resources, numerical methods are becoming of great interest to the quantum gravity community. In the context of spin foam theory, we developed and we keep improving `sl2cfoam`, a C based high-performance library, to evaluate the vertex amplitude of the lorentzian EPRL model. We used the library to numerically confirm the single vertex asymptotics of the amplitude [15]. Different numerical techniques are also employed to analyze the renormalization group flow of the theory [16, 17, 18]. Finding fixed points in the flow and identifying phase transitions would allow us to understand the open question of the diffeomorphism invariance. The evaluation of the transition amplitude with quantum computing methods is under development [19]. Recently the Encyclopedia of Quantum Geometries [20], a public repository for computational projects in quantum gravity, has been created.

However, many questions remain unanswered. The most concerning one is the so-called *flatness problem*, firstly mentioned by Freidel and Conrady [21], and later explored by Bonzom [22] and Hellmann and Kaminski [23]. They argue that the EPRL partition function, in the semiclassical limit, is dominated by classical flat geometries. If confirmed, this would be a clear indication that the simplicity constraints (essentials in reducing topological BF theory to General Relativity) are not imposed correctly, and then the model would be seriously put in question. We strongly believe we will be able to give a definitive answer to this question using numerical techniques.

---

[*]dona@cpt.univ-mrs.fr

[†]gozzini@cpt.univ-mrs.fr

[‡]sarno@cpt.univ-mrs.fr

125

In this paper, we make the first step in this direction. In spin foam literature, the large spin limit of the theory is studied by uniformly rescaling the boundary spins and analyzing the oscillatory behavior of the amplitude. While this approach works for the analytic computation, it is not well suited for numerical analysis. The evaluation of the scaling of a single vertex amplitude is very taxing on computational time and resources. As shown recently in [24], while the small spin regime of the amplitude is entirely under control, the large spins region demands more attention. The estimation of the frequency of the oscillation from the numerical data is hard since, in general, the oscillation is orders of magnitude faster than the sampling rate. Therefore we cannot employ Fourier analysis and we must devise different computational techniques.

We focus on the link between quantum amplitudes and classical geometries, setting aside all the technical complications arising in complex spin foam models. Motivated by the path integral formulation of quantum mechanics, we look at stationary phase points in the bulk spins summation of the spin foam amplitude. We find them numerically evaluating partial sums and running sums of the amplitude. We work with a spin foam amplitude with three vertices and one internal face within the three dimensional $SU(2)$ topological spin foam model. This model was firstly proposed by Ponzano and Regge to describe euclidean three dimensional quantum gravity [25] and it is nowadays well-known and well studied by the quantum gravity community. Therefore, it is the perfect playground for our analysis, as analytical control is crucial to develop new reliable numerical tools. The technique we develop in this work can be immediately generalized to the EPRL model via the decomposition of the amplitude introduced in [26].

The code and the accompanying Mathematica notebooks used for the geometric reconstruction and the data analysis are publicly available [28]. The code used in this paper is written in C and based on the `wigxjpf` [27] and `sl2cfoam` [24] libraries. All the computations are performed on personal laptops using Intel i7-8650U cores and 16 GB of memory in seconds or minutes at most.

2   Propagator in quantum mechanics

In this section, we briefly review the properties of the propagator in the path integral formulation of quantum mechanics. The composition of propagators is analog to the one of vertex amplitudes in spin foam models. Therefore, studying the semiclassical limit in this simple context can be propaedeutic for the analysis performed in the rest of the paper. The transition amplitude of a non-relativistic particle going from the position x_0 at time t_0 to position x_1 at time t_1 with $t_0 < t_1$ can be computed using the path integral formalism as:

$$\mathcal{K}\left(x_1, t_1; x_0, t_0\right) = \int_{x(t_0)=x_0}^{x(t_1)=x_1} \mathcal{D}\left[x(t)\right] \, e^{\frac{i}{\hbar} S[x(t)]} \, , \tag{1}$$

where $S[x(t)]$ is the classical action functional and we integrate over all paths with fixed boundary condition $x(t_0) = x_0$ and $x(t_1) = x_1$. The transition amplitude (1) is also called the *propagator* of the system.

In the semiclassical limit, identified by $\hbar \to 0$, we can evaluate the transition amplitude by performing a stationary phase approximation of the path integral. The equation characterizing the stationary phase condition reads

$$\frac{\delta S}{\delta x} = 0 \, , \tag{2}$$

which is the Euler-Lagrange equation of motion that arise from the least action principle of classical mechanics. This indicates that classical paths dominate the path integral in the semiclassical regime. In this limit, we approximate the transition amplitude with

$$\mathcal{K}\left(x_1, t_1; x_0, t_0\right) \approx \left(\frac{i}{2\pi\hbar} \frac{\partial^2 S[x^c(t)]}{\partial x_0 \partial x_1}\right)^{\frac{1}{2}} \exp \frac{i}{\hbar} S[x^c(t)] \, , \tag{3}$$

where $x^c(t)$ is the classical path (solution of the classical equations of motion) that satisfies the boundary condition $x^c(t_0) = x_0$ and $x^c(t_1) = x_1$. The prefactor, in general, is a function of the Hessian of the action on the stationary phase path. Equation (3) holds for the case of quadratic Lagrangians, we refer to textbooks for the detailed derivation [29]. If multiple classical paths exist (for example in the case of a particle in a box) each one of them contributes to the semiclassical limit of the propagator.

126

The propagator (1) satisfies also a composition property [30]. Given an intermediate time $t_0 < t_m < t_1$ the propagator between the initial and the final point can be expressed as the integral over all the possible intermediate positions of two intermediate transition amplitudes:

$$\mathcal{K}\left(x_1, t_1; x_0, t_0\right) = \int \mathrm{d}x_m\, \mathcal{K}\left(x_1, t_1; x_m, t_m\right) \mathcal{K}\left(x_m, t_m; x_0, t_0\right) \ . \tag{4}$$

Can we apply the stationary phase approximation technique to evaluate the integral over the intermediate positions (4) in the semiclassical limit? It is useful to look at two simple examples first.

Free particle The propagator of a free particle of mass m is given by [30]:

$$\mathcal{K}\left(x_1, t_1; x_0, t_0\right) = \sqrt{\frac{m}{i\hbar\, 2\pi(t_1 - t_0)}}\, \exp \frac{im}{2\hbar}\frac{(x_1 - x_0)^2}{t_1 - t_0} \ . \tag{5}$$

Given an intermediate time $t_0 < t_m < t_1$ the composition property of the propagator (4) results in the equation

$$\mathcal{K}\left(x_1, t_1; x_0, t_0\right) = \int \mathrm{d}x_m\ \frac{m}{i\hbar\, 2\pi\sqrt{(t_1 - t_m)(t_m - t_0)}}\, \exp \frac{im}{2\hbar}\left(\frac{(x_1 - x_m)^2}{t_1 - t_m} + \frac{(x_m - x_0)^2}{t_m - t_0}\right) . \tag{6}$$

In the semiclassical limit, we can compute the integral over intermediate positions and, to find if a point dominates the integral, we search for the stationary of the phase of the integrand

$$\frac{d}{dx_m}\frac{m}{2}\left(\frac{(x_1 - x_m)^2}{t_1 - t_m} + \frac{(x_m - x_0)^2}{t_m - t_0}\right) = 0 \ .$$

The solution to this equation is given by

$$x_m(t_m) = \frac{x_1 - x_0}{t_1 - t_0}\, t_m + \frac{x_0 t_1 - x_1 t_0}{t_1 - t_0} \ ,$$

the position of a non-relativistic free particle at time t_m with boundary conditions $x(t_0) = x_0$ and $x(t_1) = x_1$.

Harmonic oscillator We can perform a similar analysis also for the harmonic oscillator of mass m and frequency ω. The propagator is given by [30]

$$\mathcal{K}\left(x_1, t_1; x_0, t_0\right) = \sqrt{\frac{m\omega}{i\hbar\, 2\pi \sin\omega(t_1 - t_0)}}\, \exp \frac{im\omega}{2\hbar}\frac{(x_0^2 + x_1^2)\cos\omega(t_1 - t_0) - 2x_0 x_1}{\sin\omega(t_1 - t_0)} \ . \tag{7}$$

We can analyze the composition property of the propagator (4) in the semiclassical limit, as in the case of the free particle. We use the stationary phase approximation to evaluate the integral over intermediate positions, and find a stationary phase point if

$$\frac{d}{dx_m}\frac{m\omega}{2}\left(\frac{(x_m^2 + x_1^2)\cos\omega(t_1 - t_m) - 2x_m x_1}{\sin\omega(t_1 - t_m)} + \frac{(x_0^2 + x_m^2)\cos\omega(t_m - t_0) - 2x_0 x_m}{\sin\omega(t_m - t_0)}\right) = 0 \ . \tag{8}$$

This equation is solved by

$$x_m(t_m) = \frac{x_1 \sin\omega(t_0 - t_m) - x_0 \sin\omega(t_1 - t_m)}{\sin\omega(t_0 - t_1)} \ , \tag{9}$$

which is the position of the harmonic oscillator at time t_m with boundary conditions $x(t_0) = x_0$ and $x(t_1) = x_1$.

General case. In the general case an explicit, analytic form for the propagator is not available. To perform the analysis we introduce the following notation: we denote with $S_{t_0}^{t_1}$ the action evaluated between the time t_0 and t_1, and we explicit in the classical solution the boundary condition $x^c(t, x_0, x_1)$ such that $x^c(t_0, x_0, x_1) = x_0$ and $x^c(t_1, x_0, x_1) = x_1$. We then evaluate the propagators in the semiclassical regime (3) in the right hand side of (4) and obtain

$$\mathcal{K}(x_1, t_1; x_0, t_0) \approx \int dx_m \, f(x_0, x_m, x_1) \exp \frac{i}{\hbar} \left(S_{t_0}^{t_m}[x^c(t, x_0, x_m)] + S_{t_m}^{t_1}[x^c(t, x_m, x_1)] \right) \tag{10}$$

where we summarized in $f(x_0, x_m, x_1)$ all the prefactors in (3). We can combine the actions into the action evaluated between the starting and final time t_0 and t_1

$$S_{t_0}^{t_m}[x^c(t, x_0, x_m)] + S_{t_m}^{t_1}[x^c(t, x_m, x_1)] = S_{t_0}^{t_1}[\Theta(t_m - t)x^c(t, x_0, x_m) + \Theta(t - t_m)x^c(t, x_m, x_1)] , \tag{11}$$

joining the two classical solutions on the shared point x_m at time t_m. We know that the classical path $x^c(t, x_0, x_1)$ is an extremum of the action functional $S_{t_0}^{t_1}[x(t)]$, and the "piecewise-classical" test functions in the r.h.s. of (11) correspond to $x^c(t, x_0, x_1)$ precisely when $x_m = x_m^c \equiv x^c(t_m, x_0, x_1)$, i.e. x_m is equal to the classical intermediate position x_m^c. Therefore, x_m^c is a point of stationary phase for (4). The argument is readily extended to the case of multiple solutions of the equations of motions, which will result in multiple intermediate stationary points, see Fig. 1
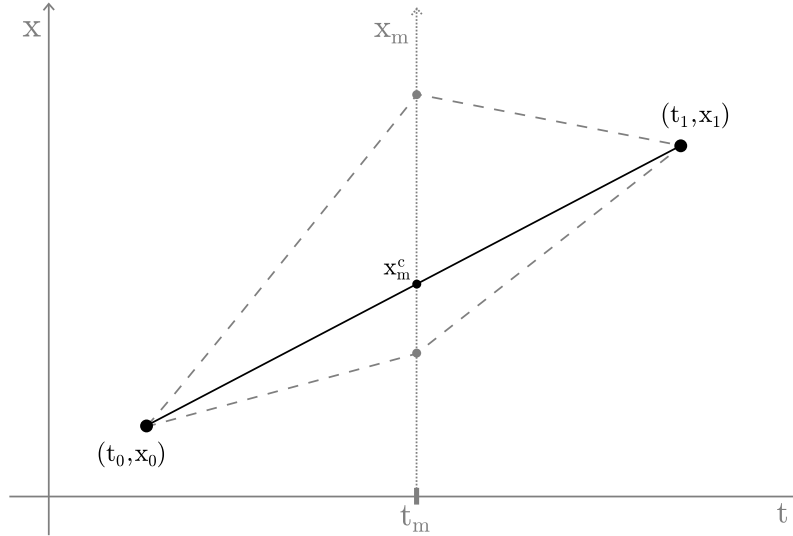

Figure 1: *A graphical representation of (11) in the case of a free particle. The path integral is performed along all "piecewise-classical" paths joining at the intermediate time t_m. The integral is dominated by the stationary phase point corresponding to the solution of the classical equations of motion, the straight black continuous line in the picture.*

3   Euclidean three dimensional spin foam model

General relativity in three space-time dimensions has no propagating gravitational degrees of freedom. It is an example of topological BF theory and the spin foam quantization program can be easily implemented. The theory is still of relevant interest for us since we can use it to address many conceptual issues of spin foam theory in a simple framework. In this section, we will briefly review the construction of the euclidean three dimensional topological spin foam model. We refer to [31, 32] for a detailed and complete presentation of BF theories and their relation to spin foams.

Formally we write the partition function of the three dimensional BF theory (in the first-order formalism)

$$\mathcal{Z} = \int \mathcal{D}[e]\mathcal{D}[\omega] \exp(i \int_{\mathcal{M}} Tr(e \wedge F(\omega)) , \tag{12}$$

where the manifold $\mathcal{M}$ is assumed to be compact and orientable, ω is an $SU(2)$ connection and the triad field e is a 1-form taking values on the $SU(2)$ algebra. $F(\omega)$ is the curvature of the connection ω. We can perform the functional integration over the triad field e in (12) obtaining the expression

$$\mathcal{Z} = \int \mathcal{D}[\omega]\delta(F(\omega)) \ . \tag{13}$$

The partition function of the theory is the integral over all the flat connections $(F(\omega) = 0)$ on $\mathcal{M}$. The above expression is formal, so to make it concrete we discretize the manifold (M) using a triangulation Δ. The triangulation Δ defines an abstract two-complex Δ^* given by a set of vertices (dual to the tetrahedra of Δ), edges (dual to triangles of Δ) and faces (dual to segments of Δ). The connection ω is represented by g_e the holonomy along each edge e of Δ^*. The discrete partition function reads

$$\mathcal{Z}(\Delta) = \int \prod_e dg_e \prod_f \delta(g_{e_1} \dots g_{e_n}) \ , \qquad \text{with } e_i \subset f \tag{14}$$

where dg_e is the Haar measure over $SU(2)$, δ is the Dirac delta function on $SU(2)$ and the product $g_{e_1} \dots g_{e_n}$ is the holonomy around the face f of Δ^*. The delta function constrains the holonomy around each face to be the identity, this is equivalent to parallel transporting around the face with a flat connection. We can expand the $\delta(g)$ function on the basis of Wigner functions $D^j(g)$ using the Peter-Weyl theorem $\delta(g) = \sum_j (2j+1)Tr(D^j(g))$. The partition function then becomes

$$\mathcal{Z}(\Delta) = \sum_{j_f} \int \prod_e dg_e \prod_f (2j_f + 1)Tr(D^{j_f}(g_{e_1} \dots g_{e_n})) \tag{15}$$

$$= \sum_{j_f} \prod_f (2j_f + 1) \prod_v \ \begin{array}{c}\text{[graphical diagram]}\end{array} \ . \tag{16}$$

We introduced a graphical notation for representing spin foam amplitudes. Edges are made of strands, each strand is a representation matrix of $SU(2)$, each box on an edge is an integral over the $SU(2)$ group element associated to that edge. We re-organized the product over faces as a product over vertices that are connected to each other following the connectivity of the two-complex Δ^*. The integrals over $SU(2)$ can be performed exactly and expressed in terms of $SU(2)$ invariants. The resulting spin foam partition function is usually presented in the following form

$$\mathcal{Z}(\Delta) = \sum_{j_f} \prod_f A_f \prod_e A_e \prod_v A_v \tag{17}$$

where the sum is over all the possible quantum numbers of the product of face amplitudes A_f, edge amplitudes A_e and vertex amplitudes A_v. The spin foam model for three dimensional euclidean gravity is given by trivial edge amplitude $A_e = 1$, face amplitude equal the the SU(2) irrep dimension $A_f = 2j_f + 1$ and vertex amplitude given by the Wigner $\{6j\}$ symbol of the six spins entering that vertex

$$A_v = \left\{ \begin{array}{ccc} j_1 & j_2 & j_3 \\ j_4 & j_5 & j_6 \end{array} \right\} = \ \begin{array}{c}\text{[graphical diagram]}\end{array} \ . \tag{18}$$

We use the same convention and notation of [33] for the evaluation and definition of $SU(2)$ invariants and their graphical representation. The orientation of the $\{6j\}$ symbol needs to be picked carefully and coherently in the whole amplitude [34] [1]

---

[1]In [34] the vertex amplitude has a phase for every node with a bulk spin. In our graphical notation this corresponds to change a sign on that particular $\{6j\}$ symbol node. We prefer to fix a triangulation and then to glue the tetrahedra in a coherent way, see Appendix A for an explicit computation.

The spin foam model we derived above reproduces the transition amplitude between quantum geometries first proposed in the 60s by Ponzano and Regge [25]. They were motivated by their discovery of the large spins asymptotic formula of the $\{6j\}$ symbol. If an euclidean tetrahedron with lengths given by $j_f + 1/2$ exists, namely its squared volume is positive $V^2 > 0$, then:

$$A_v \sim \frac{1}{\sqrt{12\pi V}} \cos(S_{\mathcal{R}}(j_f) + \frac{\pi}{4}) \; , \qquad (19)$$

where $S_{\mathcal{R}}$ is the Regge action of the tetrahedron, given by

$$S_{\mathcal{R}}(j_f) = \sum_f (j_f + \frac{1}{2})\Theta_f \; . \qquad (20)$$

and Θ_f are the external dihedral angles of the tetrahedron. If such euclidean tetrahedron does not exist, namely if $V^2 < 0$, the amplitude is exponentially suppressed.

Regge calculus [35] provides a discretized version of general relativity on a triangulation. Thanks to (19), the Ponzano-Regge model in the large spin limit shows a clear connection to (discrete three dimensional euclidean) general relativity and, therefore, can possibly describe a quantum theory of gravity. The derivation of the model from topological three dimensional BF theory was formulated later [36]. A first numerical check of formula (19) was put forward in the original paper. However, thanks to the technological progresses of the last half-century, testing the formula for arbitrary large spins is now accessible to any personal computer, see Fig. 2.
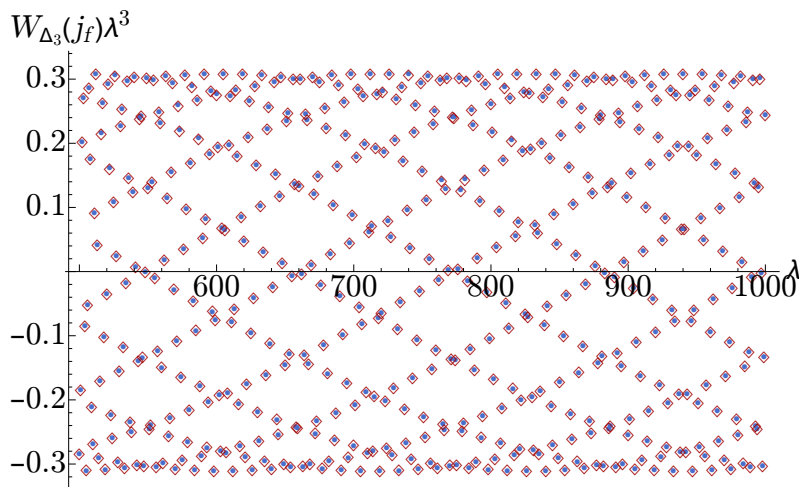

Figure 2: *Uniform scaling of the Ponzano-Regge vertex amplitude for spins $j_1 = j_2 = j_3 = \lambda$ and $j_4 = j_5 = j_6 = 2\lambda$ for a scaling parameter λ between 500 and 1000. The red diamonds are the values of the $\{6j\}$ symbol while the blue dots are the values of the asymptotic formula (19).*

A key feature of the Ponzano-Regge model is its formal triangulation independence: the amplitude is preserved by any Pachner move (a local change of the triangulation that does not modify the topology) up to a divergent overall factor. We can understand this invariance as the discrete equivalent of diffeomorphism invariance of the classical theory. The divergences can be explained as a residual action of the diffeomorphisms group acting on the triangulation [37]. They can be regularized with an appropriate gauge fixing procedure of by trading the $SU(2)$ group for its quantum counterpart. The model obtained in this way is the so-called Turaev-Viro model[38] and is usually interpreted as a three-dimensional quantum gravity model with a non-vanishing cosmological constant.

4 The Δ_3 transition amplitude

In this paper, we focus on the Δ_3 triangulation formed by three tetrahedra sharing a common segment. In Figure 3 we represent the corresponding dual 2-complex. It consists of three vertices, one bulk face, and

nine boundary faces. This triangulation is the simplest one with a single bulk face.

Six triangles joined by all their sides form the boundary of the triangulation. Therefore, the boundary graph consists of six 3-valent nodes joined by all their links. The nine links, colored with spins $j_1, \ldots, j_9$, are dual to segments of the triangulation. We denote with x the spin associated with the bulk face.
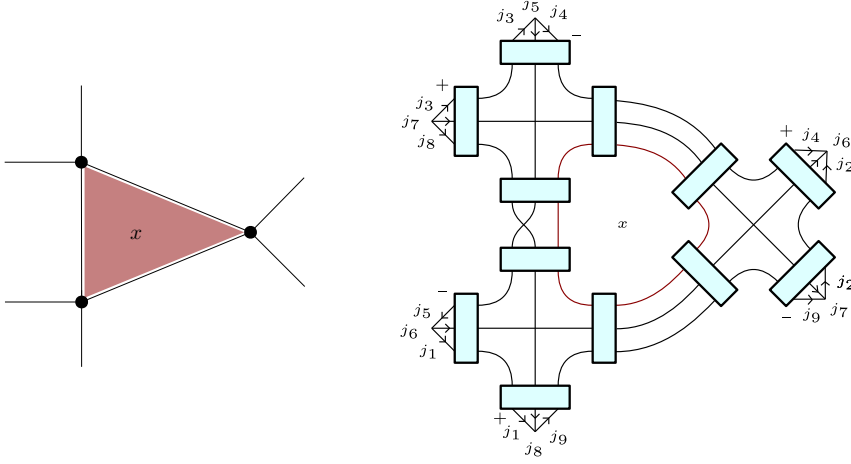

Figure 3: *Left: The 2-complex dual to the Δ_3 triangulation. We highlighted in red the internal face. Right: Spin foam diagram of the transition amplitude associated to the Δ_3 triangulation. We picked a conventional orientation for the faces and we denoted as boxes the integrals over the $SU(2)$ group.*

Following the prescriptions given in Section 3 we can write the Δ_3 transition amplitude for the Ponzano-Regge model

$$W_{\Delta_3}(j_f) = (-1)^{\chi} \sum_x (-1)^x (2x+1) \left\{ \begin{array}{ccc} j_5 & j_8 & x \\ j_9 & j_6 & j_1 \end{array} \right\} \left\{ \begin{array}{ccc} j_9 & j_6 & x \\ j_4 & j_7 & j_2 \end{array} \right\} \left\{ \begin{array}{ccc} j_4 & j_7 & x \\ j_8 & j_5 & j_3 \end{array} \right\} \tag{21}$$

where $\chi = \sum_{f=1}^{9} j_f$ is a consequence of the convention we used for the boundary data. We report a detailed derivation of (21) in Appendix A. Because of triangular inequalities the summation over the bulk spin is bounded by $x_{min} = \text{Max} \{|j_4 - j_7|, |j_5 - j_8|, |j_6 - j_9|\}$ and $x_{max} = \text{Min} \{j_4 + j_7, j_5 + j_8, j_6 + j_9\}$. [2]

5 Numerical analysis

Is the summation over the bulk spin x (21) dominated by some specific value of x? The question is similar to the one we asked in Section 2 for a one-dimensional quantum mechanical system. However, since we are interested in finding a technique applicable to any spin foam model, where analytical computation is, in general, not possible or challenging, we resort to numerical methods.

The evaluation of the amplitudes presented in this paper is performed using a C code and is based on wigxjpf, a high-performance library to efficiently compute and store $\{6j\}$ symbols with very high spins [27]. Computations of the amplitudes take from seconds to minutes depending on the order of magnitude of the spins. It is also interesting to point out that some numerical computations were already present in the original paper by Ponzano and Regge.

In this work we develop a technique to determine if any bulk spin dominate the Δ_3 transition amplitude (21) with very large boundary spins j_f. We study the terms $w_{\Delta_3}(j_f, x)$ of the summation (21):

$$w_{\Delta_3}(j_f, x) = (-1)^x (2x+1) \left\{ \begin{array}{ccc} j_5 & j_8 & x \\ j_9 & j_6 & j_1 \end{array} \right\} \left\{ \begin{array}{ccc} j_9 & j_6 & x \\ j_4 & j_7 & j_2 \end{array} \right\} \left\{ \begin{array}{ccc} j_4 & j_7 & x \\ j_8 & j_5 & j_3 \end{array} \right\} . \tag{22}$$

We start by plotting $w_{\Delta_3}(j_f, x)$ for all the admitted values of the bulk spin x in Figure 4. By visual inspection, we observe some interesting features. The function is highly oscillating, therefore we expect cancellations

---

[2]Formula 21 can be manipulated into the reducible $\{9j\}$ symbol as shown at page 466 of [33]. The irreducible $\{9j\}$ symbol has a different spin connectivity and a different geometrical interpretation, see [39].

to play a crucial role. Moreover, starting from the center and going towards larger or smaller spins, the function seems to increase in average absolute value until two particular values of x. Beyond those values, the function becomes exponentially small. These two particular points correspond to the last set of (large) spins in the classically allowed region of all the $\{6j\}$ symbols, see [39] for more details. After those points the spins of at least one of the $\{6j\}$ symbols is classically forbidden[3] and therefore we have an exponential suppression of w_{Δ_3}.
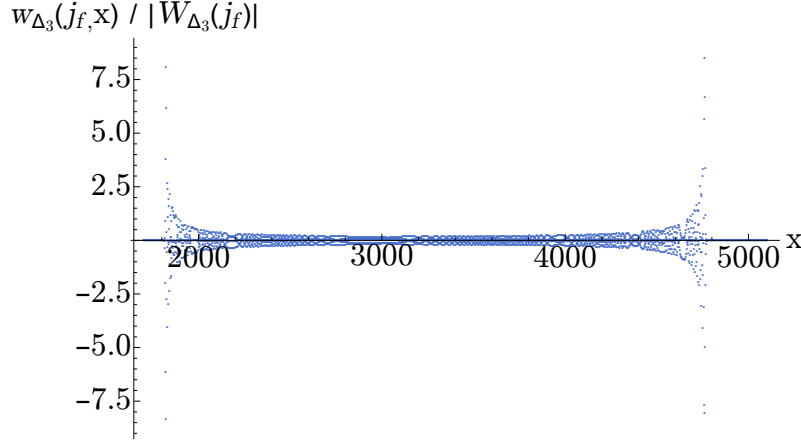

Figure 4: *Discrete plot of the function w_{Δ_3} as a function of the bulk spin x for the boundary spins $j_1 = j_2 = j_3 = j_7 = j_8 = j_9 = \lambda$ and $j_4 = j_5 = j_6 = 2\lambda$ with $\lambda = 1700$. We highlight with red vertical lines the position of the stationary phase points.*

The stationary phase approximation is an essential technique to evaluate integrals of rapidly oscillating functions. Given a one dimensional integral

$$\mathcal{I} = \int dx \, g(x) e^{i\lambda f(x)} \, , \tag{23}$$

we can approximate it with a sum of contributions from points where the derivative of the oscillatory phase f vanish, i.e. stationary phase points

$$\mathcal{I} = \sum_y \sqrt{\frac{2\pi}{\lambda |f''(y)|}} g(y) + o(\lambda^{-1/2}) \, , \qquad \text{where} \qquad f'(y) = 0 \, . \tag{24}$$

At the leading order, the result of the integration does not depend on the specific form of the integration domain, as long as it contain the same stationary phase points

$$\mathcal{I} = \sum_y \int_{I_y} dx \, g(x) e^{i\lambda f(x)} + o(\lambda^{-1/2}) \tag{25}$$

where I_y is a neighborhood of the stationary phase point y.

Inspired by the stationary phase analysis for one-dimensional integrals, we look for points with similar properties in the discrete. First, we look at the partial sum

$$P_w(j_f, x) = \sum_{x'=x_{min}}^{x} w_{\Delta_3}(j_f, x') \, , \tag{26}$$

where we sum over the internal spin up to a variable cutoff x. If there are no stationary phase points of w_{Δ_3} in the interval $[x_{min}, x]$ then we expect the partial sum to vanish due to destructive interference. However,

---

[3]It is not possible to construct a euclidean tetrahedron with those spins as lengths.

increasing x we expect to observe a significant change of the value of the partial sum $P_w(j_f, x) \neq 0$ every time $[x_{min}, x]$ includes a new stationary phase point. In Figure 5 we observe this behavior.
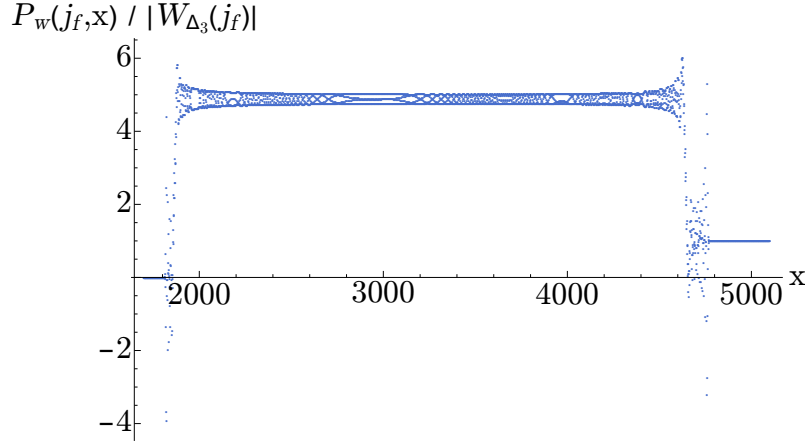

$P_w(j_f,\text{x}) \; / \; |W_{\Delta_3}(j_f)|$

Figure 5: *Numerical analysis of the partial sum $P_w(j_f, x)$ as a function of the bulk spin x with boundary spins $j_1 = j_2 = j_3 = j_7 = j_8 = j_9 = \lambda$ and $j_4 = j_5 = j_6 = 2\lambda$ with $\lambda = 1700$ normalized to the value of the amplitude $W_{\Delta_3}(j_f)$.*

Analogously, we define the running sum

$$R_w(j_f, x) = \sum_{I_x^c} w_{\Delta_3}(j_f, x') \tag{27}$$

where the sum is performed on an interval $I_x^c = |x' - x| < c$ centered in x and of width $2c$. For large j_f we expect the running sum to vanish unless a stationary phase point is included in I_x^c. Tuning the size of the interval c sufficiently small we can assume to have at most one critical point in I_x^c. As a function of the center of the interval x the running sum $R_w(j_f, x)$ is extremal at the stationary phase points.

Estimating the location of the stationary phase points from the running sum is, in general, a difficult task. We implemented an algorithm that resulted in being reliable in all the cases we analyzed. We pick three interval sizes c_1, c_2, c_3 uniformly at random. We should not choose the interval size too small, to allow cancellations between $w_{\Delta_3}(j_f, x')$ in I_x^c, or too large, to retain enough resolution in the center of the interval x. With this in mind, we decided to limit the possible interval sizes to a reference interval size $c = \sqrt{x_{max} - x_{min}}/2$ (equal to half of the square root of the number of the available data points) plus or minus 25%. We compute the running sum for all three values of c_i, multiply them and consider the absolute value:

$$\overline{R_w(j_f, x)} = |R_w(j_f, x)_1 R_w(j_f, x)_2 R_w(j_f, x)_3| . \tag{28}$$

This step aims at eliminating as much as possible the dependence from the choice of the interval size. At the same time, this procedure has the effect of smoothing the oscillations around the peaks. They are an artifact of the finite interval size, and they interfere destructively when multiple running sums are multiplied together. We proceed by discarding the points of $\overline{R_w(j_f, x)}$ that in absolute value are smaller then the 0.1% of the of the absolute maximum. At this step, we use Mathematica's statistical tools to analyze $\overline{R_w(j_f, x)}$ and extract the positions of the peaks. We iterate this procedure ten times (with different random choices of interval sizes c_i each time) and compute the average and standard deviation of the resulting peak position estimates. The Mathematica notebooks used to estimates the locations of the stationary phase points in all the amplitudes analyzed in this paper are publicly available [28].

Given a spin foam amplitude with one bulk face, we summarize the algorithm we propose to find the stationary phase points in the bulk sum in the following
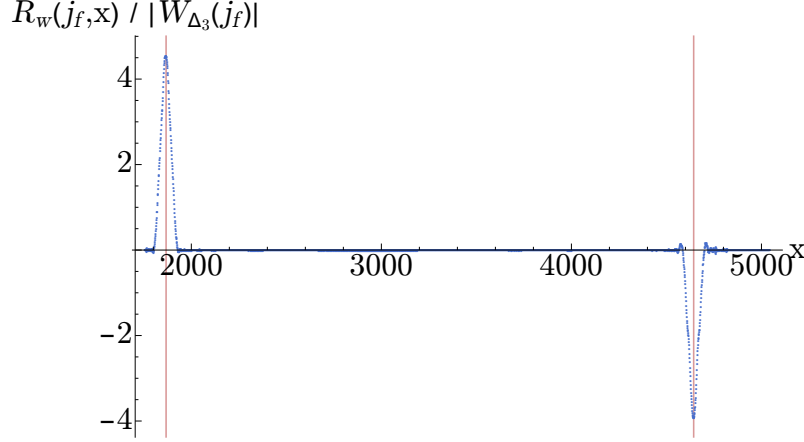
$R_w(j_f,\text{x}) \, / \, |W_{\Delta_3}(j_f)|$

Figure 6: *The running sum $R_w(j_f, x)$ as a function of the bulk spin x with boundary spins $j_1 = j_2 = j_3 = j_7 = j_8 = j_9 = \lambda$ and $j_4 = j_5 = j_6 = 2\lambda$ with $\lambda = 1700$ normalized to the value of the amplitude $W_{\Delta_3}(j_f)$. With highlight the stationary phase points detected by our numerical method (29) with two red lines. We used the reference interval size equal to half the square root of the number of data points.*

Algorithm 1 Numerical algorithm to estimate the stationary phase points in spin foam amplitudes.

1: Choose a set of boundary spins and compute all the terms of the sum over the bulk spin x
2: **repeat** the peak position estimate
3:   Compute a reference interval size $c = \sqrt{x_{max} - x_{min}}/2$
4:   Select three interval sizes c_i uniformly at random in $[0.75, 1.25]c$
5:   Compute the running sums with interval size c_i and multiply them together
6:   Take the absolute value and obtain $\overline{R_w(j_f, x)}$
7:   Set a threshold (e.g. 0.1% of the largest peak) and ignore smaller values of $\overline{R_w(j_f, x)}$
8:   Use a peak finding algorithm to determine the peaks of $\overline{R_w(j_f, x)}$
9: **until** 10 times
10: Compute the mean and the standard deviation of the peaks for different interval sizes
11: They estimate the stationary phase points of the amplitude and their errors

---

The procedure is completely general and can be applied for any choice of boundary spins j_f. As a concrete example, we analyzed the amplitude (21) with a specific choice of boundary spins. We choose high spins because we expect the stationary phase points to be fairly evident, the stationary phase approximation being an asymptotic approximation. We do not choose the case with all equal spins since one stationary phase point will be located at $x = 0$, thus making the analysis confusing. A minimal variation from the equal-spin case is given by $j_1 = j_2 = j_3 = j_7 = j_8 = j_9 = \lambda$ and $j_4 = j_5 = j_6 = 2\lambda$ with a scale factor fixed at $\lambda = 1700$. Applying the algorithm 1 described in this section we can estimate the position of the two stationary phase points

$$x_1 = 1866 \pm 3 \qquad x_2 = 4644 \pm 3 \ . \tag{29}$$

We compare them with their analytic values in the next section. To illustrate the result of our algorithms we superimpose the values of the stationary phase points (29) to the running sum in Figure 6.

In this section, we performed computations with a huge scale factor of $\lambda = 1700$. While this is ideal for observing the stationary phase points cleanly, the same regime is out of reach for the $SL(2, \mathbb{C})$ EPRL model and the technical tools available to us. At very low boundary spins all bulk spins are important to evaluate the amplitude. However, the presence of stationary phase points in the partial sum is evident already at spins of order ~ 30. We repeat the calculation for a scale factor $\lambda = 30, 40, 50, 60$ and we report it in Figure 7 together with the position of the two saddle points obtained with our numerical analysis in Table 30. From the final value of the partial sum that can be read off these four snapshots at different scale factors, one can also spot the oscillation of the amplitude.

This result is significant. In analogy to the results on a single vertex [40] we show that the semiclassical regime is reached at relative low spins that we can explore numerically.
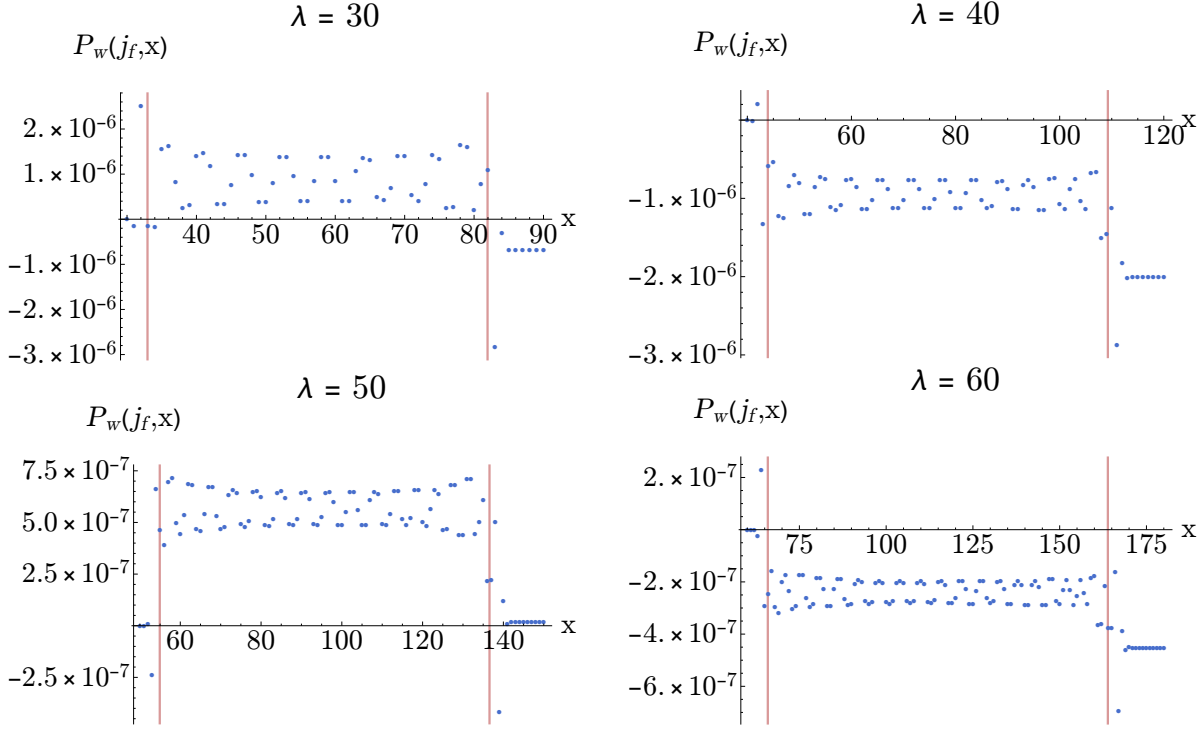

Figure 7: *Partial sum $P_w(j_f, x)$ as a function of the bulk spin x with boundary spins $j_1 = j_2 = j_3 = j_7 = j_8 = j_9 = \lambda$ and $j_4 = j_5 = j_6 = 2\lambda$ and scale factors $\lambda = 30, 40, 50, 60$. Notice the change of value of the partial sum in correspondence of the two stationary phase points obtained with our algorithm. It is evident also for these low values of the scaling parameter.*

Using our algorithm, we obtain the following estimates for the position of the stationary phase points at low spins. We compare them with their analytic counterpart in the next section.

$$
\begin{aligned}
&\lambda = 30 : &&x_1 = 34 \pm 3 &&x_2 = 82 \pm 1 &&\text{(30)}\\
&\lambda = 40 : &&x_1 = 45 \pm 2 &&x_2 = 109 \pm 1 \\
&\lambda = 50 : &&x_1 = 57 \pm 2 &&x_2 = 137 \pm 1 \\
&\lambda = 60 : &&x_1 = 67 \pm 2 &&x_2 = 164 \pm 1
\end{aligned}
$$

The numerical analysis we proposed in this section is adapted to spin foam amplitudes with one bulk face like (21). Our algorithm can be extended to spin foam amplitudes with multiple bulk faces. Instead of describing the general strategy let us consider the example of an amplitude with two internal faces

$$W_\Delta(j_f) = \sum_{x,y} w_\Delta(j_f, x, y) . \tag{31}$$

First we apply our analysis to

$$wx_\Delta(j_f, x) = \sum_y w_\Delta(j_f, x, y) , \tag{32}$$

and find the x coordinate of the stationary phase point candidates. Say, for example, that we find two of such points x_1 and x_2. We now repeat our analysis to

$$wy_\Delta(j_f, y) = \sum_x w_\Delta(j_f, x, y) , \tag{33}$$

135

and find the y coordinate of the stationary phase point candidates. At this stage we have four different stationary phase point candidates (x_1, y_1), (x_1, y_2), (x_2, y_1), (x_2, y_2). If, for example, (x_1, y_1) is a stationary phase point but (x_2, y_1) is not, our algorithm applied to

$$wx'_\Delta(j_f, x) = \sum_{I^{c_x}_{y_1}} w_\Delta(j_f, x, y) , \tag{34}$$

for some interval size c_x will result in a peak detection only for x_1 but not x_2. Analogously, if, for example, (x_2, y_2) is a stationary phase point but (x_1, y_2) is not, our algorithm applied to

$$wx''_\Delta(j_f, x) = \sum_{I^{c_y}_{y_2}} w_\Delta(j_f, x, y) , \tag{35}$$

for some interval size c_y will result in a peak detection only for x_2 but not x_1. This procedure can be iterated for any number of bulk faces ($\#faces$) and any number of stationary phase points ($\#ssp$). However, it could be resources intensive to find the true stationary phase points among the $(\#ssp)^{\#faces}$ candidates.

Our numerical procedure has two significant advantages that will prove to be crucial in the analysis of more complicated spin foam models. The terms of the summations need to be computed only once; the rest of the algorithm consists only in performing partial summations. Moreover, the peak detection algorithm is applied only on one-dimensional summations, therefore, we do not need to adapt it case by case.

6 Geometrical interpretation

The two stationary phase points we identified with our numerical analysis have an interesting geometric interpretation. For large spins $j_f \gg 1$ we can also assume that x is large [4]. Therefore, in the expression for the amplitude (21), we approximate each vertex amplitude with its asymptotic expression (19) in terms of the Regge action of the classical tetrahedron with edge lengths equal to spins, as already shown in [25]. If we denote the three vertex amplitudes as A_1, A_2, A_3 and the corresponding Regge actions as S_1, S_2, S_3 the summand (22) reads:

$$w_{\Delta_3}(x) = (-1)^x(2x+1)A_1(x)A_2(x)A_3(x) \propto (-1)^x \cos\left(S_1(x) + \frac{\pi}{4}\right)\cos\left(S_2(x) + \frac{\pi}{4}\right)\cos\left(S_3(x) + \frac{\pi}{4}\right) , \tag{36}$$

where we left implicit the dependence on the boundary spins j_f and we isolated the oscillatory part of the function summarizing the amplitudes as A_f. Furthermore, motivated by the numerical analysis in the previous section, we assume that the bulk spins x can assume continuous values to perform a stationary phase point computation.

If we rewrite the cosines as a sum of conjugated exponentials, we obtain for the summand

$$w_{\Delta_3}(x) \propto e^{i\pi x}\left(e^{i\,(S_1(x)+S_2(x)+S_3(x)+\frac{3}{4}\pi)} + e^{i\,(S_1(x)+S_2(x)-S_3(x)+\frac{\pi}{4})} \right.$$
$$\left. + e^{i\,(S_1(x)-S_2(x)+S_3(x)+\frac{\pi}{4})} + e^{i\,(-S_1(x)+S_2(x)+S_3(x)+\frac{\pi}{4})} + c.c. \right) , \tag{37}$$

where we used an exponential notation for the phase $(-1)^x = e^{i\pi x}$. By linearity, we can search for stationary phase points of each of the eight terms in (37) independently and sum the results. The stationary phase equation for the first term is the following

$$\frac{d}{dx}\left(\pi x + S_1(x) + S_2(x) + S_3(x)\right) = 0 , \tag{38}$$

and analog equations hold for all the other seven terms of (37) that differ for different signs in front of the Regge actions. The derivative of the actions $S_i(x)$ with respect to one spin (edge length) has been computed

---

[4]Under a uniform rescaling of the spins $j_f \to \lambda j_f$ also the bounds of the summation rescale in the same way $x_{min} \to \lambda x_{min}$ and $x_{max} \to \lambda x_{max}$.

in [35] and reads

$$\frac{dS_i}{dx} = \frac{d}{dx} \sum_f j_f \Theta^i_f(x) = \Theta^i_x + \sum_f j_f \frac{d}{dx} \Theta^i_f(x) = \Theta^i_x \ , \tag{39}$$

where Θ^i_f is the external dihedral angle in the tetrahedron i relative to the edge f. The total variation of the dihedral angles with respect to the edge lengths is zero [35, 25]. Therefore, the stationary phase equation for the first term of (37) is

$$\pi + \Theta^1_x + \Theta^2_x + \Theta^3_x = 0 \ . \tag{40}$$

and the other seven are similar. The presence of terms with all the possible signs was discussed in [25] and is associated with all the possible orientations of the tetrahedra. Moreover, in [25] it was also proved that in general there are at most two solutions to this set of stationary phase equations.

Geometrically, the two values of x that solve (40) correspond to the only two geometries made of three tetrahedra glued together following the connectivity of Δ_3 that are embeddable in flat euclidean three dimensional space. Notice that (40) is equivalent to require the deficit angle around the bulk edge to vanish. We interpret equation (40) as the one responsible, in the large spin limit, for selecting flat classical geometries compatible with the boundary data.

In the case of the boundary data used in our numerical study the only relevant stationary phase equation is (40). Its two solutions are

$$x_1 = \lambda \frac{1}{3}(\sqrt{33} - \sqrt{6}) \approx 1867.2 \qquad x_2 = \lambda \frac{1}{3}(\sqrt{33} + \sqrt{6}) \approx 4643.3 \tag{41}$$

and correspond to the two geometries rendered in Figure 8 and 9.

We can compare them with their numerical estimates (29) and notice they are compatible within the allowed numerical uncertainty.
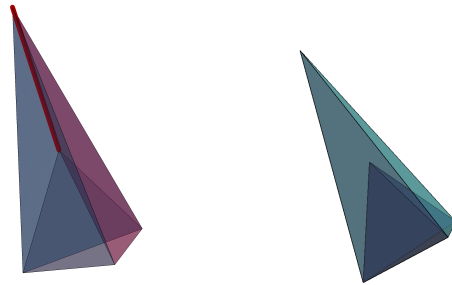

Figure 8: *Left: Classical flat geometry corresponding to the solution x_1 of the stationary phase equations. The three tetrahedra are glued together and share an internal segment (in red). Right: The same geometry can be interpreted as two tetrahedra sharing a triangle.*
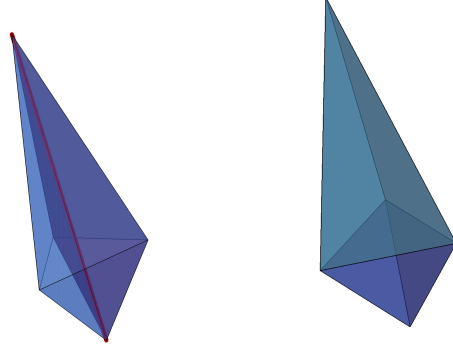
Figure 9: *Left: Classical flat geometry corresponding to the solution x_2 of the stationary phase equations. The three tetrahedra are glued together and share an internal segment (in red). Right: The same geometry can be interpreted as the subtraction of two tetrahedra sharing a triangle.*

Using the invariance under change of triangulation of the Ponzano-Regge model, we can perform exactly the summation in (21):

$$W_{\Delta_3}(j_f) = \left\{ \begin{array}{ccc} j_1 & j_2 & j_3 \\ j_4 & j_5 & j_6 \end{array} \right\} \left\{ \begin{array}{ccc} j_1 & j_2 & j_3 \\ j_7 & j_8 & j_9 \end{array} \right\} . \tag{42}$$

This formula is also known as Biedenharn-Elliott identity. We apply the asymptotic formula (19) to the right-hand side of (42) in the large spin limit. The emerging three dimensional geometry is a combination of two tetrahedra, one per $\{6j\}$ symbol, sharing a face:

$$W_{\Delta_3}(j_f) \approx A_u A_d \cos\left(S_u + \frac{\pi}{4}\right) \cos\left(S_d + \frac{\pi}{4}\right) = \frac{A_u A_d}{2} \cos\left(S_u + S_d + \frac{\pi}{2}\right) + \frac{A_u A_d}{2} \cos\left(S_u - S_d\right) \tag{43}$$

where in the last equality we used a trigonometric identity. The two terms can be interpreted as two different geometries. The Regge actions of the two tetrahedra S_u and S_d are summed in the first term $S_+ = S_u + S_d$, reproducing the Regge action of the first geometry in Figure 8. The second term contains the difference $S_- = S_u - S_d$, the Regge action of the second geometry in Figure 9. The minus sign is crucial to reproduce the correct dihedral angles around the edges shared by the two tetrahedra.

Already for small values of the scale parameter $\lambda = 30, 40, 50, 60$ we observe good agreement between the analytical calculation of the stationary phase points (41) with our numerical estimate (30). We report both of them in the table below for the convenience of the reader. This is a strong indication that our method is robust even at low spins.

	numerical		analytic	
	x_1	x_2	x_1	x_2
$\lambda = 30:$	34 ± 3	82 ± 1	32.9	81.9
$\lambda = 40:$	45 ± 2	109 ± 1	43.9	109.2
$\lambda = 50:$	57 ± 2	137 ± 1	54.9	136.6
$\lambda = 60:$	67 ± 2	164 ± 1	65.9	163.9

7 Disentangling classical geometries

From (43) we deduced that the two classical geometries emerging from the stationary phase analysis of the bulk summation of (21) could also be extracted from a uniform rescaling of the boundary spins. Numerically, we can compare the asymptotic formula (43) with the amplitude (21) and find perfect agreement, see Fig. 10.
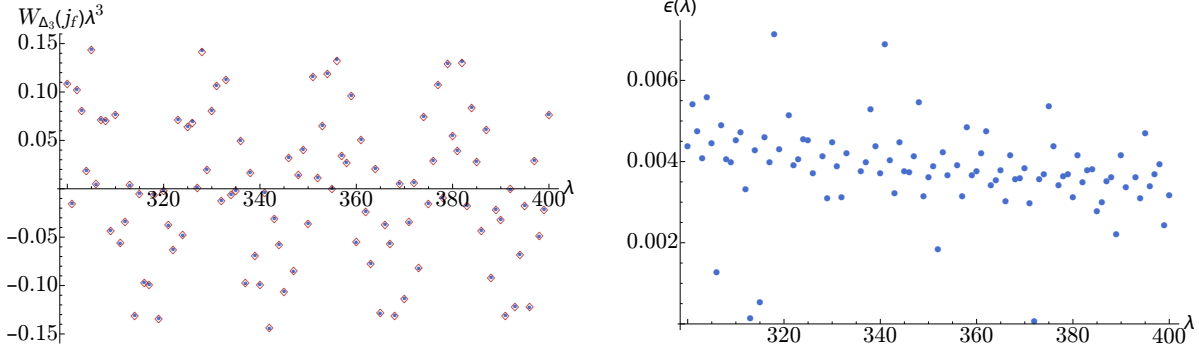
Figure 10: *Left: The asymptotic limit of the Δ_3 amplitude for the considered isosceles configuration with spins equal to λ and 2λ. We use red diamonds to represent the numerical evaluation of the amplitude and blue dots to represent the analytical asymptotic expression given by 43. Right: The relative error $\epsilon(\lambda) = |W_{\Delta_3}^{num}(\lambda j_f) - W_{\Delta_3}^{asym}(\lambda j_f)|/|W_{\Delta_3}^{asym}(\lambda j_f)|$ between the numerical evaluation of the amplitude and the analytic asymptotic formula.*

Is it possible to isolate different oscillatory contributions in the large spin regime? A consequence of the stationary phase analysis discussed in Section 5 is the following. If we limit the sum over the bulk spin in an interval centered around one of the stationary phase points corresponding to a classical geometry (cl) we obtain a function that asymptotically oscillate with a frequency equal to its Regge action. We define

$$W_{cl}(j_f) = \sum_{|x-x_{cl}|<\delta} (-1)^x (2x+1) \left\{ \begin{matrix} j_5 & j_8 & x \\ j_9 & j_6 & j_1 \end{matrix} \right\} \left\{ \begin{matrix} j_9 & j_6 & x \\ j_4 & j_7 & j_2 \end{matrix} \right\} \left\{ \begin{matrix} j_4 & j_7 & x \\ j_8 & j_5 & j_3 \end{matrix} \right\} \approx A_{cl} \cos\left(S_{cl} + \phi_{cl}\right)$$

(44)

where δ will depend on both the boundary spins and the scaling parameter. In the limit of infinite scaling parameter, the dimension of the interval can be set as small as possible. However, for a finite scaling parameter, we need to choose δ empirically.

We numerically evaluated (44) with boundary spins $j_1 = j_2 = j_3 = j_7 = j_8 = j_9 = \lambda$ and $j_4 = j_5 = j_6 = 2\lambda$ and all scale factors between $\lambda = 1000$ and $\lambda = 1100$. We fix the parameter $\delta = 4\sqrt{x_{max} - x_{min}}$ and we consider both $x_{cl1} = \lambda(\sqrt{33} + \sqrt{6})/3$ and $x_{cl2} = \lambda(\sqrt{33} - \sqrt{6})/3$. We report the comparison between the analytic formula (44) with the actions determined in (43) and the numeric evaluation in Figure 11.
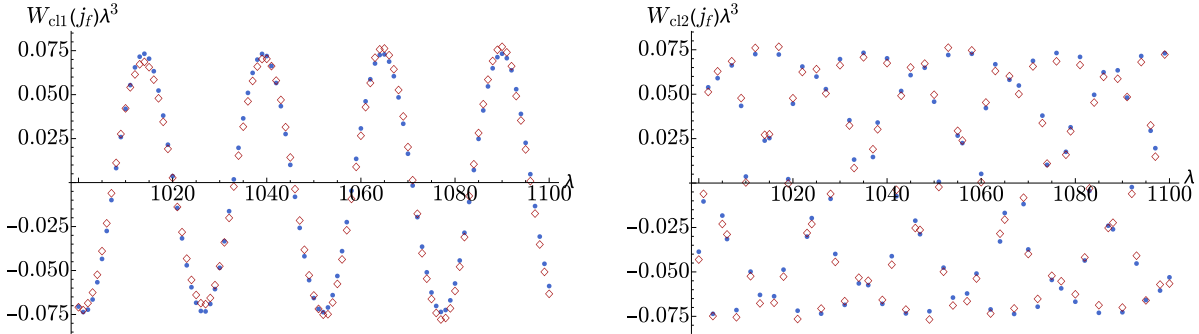

Figure 11: *The asymptotic limit W_{cl} with the scale parameter λ between 1000 and 1100. The red diamonds are the numerical data and the blue dots are the analytical formula. Left: We show the good agreement between the asymptotic formula (44) for the first classical geometry defined by x_{cl1} and the numerical data obtained while summing around it. Right: We show the good agreement between the asymptotic formula (44) for the second classical geometry defined by x_{cl2} and the numerical data obtained while summing around it.*

8   More than three vertices

The numerical analysis developed in Section 5 apply directly to any spin foam amplitude with one bulk face. In this Section we will consider the triangulation Δ_4. This consists of four tetrahedra sharing a common

segment. The dual two-skeleton consists of four vertices, one bulk face, and twelve boundary faces. We associate to each boundary face a spin j_f with $f = 1, \ldots, 12$ and we denote the bulk face as x, see Fig. 12.
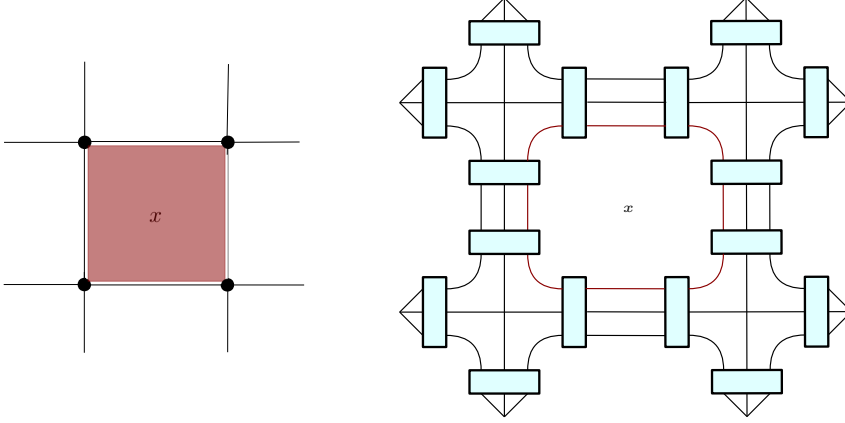

Figure 12: *Left: The 2-complex dual to the Δ_4 triangulation. We highlighted in red the internal face. Right: Spin foam diagram of the transition amplitude associated to the Δ_4 triangulation.*

The associated transition amplitude in the Ponzano-Regge model is

$$W_{\Delta_4}(j_f) = (-1)^\chi \sum_x (-1)^x (2x+1) \left\{ \begin{array}{ccc} j_5 & j_8 & x \\ j_9 & j_6 & j_1 \end{array} \right\} \left\{ \begin{array}{ccc} j_9 & j_6 & x \\ j_4 & j_7 & j_2 \end{array} \right\} \left\{ \begin{array}{ccc} j_4 & j_7 & x \\ j_{11} & j_{10} & j_3 \end{array} \right\} \left\{ \begin{array}{ccc} j_{10} & j_{11} & x \\ j_8 & j_5 & j_{12} \end{array} \right\}$$

(45)

where $\chi = \sum_{f=1}^{12} j_f$ is a consequence of the convention we used for the boundary data. Again, because of triangular inequalities, the summation over the bulk spin is bounded by
$x_{min} = \text{Max}\{|j_4 - j_7|, |j_5 - j_8|, |j_6 - j_9|, |j_{10} - j_{11}|\}$ and $x_{max} = \text{Min}\{j_4 + j_7, j_5 + j_8, j_6 + j_9, j_{10} + j_{11}\}$.

We report the result of our analysis in Figure 13 and 14 where we considered $j_1 = j_2 = j_3 = j_7 = j_8 = j_9 = j_{11} = j_{12} = \lambda$ and $j_4 = j_5 = j_6 = j_{10} = 2\lambda$ with a scale factor fixed at $\lambda = 1750$. We can clearly see the presence of four stationary phase points. We estimate their position using the algorithm (1) and we obtain

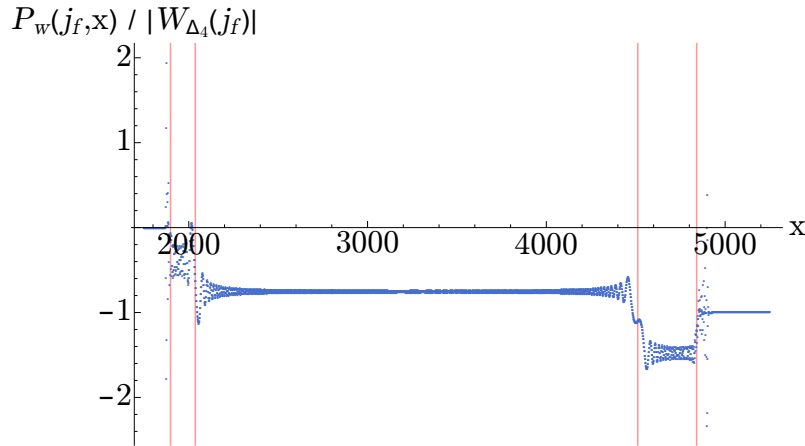$$x_1 = 2036 \pm 4 \qquad x_2 = 4509 \pm 11 \qquad x_3 = 1896 \pm 6 \qquad x_4 = 4841 \pm 5 \tag{46}$$

Figure 13: *Numerical analysis of the normalized partial sum P_w as a function of the bulk spin x with $\lambda = 1750$. We highlight the stationary phase points x_i (46) with red lines.*
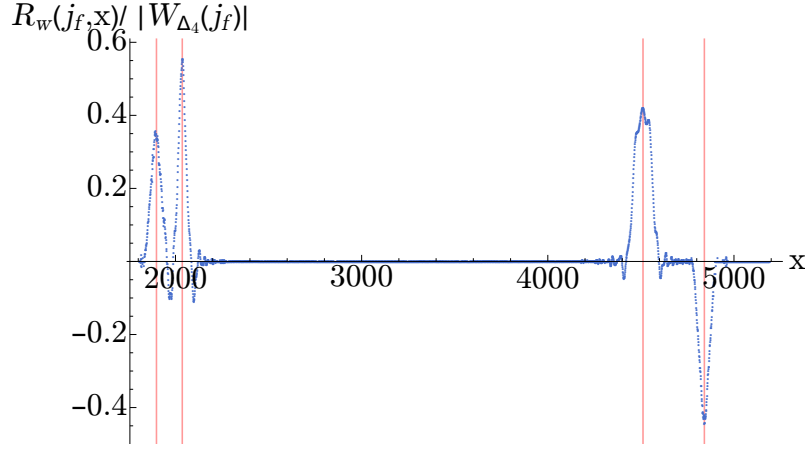
140

Figure 14: *Numerical analysis of the normalized running sum R_w as a function of the bulk spin x with $\lambda = 1750$. We highlight the stationary phase points x_i (46) with red lines.*

To interpret them geometrically, we perform an analytical stationary point analysis as in Section 6. The first two solutions are

$$x_1 = \sqrt{4 - \sqrt{7}}\lambda \approx 2036.5 \qquad x_2 = \sqrt{4 + \sqrt{7}}\lambda \approx 4511.4 \tag{47}$$

and correspond to the two possible flat embedding of four tetrahedra compatible with the given boundary lengths in complete analogy with the Δ_3, see Figure 15 for a three dimensional rendering. The other two $x_{3,4} =$

$$x_3 = \sqrt{3 + \sqrt{2} - \sqrt{2\left(1 + 3\sqrt{2}\right)}}\lambda \approx 1897.8 \qquad x_4 = \sqrt{3 + \sqrt{2} + \sqrt{2\left(1 + 3\sqrt{2}\right)}}\lambda \approx 4841.0 \tag{48}$$

correspond to a geometry where two tetrahedra cancel each other while the other two have a flat embedding. The four analytical values for x_i are compatible with the numerical estimates (46), see Fig. 15.
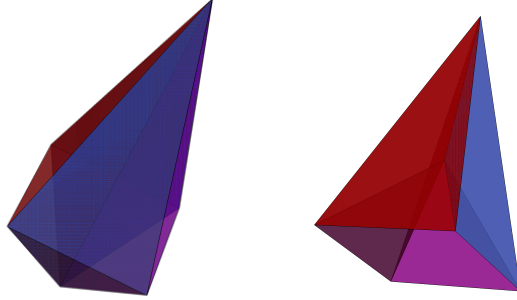

Figure 15: *The classical flat geometries corresponding to the solution x_1, x_2 of the stationary phase equations*
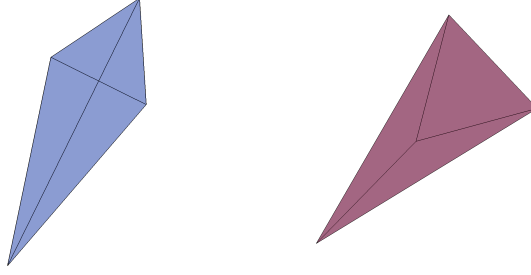
Figure 16: *The classical flat geometries corresponding to the solution x_3, x_4 of the stationary phase equations*

9   Phase deformation and curvature

The flatness condition (40) is a consequence of the phase choice $(-1)^x = \exp i\pi x$ in (21). A simple, yet intriguing, variation consists in modifying this phase by replacing the angle π with an arbitrary real angle $\alpha\pi$ with $0 < \alpha \leq 2$.

$$W^c_{\Delta_3}(j_f) = (-1)^\chi \sum_x e^{i\alpha\pi x}(2x+1) \left\{ \begin{matrix} j_5 & j_8 & x \\ j_9 & j_6 & j_1 \end{matrix} \right\} \left\{ \begin{matrix} j_9 & j_6 & x \\ j_4 & j_7 & j_2 \end{matrix} \right\} \left\{ \begin{matrix} j_4 & j_7 & x \\ j_8 & j_5 & j_3 \end{matrix} \right\} \tag{49}$$

In previous case, $\alpha = 1$, the summation over the bulk spin x is dominated by flat geometries and the stationary phase equations (40) can be interpreted as imposing the sum of the dihedral angles around the bulk hinge of the three tetrahedra to zero. The modification of the phase introduce curvature á la Regge: the bulk summation is dominated by geometries with a deficit angle $\delta = (\alpha - 1)\pi$.

This modification of the amplitude breaks the triangulation invariance of the theory and suggests that we are introducing local degrees of freedom compatible with the presence of curvature.

In general, the new amplitude (49) is a complex number and we look at its real (or imaginary) part. If one insists on working with real amplitudes they can replace the phase $\exp i\alpha\pi x$ with $\cos \alpha\pi x$ (or $\sin \alpha\pi x$). The stationary phase points of the real part and the imaginary part are the same since they differ only by a phase shift of $\pi/2$, see Fig. 17.

Our numerical analysis shows the presence of more then two stationary points, for example in Figure 18 we find six stationary phase points corresponding to the values

$$x_1 = 898 \pm 4 \qquad\qquad x_2 = 975 \pm 4 \qquad\qquad x_3 = 1149 \pm 3$$
$$x_4 = 2852 \pm 3 \qquad\qquad x_5 = 3374 \pm 4 \qquad\qquad x_6 = 3655 \pm 3$$

The modified analytical stationary phase equations now depends on α,

$$\alpha\pi \pm \Theta^1_x \pm \Theta^2_x \pm \Theta^3_x = 0 \mod 2\pi \ . \tag{50}$$

The phase deformation lifts some "degeneracies" that are implicit in the original flatness condition (40). In particular, the argument that there is only a unique choice of signs in (37) that admits two real solutions does not apply in this case, similarly to what happens for the Δ_4 amplitude (45). The analytic solution to

the deformed flatness condition (50) are

$$x_1 = \lambda\sqrt{\frac{9}{4} + \frac{1}{\sqrt{5}} - \sqrt{\frac{1}{10}\left(37 + 9\sqrt{5}\right)}} \approx 898$$

$$x_2 = \lambda\frac{1}{2}\sqrt{13 - \frac{2\left(2 + \sqrt{32 + 46\sin\left(\frac{\pi}{30}\right) - 18\cos\left(\frac{\pi}{15}\right)}\right)}{1 + \sin\left(\frac{\pi}{30}\right)}} \approx 973$$

$$x_3 = \lambda\sqrt{\frac{9}{4} - \frac{1}{\sqrt{5}} - \sqrt{\frac{1}{10}\left(37 - 9\sqrt{5}\right)}} \approx 1150$$

$$x_4 = \lambda\sqrt{\frac{9}{4} - \frac{1}{\sqrt{5}} + \sqrt{\frac{1}{10}\left(37 - 9\sqrt{5}\right)}} \approx 2853$$

$$x_5 = \lambda\frac{1}{2}\sqrt{13 + \frac{2\left(\sqrt{32 + 46\sin\left(\frac{\pi}{30}\right) - 18\cos\left(\frac{\pi}{15}\right)} - 2\right)}{1 + \sin\left(\frac{\pi}{30}\right)}} \approx 3370$$

$$x_6 = \lambda\sqrt{\frac{9}{4} + \frac{1}{\sqrt{5}} + \sqrt{\frac{1}{10}\left(37 + 9\sqrt{5}\right)}} \approx 3654$$

that are compatible with our numerical estimates. In this case, in contrast with the Δ_3 case, the six stationary phase points are solutions of different equations. Recovering all of them is a good test for the solidity of our analysis. These stationary phase points may or may not correspond to geometrical triangulations that we can interpret as Regge-curved along the common hinge.
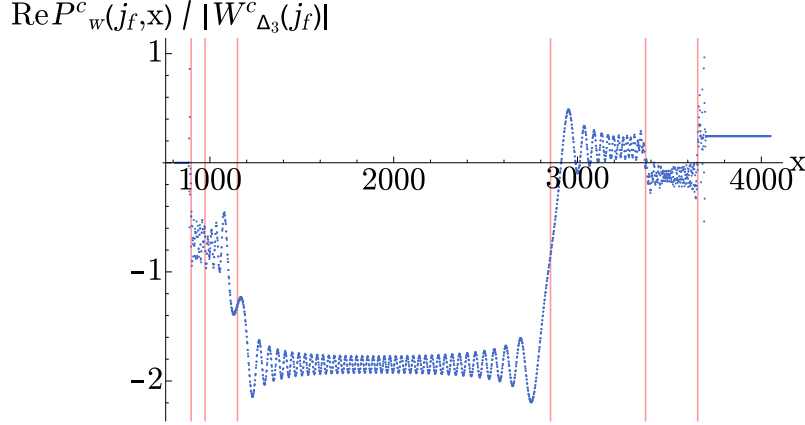

Figure 17: *Real part of the normalized partial sum P_w^c as a function of the bulk spin x for the boundary spins $j_1 = j_2 = j_3 = j_7 = j_8 = j_9 = \lambda$ and $j_4 = j_5 = j_6 = \frac{3}{2}\lambda$ with $\lambda = 1620$ and deformation parameter $\alpha = 0.6$. We observe six different stationary phase points corresponding to the solutions of the three possible equations for the deficit angle.*

Figure 18: *Absolute value of the normalized running sum R_w^c as a function of the bulk spin x for the boundary spins $j_1 = j_2 = j_3 = j_7 = j_8 = j_9 = \lambda$ and $j_4 = j_5 = j_6 = \frac{3}{2}\lambda$ with $\lambda = 1620$ and deformation parameter $\alpha = 0.6$. We observe six different stationary phase points corresponding to the solutions of the three possible equations for the deficit angle.*
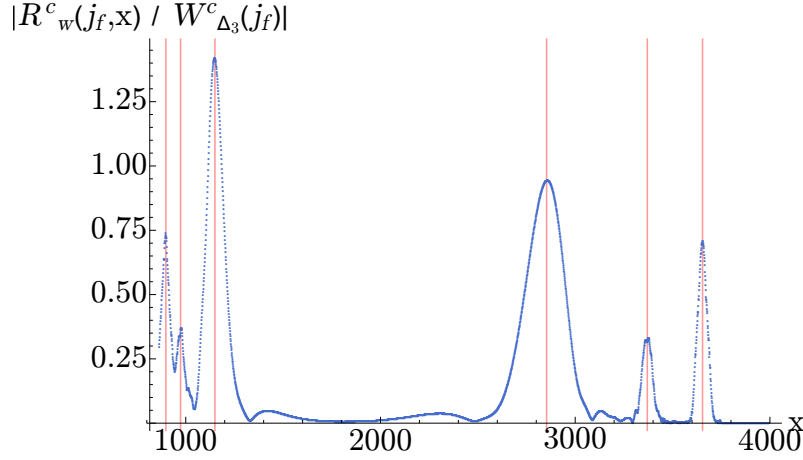
We also found cases with four stationary phase points which correspond to two Δ_3 geometries with non-null positive deficit angle *and* non-null negative deficit angle. We can naively interpret them as the superposition of two (Regge-)curved geometries, one positively curved and one negatively curved, with curvature around the bulk hinge. The general nature of the geometries emerging from the analysis is not clear.

Interestingly, a similar modification of the Ponzano-Regge model has been previously made in [41]. They proposed to insert a character of a specific group element in the amplitude and they interpret it as the presence of a massive spinning particle that introduce a conical singularity dual to the face.

10 Conclusion and Outlook

We presented a numerical method to study the semiclassical limit of spin foam amplitudes with many vertices. In the path integral formulation of quantum mechanics, the composition of two propagators is dominated by classical trajectories. Similarly, the summation over bulk spins of a spin foam transition amplitude is dominated by stationary phase points. We estimate the location of the stationary phase points analyzing the running sum (27) with different interval sizes. The stationary phase points correspond to classical geometries that are solutions of the equations of motion of a classical underlying theory. We test our method on the Δ_3 transition amplitude, the simplest amplitude with three vertices and one bulk face, within the Ponzano-Regge model.

The two emergent classical geometries are three tetrahedra glued together along a common segment.In this case we can compute the stationary phase points analytically and confront them with our numerical estimates and we find amazing agreement. This confirm the interpretation of the Ponzano-Regge model as a spin foam model for three dimensional euclidean quantum gravity. The stationary phase points in the sums over the bulk faces corresponds to the solutions of the classical Regge equations of motion.

Our numerical investigation can be extended to spin foam amplitudes with multiple bulk faces analyzing one face at a time while summing over the others.

Our method has more interesting applications to more complex spin foam models, as the EPRL model. In these cases, analytical computations to determine the stationary phase points for multi-vertices amplitudes are not present in the literature. This absence led to various arguments [21, 22, 23] claiming that the semiclassical limit of the EPRL model is dominated only by flat geometries, hence failing to reproduce General Relativity in this limit. In the euclidean $SO(4)$ formulation of the theory preliminary analytical [42] and numerical [43] studies suggest that this is not the case.

Almost all the semiclassical results are based on the uniform rescaling of the amplitude. This approach is very costly numerically [15]. The method hereby proposed offers a viable alternative and only requires

to compute an amplitude at fixed rescaling parameter. Moreover, it provides a clear signature of the semi-classical geometries where instead extracting the Regge action from the fast oscillating data is bound to fail.

We extended our analysis treating also a four vertices amplitude and we proposed a simple modification of the Ponzano-Regge model to include local curvature. In both cases our numerical analysis is able to estimate with great accuracy the location of the saddle points that we can compute analytically. This is an indication that the algorithm we propose is robust.

The next step is to apply our method to a four dimensional BF spin foam model and to the lorentzian EPRL model. In particular, we want to study a four dimensional triangulation and assign coherent boundary data compatible with a curved bulk geometry. If stationary phase points corresponding to curved geometries are present in the EPRL case we would conclude that the model is not flat.

11   Acknowledgments

Appendices

A Derivation of Δ_3 spinfoam amplitude

In this section, we derive the explicit form of the amplitude (21). Using the graphical notation we briefly introduced in (15), see [33] for more details, we start from the amplitude:

$$W_{\Delta_3}(j_f) = (-1)^{2j_6}(-1)^{j_1+j_2+j_3+j_4+j_6+j_7+j_9} \tag{51}$$

The sign next to each box indicates the order in which the spins has to be read into the $(3jm)$ symbol. $+$ means anticlockwise order while $-$ clockwise order. The integrals over $SU(2)$ can be performed exactly in terms of invariants, in particular $\{6j\}$ symbols and $(3jm)$ symbols

$$W_{\Delta_3}(j_f) = (-1)^{2j_6}(-1)^{j_1+j_2+j_3+j_4+j_6+j_7+j_9} \sum_x (2x+1) \tag{52}$$

The twisted theta graph is the contraction over all the magnetic indices of a $(3jm)$ symbol with spins (j_5, j_8, x) and a $(3jm)$ symbol with spins (j_8, j_5, x). Notice the permutation of the first two columns. The evaluation of the twisted theta graph results in the phase $(-1)^{j_8+j_5+3x}$. We denote with $\chi = j_1 + j_2 + j_3 + j_4 + j_5 + j_6 + j_7 + j_8 + j_9$. Using the definition of the $\{6j\}$ symbol (18) and inverting some arrows where needed at the cost of a $(-1)^{j_f}$ phase [33] we obtain

$$W_{\Delta_3}(j_f) = (-1)^\chi \sum_x (-1)^x (2x+1) \begin{Bmatrix} j_5 & j_8 & x \\ j_9 & j_6 & j_1 \end{Bmatrix} \begin{Bmatrix} j_9 & j_6 & x \\ j_4 & j_7 & j_2 \end{Bmatrix} \begin{Bmatrix} j_4 & j_7 & x \\ j_8 & j_5 & j_3 \end{Bmatrix}. \tag{53}$$

The global phase of the amplitude depends on the conventions used and on the choice of the boundary configuration.

References

[1] J. Engle, E. Livine, R. Pereira and C. Rovelli, "LQG vertex with finite Immirzi parameter," Nucl. Phys. B **799**, 136 (2008) doi:10.1016/j.nuclphysb.2008.02.018 [arXiv:0711.0146 [gr-qc]].

[2] E. R. Livine and S. Speziale, "A New spinfoam vertex for quantum gravity," Phys. Rev. D **76**, 084028 (2007) doi:10.1103/PhysRevD.76.084028 [arXiv:0705.0674 [gr-qc]].

[3] E. R. Livine and S. Speziale, "Consistently Solving the Simplicity Constraints for Spinfoam Quantum Gravity," EPL **81**, no. 5, 50004 (2008) doi:10.1209/0295-5075/81/50004 [arXiv:0708.1915 [gr-qc]].

[4] L. Freidel and K. Krasnov, "A New Spin Foam Model for 4d Gravity," Class. Quant. Grav. **25**, 125018 (2008) doi:10.1088/0264-9381/25/12/125018 [arXiv:0708.1595 [gr-qc]].

[5] J. W. Barrett, R. J. Dowdall, W. J. Fairbairn, H. Gomes and F. Hellmann, "Asymptotic analysis of the EPRL four-simplex amplitude," J. Math. Phys. **50**, 112504 (2009) doi:10.1063/1.3244218 [arXiv:0902.1170 [gr-qc]].

[6] J. W. Barrett, R. J. Dowdall, W. J. Fairbairn, F. Hellmann and R. Pereira, "Asymptotic analysis of lorentzian spin foam models," PoS QGQGS **2011**, 009 (2011). doi:10.22323/1.140.0009

[7] E. Bianchi, L. Modesto, C. Rovelli and S. Speziale, "Graviton propagator in loop quantum gravity," Class. Quant. Grav. **23**, 6989 (2006) doi:10.1088/0264-9381/23/23/024 [gr-qc/0604044].

[8] S. Speziale, "Background-free propagation in loop quantum gravity," Adv. Sci. Lett. **2**, 280 (2009) doi:10.1166/asl.2009.1036 [arXiv:0810.1978 [gr-qc]].

[9] E. Bianchi, E. Magliaro and C. Perini, "LQG propagator from the new spin foams," Nucl. Phys. B **822**, 245 (2009) doi:10.1016/j.nuclphysb.2009.07.016 [arXiv:0905.4082 [gr-qc]].

[10] E. Bianchi and Y. Ding, "Lorentzian spinfoam propagator," Phys. Rev. D **86**, 104040 (2012) doi:10.1103/PhysRevD.86.104040 [arXiv:1109.6538 [gr-qc]].

[11] M. Christodoulou, C. Rovelli, S. Speziale and I. Vilensky, "Planck star tunneling time: An astrophysically relevant observable from background-free quantum gravity," Phys. Rev. D **94**, no. 8, 084035 (2016) doi:10.1103/PhysRevD.94.084035 [arXiv:1605.05268 [gr-qc]].

[12] E. Bianchi, C. Rovelli and F. Vidotto, "Towards Spinfoam Cosmology," Phys. Rev. D **82**, 084035 (2010) doi:10.1103/PhysRevD.82.084035 [arXiv:1003.3483 [gr-qc]].

[13] G. Sarno, S. Speziale and G. V. Stagno, "2-vertex lorentzian Spin Foam Amplitudes for Dipole Transitions," Gen. Rel. Grav. **50**, no. 4, 43 (2018) doi:10.1007/s10714-018-2360-x [arXiv:1801.03771 [gr-qc]].

[14] F. Gozzini and F. Vidotto, "Primordial fluctuations from quantum gravity," arXiv:1906.02211 [gr-qc].

[15] P. Dona, M. Fanizza, G. Sarno and S. Speziale, "Numerical study of the lorentzian EPRL spin foam amplitude," arXiv:1903.12624 [gr-qc].

[16] B. Bahr and S. Steinhaus, "Numerical evidence for a phase transition in 4d spin foam quantum gravity," Phys. Rev. Lett. **117**, no. 14, 141302 (2016) doi:10.1103/PhysRevLett.117.141302 [arXiv:1605.07649 [gr-qc]].

[17] B. Bahr, S. Kloser and G. Rabuffo, "Towards a Cosmological subsector of Spin Foam Quantum Gravity," Phys. Rev. D **96**, no. 8, 086009 (2017) doi:10.1103/PhysRevD.96.086009 [arXiv:1704.03691 [gr-qc]].

[18] B. Bahr, G. Rabuffo and S. Steinhaus, "Renormalization of symmetry restricted spin foam models with curvature in the asymptotic regime," Phys. Rev. D **98**, no. 10, 106026 (2018) doi:10.1103/PhysRevD.98.106026 [arXiv:1804.00023 [gr-qc]].

[19] J. Mielczarek, "Spin Foam Vertex Amplitudes on Quantum Computer – Preliminary Results," doi:10.3390/universe5080179 arXiv:1810.07100 [gr-qc].

[20] The repositories for the "Encyclopedia of Quantum Geometries" can be found at the address zenodo.org/communities/enqugeo.

[21] F. Conrady and L. Freidel, "On the semiclassical limit of 4d spin foam models," Phys. Rev. D **78**, 104023 (2008) doi:10.1103/PhysRevD.78.104023 [arXiv:0809.2280 [gr-qc]].

[22] V. Bonzom, "Spin foam models for quantum gravity from lattice path integrals," Phys. Rev. D **80**, 064028 (2009) doi:10.1103/PhysRevD.80.064028 [arXiv:0905.1501 [gr-qc]].

[23] F. Hellmann and W. Kaminski, "Holonomy spin foam models: Asymptotic geometry of the partition function," JHEP **1310**, 165 (2013) doi:10.1007/JHEP10(2013)165 [arXiv:1307.1679 [gr-qc]].

[24] P. Dona and G. Sarno, "Numerical methods for EPRL spin foam transition amplitudes and lorentzian recoupling theory," Gen. Rel. Grav. **50**, 127 (2018) doi:10.1007/s10714-018-2452-7 [arXiv:1807.03066 [gr-qc]].

[25] G. Ponzano, T. Regge, "Semiclassical limit of Racah coefficients," Spectroscopic and group theoretical methods in physics (1968), 1-58 pp.

[26] S. Speziale, *Boosting Wigner's nj-symbols*, J. Math. Phys. **58** (2017), no. 3 032501 [`1609.01632`].

[27] H. T. Johansson and C. Forssén, "Fast and accurate evaluation of wigner 3j, 6j, and 9j symbols using prime factorisation and multi-word integer arithmetic," SIAM J. Sci. Statist. Comput. **38** (2016) A376–A384

[28] At the address `bitbucket.org/giorgiosarno/ponzanoregge_delta3` there are the Mathematica's notebooks to perform the geometrical reconstruction for the Δ_3 amplitude. The C-codes we used to compute the bulk distribution are also available.

[29] L. S. Schulman, "Techniques And Applications Of Path Integration," New York, Usa: Wiley (1981) 358p

[30] J. J. Sakurai, "Modern Quantum Mechanics," ,Addison Wesley (1993) 500p

[31] J. C. Baez, "An Introduction to spin foam models of quantum gravity and BF theory," Lect. Notes Phys. **543**, 25 (2000) doi:10.1007/3-540-46552-9 [gr-qc/9905087].

[32] A. Perez, "The Spin Foam Approach to Quantum Gravity," Living Rev. Rel. **16** (2013) 3 doi:10.12942/lrr-2013-3 [arXiv:1205.2019 [gr-qc]].

[33] D. A. Varshalovich, A. N. Moskalev and V. K. Khersonsky,"Quantum Theory of Angular Momentum: Irreducible Tensors, Spherical Harmonics, Vector Coupling Coefficients, 3nj Symbols",World Scientific, Singapore, (1988).

[34] J. W. Barrett and I. Naish-Guzman, "The Ponzano-Regge model," Class. Quant. Grav. **26**, 155014 (2009) doi:10.1088/0264-9381/26/15/155014 [arXiv:0803.3319 [gr-qc]].

[35] T. Regge, "General Relativity Without Coordinates," Nuovo Cim. **19**, 558 (1961). doi:10.1007/BF02733251

[36] J. Iwasaki, "A Definition of the Ponzano-Regge quantum gravity model in terms of surfaces," J. Math. Phys. **36**, 6288 (1995) doi:10.1063/1.531245 [gr-qc/9505043].

[37] L. Freidel and D. Louapre, "Diffeomorphisms and spin foam models," Nucl. Phys. B **662** (2003) 279 doi:10.1016/S0550-3213(03)00306-7 [gr-qc/0212001].

[38] V.G. Turaev and O.Y. Viro, "State sum invariants of 3 manifolds and quantum 6jsymbols," Topology, 31:865–902, 1992.

[39] H. M. Haggard and R. G. Littlejohn, "Asymptotics of the Wigner 9j symbol," Class. Quant. Grav. **27**, 135010 (2010) doi:10.1088/0264-9381/27/13/135010 [arXiv:0912.5384 [gr-qc]].

[40] P. Dona, M. Fanizza, G. Sarno and S. Speziale, "SU(2) graph invariants, Regge actions and polytopes," Class. Quant. Grav. **35**, no. 4, 045011 (2018) doi:10.1088/1361-6382/aaa53a [arXiv:1708.01727 [gr-qc]].

[41] L. Freidel and D. Louapre, "Ponzano-Regge model revisited I: Gauge fixing, observables and interacting spinning particles," Class. Quant. Grav. **21**, 5685 (2004) doi:10.1088/0264-9381/21/24/002 [hep-th/0401076].

[42] J. R. Oliveira, "EPRL/FK Asymptotics and the Flatness Problem," Class. Quant. Grav. **35**, no. 9, 095003 (2018) doi:10.1088/1361-6382/aaae82 [arXiv:1704.04817 [gr-qc]].

[43] V. Bayle, F. Collet and C. Rovelli, '"Short-scale Emergence of Classical Geometry, in euclidean Loop Quantum Gravity," arXiv:1603.07931 [gr-qc].

Chapter 8

Numerical analysis of spin foam dynamics and the flatness problem

Numerical analysis of spin foam dynamics and the flatness problem

Pietro Donà,[*]   Francesco Gozzini,[†]   Giorgio Sarno[‡]

CPT, Aix-Marseille Université, Université de Toulon, CNRS, 13288 Marseille, France

June 29, 2020

Abstract

In this paper we apply a recently proposed numerical algorithm for finding stationary phase points in spin foam amplitudes. We study a spin foam amplitude with three vertices and a bulk face in 4d BF theory. We fix the boundary coherent states to three possible triangulations, one with zero deficit angle on the bulk face and two with non-zero deficit angle. We compute the amplitude numerically and we find a stationary phase point already at low spins in all the three cases. We comment on how this result contrasts with the claims of flatness problem in spin foam theories. We point out where these arguments may be misleading and we propose further computations to definitively answer the question.

1   Introduction and Motivations

The EPRL-FK spin foam theory [1, 2] is an attempt to define the dynamics of loop quantum gravity. It provides a regularized, background-independent and Lorentz covariant quantum gravity path integral with the definition of a partition function on a triangulation. The theory assigns transition amplitudes to spin network states on the boundary of a triangulation.

Recovering General Relativity (or at least a discrete version of it) in the semiclassical limit is a fundamental test for spin foam theories. The large spin limit of the EPRL vertex amplitude has been largely explored in both euclidean [3] and lorentzian versions [4]. Remarkably, under a homogeneous rescaling of all the spins, the single vertex amplitude with coherent boundary data contains the Regge action, a discrete formulation of General Relativity.

However, in the case of extended triangulations, the semiclassical limit of the theory is not completely understood. In particular, the question of what semiclassical geometries dominate the summations over bulk degrees of freedom is still open.

Different calculations suggest that the summation over bulk degrees of freedom is dominated by flat geometries[1]. This observation, often called *flatness problem*, has been mentioned by Freidel and Conrady [5], Bonzom [6], and Han [7]. Hellmann and Kamiński [8] proposed a different analysis, based on the calculation of the wavefront set of the spin foam partition function and a geometrical interpretation of its variables, and they found a similar problem.

A more refined stationary phase analysis of the euclidean EPRL model has been carried out by Oliveira in [9]. They include all the constraints on the boundary data necessary to obtain a non-exponentially suppressed vertex amplitude. The initial claim that the flatness problem is not present in that setting has been recently questioned by Kaminski and Engle [10]. It has been suggested that taking only large spins is not the right way to access the semiclassical regime of the theory [11, 12, 13].

The importance of numerical methods for the investigation of spin foam theories grew considerably in recent years. The software library `sl2cfoam` is a C based high-performance library and is the foundation for the numerical computation of general spinfoam amplitudes, both in 3 and 4 dimensions, with topological

---

[*]dona@cpt.univ-mrs.fr

[†]gozzini@cpt.univ-mrs.fr

[‡]sarno@cpt.univ-mrs.fr

[1]Precisely, only geometries with a deficit angles around bulk faces multiple of $4\pi/\gamma$.

BF or lorentzian EPRL models [14]. The library is based on the factorization [15] and was used to explore the large spin limit of both models [16, 17].

While still at the early stages, the evaluation of many-vertices spinfoam amplitudes is possible. In a recent work [18], we have developed an algorithm to determine the existence and estimate the position of stationary phase points in the summations over the spins of internal faces. We tested its effectiveness applying it to BF spin foam theory in 3D (the Ponzano-Regge model), where the stationary phase points are directly connected to the solution of the equations of motion of euclidean Regge calculus. We adapt the algorithm to the BF spin foam theory in 4D. This topological model is the starting point for the construction of physical spin foam models like the EPRL model. For this reason, there are many similarities between the two. For example, the boundary states of the transition amplitudes are the same, as well as the semiclassical geometries emerging from the single vertex asymptotics. What geometries dominate the BF transition amplitudes in the large spin limit is an interesting question on its own.

In this work, we focus on the Δ_3 triangulation, formed by three 4-simplices sharing a common triangle. It is the simplest triangulation with many vertices and a bulk face, and it is the standard example used in the flatness problem literature [19, 9, 8].

Solutions of the classical equation of motion dominate the summation over the bulk degrees of freedom in the large spin limit. We expect them to manifest through the presence of stationary phase points. Note that in classical Regge calculus, the Δ_3 triangulation is too simple to give non-trivial dynamics since boundary conditions fix all the lengths. Hence, this triangulation is not a good example to probe the large spin limit of the EPRL model if we suppose the classical underlying theory to be (area-angle) Regge Calculus. Nevertheless, the study of this amplitude can teach us some valuable lessons.

We find an unexpected result. We construct three examples of the 4D euclidean Regge Δ_3 triangulation. One is the flat triangulation characterized by a zero deficit angle around the shared triangle. The other two are curved triangulations. We compute the coherent amplitude associated with each triangulation, and we look for stationary phase points in the internal spin, dual to the shared triangle. We find the presence of a stationary phase point in all the cases. We estimate its value, and we find it compatible with the area of the dual triangle of the prescribed triangulation.

If we apply arguments similar to the ones claiming flatness of the EPRL model to BF theory, we would infer that curved triangulations should be suppressed in the sum. Therefore we would not expect to find any stationary phase point in this case. This shows tension between our results and the arguments declaring that the EPRL model is flat.

The paper is organized as follows. In Section 2 we review the spin foam formulation of BF theory and the Δ_3 transition amplitude. Section 3 describes the Regge triangulations we use to construct the boundary data of the amplitude. In Section 4 we illustrate the algorithm we use to search for stationary phase points and its application. We review the main arguments of the flatness problem of the EPRL model applied to the topological BF model in Section 5. We conclude with a summary of our numerical results and their implications.

All the computations are performed on the CPT servers in Marseille. Each machine is equipped with a 32 cores CPU Intel(R) Xeon(R) Gold 6130 with a base frequency of 2.10 GHz and 196 GB of RAM. In the public repository [20] we publish the C code used to calculate the transition amplitudes along with the Wolfram Mathematica notebooks used to prepare the boundary data and to perform the numerical stationary phase point analysis.

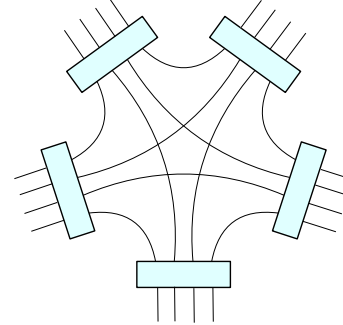## 2 BF theory and the Δ_3 transition amplitude

General Relativity in four dimensions can be written as a BF theory with constraints. This is the starting point in the construction of many spin foam models, as the lorentzian EPRL model. In this paper, we study the spin foam formulation of the $SU(2)$ BF theory on a four-dimensional manifold. For a detailed overview of BF theory and its relations with spin foam models, see [21] or [22]. A triangulation Δ of the manifold is dual to a two-complex $\Delta^\star$ that consists of a set of vertices (dual to the 4-simplices), edges (dual to the tetrahedra) and faces (dual to the triangles). We assign an SU(2) holonomy g_e to each half-edge of the

triangulation. The partition function of the theory discretized on Δ is given by

$$\mathcal{Z}(\Delta) = \int \prod_e dg_e \prod_f \delta(g_{e_1} \ldots g_{e_n}) \ , \qquad \text{with } e_i \subset f \ , \tag{1}$$

the product $g_{e_1} \ldots g_{e_n}$ is the holonomy around the face f, and dg_e is the Haar measure on $SU(2)$. We expand the delta function using the Peter-Weyl theorem as $\delta(g) = \sum_j (2j+1) Tr(D^j(g))$, where $D^j(g)$ are the Wigner matrices of the SU(2) representation of spin j. We get

$$\mathcal{Z}(\Delta) = \sum_{j_f} \int \prod_e dg_e \prod_f (2j_f + 1) Tr(D^{j_f}(g_{e_1} \ldots g_{e_n})) \tag{2}$$

$$= \sum_{j_f} \prod_f (2j_f + 1) \prod_v \quad\text{}\quad . \tag{3}$$

It is useful to introduce a graphical notation for spin foam vertices. Every box represents one integral over SU(2), each line is an irreducible representation of SU(2), and each edge contains four lines. For more details on graphical notations see [23, 16]. We reorganized the partition function as a product over the vertices of $\Delta^\star$ (4-simplices of Δ) and a sum over all the spins. Furthermore, the integrations over SU(2) can be performed explicitly, introducing a sum per edge over a 4-valent intertwiner space i_e. We obtain the familiar form for the partition function in terms of amplitudes

$$\mathcal{Z}(\Delta) = \sum_{j_f, i_e} \prod_f A_f \prod_e A_e \prod_v A_v \ . \tag{4}$$

The face amplitude and the edge amplitude are given respectively by the dimensional factors $A_f = 2j_f + 1$ and $A_e = 2i_e + 1$. The vertex amplitude A_v is given by a $\{15j\}$ symbol. In this work we use the $\{15j\}$ symbols of the first type (see Appendix A for our conventions).

Curiously, the vertex amplitude of this theory with coherent boundary data contains the Regge action of a 4-simplex in the large spin limit. This connection with discrete gravity has been extensively studied both analytically [24] and numerically [16], and is limited to a single vertex. The topological nature of the model is encoded in the delta functions that appear in triangulations with internal faces.

We study the spin foam transition amplitude of the Δ_3 triangulation. The 2-complex dual to the Δ_3 triangulation is represented in Figure 1. It is the simplest amplitude with 3 vertices, 18 boundary faces and one internal face. Each vertex shares an edge with the other two and has three boundary edges.

The boundary data consist of coherent states parametrized by 18 spins and 36 unit normals, one spin and two normals per each strand of the spin foam diagram. We denote with j_{abc} each boundary spin and with x the internal spin. In the next section, we study the four-dimensional geometry we use to specify the boundary data; the notation will be clearer then. The spin foam transition amplitude, omitting the summation over x and the associated face amplitude, is represented using the graphical notation in Figure 1. We refer to (26) in appendix C for the complete picture with all the spin labels and orientations of the faces.
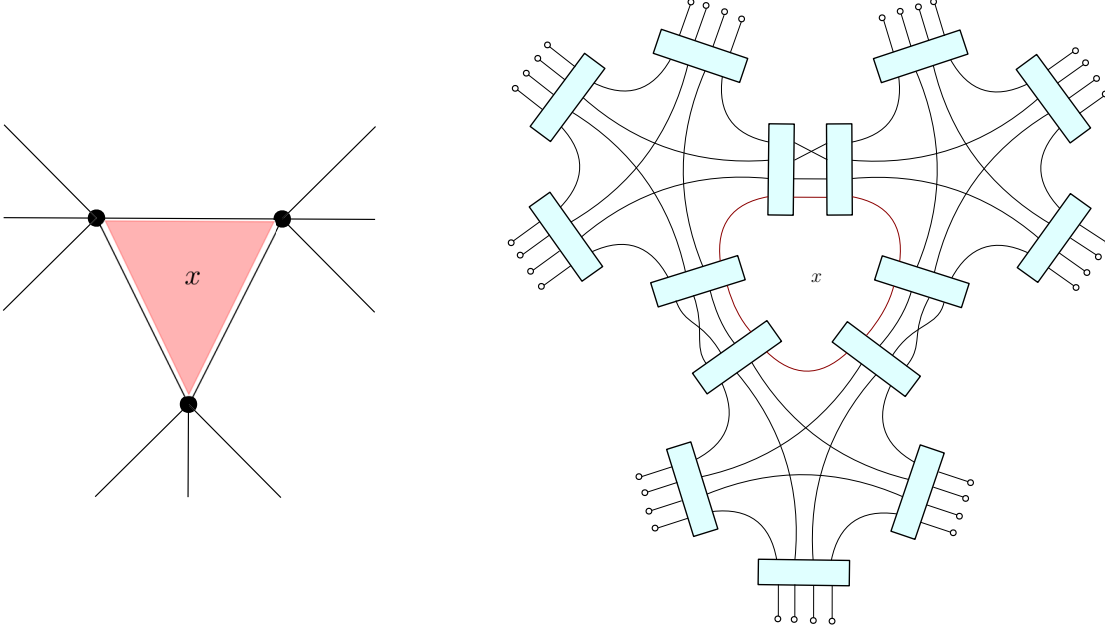
Figure 1: *Left: The 2-complex of the Δ_3 triangulation. We highlight in red the bulk face. Right: The Δ_3 spin foam amplitude in graphical notation. We are omitting a summation over the internal spin x and a dimensional factor $2x+1$. The boxes represent integrals over the $SU(2)$ group, and the strands are irreducible representations labeled by a spin j_{abc}. The empty dots on the boundary represents the $SU(2)$ coherent states.*

We perform the $SU(2)$ integrals and obtain the Δ_3 spin foam amplitude in terms of $\{15j\}$ symbols (see appendix C for more details)

$$W_{\Delta_3}(j_f, \vec{n}_{fa}) = (-1)^\chi \sum_x w_{\Delta_3}(x, j_f, \vec{n}_{fa}) \tag{5}$$

$$= (-1)^\chi \sum_x (-1)^x (2x+1) \sum_{k_b} \left(\prod_b (-1)^{k_b}(2k_b+1) \right) \sum_{i_a} \left(\prod_a (2i_a+1)c_{i_a}(\vec{n}_{fa}) \right)$$

$$\times \left\{ \begin{array}{ccccc} i_1 & j_{345} & k_1 & j_{145} & i_2 \\ j_{235} & x & j_{134} & j_{124} & j_{245} \\ j_{125} & k_2 & j_{123} & i_3 & j_{234} \end{array} \right\} \left\{ \begin{array}{ccccc} i_4 & j_{123} & k_2 & j_{235} & i_5 \\ j_{136} & x & j_{125} & j_{256} & j_{236} \\ j_{356} & k_3 & j_{156} & i_6 & j_{126} \end{array} \right\}$$

$$\times \left\{ \begin{array}{ccccc} i_7 & j_{156} & k_3 & j_{136} & i_8 \\ j_{145} & x & j_{356} & j_{346} & j_{146} \\ j_{134} & k_1 & j_{345} & i_9 & j_{456} \end{array} \right\}$$

where $\chi = 2(j_{123}+j_{234}+j_{124}+j_{134}+j_{456}+j_{156}+j_{346}+j_{356}+j_{235})+j_{123}+j_{345}+j_{156}$ is a phase function only of the boundary spins, i_a are the boundary intertwiners, k_b are the internal intertwiners and the sum over the spin x is bounded by triangular inequalities. The complex coefficients $c_{i_a}(\vec{n}_{fa})$ are the Livine-Speziale coherent intertwiners in the recoupling basis, they depend on the normals $\vec{n}_{fa}$ and areas of the tetrahedron a (see appendix B for their definition).

3 The Δ_3 geometry

The Δ_3 triangulation is formed by three 4-simplices, sharing a common triangle. The boundary of the triangulation consists of nine tetrahedra and the bulk consists of three tetrahedra all sharing the common triangle x.
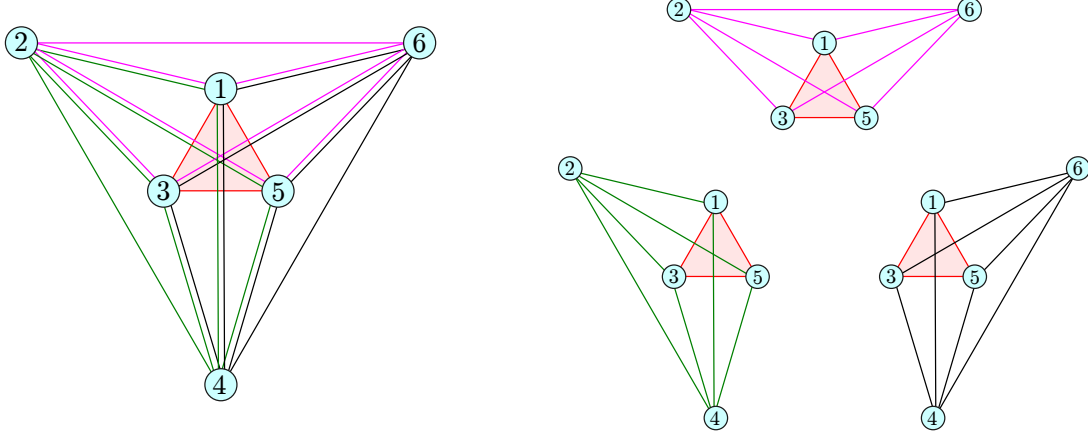
Figure 2: *Left: The geometry of the Δ_3 triangulation. The numbered circles correspond to points. Lines correspond to segments. Each color corresponds to a different 4-simplex. The bulk triangle is highlighted in red. Right: The three 4-simplices are shown separately.*

We associate to each boundary tetrahedron a coherent state characterized by 4 spins, the areas of its faces, and 4 unitary vectors, the outward normals to the faces of the tetrahedron. The triangulation is made of points, segments, faces and tetrahedra. We use the triangulation representation in Figure 2 as reference. The boundary spins j_{abc} are labeled by a triple of points a, b, c since they correspond to triangles. We decide to focus on Regge geometries, fully characterized by their 15 lengths ℓ_{ab} of the segment joining points a, b. Notice that all the lengths belong to at least one boundary tetrahedron, therefore fixing the boundary determines the triangulation completely.

For simplicity and easier computability, we restrict our analysis to geometries with a high degree of symmetry. We require "cylindrical" symmetry forcing the three 4-simplices to be identical. This symmetry requires the bulk triangle to be equilateral ($\ell_{13} = \ell_{35} = \ell_{15}$) and the bulk tetrahedra to be isosceles, having an equilateral base and three identical isosceles faces ($\ell_{12} = \ell_{25} = \ell_{23} = \ell_{16} = \ell_{36} = \ell_{56} = \ell_{34} = \ell_{14} = \ell_{45}$). The remaining three lengths also have to be equal ($\ell_{26} = \ell_{24} = \ell_{46}$).

Furthermore, we require all the areas of the boundary triangles to be the same, and this fixes $\ell_{13} = \ell_{26}$. The symmetry reduces the degrees of freedom of the Regge triangulation from 15 to 2, for example, ℓ_{12} and ℓ_{13}. In terms of the lengths, we can compute all the geometric quantities of the triangulations: areas, three and four-dimensional volumes and two, three and four-dimensional dihedral angles. It is interesting to compute the area of the boundary triangles λ and α the 4D dihedral angle around the bulk triangle of one 4-simplex:

$$\lambda = \frac{1}{4}\ell_{13}\sqrt{4\ell_{12}^2 - \ell_{13}^2}\,, \qquad \sin^2\alpha = \frac{3}{4}\ell_{13}^2\frac{12\ell_{12}^2 - 7\ell_{13}^2}{(\ell_{13}^2 - 3\ell_{12}^2)^2}\,. \tag{6}$$

They are independent variables and under a linear rescaling of the lengths λ scales quadratically while α does not scale. In the following, we identify with λ the scale of the triangulation.

Another interesting geometrical quantity for our analysis is the value of the area of the shared triangle

$$x_g = \frac{\sqrt{3}}{4}\ell_{13}^2 = 3\left(\frac{6 + \sin^2\alpha + 6\sqrt{1 - \sin^2\alpha}}{48 + \sin^2\alpha}\right)^{\frac{1}{2}}\lambda\,. \tag{7}$$

For Regge geometries curvature can be expressed in terms of deficit angles associated to triangles shared between 4-simplices. In the particular class of symmetric triangulations we are considering the deficit angle associated with the shared triangle is

$$\delta = 2\pi - 3\alpha\,. \tag{8}$$

We parametrize the triangulations in this paper with λ and δ instead of the two lengths. Once the triangulation is specified, we compute all the normals of the boundary tetrahedra to use them in defining the boundary coherent states.

155

In this work we consider the flat triangulation characterized by $\delta = 0$ at various scales λ, a first curved triangulation characterized by $\delta \approx 3.60$ at scale $\lambda = 20$, and a second curved triangulation characterized by $\delta \approx 2.47$ at scale $\lambda = 20$. The chosen parameters of the curved triangulations are particularly convenient for this numerical analysis. We motivate our choice of focusing on a single scale for the curved configurations in the next section. All the notebooks we used to compute all the geometric data and the boundary normals for the three triangulations are available in [20].

4 Numerical analysis

The algorithm in [18] is designed to determine the presence and estimate the value of stationary phase points in summations over spin foam bulk spins. We adapt it to the amplitude in examination that we study for different choices of boundary data. In this section, we briefly recall features of the algorithm, and we highlight the differences with the original version. We refer to the original paper for a detailed explanation.

The amplitude (5) involves a sum over the spin x of the internal face and the intertwiners k_b of the three internal edges. For brevity let us omit the dependence on the boundary data j_f, $\vec{n}_{fa}$ on the summand $w_{\Delta_3}(x) \equiv w_{\Delta_3}(x, j_f, \vec{n}_{fa})$. First, we compute $w_{\Delta_3}(x)$ for each value of the internal spin x using the library `sl2cfoam` [14]. We focus on two quantities

$$P_w(x) = \sum_{x' = x_{\min}}^{x} w_{\Delta_3}(x') \,, \qquad \text{and} \qquad R_w(x) = \sum_{x' \in I_x^c} w_{\Delta_3}(x') \,, \tag{9}$$

where I_x^c is an interval centered in x with width $2c$. We call them respectively the *partial sum* and the *running sum*. The algorithm is based on the behavior of these two quantities in the presence of stationary phase points for W_{Δ_3}.

Suppose that x_0 is a stationary phase point for W_{Δ_3}. The sum over the internal spin interferes destructively away from x_0 and constructively near x_0. The partial sum $P_w(x)$ stays roughly constant away from x_0 and has a sudden "jump" near x_0. Similarly, the running sum $R_w(x)$ is close to zero away from x_0 and peaks at x_0. The width of the peak depends on the parameter c, the size of the interval that characterizes the running sum.

Second, we consider $\overline{R_w(x)} = |R_w(x)_{c_1} R_w(x)_{c_2} R_w(x)_{c_3}|$ correlating three running sums with different interval sizes c_i and we use a Mathematica's built-in function to locate the peaks of $\overline{R_w(x)}$. We repeat this step for all the possible triples of c_i in a reference set. Since we are working at smaller spins then [18] in this work we use as reference set $c = \sqrt{x_{max} - x_{min}}/2$ plus or minus 50%. The numerical estimate of the stationary phase point is given by the average of the outcomes of this procedure with an error given by the standard deviation (both values are rounded to the nearest integer). This aims to eliminate the dependence of our analysis from the choice of a particular interval.

The first triangulation we study is the flat one. We report in Figure 3 the running sum and the partial sum for this configuration at $\lambda = 30$.
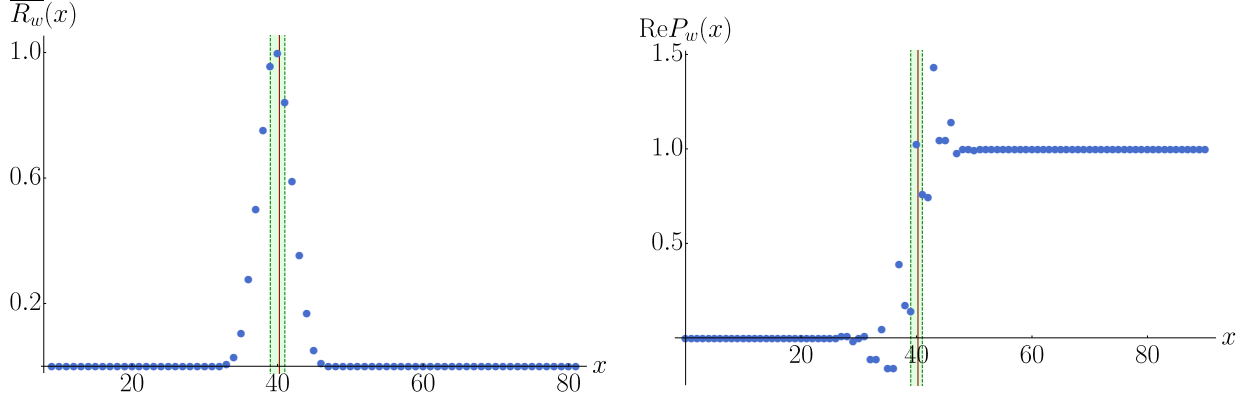
Figure 3: *Flat configuration. Left: Averaged running sum $\overline{R_w(x)}$ with interval sizes 2,6, and 10. We normalize respect to the value of its maximum. Right: Real part of the partial sum $P_w(x)$ normalized respect the absolute value of the amplitude. In both plots, we mark with a red line the value of the geometrical area of the bulk triangle, and with a green band the values of the numerical estimate of the stationary phase point within one standard deviation.*

Our algorithm is implemented in Mathematica, the notebooks are available in [20]. We estimate the presence of a stationary phase point for spin $x_{n_0} = 40 \pm 1$. The value of the geometric area shared by the three 4-simplices (7) for the flat configuration is $x_{g_0} = 1.34\,\lambda \approx 40.2$. It is in perfect agreement with our numerical analysis.

To corroborate the result we repeat the analysis at other scales $\lambda = 10, 12, 14, 16, 18, 20$. We summarize in Table 4 the numerical estimate of the stationary phase point and the geometric area of the shared triangle. Signatures of the stationary phase point are present at all scales, and its position is always compatible with its geometric counterpart. We also note the resources necessary to perform the computations on our server.

	numerical	analytical	memory (GB)	time (h)
$\lambda = 10:$	13 ± 1	13.4	2	0.2
$\lambda = 12:$	16 ± 1	16.1	6	0.4
$\lambda = 14:$	18 ± 1	18.8	16	0.9
$\lambda = 16:$	21 ± 1	21.5	33	3
$\lambda = 18:$	23 ± 1	24.1	65	7.8
$\lambda = 20:$	26 ± 1	26.8	121	21
$\lambda = 30:$	40 ± 1	40.2	~ 2500	~ 2700

Table 1: *We compare the numerical estimate of the stationary phase point with the geometrical area at different scales. For each calculation, we report the time (in hours) and the memory (in GB) required for these computations on our server. Time and memory for $\lambda = 30$ are an estimation based on the previous points. The computation, in this case, was performed on multiple machines, a piece at a time and took more than two months to complete.*

Notice that the agreement is excellent even at small scales. This confirms the result of [16, 17], the asymptotic regime is reached already at relatively low spins. Moreover, at larger scales λ, the computation becomes computationally demanding both on memory and time. This motivated us to focus only on $\lambda = 20$ for other boundary data, the best compromise in terms of results and our computational resources.

We perform our numerical analysis also for boundary data corresponding to the two curved triangulations we described in 3 at scale $\lambda = 20$. We report in Figure 4 and 5 the running sum and the partial sum for these configurations.
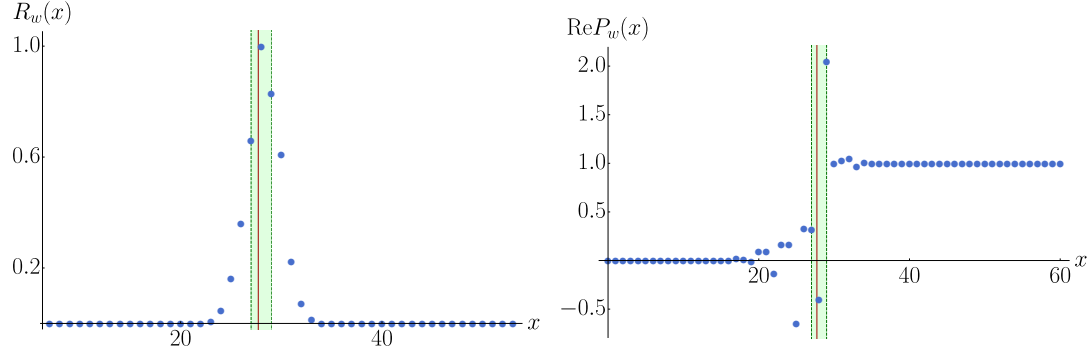
Figure 4: *First curved configuration. Left: Averaged running sum $\overline{R_w(x)}$ with interval sizes $2,6$, and 10. We normalize respect to the value of its maximum. Right: Real part of the partial sum $P_w(x)$ normalized respect the absolute value of the amplitude. In both plots, we mark with a red line the value of the geometrical area of the bulk triangle, and with a green band the values of the numerical estimate of the stationary phase point within one standard deviation.*

Figure 5: *Second curved configuration. Left: Averaged running sum $\overline{R_w(x)}$ with interval sizes $2,6$, and 10. We normalize respect to the value of its maximum. Right: Real part of the partial sum $P_w(x)$ normalized respect the absolute value of the amplitude. In both plots we mark with a red line the value of the geometrical area of the bulk triangle, and with a green band the values of the numerical estimate of the stationary phase point within one standard deviation.*
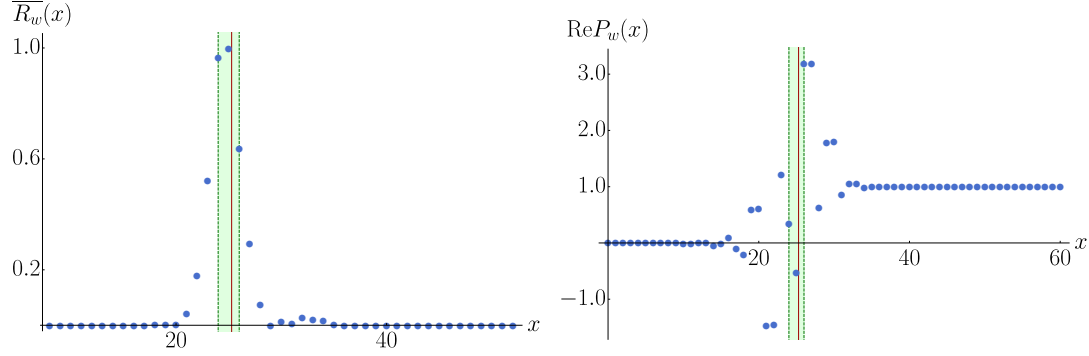
In both cases, we see a clear signature of the existence of a stationary phase point. For the first curved configuration we estimate the position of the stationary phase point for spin $x_{n_1} = 28 \pm 1$. It is compatible with the geometric area (7) of the curved triangulation $x_{g_1} = 1.39 \ \lambda \approx 27.8$. Analogously, for the second curved configuration we find a stationary phase point at spin $x_{n_2} = 25 \pm 1$. Also in this case it is compatible with the expected geometric area $x_{g_2} = 1.26 \ \lambda \approx 25.2$.

5 Flatness arguments applied to W_{Δ_3}

In this section, we repeat the principal arguments for flatness of the EPRL model, on BF theory. To be specific we focus on the W_{Δ_3} amplitude (5). We sketch the various arguments to keep the exposition as clear as possible, and we refer to the original papers for more details. The arguments [5, 6, 7] are based on the large spins approximation of the vertex amplitude. They approximate the integrals over the group using saddle point techniques, and then they look for stationary phase points in the sum over the bulk degrees of freedom. Inserting a resolution of the identity in terms of SU(2) coherent states in each internal edge the summand of the amplitude reduces to

$$w_{\Delta_3}(x, j_f, \vec{n}_{fa}) \propto A_1(x, j_f, \vec{n}_{fa}) A_2(x, j_f, \vec{n}_{fa}) A_3(x, j_f, \vec{n}_{fa}) \tag{10}$$

158

where $A_i(x, j_f, \vec{n}_{fa})$ are the $\{15j\}$ symbols contracted with coherent intertwiners. The proportional symbol in (10) indicates that we are omitting multiple dimensional factors and the integrals coming from the resolution of the identities we inserted. They both play no role in the calculation we illustrate in this section.

If the boundary spins j_f are large, we can safely assume that also the spin of the bulk face x is large. The asymptotic expansion of the coherent $\{15j\}$ symbols was studied in [24, 16]: if the boundary data of the coherent vertex forms the boundary a euclidean 4-simplex, the amplitude can be approximated with

$$A_i(x, j_f, \vec{n}_{fa}) \approx N_i(x, j_f, \vec{n}_{fa}) \cos(S_i(x, j_f, \vec{n}_{fa})) \tag{11}$$

where the factor N_i contains numerical constants and the hessian, both of them are not relevant for the following considerations. The function $S_i = \sum_{f \in v_i} j_f \theta_{f,i} + x\theta_{x,i}$ is the Regge action for the 4-simplex: the sum runs over the triangles f (faces) belonging to the ith 4-simplex (vertex) v_i, j_f are the areas of the triangles and $\theta_{f,i}$ the 4D dihedral angles around the triangle f of the 4-simplex i. The dihedral angles can be reconstructed from orientation invariant scalar products between the normals $\vec{n}_{fa}$ using the spherical cosine law. In this analysis, we assume that vector geometries play no role or can be ignored by selecting the boundary data for the Δ_3 amplitude appropriately.

In the large spin regime (10) is proportional to

$$w_{\Delta_3}(x) \propto \cos(S_1(x)) \cos(S_2(x)) \cos(S_3(x)) = e^{i(S_1(x)+S_2(x)+S_3(x))} + e^{i(S_1(x)+S_2(x)-S_3(x))} + \tag{12}$$
$$e^{i(S_1(x)-S_2(x)+S_3(x))} + e^{i(-S_1(x)+S_2(x)+S_3(x))} + c.c. ,$$

where we omitted the dependence on boundary spins j_f and normals $\vec{n}_{fa}$ that we consider fixed from this point on. By linearity, we can search for stationary phase points of each of the eight terms in (12) independently and sum the results. We focus on the first term, the analysis of the others is similar. The derivative of the Regge action S_i respect to the area x is given by $\delta S_i(x)/\delta x = \theta_{x,i}$. The stationary phase points are the solutions of the equation

$$\frac{\delta}{\delta x}(S_1(x) + S_2(x) + S_3(x)) = \theta_{x,1} + \theta_{x,2} + \theta_{x,3} = 0 \tag{13}$$

and this apparently implies that flat geometries dominate the summation over the bulk degrees of freedoms in the large spin limit. Notice that if we complete the analysis with the other terms in (12) we would obtain that the *oriented* deficit angle is vanishing. In this section we disregard this additional but distinct complication, that was discussed in length in the *proper vertex* literature [25].

The main counterargument to this analysis is that (11) holds only if some constraints (closure and shape matching) are satisfied by the boundary data. Therefore, the variables are not independent and we cannot take the variation in (13) without including the constraints in the action.

Recently Oliveira [9] proposed a more accurate stationary phase point analysis taking into account also these constraints. They studied the spin foam transition amplitude on the Δ_3 2-complex in the euclidean EPRL model. The original paper claimed that in this setting the flatness problem was not present, however Kamiński and Engle [10] corrected an oversight obtaining flatness once again. The analysis is based on the Malgrange preparation theorem. This approximation is valid in an entire neighborhood of a solution of the closure and shape matching constraints x_0. The effect on (13) is the addition of a purely imaginary term

$$\frac{\delta}{\delta x}(S_1(x) + S_2(x) + S_3(x) + i\mu(x - x_0)^2) = \theta_{x,1} + \theta_{x,2} + \theta_{x,3} + i\, 2\mu(x - x_0) = 0 , \tag{14}$$

where μ depends on everything but x. To solve (14) we need both the real and the imaginary part to vanish.
[2] This is possible only if x is a solution of the constraints $x = x_0$ and the flatness condition is satisfied, $\theta_{x,1} + \theta_{x,2} + \theta_{x,3} = 0$.

Hellmann and Kamiński [8] suggested an argument for the flatness of the EPRL model based on a different strategy. First, they perform the summation over the bulk degrees of freedom and then they look for saddle points in the integrals over the holonomies. In the large boundary spins limit, the holonomies dominating

---

[2]The same conclusion is obtained in [10] in a more rigorous way. Instead of looking for stationary phase points they perform the summation over x using the Poisson resummation. The flatness condition is derived by requiring a non exponentially suppressed sum.

the spin foam integrals are the ones contained in the wavefront set [26] of the partition function. The wavefront set of W_{Δ_3} fixes the product of the group elements around its bulk face $g_x = \mathbb{1}$. If we parametrize $g_x = \exp(i\Theta \vec{m} \cdot \vec{\sigma}/2)$ this condition imposes $\Theta = 0$. Following [8] we can map [3] g_x into the geometrical holonomy around the triangle shared by the three 4-simplices. In this case, Θ can be interpreted as 2π minus the deficit angle around the internal face, obtaining the flatness condition.

6   Conclusion

We presented a numerical exploration of the semiclassical limit of the Δ_3 transition amplitude in the 4d BF spin foam model. We computed the transition amplitude with coherent boundary data corresponding to Regge triangulations, both flat and curved. We found a stationary phase point in the sum over the bulk spin with value compatible with the area of the dual triangle of the prescribed triangulation in all the three cases.

This was at first surprising. The *flatness problem* argues that the partition function of the EPRL spin foam theory, in the semiclassical limit, is dominated by flat geometries. Usually, this is interpreted as an indication that the simplicity constraints, responsible for reducing a topological BF theory to General Relativity, are not imposed correctly. The same arguments, applied directly to SU(2) BF spin foam theory, indicate that curved geometries should be suppressed in the large boundary spins limit. This is in contradiction with our numerical result.

The classical equations of motion of BF theory impose the curvature of the spin connection to be vanishing. However, no equations additionally require the connection to be metric. The notion of curvature in terms of deficit angles, as in Regge calculus, is not appropriate in this case.

In our opinion, this is the crucial misstep in the various claims of flatness of the EPRL spin foam theory. If one insists on a simplicial interpretation of the large spin regime of BF spin foam theory, *flatness* does not require vanishing deficit angles, but, on the contrary, any deficit angle is allowed. Equivalently, as stated in [29], the deficit angles do not measure the holonomy of a connection.

In fact, the sums over the internal spins and the SU(2) integrals of the transition amplitude can be performed exactly, reducing it to a coherent $\{3nj\}$ symbol. The large spin asymptotic of general coherent SU(2) invariants is well understood [16, 30]: the spin foam amplitude is not suppressed if the boundary data satisfy closure and shape matching constraints. The requirement of flat embedding in four-dimensional euclidean space is not necessary.

In a recent paper [13], the authors explored the large spin limit of an effective spin foam model related to area-angle Regge calculus. They show that curved geometries are suppressed unless one considers a small Immirzi parameter in addition to large spins. They enrich their analysis with a numerical study confirming their findings. This calculation shows exactly the origin of the tension between our results and the various flatness arguments. These works share the common hypothesis that the asymptotic expression (11) holds also for extended triangulations. We have preliminary indications [31] that, while this expansion is correct for a single vertex, more care is needed in the presence of internal faces. All the flatness arguments become compatible with our numerical result if the angles in (11) are not dihedral angles. What these arguments require to vanish is an angle related to the triangulation but that can not be interpreted as a pure deficit angle.

The study of the semiclassical limit of the EPRL spin foam theory remains a pressing issue. If we anticipate to obtain Regge calculus in the large spins regime we must study transition amplitudes with nontrivial classical equations of motion. We believe that numerics will play a central role in future studies of spin foams. The numerical algorithm we described in this paper is powerful and can be applied to general amplitudes, with many vertices and internal faces, and different theories. We plan to use it to make a direct comparison of the large spin regime of BF and EPRL spin foam theories and finally provide an answer to this important question.

---

[3]For Regge boundary data, the coherent $\{15j\}$ symbol has two distinct saddle points. Up to gauge, the product of the two group elements on a wedge at the saddle point is characterized by $\pm$ the dihedral angle associated with that wedge. Each solution is responsible for one exponential forming the cosine in (11). If we take the saddle points of the three vertices with angles with the same sign, the angle of g_x is $\pm$ the sum of dihedral angles around the shared triangle. With these two group elements, we use the map between $SU(2) \times SU(2)$ and $SO(4)$ to derive a non trivial $SO(4)$ geometrical holonomy, that is a rotation of angle Θ on the plane orthogonal to the shared triangle.

7 Acknowledgments

Appendices

A   Convention for the $\{15j\}$ symbol

The $\{15j\}$ symbol we use in this work is the irreducible $\{15j\}$ symbol of first type, following the convention of [27]. The definition and its graphical representation is the following

$$
= \left\{ \begin{array}{ccccc} j_1 & j_2 & j_3 & j_4 & j_5 \\ l_1 & l_2 & l_3 & l_4 & l_5 \\ k_1 & k_2 & k_3 & k_4 & k_5 \end{array} \right\} = \tag{15}
$$

$$
= (-1)^{\sum_{i=1}^{5} j_i + l_i + k_i} \sum_s (2s+1) \left\{ \begin{array}{ccc} j_1 & k_1 & s \\ k_2 & j_2 & l_1 \end{array} \right\} \left\{ \begin{array}{ccc} j_2 & k_2 & s \\ k_3 & j_3 & l_2 \end{array} \right\} \tag{16}
$$

$$
\times \left\{ \begin{array}{ccc} j_3 & k_3 & s \\ k_4 & j_4 & l_3 \end{array} \right\} \left\{ \begin{array}{ccc} j_4 & k_4 & s \\ k_5 & j_5 & l_4 \end{array} \right\} \left\{ \begin{array}{ccc} j_5 & k_5 & s \\ j_1 & k_1 & l_5 \end{array} \right\} . \tag{17}
$$

B   Coherent states

Coherent states are a fundamental ingredient to study the semiclassical behavior of a spin foam amplitude. We briefly review the conventions used in this paper. For more details we refer to [28] or to other numerical works [16] and [14]. A SU(2) coherent state $|j, \vec{n}\rangle$ in the irreducible representation of spin j is given by the action on the lowest weight state $|j, -j\rangle$ of a SU(2) group element g_n corresponding to the rotation that transforms the unitary vector $\vec{z} = (1, 0, 0)$ into $\vec{n} = (\sin\Theta\cos\Phi, \sin\Theta\sin\Phi, \cos\Theta)$. This coherent state minimizes the uncertainty in the two directions orthogonal to $\vec{n}$. The Euler angles of group element g_n are related to the angles Θ and Φ by

$$
g_n = e^{-i\Phi\frac{\sigma_z}{2}} e^{-i\Theta\frac{\sigma_y}{2}} e^{i\Phi\frac{\sigma_z}{2}} , \tag{18}
$$

where we expressed the SU(2) generators $i\vec{\sigma}/2$ in terms of the Pauli matrices. The scalar product between a coherent state and a state in the magnetic basis is given by

$$
\langle j, m | j, \vec{n}\rangle = \langle j, m | D^{(j)}(g_n) | j, \vec{n}\rangle = D^{(j)}_{m-j}(g_n) = D^{(j)}_{m-j}(\Phi, \Theta, -\Phi) , \tag{19}
$$

where $D^{(j)}_{m-j}(\Phi, \Theta, -\Phi)$ is the Wigner matrix element of g_n parametrized in terms of its Euler angles. These conventions are used by sl2cfoam and Wolfram Mathematica.

SU(2) coherent states form an overcomplete basis in the irreducible representation of spin j space

$$
\mathbb{1}^{(j)} = (2j+1) \int_{S^2} d\vec{n} \, |j, \vec{n}\rangle \langle j, \vec{n}| , \tag{20}
$$

where $d\vec{n}$ is the normalized measure on the sphere.

A 4-valent intertwiner in the recoupling basis is given by

$$|j_i; j_{12}\rangle = \sum_{m_1} \begin{pmatrix} j_1 & j_2 & j_3 & j_4 \\ m_1 & m_2 & m_3 & m_4 \end{pmatrix}^{(j_{12})} |j_1 m_1\rangle |j_2 m_2\rangle |j_3 m_3\rangle |j_4 m_4\rangle \tag{21}$$

and the $(4jm)$ symbol is given by the contraction

$$\begin{pmatrix} j_1 & j_2 & j_3 & j_4 \\ m_1 & m_2 & m_3 & m_4 \end{pmatrix}^{(j_{12})} = \sum_m (-1)^{j_{12}-m} \begin{pmatrix} j_1 & j_2 & j_{12} \\ m_1 & m_2 & m \end{pmatrix} \begin{pmatrix} j_{12} & j_3 & j_4 \\ -m & m_3 & m_4 \end{pmatrix}. \tag{22}$$

Finally we can define a coherent tetrahedron as the projection on the intertwiner space of the tensor product of four SU(2) coherent states. Each one of them is associated to a face of the tetrahedron with area j_i and normal $\vec{n}_i$

$$c_{j_{12}}(\vec{n}_i) := \langle j_i; j_{12} | j_1, \vec{n}_1; j_2, \vec{n}_2; j_3, \vec{n}_3; j_4, \vec{n}_4 \rangle \tag{23}$$

$$= \begin{pmatrix} j_1 & j_2 & j_3 & j_4 \\ m_1 & m_2 & m_3 & m_4 \end{pmatrix}^{(j_{12})} D^{(j_1)}_{m_1-j_1}(g_{n_1}) D^{(j_2)}_{m_2-j_2}(g_{n_2}) D^{(j_3)}_{m_3-j_3}(g_{n_3}) D^{(j_4)}_{m_4-j_4}(g_{n_4}). \tag{24}$$

The graphical representation of an SU(2) coherent state is given by a line ending on a little circle while the coherent states coefficients are represented by

$$|j, \vec{n}\rangle = \quad\quad c_{j_{12}}(\vec{n}_i) = \quad\quad . \tag{25}$$

C   Derivation of the Δ_3 spin foam amplitude

In this appendix we derive the formula (5) for the spin foam transition amplitude associated to the Δ_3 triangulation starting from its integral representation. We use the SU(2) graphical calculus to represent the amplitude as

$$W_{\Delta_3}(j_f, \vec{n}_{fa}) = \sum_x (2x+1) \tag{26}$$

where we picked a conventional orientation of the faces that are capped by coherent states on both ends, represented by empty circles. We label the 4-simplices using the five points, the edges, dual to a tetrahedron,

are labeled by four points and the faces, dual to triangles, are labeled by three points. We highlight in red the internal face x.

We perform the integrations over $SU(2)$ and we get

$$W_{\Delta_3}(j_f, \vec{n}_{fa}) = \sum_x (2x+1) \sum_{k_b} \left(\prod_b (2k_b+1)^2 \right) \sum_{i_a} \left(\prod_a (2i_a+1)c_{i_a}(\vec{n}_{fa}) \right) \times \tag{27}$$

$$(28)$$

To keep the picture as simple as possible we opted for not using the graphical representation of the coherent tetrahedra $c_{i_a}(\vec{n}_{fa})$ that we factorize. The "dipole" like diagrams contribute with a phase and the inverse dimension of the intertwiner space

$$= \frac{(-1)^{k+j_1+j_2}}{2k+1} \ . \tag{29}$$

We invert the orientation of some internal lines to conform with (15) and obtain the Δ_3 transition amplitude in terms of three $\{15j\}$ symbols

$$W_{\Delta_3}(j_f, \vec{n}_{fa}) = (-1)^\chi \sum_x (-1)^x (2x+1) \sum_{k_b} \left(\prod_b (-1)^{k_b}(2k_b+1) \right) \sum_{i_a} \left(\prod_a (2i_a+1)c_{i_a}(\vec{n}_{fa}) \right) \tag{30}$$

$$(31)$$

with $\chi = 2(j_{123} + j_{234} + j_{124} + j_{134} + j_{456} + j_{156} + j_{346} + j_{356} + j_{235}) + j_{123} + j_{345} + j_{156}$. This phase is obtained from the contributions of (29) and $(-1)^{2j}$ required to invert the orientation of an internal line of spin j. We finally derive (5).

163

References

[1] J. Engle, E. Livine, R. Pereira, and C. Rovelli, "LQG vertex with finite immirzi parameter," *Nucl. Phys. B*, vol. 799, pp. 136–149, 2008.

[2] L. Freidel and K. Krasnov, "A New Spin Foam Model for 4d Gravity," *Class. Quant. Grav.*, vol. 25, p. 125018, 2008.

[3] J. W. Barrett, R. Dowdall, W. J. Fairbairn, H. Gomes, and F. Hellmann, "Asymptotic analysis of the eprl four-simplex amplitude," *J. Math. Phys.*, vol. 50, p. 112504, 2009.

[4] J. W. Barrett, R. J. Dowdall, W. J. Fairbairn, F. Hellmann, and R. Pereira, "Lorentzian spin foam amplitudes: graphical calculus and asymptotics," *Classical and Quantum Gravity*, vol. 27, p. 165009, jul 2010.

[5] F. Conrady and L. Freidel, "On the semiclassical limit of 4d spin foam models," *Phys. Rev. D*, vol. 78, p. 104023, 2008.

[6] V. Bonzom, "Spin foam models for quantum gravity from lattice path integrals," *Phys. Rev.*, vol. D80, p. 064028, 2009.

[7] M. Han, "Semiclassical Analysis of Spinfoam Model with a Small Barbero-Immirzi Parameter," *Phys. Rev. D*, vol. 88, p. 044051, 2013.

[8] F. Hellmann and W. Kaminski, "Holonomy spin foam models: Asymptotic geometry of the partition function," *JHEP*, vol. 10, p. 165, 2013.

[9] J. R. Oliveira, "EPRL/FK asymptotics and the flatness problem," *Class. Quant. Grav.*, vol. 35, no. 9, p. 095003, 2018.

[10] J. Engle and W. Kaminski, private communications and ILQGS seminar "Panel on the status of the vertex"

[11] E. Magliaro and C. Perini, "Emergence of gravity from spinfoams," *EPL*, vol. 95, no. 3, p. 30007, 2011.

[12] M. Han, "On Spinfoam Models in Large Spin Regime," *Class. Quant. Grav.*, vol. 31, p. 015004, 2014.

[13] S. K. Asante, B. Dittrich, and H. M. Haggard, "Effective Spin Foam Models for Four-Dimensional Quantum Gravity," arXiv:2004.07013, 2020.

[14] P. Dona and G. Sarno, "Numerical methods for eprl spin foam transitionamplitudes and lorentzian recoupling theory," *Gen. Rel. Grav.*, vol. 50, p. 127, 2018.

[15] S. Speziale, "Boosting Wigner's nj-symbols," J. Math. Phys. **58** (2017) no.3, 032501, doi:10.1063/1.4977752

[16] P. Dona, M. Fanizza, G. Sarno, and S. Speziale, "SU(2) graph invariants, regge actions and polytopes," *Class. Quant. Grav.*, vol. 35, no. 4, p. 045011, 2018.

[17] P. Dona, M. Fanizza, G. Sarno, and S. Speziale, "Numerical study of the lorentzian engle-pereira-rovelli-livine spin foam amplitude," *Phys. Rev.*, vol. D100, no. 10, p. 106003, 2019.

[18] P. Dona, F. Gozzini, and G. Sarno, "Searching for classical geometries in spin foam amplitudes: a numerical method," Class. Quant. Grav. **37** no.9, 2020.

[19] V. Bayle, F. Collet, and C. Rovelli, "Short-scale Emergence of Classical Geometry, in Euclidean Loop Quantum Gravity," 2016.

[20] The code to compute the amplitude, the Wolfram Mathematica notebooks that compute the boundary data and perform the numerical analysis of the amplitude are available here.

[21] J. C. Baez, "An Introduction to spin foam models of quantum gravity and BF theory," *Lect. Notes Phys.*, vol. 543, pp. 25–94, 2000.

[22] A. Perez, "The spin foam approach to quantum gravity," *Living Rev. Rel.*, vol. 16, p. 3, 2013.

[23] D. A. Varshalovich, A. N. Moskalev, and V. K. Khersonskii, *Quantum Theory of Angular Momentum.* World Scientific, 1988.

[24] J. W. Barrett, W. J. Fairbairn, and F. Hellmann, "Quantum gravity asymptotics from the su(2) 15j symbol," *Int. J. Mod. Phys. A*, vol. 25, pp. 2897–2916, 2010.

[25] J. Engle, "Proposed proper Engle-Pereira-Rovelli-Livine vertex amplitude," *Phys. Rev. D*, vol. 87, no. 8, p. 084048, 2013.

[26] L. Hörmander, "The Analysis of Linear Partial Differential Operators I: Distribution Theory and Fourier Analysis," Classics in Mathematics, Springer Berlin Heidelberg, 2015.

[27] A. P. Yutsis, I. B. Levinson, and V. V. Vanagas, "Mathematical apparatus of the theory of angular momentum," Israel Program for Scientific Translations for National Science Foundation and the National Aeronautics and Space Administration, Washington D.C.,1962. 1962.

[28] A. M. Perelomov, *Generalized coherent states and their applications.* Texts and monographs in physics, Berlin: Springer, 1986. OCLC: 12972287.

[29] J. W. Barrett, M. Rocek and R. M. Williams, "A Note on area variables in Regge calculus," Class. Quant. Grav. **16** (1999), 1373-1376 doi:10.1088/0264-9381/16/4/025

[30] P. Dona and S. Speziale, "Large spin limit of the EPRL-KKL spin foam vertex amplitude," in preparation.

[31] P. Dona and S. Speziale, "Asymptotic of spin foam amplitudes with many vertices," in preparation.